Molecular Mechanisms of Lymphatic Invasion in Pancreatic Ductal Adenocarcinoma.

Naidoo, Kalnisha

Molecular Mechanisms of Lymphatic Invasion in Pancreatic Ductal Adenocarcinoma

Kalnisha Naidoo

PhD Thesis

Barts Cancer Institute
Centre for Molecular Oncology
Barts and the London School of Medicine and Dentistry
Queen Mary University of London

For the shades...

‘Matter, that thing the most solid and well-known, which you are holding in your hands and which makes up your body, is now known to be mostly empty space. Empty space and points of light. What does this say about the reality of the world?

Jeanette Winterson, *Sexing the Cherry*

DECLARATION

I declare that the work presented in this thesis is my own, except where stated otherwise in the text and this work has not been submitted for any other degree or professional qualification except as specified. The work was performed between September 2008 and December 2011 in the Centre for Molecular Oncology, Barts Cancer Institute, Barts and The London School of Medicine and Dentistry, Queen Mary University of London.

(Kalnisha Naidoo)

May 2012

ABSTRACT

Pancreatic Ductal Adenocarcinoma (PDAC) is one of the five leading causes of cancer-related deaths in the West, and this, largely, is due to metastatic disease. In order to better understand PDAC metastatic spread and identify novel therapeutic targets, we analysed the proteome of primary tumours and matched lymph node (LN) metastases. As frozen specimens of metastatic lesions are scarce, we examined formalin-fixed paraffin-embedded (FFPE) tissues. Whilst such tissue is in routine diagnostic use, the cross-linkages induced by fixation have, in the past, precluded proteomic investigation for research purposes. Recent technological advances have, however, overcome this technical limitation.

Using laser capture microdissection (P.A.L.M system), we isolated malignant epithelia from seven FFPE primary PDAC tumours and matched LN metastases. Following dissection, samples were analysed in duplicate using Multidimensional Protein Identification Technology (MudPIT); this resulted in the identification of 1504 proteins, 854 of which were common to all samples analysed. Comparison of the obtained proteins with data from previous proteomics studies on pancreatic tissue, pancreatic juice, serum and urine resulted in a less than 30 % overlap, indicating that our study has expanded the current database of proteins expressed in this malignancy substantially. Statistical analysis further showed that 115/854 proteins (13.5%) were significantly differentially expressed (g-value ≥ 3.8). Two proteins, S100P and 14-3-3 sigma, with highly significant g-values were confirmed to be significantly differentially expressed (S100P: $p = 0.05$ and 14-3-3 sigma: $p < 0.001$)

in a larger series of 55 cases of matched primary PDAC and LN metastases using immunohistochemistry.

We chose to investigate further the roles of S100P in lymphatic invasion *in vitro* and *in vivo*. By co-culturing a Panc1 S100P-overexpressing clone (S5L), or a vector control clone (V3L), with human dermal lymphatic endothelial cells (HDLEC), we were able to show that different receptors mediate S5L adhesion to resting and activated HDLEC as opposed to V3L; and that the presence of S5L cells in these co-cultures significantly increased permeability at one ($p = 0.02$), four ($p = 0.002$) and eight ($p = 0.007$) hours post-seeding, and significantly increased translymphatic endothelial migration at 72 hours ($p = 0.006$). Using the V3L and S5L cell lines, which were transduced to express luciferase, we also created an orthotopic mouse model of PDAC, as well as experimental metastatic mouse models, in CD1 nude mice. These models were used to evaluate the effects of S100P on primary tumour growth, metastasis and site-specific growth. S100P was only found to significantly increase primary tumour growth in this model ($n = 10$ animals/group), both by bioluminescence ($p = 0.002$) and tumour weight ($p = 0.01$). No metastases (spontaneous and/or experimental) were seen however. Thus, this model can be used to evaluate the anti-tumour efficacy of novel therapies to S100P in the future.

ACKNOWLEDGEMENTS

To my supervisor, Dr Tatjana Crnogorac-Jurcevic, thank you for your supervision and guidance during this process.

To my co-supervisor, Prof Ian Hart, thank you for your relentless pursuit of perfection; for your perceptive insights; and for your take on the art of the soluble. It has been a privilege.

To my collaborators, Richard Jones, Hemant Kocher and Nilukshi Wijesuriya, thank you for all your help with the proteomics work. To Nilu, for being an older sister. And to Hemant, for your quiet counsel when I most needed it.

To my colleagues: Sayka Barry, Kate Lines, Tomasz Radon, Laurent Dumartin and Wasfi Alrawashdeh, thanks for creating a great atmosphere for scientific thought. Special thanks to Wasfi for his help with the orthotopic mouse model. Also, to Rachel Barrow and Lara Boyd, this process would not have been possible without your advice, insight and friendship.

To the network of friends that I have accumulated through my travels, thank you for your constant support across multiple time-zones. I shudder to think how I would have survived this PhD without Skype and Facebook. Special thanks to my housemate Colin and my cousin Kesh who survived the sarcoid.

To Kebs, thank you for always letting me darken your doorstep, and for your generosity of self.

To Louise, because if nobody speaks of remarkable things...

To my sisters, Prishani and Sanushka, who stand at-the-ready, waiting to catch me and mop up my tears, as big sisters should. And for being as curious as I am in your exploration of the world at large.

To my nephew, Akhil, for reminding me of what the world looks like unjaded.

To Aunthy Thols and Uncle Jackie, my feet always seem to find their way to 64 Galpins Rd whenever things look grim. You have been my home away from home.

And finally, to my parents, who have shaped their lives around mine being better. I am so grateful for your constant love and support. Thank you for understanding that I always have to do it my way – even if it means getting hurt in the process.

TABLE OF CONTENTS

LIST OF TABLES

LIST OF FIGURES

APPENDICES

GLOSSARY OF ABBREVIATIONS

Ab	Antibody
ADH	Atypic ductal hyperplasia
ALT	Alternative lengthening of telomeres
ANGPT2	Angiopoeitin 2
ATP	Adenosine triphosphate
BCA	Bicinchoninic acid
BM	Basement membrane
BSA	Bovine serum albumin
BTL	Barts and the London
BVEC	Blood vascular endothelial cells
CCL21	Chemokine ligand 21
CCR7	Chemokine receptor 7
cDNA	Complementary DNA
CID	Collision-induced dissociation
CK-8	Cytokeratin-8
CLEC-2	C-type lectin domain family receptor 2
CLEVER-1	Common lymphatic endothelial and venous endothelial receptor 1
CM	Conditioned media
CNS	Central nervous system
DEPC	Diethyl pyrocarbonate
DNA	Deoxyribonucleic acid
DNase	Deoxyribonuclease

DMEM	Dulbecco’s Modified Eagle’s Medium
DMSO	Dimethyl sulfoxide
DPC4	Deleted in pancreatic cancer 4
DTC	Disseminated tumour cells
DTT	Dithiothreitol
ECM	Extracellular matrix
ECS	Extracellular space
EDA FN	Fibronectin containing extra type III domain A
EDTA	Ethylenediamine tetraacetate
EFNB2	Ephrin B2
ELISA	Enzyme-linked immunosorbent assay
EMILIN1	Elastin microfibril interfacer 1
EMT	Epithelial-mesenchymal transition
FC	Flow cytometry
FCS	Foetal calf serum
FDR	False Discovery Rate
FFPE	Formalin-fixed paraffin-embedded
FN	Fibronectin
FOXC2	Forkhead box C2
GEP	Gene expression profiles
GICRMDP	Gastrointestinal Cancer Rapid Medical Donation Program
HA	Hyaluronic acid
HA-H	Melanoma cell line expressing high levels of hyaluronic acid
HA-L	Melanoma cell line expressing low levels of hyaluronic acid
HDLEC	Human dermal lymphatic endothelial cells

HER2/Neu	Human epidermal growth factor receptor 2
HPNE	Human Pancreatic Nestin Expressing
HSC 70	Heat shock cognate 71kDa protein
hTERT	Holoenzyme telomerase
HUVEC	Human umbilical venous endothelial cells
ICAM-1	Inter-cellular adhesion molecule -1
ICC	Immunocytochemistry
IFN	Interferon
IHC	Immunohistochemistry
IPA	Ingenuity Pathway Analysis
LC/MS/MS	Liquid chromatography mass spectometry
LCM	Laser capture microdissection
LEC	Lymphatic endothelial cells
LLC	Lewis Lung Carcinoma
LN	Lymph node
LPE	Local-Pooled-Error test
LVD	Lymphatic vessel density
LYVE-1	Lymphatic vessel endothelial hyaluranon receptor -1
MADH4	mothers against decapentaplegic, Drosophila, homolog of, 4
MALDI-TOF	Matrix-assisted laser desorption and ionisation time-of-flight
MDCK	Madin-Darby Canine Kidney
MS	Mass spectometry
MudPIT	Multidimensional Protein Identification Technology
NF-KB	Nuclear factor kappa-light-chain-enhancer of activated B cells
NHS	National Health Service

OD	Optical density
PAGE	Poly Acrylamide Gel Electrophoresis
PanIN	Pancreatic Intra-epithelial Neoplasia
PCR	Polymerase chain reaction
PBS	Phosphate-buffered saline
PDAC	Pancreatic Ductal Adenocarcinoma
PDPN	Podoplanin
PECAM	Platelet endothelial cell adhesion molecule
POT1	Protection of telomeres protein 1
Prox-1	Prospero homeobox 1
Ptch	Patched
RAGE	Receptor for advanced glycation end-products
RhoA	Ras homolog gene family, member A
RNA	Ribonucleic acid
RNase	Ribonuclease
ROI	Region of interest
RP	Reverse phase
SAGE	Serial analysis of gene expression
S5L	S100P over-expressing cells that express luciferase
SCM	Serum-containing media
SCX	Strong cation exchange resin
SFM	Serum-free media
SDS	Sodium dodecyl sulphate
SHH	Sonic Hedgehodge
shRNA	Short hairpin RNA

siRNA	Short interfering RNA
SMAD4	Smad family member 4
SMO	Smoothened
Sox-1	SRY-related HNG domain transcription factor
TGF-β	Transforming growth factor β
TLEM	Translymphatic endothelial migration
TMA	Tissue microarray
TNF	Tumour necrosis factor
TNM	Tumour node metastasis
TP53	Tumour protein 53
TRF1	Telomeric repeat binding factor 1
V3L	Vector control cells that express luciferase
VCAM-1	Vascular cell adhesion molecule-1
VE-Cadherin	Vascular endothelial cadherin
VEGF	Vascular endothelial growth factor
VEGFR	Vascular endothelial growth factor receptor
WB	Western blot
ZO	Zona occludens
2D-DIGE	Two-dimensional difference gel electrophoresis

1. INTRODUCTION

1.1 Pancreatic Ductal Adenocarcinoma

Pancreatic Ductal Adenocarcinoma (PDAC) causes an estimated 227,000 deaths per year worldwide, and ranks as one of the five leading causes of cancer-related deaths in the Western world. The five-year survival rate for PDAC is less than 5%, regardless of age, race and/or sex (1,2). These statistics reflect the fact that little progress has been made in the past 30 years in the management of this disease. Due to the latent, non-specific nature of the symptoms, most patients present late, once metastases already are present. Thus, there is an urgent need to increase our understanding of the pathogenesis of PDAC; improve our capacity both to diagnose this disease earlier and monitor its progression; and to develop novel therapies to treat metastatic disease.

1.1.1 Multi-step Tumourigenesis

The multi-step model of PDAC progression is well-established (**Figure 1**). It describes the histological and genetic changes that occur in the pancreatic ductal epithelia as cancer develops (3–5).

Initially, the normal epithelium undergoes premalignant change, transitioning through three stages of 'Pancreatic Intra-epithelial Neoplasia' (PanIN). These lesions, characteristically, are contained by an intact basement membrane, and are classified according to the amount of cytological and architectural atypia present. The normal

pancreatic duct is lined by simple cuboidal epithelium. In PanIN-1, cells undergo metaplasia in which a change from cuboidal to columnar epithelium occurs (PanIN-1A). In addition, cells adopt either a papillary, micropapillary or basally pseudostratified architecture (PanIN-1B). PanIN-2 lesions, by definition, show nuclear abnormalities, e.g. loss of polarity, hyperchromatism, nuclear crowding, enlarged nuclei and pseudostratification. Mitotic figures are rare at this stage but, if present, they should be nonluminal and not atypical. In PanIN-3 (carcinoma in-situ), the dysplasia is more pronounced at a cytonuclear level. Architecturally, cells begin budding into the lumen (cribriforming), and luminal necrosis may be present. Invasive cancer is defined by a breach of basement membrane, with cells moving out into the surrounding tissue (3–5).

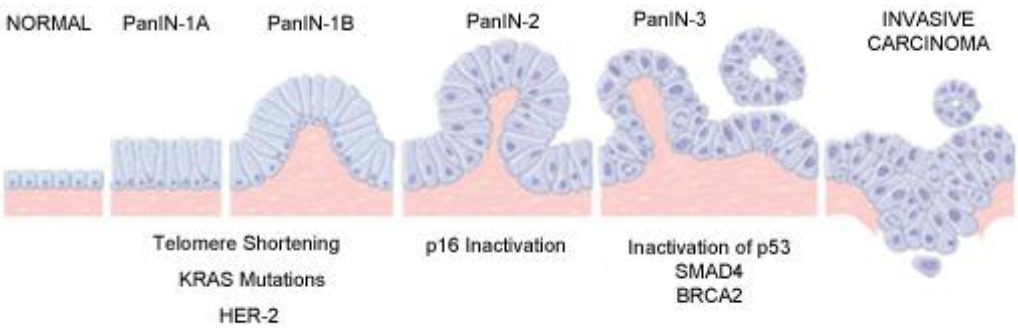

Figure 1 Progression model for the development of PDAC. Histological changes showing a progressive increase in cytological and architectural atypia are paralleled by a sequence of molecular alterations. These changes are thought to follow a linear temporal progression. However, the total number of mutations acquired is more important than the order in which they appear (Adapted from Robbins and Cotran Pathological Basis of Disease (5)).

Concurrent with these histological changes, a number of genetic changes occur.

Telomere shortening is the earliest genetic change seen in PDAC (6). These structures are located at the ends of chromosomes and in humans contain the tandemly repeated hexanucleotide sequence 5'-TTAGGG-3' in conjunction with a number of telomere-binding proteins such as TRF1 and POT1 (7,8). These together form the functional telomere, which acts as a 'protective shield', preventing chromosomes from fusing with one another. Telomere loss occurs with every cell division, resulting ultimately in breakage-fusion-bridge cycles, and a resultant increase in chromosomal instability (9–13). Whilst it has been shown that telomere loss is important for the initiation of carcinogenesis, equally important is the emergence of the holoenzyme telomerase (hTERT) at a later stage in carcinogenesis, particularly at the point of conversion from a premalignant lesion to an invasive one (14). There are conflicting data at present as to the relevance of hTERT expression in PDAC. Current reports of hTERT mRNA quantification in PDAC tissues range from 41% to 83% (15,16). Whilst hTERT quantification in pancreatic juice indicates expression in the majority of PDACs, such tests currently are unable to distinguish benign from malignant disease (16,17). Furthermore, mouse data suggest that pancreatic carcinogenesis can progress in the absence of functional telomerase, raising the question of whether or not an alternative lengthening of telomeres (ALT) mechanism exists in PDAC (18). Finally, even in the absence of hTERT or ALT, the high prevalence of p53 mutations in PDAC (see below) may accelerate progression to invasive PDAC by allowing chromosomally unstable cells to proliferate by failing to initiate apoptosis and/or crisis (19).

In PanIN-1, the functional alteration of two proto-oncogenes, HER-2/Neu and KRAS, permanently activates intracellular signalling pathways, affecting proliferation, cell-cycle, apoptosis, cell shape and motility.

HER-2/Neu, a tyrosine kinase receptor of the epidermal growth factor receptor family, rarely is over-expressed in histologically normal pancreatic ducts, but is over-expressed in 80% of PanIN-1 lesions (20). However, the expression levels of HER-2/Neu in PDAC are significantly lower, averaging across studies at less than 30% (20–24). These HER-2/Neu positive tumours typically result from increased transcription and translation of this receptor, with gene amplification being present in fewer cases; no mutations or receptor truncations have been identified, as yet (23,25). Several studies have shown that a positive HER-2/neu status significantly correlates with tumour stage, and negatively affects survival (23,26). However, no positive association with tumour grade has been demonstrated (26,27). In fact, HER-2/Neu has been shown to be absent in poorly differentiated PDAC tumours, and strongly expressed in moderately or well differentiated tumours. The use of anti-HER-2/Neu antibodies as adjuvant therapy for PDAC currently is under clinical investigation (28).

KRAS undergoes a point mutation in 80–90% of PanIN-1 lesions - predominantly at codon 12, although codons 13 and 61 also can be affected (5,29). This results in constitutive activation of this GTP-binding protein. Furthermore, the expression of oncogenic KRAS in the pancreas of animal models, without other genetic abnormalities, is sufficient to induce the development of PanIN lesions which closely resemble human morphology (30,31). Interestingly, as oncogenic KRAS expression

in mouse models is driven by PDX-1 in the islet cells and P48/PTF-1A in the acinar cells of the pancreas, these models suggest that PDAC originates in the acinar, rather than the ductal, epithelia. Recently however, Shi et al. used the 'almost ubiquitous' expression of KRAS mutations in PDAC to trace the 'cell of origin' from which PDAC arises in human tissue samples (32). Acinar and stromal cells were found to express wild-type KRAS in this study, whilst cells from PanIN lesions expressed mutated KRAS. Of note, only acino-ductal metaplastic (ADM) lesions associated with PanIN, and not isolated ADM, harboured KRAS mutations. Furthermore, each ADM mutation found was identical to the mutation found in the associated PanIN lesion(s). Thus, the authors suggest that pancreatic neoplasia does not originate in acinar cells, in contrast to data obtained from mouse models

Activation of tumour oncogenes is followed by loss of tumour suppressor genes in PanIN-2 and PanIN-3. This allows cells to overcome senescence, resulting in unopposed proliferation. The three most common tumour suppressor genes inactivated in PDAC are CDKN2A/p16^{ink4A}, TP53 and DPC4/SMAD4. Furthermore, for all three of these genes, inactivation is due largely to loss of heterozygosity (LOH). A summary of these genes, including chromosomal location, mechanism of action and prevalence can be found in **Table 1** (5).

Table 1 The chromosomal location, normal mechanisms of action, and prevalence of three tumour suppressor genes commonly affected in PDAC (5).

Gene	Location	Mechanism of Action (in normal cells)	Prevalence in PDAC
CDKN2/p16^{INK4A}	9p21	• Cell cycle arrest (via CDK4/6)	• 95% of PDAC
TP53	17p13	• Cell cycle arrest • DNA repair • Apoptosis • Blocks angiogenesis	• 50-70% of PDAC
DPC4/SMAD4	18q21	• TGF-β induced growth inhibition	• 55% of PDAC

The gene CDKN2/INK4A encodes the protein p16, which inhibits cell cycle progression from G1 into S phase by binding to the cyclin-dependent kinases Cdk4 and Cdk6, thus preventing these molecules from binding to cyclin D1 (33). Mechanisms of p16 loss include homozygous deletion, intragenic mutation with loss of the second allele and epigenetic silencing by promoter methylation (34–36). Loss of nuclear p16 is found in PanINs associated both with cancer and chronic pancreatitis, although the frequency is lower in chronic pancreatitis (37).

The bi-allelic inactivation of the TP53 gene almost always is due to a combination of intragenic mutation with loss of the second allele (38). Loss or alteration of p53

protein allows cells to bypass DNA damage checkpoints and evade apoptosis (39). In addition, as mentioned above, there is now evidence that p53 loss may contribute to the genomic instability seen in PDAC (19,40). Generally, p53 loss is considered to be a late event in PDAC progression, with accumulation of this protein being seen in advanced PanIN 3 lesions (41).

Lastly, loss of the Deleted in Pancreatic Cancer 4 or DPC4 gene (also known as SMAD4 or MADH4) results in an interference with intracellular signalling downstream of the transforming growth factor β (TGF- β) family of cell surface receptors, decreasing growth inhibition and increasing proliferation (33,42). DPC4 loss is a late event in PDAC progression, and is evident only in PanIN 3 lesions (43).

Interestingly, the combination of each of these tumour suppressor genes with KRAS mutations in mice results in the development of invasive pancreatic cancer; a phenomenon whose utilisation has increased the number of mouse models available for preclinical investigation (40,44,45).

1.2 Metastasis

1.2.1 Tumour Evolution and Spread

Metastasis has been defined as ‘the spread of cells from the primary neoplasm to distant organs, and their relentless growth’ (46).

It has long been thought that tumours invade and spread through a series of sequential steps termed ‘the invasion-metastasis cascade’ (**Figure 2**) (46). According to this model, locally invasive cancer cells gain entry into blood or lymphatic vessels (intravasate), survive and travel in these vessels to distant sites, where they move out of the vessels (extravasate) into foreign environments. Secondary tumour growth (colonisation) occurs initially as micrometastases (i.e. single or small clumps of cells) which, over time, adapt and grow into macrometastases (> 2 mm in diameter).

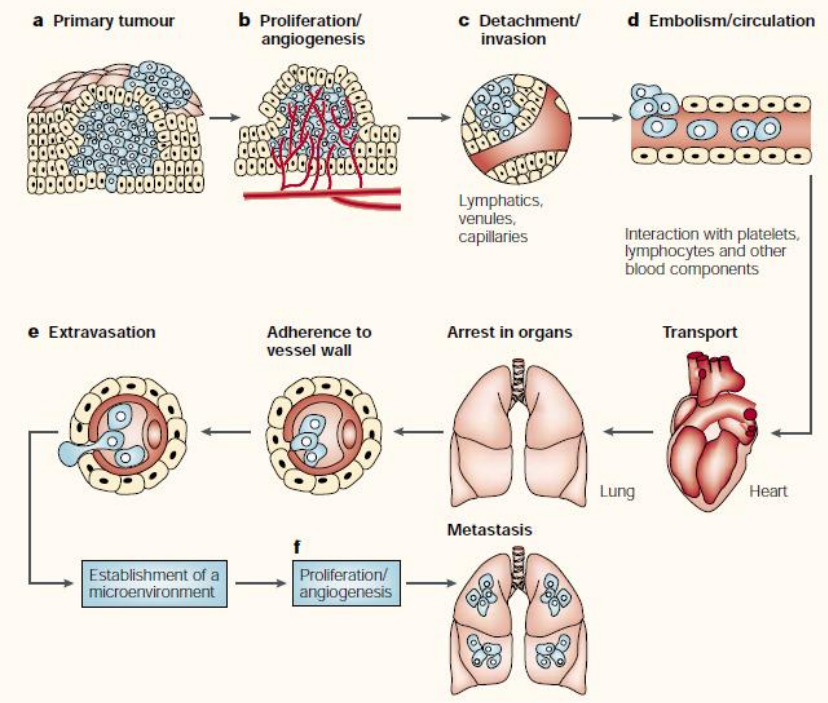

Figure 2 The 'invasion-metastasis cascade'. **a.** Cellular transformation and primary tumour growth. **b.** Extensive vascularisation (angiogenesis) must occur for the primary tumour to exceed 1-2 mm in diameter. **c.** Intravasation. **d.** Survival inside the lymphatic and blood circulatory systems. **e.** Extravasation. **f.** Colonisation (46)

According to the classic theory of metastasis (46), metastatic tumours are derived from a single clone. As a tumour grows, the tumour population becomes increasingly genetically unstable, giving rise to 'intra-lesional heterogeneity'. Within this evolving population, selection pressures and epigenetic mechanisms then govern which clone(s) will be able to metastasise. Thus, each metastatic tumour arises from a single progenitor cell (inter-lesional heterogeneity) which then establishes a heterogenous metastatic tumour via the same process that occurred in the primary tumour. This theory was founded largely on the work of Fidler and Kripke, and is

based on data obtained from experiments in which cell lines (predominantly melanoma) were grown and/or injected into mouse models (46–48). A variety of techniques were used in order to create clones with varying metastatic capacities, including the *in vitro* and *in vivo* selection of clones from parental cell lines, and radiation-induced genetic instability. An intriguing finding of these studies, and one which often is forgotten, is that tumour heterogeneity exerts a stabilising effect on the tumour population. Indeed, a parental cell line maintains its metastatic capacity for years *in vitro*, whilst individual clones which are either isolated from this parental population or subjected to a strong selection pressure, e.g. chemotherapy, show an increased metastatic potential. When these clones are once again merged into a polyclonal population however, equilibrium is restored. Thus, 'the society of tumour cells imposes regulatory constraints upon its individual members'. For Fidler and Hart, the very existence of this phenomenon argues against the random nature of metastasis, and suggests that, as this process is regulated, it can be successfully manipulated by therapeutic intervention (46–48).

The advent of sequencing technology has allowed for these analyses to be extended to human tissues. Using 'comparative lesion sequencing' in colorectal cancers, in conjunction with a mathematical model derived from the passenger mutation rate, Jones et al. have proposed that it takes approximately 17 years for benign adenomas to develop into advanced carcinomas whilst, thereafter, the ability to metastasise is acquired fairly quickly though a relatively small number of additional mutations (49). Based on sequencing data obtained from 13 patients, the authors propose two evolutionary models: in model A, none of the cells within the primary tumour are able to metastasise, but require only a few genetic alterations in order to gain that

capacity; and in model B, all of the cells within the primary tumour have the ability to metastasise, without any further genetic alterations being required. Whilst it could be argued that model A represents the classic theory of metastasis, model B could represent an alternative theory - that of the early 'metastatic gene signature'. In contrast to the classic theory, this suggests that metastatic potential is a pre-ordained feature of certain primary solid tumours, and is not governed by selection pressures. In 2003, Ramaswamy et al. published a 17 metastatic gene signature that could be associated with medulloblastomas and a number of adenocarcinomas (lung, breast, prostate), but not with diffuse large B cell lymphomas (50). This signature comprised genes originating from both the epithelial and stromal compartments of the analysed tumours, and reflects the fact that tumours were not laser capture microdissected before profiling. Thus, the authors emphasise that metastasis arises from the interplay of various cell populations within the tumour mass, and not from the epithelial component in isolation; a concept which reflects the hallmarks of cancer as proposed by Weinberg and Hanahan (51). Ramaswamy's paper raises an interesting question: does 'heterogeneity' exist in the epithelial population, as originally thought, or is 'heterogeneity' a product of crosstalk between a community of varied cell populations? For Fidler and Kripke, the divergence of these two models represents our inability to monitor the development of tumour heterogeneity in real time (52). If one concedes that gene expression signatures represent a snapshot in primary tumour evolution, then one cannot rule out the possibility that, if profiling were performed on a polyclonal epithelial tumour population in aggregate, some clones within the tumour mass could show a change in metastatic genes, whilst other clones simultaneously could show a change in genes governing proliferation. Thus, whilst comparing primaries and their

metastases provides us with clues as to how metastasis occurs, it cannot accurately quantify its kinetics. What is perhaps of more practical significance, however, is that analysing primary tumours for such ‘signatures’ increases our capacity to predict which tumours are most likely to metastasise, and therefore, to stratify patients in terms of risk and treatment. Thus, a move towards the molecular classification of solid tumours was established.

According to Bernards and Weinberg, one of the major implications of the ‘metastatic gene signature’ theory is that metastatic genes do not exist *per se*, but rather, that metastasis is governed by the same oncogenes and tumour suppressor genes which have been studied for years (53). The authors reason that if this were not the case, then cells with a metastatic phenotype would constitute only a small proportion of the primary tumour, which, if one considers the low success rate of individual cells trying to metastasise, would make metastasis almost impossible. Thus, the mutations that confer a replicative advantage to tumours early in tumourigenesis, must also confer a metastatic advantage later on in tumour evolution. In essence, this paper emphasises the importance of the genomic instability generated by increased proliferation, rather than tumour size, as the driver behind metastasis.

This view has been challenged by the parallel progression model (54). According to this theory, the early dissemination of cancer cells from primary tumours to various mesenchymal tissues in the body allows for the simultaneous growth of primary tumours and metastases. Evidence for this model derives, in part, from the whole genome analysis of disseminated tumour cells (DTC) isolated from pre-operative patients with breast, prostate and oesophageal cancers (55–61). In these studies,

DTCs from patient bone marrows harboured fewer genetic aberrations than their matched primary tumours. Thus, the authors conclude, dissemination must have occurred prior to the acquisition of whole genome instability. Further evidence for the early escape of cancer cells from premalignant lesions came from Husemann et al. who used transmission electron microscopy to capture cells escaping from atypic ductal hyperplastic (ADH) lesions in a Balb-NeuT transgenic mouse model; dormant cells with malignant potential were also demonstrated in the bone marrows and lungs of these mice at this premalignant stage (62). These findings were extended to 607 human breast cancer samples, in which the number of DTCs found in patient bone marrows did not correlate with tumour size, and thus, stage. The final paper challenging Weinberg's 'progression puzzle' was published in 2008 by Podsypanina et al., and showed that oncogene expression does not affect survival and extravasation of DTCs, but rather that these genes are required only for secondary tumour growth (63). These experiments were conducted in experimental metastatic mouse models; untransformed mouse mammary cells in which the transgenes MYC and KRAS, or polyoma middle-T, could be expressed inducibly, were injected into the tail veins of $Rag1^{-/-}$ mice. Lung tumours developed in the recipient mice only upon doxycycline administration at various time-points. Thus, the untransformed cells were able to survive in the bloodstream and extravasate into the lungs, remaining dormant without oncogene activation.

Finally, the 'seed and soil' theory, as originally proposed by Paget in 1889, emphasises the importance of the tumour microenvironment in the metastatic process (64). By recognising the importance of 'congenial soil' in determining the growth of a metastatic clone, Paget was the first to highlight the intricacies of the

colonisation step in the metastatic cascade. By acknowledging the importance of the 'seed', he recognised the importance of tumour as heterogenous tissue. And by emphasising the interaction of seed with soil, he recognised the selective nature of the metastasic process. His observations still hold true today.

1.2.2 Metastasis in PDAC

Little is known about the metastatic process in PDAC. This is largely due to the limited availability of tissue samples for analysis, as patients with metastatic disease are not amenable to surgery. Access to tissue samples has improved since the establishment of the Johns Hopkins Gastrointestinal Cancer Rapid Medical Donation Program (GICRMDP) which harvests rapid autopsy frozen samples for research (65); however access to surgically resectable PDAC samples and/or metastases remains difficult. Prior to the GICRMDP, only two studies had analysed the gene expression profiles (GEP) associated with PDAC metastases by correlating data obtained from fresh frozen primary tumours with clinicopathological parameters; the metastatic tissue itself was not analysed. In 2004, Nakamura et al. compared the GEP of laser microbeam microdissected PDAC to that of adjacent histologically normal ductal epithelia (n = 18 in total; n = 13 with known lymph node status) (66). Of the 606 differentially expressed genes found, 76 genes (35 up–regulated and 41 down-regulated) showed a positive association with lymph node (LN) metastases. In 2007, Kim et al. analysed the GEP of 10 macrodissected PDAC samples, five of which had positive LNs (67). In this study, 194 differentially expressed genes (66 up–regulated and 128 down-regulated) were found to positively correlate with LN metastases. Comparison of the gene sets obtained from these two studies showed

virtually no overlap, which most likely reflects the technical differences between the two studies. Firstly, Nakamura et al. isolated a pure population of cancer cells using laser microbeam microdissection, whereas Kim et al. analysed whole tissue samples which contained stromal tissue; secondly, the DNA microarray used by Kim et al. contained approximately 15,000 more genes than that used by Nakamura et al.; and lastly, Nakamura et al. analysed their data by first comparing all pancreatic cancer samples to adjacent histologically normal pancreatic tissue, and then stratified the cancer samples into those with or without LN metastases, whilst Kim et al. only compared the GEP of PDACs with LN metastases to those PDACs without LN metastases.

In 2008, Jones et al. sequenced 24 autopsy-derived primary PDAC samples, obtained from seven patients, in order to catalogue the somatic mutations found in PDAC (68). Of the 69 altered gene sets found, 31 were validated at a transcript level using serial analysis of gene expression (SAGE). Importantly, this transcriptome could be classified into 12 core signalling pathways, which are now considered to be central to PDAC pathogenesis. Although not stated in the article, these 12 pathways can, in turn, be classified into the six hallmarks of cancers (51). Importantly, the authors suggest that future therapies should aim to target the point at which these aberrations converge (i.e. the processes which they affect), rather than the genetic defects themselves.

In the same year, Campagna et al. found that very few changes occur between the transcriptomes of primary pancreatic tumours and their metastases (69). As RNA from half of the 60 available samples had degraded following macrodissection, 30

matched and unmatched frozen tissue samples ultimately were analysed, representing five surgically-resected primary PDACs; five autopsy-derived primary tumours; and 20 autopsy-derived metastases from liver, lung, peritoneum and lymph nodes. Interestingly, although no appreciable change was demonstrated between primary tumours and metastases when analysed *en masse*, differential expression was found between each matched pair, suggesting that tumours did evolve within each patient. Furthermore, 242 genes were found to be differentially expressed between the primary tumours obtained from surgery (pT2 or pT3), and the primary PDACs with co-existent metastatic disease (pT4) obtained at autopsy. Thus, it is possible that early stage primary lesions do differ significantly from metastatic lesions. As the surgical lesions were unmatched however, such a comparison was not possible in this study.

More recently, Yachida et al. (70) sequenced autopsy-derived PDAC metastases from seven patients, whose primary tumours previously had been sequenced by Jones et al. (68). Using comparative lesion sequencing, in conjunction with the mathematical model previously established for colorectal cancer (49), the authors propose a linear clonal evolution model for PDAC, in which, a 'therapeutic window of opportunity' of approximately 10 years exists during which metastasis may be prevented. A caveat to this model however, is that the kinetics are calculated using data obtained from patients with advanced metastatic disease, and may not accurately reflect the spatio-temporal evolution of metastases in real time. Furthermore, if at least 5 years are needed for metastasis to develop, as is suggested in this paper, why then do most patients with PDAC die within 5 years of diagnosis? The answer to this is not clear at present: either this model accurately

reflects the kinetics of metastasis in real time, and mortality is compounded by other factors e.g. late presentation, or the fact that the pancreas is a vital organ, loss of which results in pathophysiological disturbances which accelerates disease progression; or this model fails to include a variant of PDAC which metastasises at a faster rate.

In 2010, Campbell et al. (71) showed that genomic instability persists after dissemination in PDAC; emphasising the importance of selection and adaptation of cancers to new 'soils' as originally proposed by Paget. As in the above-mentioned studies, comparative lesion sequencing was performed on rapid autopsy-derived samples. However, for 10 of the 13 patients recruited to this study, sequencing was performed on cell lines derived from patient tissues - three representing resected primary tumours and seven representing index metastases. It could be argued, therefore, that this is the reason why the data obtained from this study match data derived from mouse studies, i.e. does altering the 'seed', for example by deriving cell lines *in vitro* from human tissue, alter the manner in which it interacts with the 'soil' in mouse models, and/or the sequencing data obtained *ex vivo*? However, evidence of clonal selection did extend to the two patients in which actual tissues (three metastases per patient) were sequenced.

To date, only one proteomic study analysing 10 primary pancreatic cancers with or without LN metastases has been performed on fresh frozen, needle microdissected samples using 2D-DIGE combined with MALDI-TOF (72). When the results of this study were correlated to clinicopathological parameters, 18 up- and 15 down-regulated proteins were found; of these, moesin, radixin and c14orf166 were

confirmed, by Western blot (WB) and Immunohistochemistry (IHC), to be up-regulated in primary PDAC with associated LN metastasis. No therapeutic targets were identified. And, most importantly, the LN metastases themselves were not analysed.

Although fresh frozen PDAC/metastatic tissues are limited in supply, a substantial archive of formalin-fixed paraffin-embedded (FFPE) tissues exists that is more readily accessible. These tissues traditionally have been considered sub-optimal for proteomic analysis; however, there is now mounting evidence that valuable information, comparable to data obtained from frozen specimens, can be retrieved from FFPE samples from a variety of human tissues (73–77), including the pancreas (78).

Whilst this ‘equivalence of fresh/frozen and FFPE proteomes’ was initially reported on prostatic tissues (73), the most comprehensive analysis was performed by Sprung et al. in 2009 (77). In this study, colon adenoma samples of a fixed dimension (60 µm diameter) were either snap-frozen or fixed in 10% formalin for 24 hours. All samples then underwent tryptic digestion, with subsequent iso-electric focusing in order to separate the complex peptide mixtures into 20 fractions, each of which was analysed using LC/MS/MS. The rationale behind using tissues of fixed dimensions was to ensure that equal, accurate quantities of protein were analysed between fresh frozen and FFPE samples, as it is known that those amino acids which contribute to copper reduction in bicinchoninic acid (BCA) assays are also modified by formalin during fixation. Indeed, this study showed that protein measurements of FFPE samples were consistently 56% lower than that of their fresh

frozen counterparts (77). Thus, a corrective factor was introduced prior to tryptic digestion to ensure equal protein loading. Furthermore, as formalin induces intra- and inter-molecular cross-linkages at the primary amines of lysine side-chains, the authors questioned if C-terminal lysine-containing peptides would be under-represented following shotgun proteomics; a hypothesis which proved to be true upon further analysis. However, this qualitative difference in peptide production was not found to alter protein identification; rather, it was shown that data analysis is the most important determinant of protein identification. The authors showed that a combined database search of both fresh frozen and FFPE inventories simultaneously yielded better results (90% overlap) than separate database searches (67% overlap) (77). The reason for this discrepancy lies in the two peptide requirement for peptide identification i.e. at least two fragmented peptides (see below) which are obtained via MudPIT must be realigned or matched to the parent protein in order for that to count as a positive result. Whilst this reduces the number of false positives, it can increase the number of false negatives. If, for example, a protein is identified by two peptides in fresh frozen tissue, but produces only a single peptide for identification in the FFPE tissue, then it would incorrectly be logged as being present in fresh frozen tissue but absent in FFPE tissue. If the data sets are analysed simultaneously however, the fresh frozen dataset 'rescues' that FFPE single peptide in terms of protein identification, correcting this error. Thus, whilst the two peptide criteria serve to increase the sensitivity of MudPIT, simultaneous searches using multiple databases aim to improve its specificity. In addition to the significant overlap found between the two tissue types using this method, the subcellular compartmental distributions of proteins found from both fresh frozen and FFPE tissues were nearly identical. Thus, the authors conclude that human FFPE

proteomes are equivalent to human fresh frozen proteomes. Finally, this study examined the effects of the duration of formalin fixation and storage on protein yield, proving that a fixation time of up to 2 days, and long-term storage of up to 10 years duration, did not affect proteomic analysis adversely (77).

These findings were extended to the human pancreas in 2009 by Reimel et al. (78), who showed a 69% overlap in peptide identification between frozen (340 proteins in total) and FFPE (370 proteins in total) human pancreatic samples. These samples had been macrodissected, digested in trypsin and analysed using nano-LC/MS/MS (78). The authors do not specify how the data were analysed in this study however; it would be interesting to note if the fresh frozen and FFPE data had been analysed simultaneously or not, as this would explain why only a 68% overlap was obtained (77). Nevertheless, these data are particularly relevant to the current study, as they validated, for the first time, the use of FFPE pancreatic tissues for proteomic analysis. The study also widened the scope of PDAC research; as patients with early stage PDAC who are amenable to surgery routinely have metastatic lymph node tissue processed for diagnostic purposes, these tissues now were considered eligible for research proteomics. Any data obtained from such FFPE samples also could be crucial to both understanding and potentially preventing metastasis.

A number of technological advances which increase the number of proteins that can be recovered from FFPE have emerged in the past decade. The Liquid Tissue MS Protein Prep Kit, which has been available commercially since 2005 (79), has been shown to retrieve unique peptides reproducibly from laser capture microdissected (LCM) FFPE specimens for downstream ‘shotgun’ proteomics (73,80).

Improvements to this reagent over the past few years have resulted in a 10-fold decrease in the amount of starting material required for proteomic analysis (200,000 LCM cells to 20,000 LCM cells over a period of three years) (73,80), which is of great benefit in diseases where specimens are scarce, like metastatic PDAC.

The parallel development of large-scale, high-throughput proteomic technologies has further increased the amount of data that can be obtained from relatively small amounts of tissue. Multidimensional Protein Identification Technology (MudPIT) is one such technique that separates peptides in a complex mixture in two dimensions; first on the basis of charge, and then on the basis of hydrophobicity (81) (**Figure 3**). This added dimension, or 'pre-fractionation' step, further reduces sample complexity; thus MudPIT has been shown to considerably increase the number of proteins identifiable by mass spectrometry (82–84). The principle behind MudPIT is basically one of fragmentation. A protein is fragmented, both enzymatically (trypsin) and via collision-induced dissociation (CID) (mass spectrometry), in order to decrease the likelihood that mistakes are made during the *in silico* analysis when the peptide is realigned for identification. Theoretically, as the length of the fragmented peptide increases, the margin of error for realignment (and thus identification) decreases (85). If one considers that there are 20 amino acids, and if one assumes that all amino acids are equal in terms of their capacity to bind each other (which is not necessarily true), then the probability of a single amino acid occupying a particular position in a peptide sequence is 1 in 20. Thus, for a peptide that has six amino acids residues, the theoretical probability of an amino acid occupying a particular position in a peptide is 1 in 20^6 (or 1 in 64,000,000). Even with these odds however, false positives do occur (85).

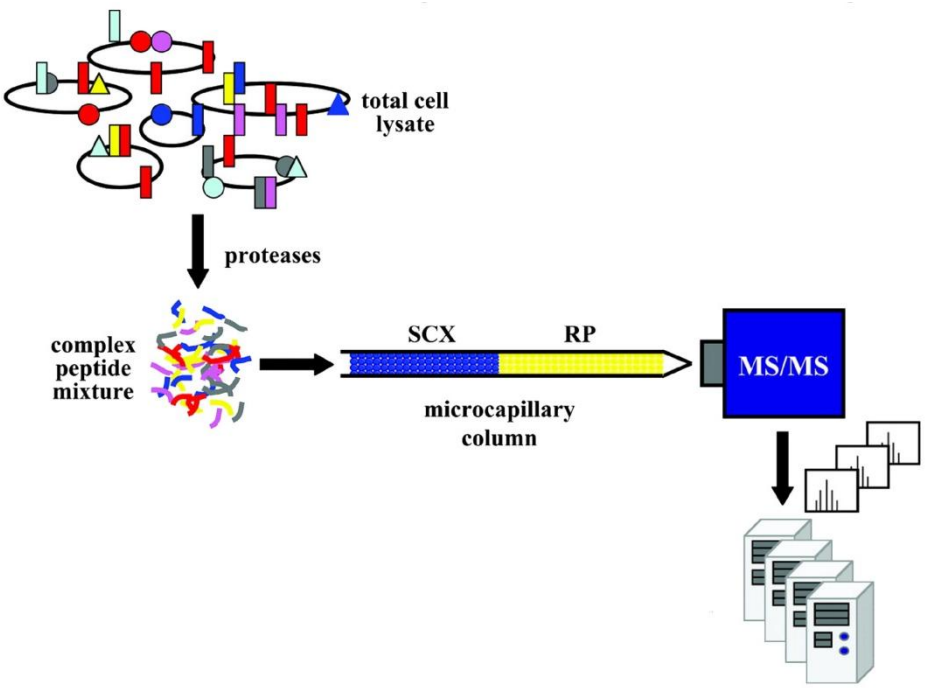

Figure 3 Multidimensional protein identification technology (MudPIT). Total cell lysate (e.g. laser capture microdissection PDAC tissue) first undergoes enzymatic digestion (e.g. using trypsin). This produces a complex peptide mixture, which subsequently is separated in two dimensions: first on the basis of charge via strong-cation exchange (SCX), and then on the basis of hydrophobicity using reverse-phase (RP) liquid chromatography. The resulting simplified or 'fractionated' peptide mixture then is analysed using mass spectrometry. The fragmented peptides resulting from this process are then realigned *in silico* in order to determine the protein composition of the starting material (Adapted from Whitelegge et al. (86)).

This is largely because protein identification is further complicated by the concept of 'peptide detectability' (87,88). This refers to the likelihood of observing a peptide in a standard proteomics experiment, and is determined by four factors: the chemical

properties of the peptide (and the parent protein); the limitations of the peptide identification method – including sample processing and digestion, the MS instrumentation, and the database(s) used; the abundance of the peptide in the sample; and the other peptides in the sample which compete with the peptide in question during the identification procedure. It could be argued, therefore, that the likelihood that a peptide will be seen in a sample is an intrinsic property of the peptide – determined directly by its primary amino acid sequence, and the location that it occupies within the composite protein. Thus, abundance alone does not determine detection (87,88). Rather, it is the quality of the method, as well as the quantity of starting material, which determines the output.

The stochastic nature of data acquisition during mass spectometry was carefully studied by Liu et al. in 2004, in order to determine the optimum conditions for sample analysis (89). Nine LC/LC/MS/MS experiments were performed on the soluble fraction of whole cell yeast lysates, during which the experimental conditions were held constant across all sample runs i.e. samples did not differ in complexity, separation resolution, and data acquisition. Even having corrected for all these variables, inter-sample reproducibility was only 76%. It was determined that, in light of this limited reproducibility, the same data could be acquired from three sample replicates as from nine, irrespective of sample origin (89). The authors also investigated how best to quantitate protein abundance in these samples by spiking four different mixtures with known quantities of six proteins. Spectral counting was shown to be an accurate measure of relative protein abundance, with a linear correlation over a dynamic range of two orders of magnitude. Spectral counts reflect the number of matched peptides, and the number of times those peptides were

observed. Thus, spectral counts can be used as a semi-quantitative measurement of protein concentrations in unlabelled protein mixtures, as well as to evaluate any changes in protein composition between different samples (89).

There has been little consensus on the statistical analysis of label-free proteomics data, particularly with regards to calculating differential protein expression. In 2006 however, Zhang et al. compared five statistical tests in evaluating differential protein expression, namely the G-test, AC test, Fisher's exact test, t-test and Local-Pooled-Error (LPE) test (90). This was done by comparing the false positive rates obtained with each statistical test when one to three sample replicates of *S. Cerevisiae* cell lysates, which had been spiked with six proteins of known concentration, were analysed using LC/MS/MS. It was found that when a large fold-change (i.e. five- to ten-fold) in protein concentration was present, the G-test, AC-test and Fisher's exact test yielded false positive rates of < 0.7%. However, when a two-fold change in differential expression was present, the t-test yielded the lowest false positive rates when > 3 replicates were used, whilst the G-test, AC-test and Fisher's exact test were superior when ≤ 2 replicates were used. Thus, the authors conclude that the t-test should be used when three or more replicates are analysed, whilst the G-test, AC-test or Fisher's exact test should be used when less than three replicates are available (90).

1.2.3 S100P in PDAC

S100P, a 10.4 kDa EF-hand calcium-binding protein, has been a long-standing focus in our laboratory. A number of previous studies have investigated the importance of

this protein in PDAC (91–97). We have shown that S100P (transcript and protein) is absent in normal pancreatic ductal epithelia, progressively increased in PanIN lesions, and is expressed in > 90% of primary PDACs in human tissue samples (91,92). In a similar study performed by Logsdon et al., S100P was confirmed to be expressed exclusively in the neoplastic epithelial compartment of PDAC, using GEP with subsequent IHC validation (93). Importantly, analysis of S100P expression in this study included a comparison with tissue samples of chronic pancreatitis, a condition which is often difficult to differentiate from PDAC (93). In 2004, Arumugam et al. showed that S100P binds to the receptor for advanced glycation end-products (RAGE), hereby increasing the proliferation and survival of NIH3TC fibroclasts (97). The authors went on to investigate the effects of S100P expression in pancreatic cell lines and in orthotopic mouse models of PDAC (95,96). They showed that S100P increased pancreatic cancer growth, survival and invasion both *in vitro* and *in vivo*; a mechanism of action which could be targeted using cromolyn, or analogues thereof (95,96). In 2007, we showed that S100P increases invasion by mediating changes in the actin cytoskeleton and up-regulating cathepsin D *in vitro* (94). These experiments were conducted using a Panc-1 cell line, which was engineered in-house to over-express S100P or a vector control (S5 and V3 cell lines respectively). Finally, we recently have found S100P to be a potential candidate gene involved in the haematological dissemination of PDAC (Sayka Barry, PhD Thesis 2009). These data were obtained from GEP experiments performed on unmatched human PDAC and liver metastases, with subsequent *in vitro* (transendothelial migration assays) and *in vivo* confirmation (Zebrafish model of metastasis). Thus, evidence for a causative role for S100P in PDAC metastasis is accumulating. However, the potential role of this protein in lymphatic metastasis has not been investigated to date.

1.3 The Biology of the Lymphatic Vasculature

The lymphatic system regulates fluid homeostasis, immune function and fat absorption. It also is involved in a number of pathological processes, including tumour metastasis. Despite this, our understanding of the molecular mechanisms controlling the lymphatic system is still in its infancy. This is due to a historical lack of defining molecular markers to establish unequivocal provenance of putative cells of the lymphatic system, as well as to the fact that lymphatic cells are difficult to observe and manipulate both *in vitro* and *in vivo*. Whilst much progress has been made in this field of late, the precise molecular features that determine cellular and fluid entry into lymphatics remain poorly understood (98,99).

1.3.1 Lymphatic Markers

Several lymphatic markers have been identified recently, although few if any are expressed exclusively by the lymphatic endothelium. The three most commonly used markers are the lymphatic vessel endothelial hyaluronan receptor 1 (LYVE-1); the transmembrane glycoprotein, podoplanin (PDPN); and the homeobox transcription factor, Prox-1 (98–100).

The transmembrane glycoprotein, LYVE-1, first described by Banerji et al. in 1999, is a member of the Link protein superfamily, which binds hyaluronic acid (HA) via a conserved link module domain (101). Developmentally, LYVE-1 is expressed as the lymphatic system starts to sprout from a subpopulation of endothelial cells in the cardinal vein (98,99). In adult tissues, it is expressed on lymphatic endothelial cells

(LEC), liver sinusoidal endothelial cells and some populations of tissue macrophages (102). However, despite its expression in lymphatic progenitor cells, the absence of LYVE-1 in mice does not impede lymphatic development; indeed, knockout mice have a normal structural and functional lymphatic system (103). LYVE-1, therefore, does not appear to be essential for lymphatic specification or lymphangiogenesis. Furthermore, LYVE-1 null mice are comparable to wild type controls in a number of pathophysiological processes, including leukocyte development and compartmentalisation; dendritic cell trafficking/migration; acute inflammation; tumour growth; tumour-associated lymphangiogenesis and HA turnover (103). A possible explanation for the latter is that LYVE-1 is 'functionally silenced' in normal LEC by autoinhibitory glycosylation, and requires activation in order to bind HA (102). Despite this, the receptor itself can still be endocytosed and degraded without binding HA (104). These contradictory findings illustrate the complexity of LYVE-1, which requires further investigation.

PDPN (podoplanin), a 38 kDa membranous glycoprotein, is expressed by lymphatic, but not blood vascular, endothelium. However, in normal human tissues, it also is expressed in kidney podocytes, skeletal muscle, in the placenta, lung and heart, in myofibroblasts of the breast and salivary glands, in osteoblasts and in mesothelial cells (105). Developmentally, like LYVE-1, PDPN is up-regulated in a subpopulation of progenitor cells in the cardinal vein, under the control of Prox-1 (see below) (98,99). In contrast to LYVE-1 however, the homozygous deletion of PDPN in mice is embryonically lethal; mice die of respiratory failure due to a shortage of type I alveolar epithelial cells (106). In addition, these mice show extensive cutaneous lymphoedema due to lymphangiectasia. Recently, it has been shown that PDPN

interacts with the platelet membrane lectin, CLEC-2, during lymphatic development, inducing platelet aggregation, which allows for the separation of lymph sacs from the cardinal vein (107,108). PDPN has also been shown to promote LEC adhesion to fibronectin (FN) and type I collagen, as well as to increase LEC migration towards fibronectin (106). Interestingly, PDPN is expressed at the invasive front in a number of squamous cell carcinomas, ovarian cancers, mesotheliomas and a subset of CNS tumours (109–114). However, contradictory evidence exists at present as to the molecular mechanisms underlying tumour migration as a consequence of podoplanin expression (105). In the Rip1Tag2 transgenic mouse model, progression of benign adenomas to carcinomas in the pancreas has been shown to involve a switch from E-cadherin to N-cadherin. This 'cadherin switch' is considered to herald epithelial-mesynchymal transition (EMT), and thus, single cell migration of cancer cells. Trangenic expression of podoplanin in these β–islet cell tumours was shown to prevent this 'cadherin switch' from occurring, and to promote collective cancer cell migration as opposed to single cell migration (105). Similar results were found when podoplanin was over-expressed in both human keratinocytes and MCF-7 breast cancer cells (105). In the latter, podoplanin expression resulted in a down-regulation of RhoA activity, which resulted in an increase in collective cell migration (114). Conversely, the expression of podoplanin in MDCK cells has been found to increase RhoA activation, resulting in an EMT, and increased single cell migration (115). Thus, it would appear that podoplanin can modulate cell migration in two different ways by modulating RhoA (114,115).

Finally, the homeobox transcription factor, Prox-1, has been described as the 'master control gene' of LEC (100). Prox-1 has been conserved throughout

evolution; its expression heralds lymphatic specification in mice, zebrafish, frogs and chicks (98). Loss of Prox-1 expression results in lymphatic agenesis, whilst over-expression of Prox-1 in blood vascular endothelial cells results in conversion to a lymphatic phenotype (98–100). Although the initial cues governing Prox-1 up-regulation require further elucidation, there is evidence that SOX-1 (SRY-related HMG domain transcription factor), MYC, Slug and Twist can induce Prox-1 expression, whilst TGFβ can inhibit its expression (98). Prox-1 has also been shown to up-regulate a number of lymphatic markers, including LYVE-1, podoplanin, VEGFR-3 and α9 integrin (98–100). In fact, it has been shown that LEC migration towards VEGF-C and VEGF-D is mediated by the integrin α9β1 and VEGFR-3, and that the expression of both these receptors is dependent on Prox-1 expression (116). This was shown in a series of experiments on human umbilical venous endothelial cells (HUVECS) and mouse embryonic stem cell derived endothelial cells, which utilised adenoviruses encoding wild-type and mutant Prox-1 and VEGFR-3 constructs, siRNA knockdown of Prox-1 and neutralising antibodies to the integrin α9β1 to study the effects of Prox-1 on LEC migration (116).

1.3.2 The Anatomy of the Lymphatic System

Most human tissues are drained by a network of blind-ending lymphatic capillaries, with the exception of the CNS and bone marrow; these initial lymphatics also are absent between striated muscles fibres and within hepatic lobules (117). A recent ultrastructural study by Baluk et al. has challenged the traditional view that lymphatics display little or no intercellular junctions (118). This study, which was conducted in mice, showed that lymphatic capillaries consist of an oak-leaf shaped

endothelium, which is secured to the surrounding extra-cellular matrix (ECM) by anchoring filaments comprising emilin and fibrillin. In contrast to blood vessels, these capillaries lie on a discontinuous basement membrane (BM), and lack pericytes. In addition, these capillaries are considerably larger than venules in size (both in terms of the dimensions of the constituent cells, as well as in vessel diameter). Uniquely, these initial lymphatics have discontinuous 'button-hole' junctions which contain parallel segments of VE-Cadherin. These buttons act as specialised anchoring junctions, allowing for the interdigitation of the adjacent cell membranes in between these buttons. These interdigitations or 'flaps' effectively function as one way valves, allowing for the easy passage of fluid and macromolecules (**Figure 4**). Thus, the repeated assembly and disassembly of cell junctions is avoided as fluid moves passively through these 'flaps' which then close, preventing the fluid from escaping out into the surrounding tissue. PECAM-1 (or CD31), a molecule common to both blood and lymphatic vasculature, also is expressed on the tips of these flaps. Functional studies in PECAM-1 null mice, however, showed that PECAM-1 was not essential for vessel function and leukocyte migration (118).

These initial lymphatics drain into collecting lymphatics, which have continuous 'zipper' junctions, again expressing VE-Cadherin (118). The LEC become spindle-shaped, and pericytes are recruited to assist with the propulsion of lymph against gravity. Initially, these pericytes form a thin monolayer around lymphatic vessels, but as the vessels enlargen, more pericytes are recruited, resulting in a more complex multilayer, which is arranged in a basket-weave fashion around the lymphatic endothelial monolayer (117,119). These smooth muscle cells have been shown to stain positive for c-kit and vimentin, suggesting that they share a common origin with

the pacemaker cells of the gastrointestinal tract (the interstitial cells of Cajal) (119). In fact, there is evidence that these cells are able to contract independently, initiating contraction in sheep lymphatics over a distance of at least 80 mm (117,120,121). Thus, collecting vessels may possess an intrinsic pump, and may not be wholly dependent on the action of the muscles surrounding them for the maintenance of lymph flow (117). Collecting vessels also contain bi-leaflet valves which prevent backflow of lymph (117,118).

Lymph passes from the periphery through a series of LNs (117). Before entering the LN, these afferent lymphatic vessels divide into smaller ducts, which enter through the lymph node capsule into the cortical sinuses. From here, lymph drains through the medullary sinuses to the LN hilum, where lymph then enters the efferent lymphatic vessels (117). This ‘percolation’ of lymph allows for the interaction of antigens with immune cells, leading to an appropriate immune response when necessary. Eventually, the lymphatic system drains into the thoracic duct and the right lymphatic duct, which drain into the blood circulatory system at the left brachiocephalic vein in the angle between the left subclavian vein and left internal jugular vein, and the right subclavian vein, respectively (122).

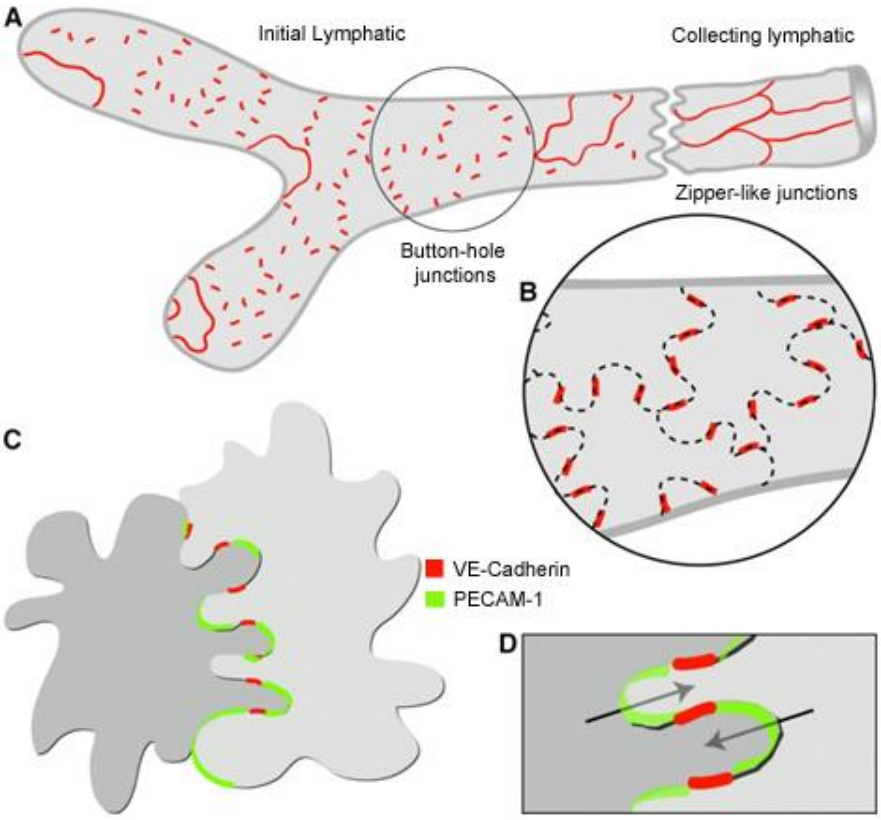

Figure 4 Schematic diagram (**A**) showing the two types of junctions between lymphatic endothelial cells. Initial lymphatics (**B**; dashed lines in **A**) are distinguished by oak-leaf endothelium with button-hole junctions, which contain VE-Cadherin (red). In between these junctions, the tips of the flaps (**C** and **D**) formed by adjacent cells express PECAM-1 (green) and function as one-way valves allowing for the easy passage of fluid and macromolecules from the interstitium into lymphatic vessels. Collecting lymphatics are distinguished by spindle-shaped endothelium with continuous zipper junctions. These collecting vessels are also surrounded by pericytes (not shown) (Adapted from Baluk et al. (118)).

1.3.3 Developmental Lymphangiogenesis

The rate of LEC turnover in adults *in vivo* is extremely low; Tritiated thymidine incorporation rates of 0.6% have been observed in LEC, implying that LECs have a half-life in the range of several years (117). Although these rates increase during embryogenesis (11.5%) and wound healing (6.8%), lymphangiogenesis, or the growth of lymphatic vessels, usually occurs slower and later than haemangiogenesis (117). In the developing human, the first lymphatic structures, the lymph sacs, can be observed at 6 to 7 weeks gestation, approximately a month after the first blood vessels are seen to develop (117,123).

Molecular profiling recently has validated the 'centrifugal' theory of lymphangiogenesis as originally proposed by Sabin in 1902 (99,100,118,124). As mentioned above, lymphangiogenesis begins with cells in the venous system. These cells begin to express Prox-1, which commits them to a lymph lineage. Once specified, LEC must proliferate and migrate into the surrounding tissue to form functional vessels. This process is governed by VEGF-C and its receptor, VEGFR-3, although a minor role for VEGF-D also has been shown (98–100,125). Both these growth factors exist as either full-length or mature forms; only the full-length forms can activate VEGFR-3, whilst only the cleaved, mature forms can activate VEGFR-2 (126). Upon activation, VEGFR-3 can form either homodimers or heterodimers with VEGFR-2 and Neuropilin-2 (98,125). Thus, mutations in these co-receptors can affect lymphangiogenesis adversely. Furthermore, the integrin $\alpha 9\beta 1$ has also been shown to be a receptor for VEGF-C and VEGF-D, and is important for the structural integrity of forming lymphatics (127).

In contrast to this ‘centrifugal’ theory, lymphangiogenesis has also been described to originate in the mesenchyme, in which cells fuse with each other and lymphatics form in a ‘centripetal’ manner (98,117,128). This theory has been largely supported by work conducted on avian embryos (98,117,129,130).

Once formed, vessels undergo remodelling and expansion. A number of genes have been found to be important in this process, including FOXC2, EFNB2, ANGPT2 and EMILIN1 (98). Podoplanin has been shown to be important for the adhesion and migration of LEC, as well as in the formation of connecting lymphatics between the superficial and deep lymphatic plexuses (106–108).

1.3.4 Interaction of Lymphatic Capillaries with the Tissue Interstitium

As lymphatic capillaries have a discontinuous BM, LEC are in direct contact with the ECM and interstitial fluid. Thus, lymphatic organisation and function is directly influenced by ECM components, by the presence or absence of growth factors within the matrix, and by changes in lymph flow (131).

Fibrillar collagens (types I, II, III, V and XI), which entrap proteoglycans and glycoproteins, provide the primary scaffold for this surrounding matrix. It has been shown that, unlike blood vascular endothelial cells, LEC can survive and form tubes in collagen type I matrices *in vitro*, even in the absence of growth factors (131,132). Under experimental conditions of flow, however, LEC organise better in a fibrin-only matrix (131,133). The high expression of collagen I and fibrin during wound healing has been shown to increase lymphangiogenesis *in vivo*. However, it has also been

shown that fragments of other collagens, such as endostatin and neostatin 7 (fragments of collagen XVIII), can inhibit lymphangiogenesis (131,134,135).

HA is a polymer of repeating D-glucuronic acid and D-N-acetylglucosamine disaccharides, ranging from 10^4 to 10^7 Da in size (136). Due to its hygroscopic properties, HA plays a key role in regulating matrix turgor and stability. There is a rapid turnover of HA in the body, with one third of HA being degraded in lymph nodes following its removal by lymphatic vessels. HA is made intracellularly, under the control of HA synthases, after which it can be extruded through the plasma membrane into the ECM, firmly anchored in the plasma membrane via synthases, or linked to cell surface receptors, like LYVE-1 or CD44 (136). By binding these receptors HA has the potential to initiate a number of signalling pathways in various cell types. The pathophysiological effects of HA are complex, and depend predominantly on the size of the HA polymer involved. With regards to LEC however, HA-rich stroma tends to stimulate lymphangiogenesis (131).

Lastly, LEC are surrounded by patches of FN. By virtue of the fact that it binds VEGF-C, trapping it within the ECM, FN has been shown to increase LEC proliferation (131,137,138). There is evidence that the splice variant, EDA FN (139), is important for normal lymphatic valve development *in vivo* through its interaction with α9 integrin (127), as well as evidence that EDA FN stimulates lymphatic tubulogenesis in tumour stroma (137). Importantly, there is an emerging role for the fibronectin-binding integrins, α9β1, α5β1, and α4β1 in the lymphatic vasculature. These dynamic heterodimeric glycoproteins play a crucial role in relating changes in the extracellular microenvironment to the intracellular space, and *vice-versa* (140–

143). Thus, integrins mediate adhesion, proliferation and migration of LEC under both physiological and pathological conditions. In addition to FN, α9β1 is known to bind VEGF-C, VEGF-D, tenascin C, collagen, laminin, thrombospondin and VCAM-1 (131). The RGD binding integrin, α5β1, has been shown to be involved in inflammation-induced lymphangiogenesis. It has also been shown to associate constitutively with VEGFR-3 *in vitro*, thus increasing VEGFR-3 mediated lymphangiogenesis (138). Finally, it has been reported that α4β1 mediates the adhesion, migration, invasion and survival of proliferating lymphatic endothelial cells (144). Conversely, inhibition of this integrin decreases both lymphangiogenesis as well as lymph node metastasis *in vivo* (144).

1.3.5 The Biology of Tumour Lymphatics

Whilst lymphatics represent a common route of spread for most cancers (99), including PDAC (145,146), little is known about the mechanisms underlying this process. In terms of collective cell migration, it is known that pre-existing lymphatics can serve as a conduit for cancer cells (147). However, the detailed mechanisms determining both single cell and collective translymphatic migration have yet to be elucidated.

While the concept of endothelial cell activation is well-established for blood vascular endothelium, the importance of activation for lymphatic endothelium is still unclear. Activation of blood vascular endothelium is defined by five core changes: expression of adhesion molecules; increased cytokine production; a loss of vascular integrity; up-regulation of HLA molecules and a change from anti- to pro-thrombotic activity

(148–150). At present, only the up-regulation of adhesion molecules and an increase in cytokine production have been shown to occur following activation of the lymphatic vasculature (99,125,151–158).

In 2006, Johnson et al. showed that the stimulation of LEC by a number of cytokines, particularly TNF-α (10 ng/ml) and IFN-γ (100 ng/ml), resulted in the up-regulation of ICAM-1, VCAM-1 and E-selectin (151). However, this study only investigated the importance of these adhesion molecules in immune function, and not in the context of cancer i.e only the effects of exogenous commercially available cytokines (and not conditioned media from cancer cells) on human dermal lymphatic endothelial cells (HDLEC) was investigated *in vitro*; the *in vitro* co-cultures experiments assessed only the interactions of dendritic cells, and not cancer cells, with activated HDLEC; and the *in vivo* experiments evaluated the presence of antigen-presenting cells attracted to the ear skin of mice following oxalozone-induced hypersensitivity; no mouse models of carcinogenesis were used in this study (151).

It was only two years later that Kawai et al. showed that conditioned media from metastatic MDA-MB-231, but not non-metastatic MCF-7, breast cancer cells increased ICAM-1 expression on human LEC (152). Furthermore, the up-regulation of ICAM-1 led to the increased adhesion of MDA-MB-231 cancer cells to human LEC, potentially through the paracrine effects of cancer cell ATP production or leakage (152). However, no other adhesion molecules were evaluated in this study.

Another molecule, the common lymphatic endothelial and vascular endothelial receptor, CLEVER-1 (also known as FEEL-1 and Stabilin-1), has been shown to be

expressed in peritumoural and intratumoural lymphatics in head and neck, and breast cancers (153). Furthermore, the intensity of CLEVER-1 expression in peritumoural lymphatics in breast carcinoma was shown to correlate positively to tumour grade (n = 72; p = 0.025) (153). However, its expression on intra- and peri-tumoural lymphatics in both head and neck (n = 17), and breast cancers (n = 72) showed no association with lymph node infiltration at the time of diagnosis (153). CLEVER-1 is a large glycoprotein which is expressed on lymphatics and high endothelial venules, and has been shown to be involved in scavenging, cell adhesion and angiogenesis (154). Exon 27 of this gene can be alternatively spliced in various tissues; however, once translated, CLEVER-1 contains 7 fasciclin domains, a proteoglycan link protein-like sequence, 22 EGF repeats and 2 RGD motifs. Most published studies on CLEVER-1 have been aimed at understanding its role in leukocyte trafficking, and not in cancer (153,154). Although blocking CLEVER-1 has been shown to decrease the transmigration of peripheral blood mononuclear cells (PBMC) *in vitro*, CLEVER-1 blockade tended to increase the adhesion of PBMC to lymphatics in static conditions (154). This raises an important question regarding the interplay between adhesion and transmigration: if PBMC binding to lymphatics decreases upon CLEVER-1 blockade, does this suggest that PBMC preferentially bind to LEC receptors for which they have a weaker affinity in order to transiently 'stick', thus facilitating migration through the lymphatic endothelium? This possibility has yet to be explored.

An emerging concept in the context of LEC activation in cancer is that of tumour-LEC crosstalk. Shields et al. have shown that the migration of the metastatic melanoma cell line A375 is dependent on CCL21 secretion by LEC (155). In addition, A375 cells

were shown to express CCR7, the receptor for CCL21 (155). This migration was proven both *in vitro* and *in vivo*. Notably, A375 cells only migrated towards LEC and not towards blood vascular endothelial cells. Furthermore, the non-metastatic melanoma subclone A375P did not migrate towards LEC. Thus, the authors suggest that CCR7 is up-regulated on melanoma cells during metastasis in response to CCL21 secretion by lymphatics, resulting in the migration of cancer cells towards lymphatics. In addition, A375 cells were found to produce VEGF-C, which induced LEC migration towards cancer cells. It was found subsequently that VEGF-C secretion by cancer cells stimulates the secretion of CCL21 by LEC via VEGFR-3. CCL21 in turn attracts cancer cells expressing the receptor CCR7 (159). Thus, chemokine crosstalk between LEC and cancer cells is a potentially important cause of lymphatic invasion as it induces the migration of cancer cells towards existing lymphatics; an action independent of their role in stimulating lymphangiogenesis (**Figure 5**).

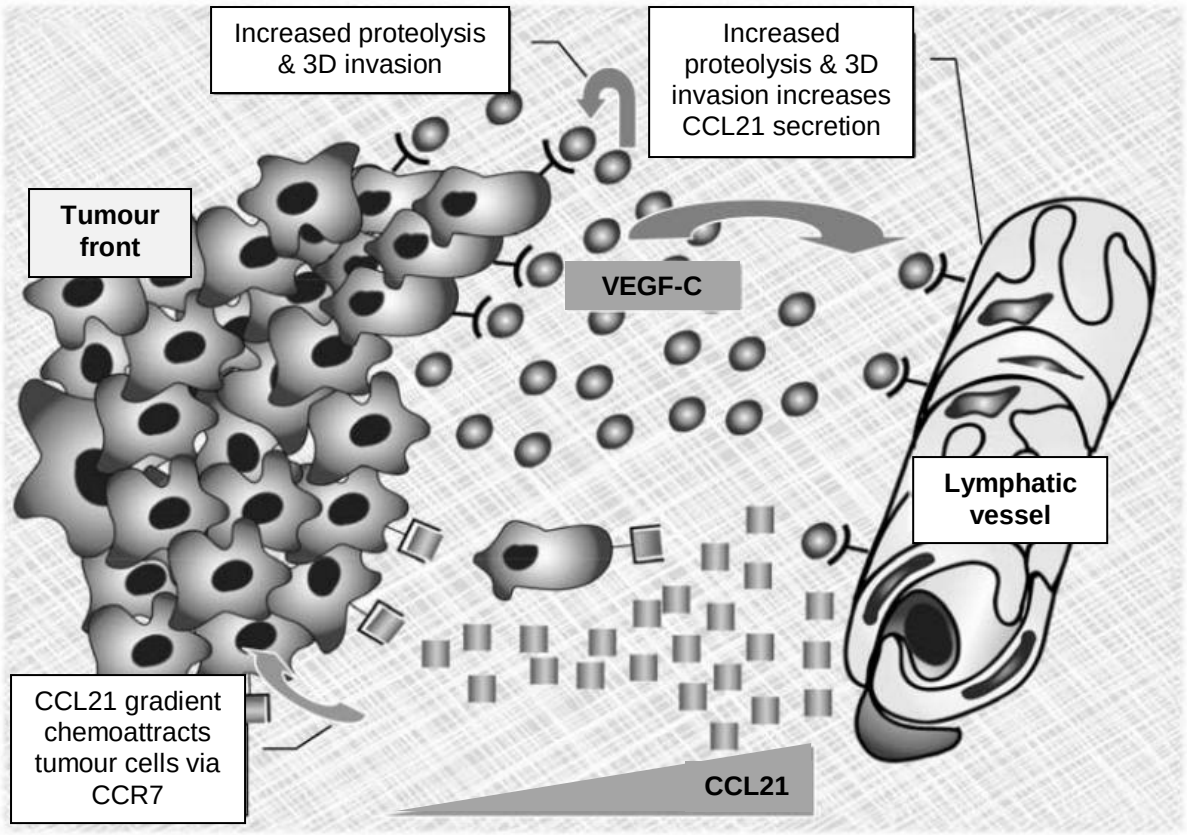

Figure 5 Cross-talk between melanoma cells and lymphatic vessels. Melanoma cells secrete VEGF-C which binds to VEGFR3 on lymphatic cells, stimulating lymphangiogenesis and inducing lymphatic endothelial cell migration. This also stimulates lymphatics to secrete CCL21, which causes cancer cells expressing the cognate receptor CCR7 to migrate towards the lymphatic vasculature (Adapted from Issa et al. (159)).

These data are in keeping with a number of other studies which have demonstrated a positive role for VEGF-C and VEGF-D in inducing lymphangiogenesis and lymphatic metastasis in melanoma (156), breast (157) and pancreatic cancer (158). With regards to the latter, it could be argued that some of these studies were sub-optimal, since they were performed in the Rip1Tag2 mouse model of pancreatic

cancer (160,161), which is representative of endocrine neoplasms and not PDAC *per se*, and/or using pancreatic cancer cell lines *in vitro* (162). Furthermore, the role of VEGF-induced lymphangiogenesis in human tissue studies remains unclear. In 2004, Kurahara et al. evaluated 58 PDACs (pancreatic head), from patients who had undergone curative resection without neoadjuvant therapies, for VEGF-C and VEGF-D expression using IHC (163). Expression of both VEGF-C ($p = 0.015$) and VEGF-D ($p = 0.02$) at the tumour margins, but not at the centre of the tumours, was found to be associated with a higher incidence of LN invasion. It was also shown in this study, by Kaplan-Meier analysis, that tumours expressing both VEGF-C and VEGF-D at the tumour margins had a worse prognosis than those expressing only one or none of these growth factors ($p = 0.017$). In 2005 however, Schneider et al. showed that whilst VEGF-C mRNA expression was significantly higher in PDAC ($n = 36$) than in normal pancreatic tissue ($n = 30$; $p < 0.001$; with expression being confirmed at a protein level by IHC), no association was found in this study between VEGF-C expression in PDAC and survival (164). Finally, Sipos et al. showed in a study involving 98 PDAC samples, that VEGF-C and VEGF-D were not up-regulated in primary PDAC (165). Even though the mRNA quantification and ELISAs were performed on a subset of these 98 cases, IHC confirmation of VEGF-C (but not VEGF-D) protein expression was performed on all 98 cases, and showed that only six of these expressed VEGF-C. Thus, these findings contradict those of the previous studies, concluding that VEGF-C does not influence lymphatic metastasis in PDAC.

Whilst it has been shown that lymph node metastasis correlates to intratumoural lymphatic vessel density (LVD) for some tumours, such as thyroid carcinoma,

melanoma, and head and neck cancers (99,166–168), there are conflicting reports for other cancers, including PDAC. Both Sipos et al. and Schneider et al. demonstrated a paucity of intra-tumoural lymphatics in PDAC, with a relative predominance of peri-tumoural lymphatics (164,165). Furthermore, no correlation between LVD and patient survival was seen in either study. Thus, the authors conclude that lymphangiogenesis did not contribute to lymphatic metastasis in PDAC (164,165). Sipos et al. confirmed these findings in three orthotopic mouse models of pancreatic cancer, in which the HPAF2, PancTu1 and PT45P1 cell lines were used, all of which showed high rates of lymphatic invasion and LN metastasis, but not increased LVD. The findings in these mouse models thus mirrored those found in the human tissue samples, supporting the conclusion that lymphangiogenesis does not contribute to lymphatic metastasis in PDAC (165).

In contrast, Bailey et al. have shown that Sonic Hedgehodge (SHH) paracrine signalling increases lymphangiogenesis in an orthotopic mouse model of pancreatic cancer, resulting in an increase in primary tumour growth, as well as an increase in both vascular and lymphatic metastasis (169). This occurs via paracrine signalling; the pancreatic cancer cells secrete SHH, a morphogenic signalling protein, which binds to a 12-pass transmembrane protein called Patched (Ptch). This binding releases the inhibitory effects of Ptch on the serpetine receptor Smoothened (SMO), which is expressed on primary cilia in the surrounding stromal cells. Primary cilia are microtubule-based organells that project into the extracellular environment from the centriole of quiescent cells. In this paper, the authors demonstrate the presence of SMO on LYVE-1 positive cells in mouse orthotopic tumours containing hTERT-HPNE pancreatic cells that had been engineered to over-express SHH. These

findings were confirmed in four human tissue samples from patients with PDAC. Furthermore, treating the orthotopic tumours with a neutralising antibody to SHH decreased lymphangiogenesis and tumour size, and decreased the number of metastatic LN. Thus, the authors suggest that SHH increases lymphangiogenesis, directly influencing metastasis, and that targeting the SHH pathway would decrease metastatic disease (169). Shultz et al. have reported that inducible re-expression of p16 decreases lymphangiogenesis and lymph node metastasis in an orthotopic mouse model of PDAC, providing further evidence for a direct association between lymphangiogenesis and LN metastasis (170).

Taken together, these data highlight the lack of consensus regarding the importance of lymphangiogenesis with regards to lymphatic invasion in PDAC, as well as to the molecular mechanisms underlying lymphangiogenesis in PDAC (160–162,169,170). However, it is clear that at present, data from human tissue samples do not seem to support a direct association between lymphangiogenesis and lymphovascular invasion in PDAC (164,165).

1.3.6 Lymph Node Status in PDAC

Although the molecular mechanisms underlying lymphatic metastasis are currently unclear, it is recognised that lymph node status is an important predictor of survival in PDAC (146). 70% of PDAC patients will have positive LNs at the time of presentation, and will benefit from extended lymphadenectomy during surgery (145). However, as sentinel lymph node mapping is not feasible for pancreatic cancer, we currently are unable to identify the 30% of patients who are LN-negative, and who

would thus unnecessarily experience the morbidity associated with extensive LN dissection (145). Importantly, for the vast majority of patients who are LN-positive, the pattern of lymph node involvement has recently been shown to correlate with survival (146).

In a retrospective analysis of 380 patients with pT3 invasive PDAC, patients with direct invasion of ≤ 2 peripancreatic LN (n = 35) showed the same overall survival as patients with node-negative disease (n = 97) (146) (The American Joint Committee on Cancer TNM classification of pancreatic cancer is shown in **Table 2**). However, patients in whom true lymphatic invasion was seen in LN (n = 248), as opposed to those patients whose tumours had directly invaded into the surrounding LNs, showed a worse overall survival when compared with patients with node-negative disease ($p < 0.001$), regardless of the number of LNs involved. Thus, the ability of cancer cells to enter into and travel through lymphatics negatively affects prognosis. Interestingly, there was a trend towards patients bearing tumours with direct LN invasion (n = 35) having an improved survival compared with patients who had true lymphatic metastasis in one or two LN (n = 42). However, this did not reach statistical significance ($p = 0.056$).

These data highlight the importance of identifying molecular markers that differentiate true lymphatic invasion in PDAC from direct extension into the surrounding LN, as these patients clearly are at higher risk and require more aggressive therapies. They also highlight the importance of determining what facilitates lymphovascular invasion in PDAC, as targeting the molecules involved potentially could prevent metastasis, and significantly decrease mortality. Finally, the

data also suggest, as Hart and Fidler concluded earlier, that the nature of lymphatic invasion in PDAC is not entirely stochastic, and that by virtue of this fact, it is both preventable and controllable (48).

Table 2 American Joint Committee on Cancer TNM classification of pancreatic cancer.

	Tumour	Node	Metastasis
X	Primary tumour cannot be assessed		
0	No evidence of primary tumour	Regional LN cannot be assessed	No distant metastases
Tis	Carcinoma in situ		
1	Limited to pancreas; ≤ 2 cm in its greatest diameter	No regional LN positive	Distant metastases
2	Limited to pancreas; ≥ 2 cm in its greatest diameter	Regional LN positive	
3	Extends beyond the pancreas but without involvement of the celiac axis or the superior mesenteric artery.		
4	Involves the coeliac axis or the superior mesenteric artery (unresectable primary tumour).		

1.4 Orthotopic Mouse Models of PDAC

The orthotopic mouse model has, for many years, served as a translational bridge which allows for the preclinical evaluation of primary tumour growth, metastasis, and potential drug therapies. The first orthotopic pancreatic xenograft model was performed in 1989, and characterised the differences between MIAPaCa2 cell growth in the pancreata of young and old nude mice over a period of two years (171). This study concluded that orthotopic implantation was feasible and superior to subcutaneous implantation in terms of tumour growth; pancreatic tumour growth was more reproducible in younger nude mice; spontaneous liver metastases were more likely to occur in experiments that lasted longer than 45 days; and primary tumour growth most often resulted in local invasion rather than haematological dissemination to the lungs and liver (171).

Subsequent experiments have shown that the rate of primary pancreatic tumour growth and the development of spontaneous metastasis is largely cell-line dependent (172). Thus, a limitation of these models is that primary orthotopic tumours do not often metastasise spontaneously. However, various ways of circumventing this problem have emerged over the past few years e.g. the inclusion of synthetic ECM (e.g. Matrigel) into the injected cell suspension (173) and/or the co-injection of pancreatic stellate cells (174,175), with such modifications being shown to enhance the development of spontaneous metastasis; and the implantation of tumour fragments, preferably from human pancreatic tumours but also from subcutaneous xenografts, has been shown to better simulate the clinical development of metastatic PDAC and create a more relevant model for drug testing

(176). In addition, a number of experimental metastasis models, largely based on the work of Nicolson, Hart and Fidler have been developed to evaluate the extravasation and colonisation steps of the metastatic cascade (177–179). In such experiments, cells are injected into the tail veins of nude mice in order to 'seed' these cells into the vasculature. Thus, intravasation from the primary tumour site is obviated, and any subsequent tumour development is seen as a direct result of the interaction of 'seed' with 'soil' (64). The technique has been modified to include intra-splenic injections (180,181), which seed cancer cells to the liver, and more recently, the intranodal injection of cancer cells into the right axillary LN for imaging purposes (182).

In addition to these models, a number of transgenic models of PDAC are available, in both zebrafish and mice (30,31,40,45). One of these mouse models, developed in 2003, targeted mutated $KRAS^{G12D}$ to the mouse pancreas (30). This mutation is commonly found in human PDAC, and results in a glycine to aspartic acid substitution, resulting in constitutive activation of the GTPase protein. These mice develop PanINs which are histologically similar to those premalignant lesions seen in humans (30). When these $KRAS^{G12D}$ mice were crossed with mice containing the Li Fraumeni mutant TP53 allele, mice developed invasive PDAC with widespread metastatic disease (40). It has also been shown that concommitent expression of $KRAS^{G12D}$ and the tumour suppressor gene DPC4/SMAD4 in mice results in mucinous cystic neoplasms of the pancreas, a distinct class of pancreatic tumours (45). Whilst these transgenic models provide us with an invaluable tool for the evaluation of novel therapeutic agents, they are costly to implement. Furthermore,

the ‘human element’ of the orthotopic transplantation model is lost, which could affect the evaluation of specific types of novel therapies e.g. antibody therapies.

Finally, the emergence of various imaging techniques has allowed for the real-time imaging of primary tumour growth and metastasis in small animal models. As these models can be used to monitor and quantify any responses to novel therapies using imaging data, they provide an alternative to the more traditional method of killing animals at specific time-points with subsequent histological examination. In other words, they reduce and refine the evaluation of carcinogenesis and novel therapies in small animal models. Imaging modalities can broadly be divided into two categories: those which have been modified and adapted from the clinic for application in small animals; and those based on macroscopic imaging using photonics (183). With regards to the latter, both fluorescence and bioluminescence have been used previously for the real-time evaluation of primary orthotopic pancreatic tumour growth (96,184,185). However, it has been shown that image resolution is complicated by tissue depth and photon scattering; this is of particular relevance to the retroperitoneal pancreas (183). Bioluminescence imaging relies on the conversion of an administered substrate (luciferin) to light in the presence of ATP, whilst fluorescence emits light following excitation of a fluorochrome at a particular wavelength. The gut, in particular, shows a high level of auto-fluorescence due to endogenous chromophores (e.g. elastin, collagen, porphyrins, tryptophan and NADPH), and chlorophyll from alfalfa, a common ingredient in laboratory murine food (186). This results in lower imaging contrast than that seen with bioluminescence (183). Thus, although both techniques will allow for adequate visualisation of the pancreas, bioluminescence is superior.

2. AIMS AND OBJECTIVES OF THE STUDY

1. To compare the proteins expressed in the epithelia of primary PDAC to the proteins expressed in LN metastatic PDAC epithelia using laser capture microdissection and MudPIT. This analysis would be performed in matched samples, i.e. primary PDAC and LN metastases were to be taken from the same patient.
2. To validate candidate proteins that are differentially expressed between primary PDAC and matched LN metastases using IHC in a larger series of matched cases. Of note, S100P would be given preference as a candidate protein should it be found to be differentially expressed.
3. To investigate the potential effects of a selected candidate protein (potentially S100P) on lymphatic invasion both *in vitro* and *in vivo*.
4. To create an orthotopic mouse model for future use in the preclinical evaluation of potential therapies that will be developed based on the proteomic screen.

3. MATERIALS AND METHODS

3.1 Cell lines

Both vector control (V3), and S100P over-expressing (S5), Panc-1 cell lines which had previously been engineered in our laboratory (94), were further engineered to stably express luciferase using a lentiviral vector by Dr David Gould (Bone and Joint Research Unit, William Harvey Research Institute, John Vane Science Centre, London, UK). These new cell lines, termed V3L and S5L, subsequently were used in all the *in vitro* and *in vivo* experiments.

Cells were grown in Dulbecco's Modified Eagle's Media (DMEM) high glucose 4.5 g/L (PAA Laboratories, Somerset, UK), supplemented with 10% heat-inactivated foetal calf serum (FCS; PAA Laboratories, Somerset, UK) and Penicillin/Streptomycin (PAA Laboratories, Somerset, UK) at a 1:100 dilution. Selection of stable cell lines was established with G418 as previously described (94). Human Dermal Lymphatic Endothelial Cells (HDLEC; PromoCell, Heidelberg, Germany), were grown in Endothelial Cell Basal Media MV2 (PromoCell, Heidelberg, Germany), supplemented with Supplement Mix (PromoCell, Heidelberg, Germany); Penicillin/Streptomycin (PAA Laboratories, Somerset, UK) at a 1:100 dilution and VEGF-C (R & D Systems, Abingdon, UK) at 5 ng/100 ml. Cells were grown in a humidified atmosphere (5% CO_2 at 37^{o}C).

During passage, cells were harvested from subconfluent cultures in exponential growth phase by overlaying the cells with a thin layer of trypsin EDTA (1% trypsin

EDTA for V3L and S5L cells; 10% trypsin EDTA for HDLEC; PAA Laboratories, Somerset, UK). Following a 3 minute incubation in a humidified atmosphere (5% CO_2 at 37^{o}C), the 75 cm^2 flask or 10 cm plate (see below) was tapped sharply to dislodge any adherent cells. An equal volume (to that of trypsin) of DMEM supplemented with 10% FCS then was added in order to inactivate the trypsin. Cell suspensions subsequently were transferred to 15 ml Falcon tubes (Becton-Dickinson, Oxford, UK), and centrifuged at 12,000 x g for 3 minutes in order to produce a pellet; the overlying media was aspirated off, and the pellet was resuspended in 10 ml of the appropriate growth medium. V3L and S5L cells were passaged into 75 cm^2 flasks (Becton-Dickinson, Oxford, UK). HDLEC were passaged into 10 cm plates (Becton-Dickinson, Oxford, UK) which had been coated with 0.5 mg/ml of FN. Cell passage was performed routinely every third day.

For the *in vivo* experiments, V3L and S5L viability was assessed prior to injection using trypan blue. Cells were resuspended at a 1:1 ratio with trypan blue, after which viability was assessed by counting the number of cells that were able to exclude trypan blue using a haemocytometer, and multiplying by a dilution factor of 2. Only cell suspensions that were > 90% viable were used in the *in vivo* experiments.

For long term storage, cells were centrifuged at 12,000 x g for 3 min, after which the pellet was resuspended in freezing media: for V3L and S5L cells, this contained 90% FCS and 10% dimethyl sulphoxide (DMSO); for HDLEC cryomedia (PromoCell, Heidelberg, Germany) was used. Cell suspensions were transferred to cryovials, frozen overnight at -80˚C, and then transferred to liquid nitrogen for storage. Cell pellets were produced by washing cells in PBS and then detaching using trypsin

EDTA. Detached cells were spun at 12,000 x g for 3 min to produce a pellet, any remaining PBS was removed and the pellets snap-frozen on dry ice. Pellets were stored at -80˚C until use.

3.2 Human Tissues

In total, 55 FFPE blocks of matched primary PDAC and LN metastases were obtained from the Pathology Departments of the General Hospital of Osijek, Croatia (17 cases) and Barts and the London (BTL) NHS Trust (38 cases). All tissues were obtained with full ethical approval from the host institutions. Clinicopathological data pertaining to all the used specimens (which I collected and collated from the two pathology departments) are shown in **Table 3**.

Table 3 Clinicopathological data. Relevant clinical and pathological parameters for the 55 cases of primary PDAC and matched LN metasatases; 38 of which were obtained from Barts and the London Hepato-Biliary Centre, London, UK, and 17 of which were obtained from the Clinical Hospital Centre Osijek, Croatia. (*grade not specified for two cases; IQR = inter-quartile range).

	BTL (n = 38)	**CROATIAN (n = 17)**
AGE (Median (IQR))	67 (58.25-71)	64 (52.33-70.11)
T1/T2/T3/T4	0/13/22/3	0/8/8/1
LN METASTASIS	38/38	17/17
RESECTION MARGIN POSITIVE	17/38	3/17
WELL/MODERATELY/POORLY DIFFERENTIATED	3/23/12	5/9/1*
PERINEURAL INVASION	27/38	11/17
LYMPHOVASCULAR INVASION	30/38	11/17
MALE/FEMALE	23/15	9/9
SURVIVAL (Median (IQR))	418.5 (300.5-527.75)	Unknown
ALIVE/DEAD/CENSORED	22/12/04	Unknown

3.3 Mice

Female CD1 nude mice (Charles River Laboratories, Kent, UK) were purchased at four weeks of age. All animals were maintained in a sterile environment on a daily 12-hour light/dark cycle. Surgical procedures were conducted when animals were five weeks of age, under aseptic conditions in a laminar flow hood. All animal work was conducted in accordance with the Animal (Scientific Procedures) Act of 1986.

3.4 RNA Isolation

3.4.1 Cell Lines

RNA was isolated from cell line pellets using the RNAqueous Total RNA isolation kit (Ambion, California, USA) according to the manufacturer's instructions. Briefly, 5 x 10^6 cells were lysed in 700 µl of lysis/binding solution and cells were passed through a 25 gauge needle (Becton-Dickinson, Oxford, UK) in order to shear DNA. An equal volume (700 µl) of 64% ethanol was then added to precipitate the RNA out of solution, and this mixture was transferred to spin columns. Following centrifugation for 1 minute at 12,000 x g, columns were washed with Wash Solution and centrifuged for 1 minute at 12,000 x g three times. The flow-through was discarded after each spin. RNA was then eluted in 40 µl of pre-warmed elution solution (at 75˚C) into a fresh collection tube by centrifuging at 12,000 x g for 30 seconds.

3.4.2 Mouse Tissue

For each sample, 50-100 mg of frozen mouse tumour was homogenised in 1 ml of TRIzol Reagent (Invitrogen, Paisley, UK) using a power homogeniser (IKA ULTRA-TURRAX, T25 basic, IKA, Staufen. Germany). Following centrifugation at 12,000 x g for 10 minutes at 4^{o}C, the supernatant was transferred to a fresh tube and incubated for 5 minutes at room temperature to permit the complete dissociation of nucleoprotein complexes. Chloroform (0.2 ml) was then added and mixed into the solution with vigorous shaking for 15 seconds. This mixture was incubated at room temperature for 3 minutes and centrifuged thereafter at 12,000 x g for 15 minutes at

4°C. Chloroform separates the mixture into two phases: the colourless upper aqueous phase (containing RNA) and the pink organic phase (containing proteins). The colourless upper aqueous phase (containing RNA) was transferred to a new tube. In order to precipitate RNA isopropanol alcohol (0.5 ml) was then added; incubated at room temperature for 10 minutes; and centrifuged at 12,000 x g for 10 minutes at 4°C. The RNA pellet was then washed with 1 ml of cold 75% ethanol, air-dried for 5-10 minutes, and dissolved in diethyl pyrocarbonate (DEPC) treated water in order to inactivate RNase enzymes and prevent RNA degradation.

3.5 RNA quantification

Samples were assessed and quantified using a NanoDrop ND-1000 spectrophotometer (NanoDrop Technologies, Thermoscientific, Wilmington, USA), with an A260/A280 ratio of > 1.95 being considered acceptable. In addition, RNA quality was assessed by gel electrophoresis for the presence of 28S and 18S rRNA (ratio 2:1). Briefly, 500 ng of the RNA was diluted in 6x blue gel loading dye (Sigma-Aldrich, Poole, UK) and run on a 1% agarose gel containing 0.5 µg/ml GelRed (Sigma, Poole, UK) at 60V for 20 minutes. Gels were visualised using a UVidoc system (UVitec, JENCONS PLS, Cambridge, UK).

3.6 Quantitative Real Time (qRT) PCR

cDNA was synthesised from 1 µg of total RNA using QuantiTect Rev. Transcription Kit (Qiagen, West Sussex, UK). Briefly, 2 µl of gDNA Wipeout Buffer (7x) was added to 1 µg of RNA and RNase-free water to a final volume of 14 µl. Following incubation

at 42^{o}C for 2 minutes, the samples were placed immediately on ice. 5 µl of master mix (containing 1 µl Quantiscript Reverse Transcriptase, 1 µl RT Primer Mix and 4 µl of Quantiscript RT Buffer, 5x) was then added, resulting in a 20 µl final reaction volume. This was incubated at 42^{o}C for 15 minutes, followed by a 3 minute incubation at 92^{o}C to inactivate Quantiscript Reverse Transcriptase. qRT-PCR was then performed on approximately 20 ng of cDNA per sample using the QuantiTect SYBR Green PCR Kit (Qiagen, West Sussex, UK) according to the manufacturer's instructions. Briefly, a total reaction volume of 20 µl was used containing the following: 10 µl of SYBR MM Buffer; 0.6 µl of each primer (at a final concentration of 0.3 µM); 2 µl cDNA (approximately 20 ng) and 6.8 µl of RNase-free water. Primers for S100P (Sigma, Poole, UK) were forward 5' TGCAGAGTGGAAAAGACAAGGAT 3' and reverse 5' CCACCTGGGCATCTCCATT 3'; primers for the human ribosomal gene S16 (Sigma, Poole, UK), which was used as a control, were forward 5' GTCACGTGGCCCAGATTTAT 3' and reverse 5' TCTCCTTCTTGGAAGCCTCA 3'. The PCR was run on the ABI7500 detection system (Applied Biosystems, California, USA). Relative quantification was performed using Ct values.

3.7 Protein Isolation

Cell line pellets were lysed in 200 µl of NP40 lysis buffer (50 mM Tris pH 7.4, 150 mM NaCl, 1 % NP40, 2 complete, EDTA-free protease inhibitor cocktail tablets (Roche Applied Sciences, Mannheim, Germany). Following lysis, samples were centrifuged at 10,000 x g for 1 minute, after which the supernatant was collected and stored at -20^{o}C until analysis.

3.8 Protein Quantification

Proteins were quantified using Pierce Coomassie Plus Assay Reagent (Thermofischer Scientific, Leicestershire, UK), according to the Bradford method. Briefly, 2 µl of sample was added together with 198 µl of Pierce Coomassie Plus Assay Reagent in a 96-well plate (Becton-Dickinson, Oxford, UK). Samples were always quantified in triplicate in relation to a BSA standard curve. Absorbance was read at 595 nm using the Dynex Revelation 4.04 program (MTX Lab Systems Inc., Virginia, USA).

3.9 Laser Capture Microdissection (LCM)

This protocol was optimised in a series of experiments performed over a period of two months, using PDAC sections that had been fixed in the same manner as the tissue which I was going to use for the final LCM. Over that time, various conditions were changed:

- I cut sections ranging in thickness from 4 to 10 µm, using the Leica RM2255 rotary microtome (Leica Microsystems, Milton Keynes, UK), in order to determine the optimal thickness for LCM;
- I changed the dehydration and rehydration times of the recommended protocol, ranging from 1 to 5 minutes in each ethanol solution, in order to decrease staining time in an effort to decrease contamination;
- I tried varying concentrations of ethanol in different combinations in order to improve the quality of staining;

- I tried staining with haematoxylin (1-5 minutes) and crystal violet (1–5 minutes), alone or in combination with eosin (10-60 seconds) in order to optimise the visualisation of sections on the P.A.L.M. system (*P.A.L.M.* Microlaser Technologies AG, Bernried, Germany). LCM was also attempted on unstained sections;
- I practised LCM area estimation on the P.A.L.M. system intra-dissection in order to improve my ability to dissect the same number of cells between cases.

The final LCM was performed over a period of three months, which included administrative delays e.g. booking times for use of the P.A.L.M. system. On average, three slides per day were dissected. Sections were cut the day before dissection; staining then commenced at 8 am in order to allow sections to air-dry adequately in order to commence LCM at midday. Thereafter, over a period of 8–10 hours, at least 10,000 cells/slide could be captured.

The final protocol can be described as follows:

Following histological examination of haematoxylin and eosin (H&E) sections, seven cases (i.e. seven primary PDAC and seven matched LN metastases) were selected for LCM. 8 μm sections were dewaxed in xylene twice, initially for 4 minutes followed by a second incubation for 3 minutes, and rehydrated through a series of graded alcohols (1 minute in 100% ethanol, 1 minute in 85% ethanol and 1 minute 70% ethanol). After staining with Mayer's haematoxylin for 2 minutes, sections were dehydrated (1 minute in 70% ethanol, 1 minute in 85% ethanol and 1 minute in

100%) and cleared in xylene for 2 minutes. Sections were then left to air-dry in a fume hood until LCM.

Approximately 10,000 to 15,000 cells per block were microdissected using the P.A.L.M. system (*P.A.L.M.* Microlaser Technologies AG, Bernried, Germany). Initially, four matched cases were dissected and pooled (PDAC1 and LN1, respectively), followed by the remaining three cases (PDAC2 and LN2, respectively). This resulted in two sample groups (PDAC and LN Metastasis), each represented by two pools; each pool comprising 40,000 to 45,000 cells. The samples were processed using Liquid Tissue (Expression Pathology Inc., Maryland, USA). Briefly, they were heated in 20 μl Liquid Tissue Buffer at 95^{o}C for 90 min. 1 μl of proteomics grade porcine trypsin was then added to each sample, after which samples were left to digest overnight in a waterbath at 37^{o}C. The peptide mixtures were then quantified using MicroBCA Assay Kit (Thermofischer Scientific, Leicestershire, UK). 2 μl of DTT was then added; samples were heated at 95^{o}C for 5 minutes before being stored at -20^{o}C.

3.10 Multidimensional Protein Identification Technology (MudPIT)

The MudPIT experiment was performed in duplicate; the first experiment was performed on PDAC1 and LN1 and the second on PDAC2 and LN2. 10 μg of each sample was diluted 20-fold in 5% acetonitrile (0.1% FA) and injected onto a 100 μm x 6 cm SCX column. The flow-through and nine subsequent fractions were collected during a 20 minute gradient separation. Buffer A was 5% acetonitrile (0.1% FA) and buffer B was 1M ammonium acetate, 5% acetonitrile (0.1% FA). Each fraction was

analysed using LC/MS/MS with a 1 hour gradient on a LTQ Orbitrap XL mass spectrometer (Thermo Scientific, San Jose, California, USA). MS/MS data were searched against the concatenated forward and reverse IPI Human v3.53 database using the Mascot (www.matrixscience.com) search engine. The database was appended with the common Repository of Adventitious Proteins (cRAP) to prevent false assignment of peptides derived from those proteins. This repository aims to identify proteins that are commonly observed in proteomics experiments, and which are classified into three general categories: common laboratory proteins; contaminant proteins which are added accidentally through dust and/or physical contact; and proteins used as molecular weights or mass spectrometry quantitation standards. Mascot output files were parsed into the Scaffold program for collation into non-redundant lists per sample (i.e. to avoid repetition of proteins in the final output) and filtering to assess false discovery rates to allow only correct protein identifications. Parameters for LTQ Orbitrap XL data require a minimum of two unique peptides matching per protein with minimum probabilities of 95% at the protein level and 50% at the corresponding peptide level. Spectral counts per protein were the output; these represent a semi-quantitative measure of abundance across samples (89). Spectral count reflects the number of matched peptides and the number of times those peptides were observed. The mass spectrometry experiments were performed at NextGen Sciences (Ann Arbor, Michigan, USA) by Dr Richard Jones.

3.11 Western Blotting

50 µg of protein per sample were incubated with 5x Laemmli buffer (0.225 mM Tris pH 6.8, 50% glycerol, 5% SDS, 0.05% bromophenol blue, 0.25 mM DTT) at 95^{o}C for 5 minutes. Samples were then loaded onto NuPAGE 4-12 % Bis-Tris gels (Invitrogen, Paisley, UK). Following transfer onto polyvinylidene difluoride Immobilon-P membrane (Millipore, Watford, UK), non-specific binding was blocked by incubating in 3% BSA in TBS-T for 30 minutes. Membranes were then incubated with anti-V5 antibody (1:1000; Invitrogen, Paisley, UK) overnight at 4^{o}C, followed by a 30 minute incubation with horseradish peroxidase (HRP)-conjugated goat anti-mouse immunoglobulin (Ig) (1:2000 Santa Cruz Biotechnology, Heidelberg, Germany) at room temperature. Bound immunocomplexes were visualised using enhanced chemiluminescence reagent (GE Healthcare, Hertfordshire, UK). HSC-70 was used as a loading control.

3.12 Immunocytochemistry (ICC)

5 x 10^{4} HDLEC were seeded onto 13 mm coverslips (Sigma, Poole, UK) in a 24-well plate (Becton-Dickinson, Oxford, UK) and left to settle overnight. The next day, following fixation in 4% paraformaldehyde and permeabilisation with 0.1% Triton X-100, non-specific binding sites were blocked with 2% bovine serum albumin. Cells were then incubated with commercially available primary antibodies at the following dilution: anti-human LYVE-1 (RELIATech, Wolfenbüttel, Germany) 1:1000; and anti-human PDPN (Abcam, Cambridge, UK) 1:1000. Secondary antibodies were Alexa Fluor 488–conjugated donkey anti-rabbit IgG (1:1000; Invitrogen Molecular Probes,

Paisley, UK), and Alexa Fluor 568–conjugated goat anti-mouse IgG, respectively. All experiments were conducted in the absence of primary antibody as a negative control.

3.13 Flow Cytometry (FC)

V3L and S5L cells were grown to confluency in 75 cm^2 flasks, trypsinised, centrifuged and re-suspended in FC media (DMEM with 0.1 % BSA) to a concentration of 4 x 10^6 cells/ml. 50 µl of cell suspension was then added to a series of 1.5 ml Eppendorf tubes (Sigma, Poole, UK) on ice, to which 50 µl of FC media containing either a primary antibody (**Table 4**); isotype control (Dako, Cambridgeshire, UK) or no primary antibody (negative control), were added. Following a 45 minute incubation on ice, cells were washed with FC media and recovered by centrifugation at 10,000 x g for 5 minutes. Following the removal of FC media, 50 µl of a 1:125 diluted, Alex-488 conjugated secondary antibody (Invitrogen Molecular Probes, Paisley, UK) was added and the suspension was incubated for a further 30 minutes on ice, in the dark. Following a second wash with FC media and recovery by centrifugation, samples were re-suspended in 300 µl of FC media, and transferred to 5 ml, round bottom tubes (BD Becton-Dickinson, Oxford, UK) for immediate analysis by FC. 10,000 events were acquired on a FACScalibur cytometer (Becton Dickinson Immunocytometry Systems, Oxford, UK) using CellQuest Pro software version 4.0.2, which also was used to analyse the data by gating live cells on a plot of forward scatter (FSC-H, which represents cell size) against side scatter (SSC-H, which represents cell granularity). A plot of fluorescence (FL1-H) against cell counts was used to quantify the number of live

cells positive for the protein of interest by manually setting the marker to incorporate < 1 % of the isotype and negative control cells. The geometric mean was then used to determine the positivity of the cells, with an arbitrary value of 5 being classified as positive. This value was set because the geometric mean of the negative control and the isotype control was between 2 and 4.

The same procedure was followed for HDLEC, except that cells initially were resuspended in FC media (Optimem 1 Reduced Serum Media with 0.1% BSA; Invitrogen, Paisley, UK) to a final concentration of 3 x 10^5 cells/ml. HDLEC were either stimulated with IFNγ (100 ng/ml, Peprotech, London, UK) or TNFα (10 ng/ml, R&D Systems, Abingdo, UK), or left in media alone, for 24 hours prior to FC.

Table 4 Antibodies used for flow cytometry and adhesion function blocking experiments.

Antigen	Supplier	Species Raised In	Final Concentration (FC)	Final Concentration (Adhesion Function Blocking)
LYVE-1	R&D Systems	goat	10 µg/ml	5 µg/ml
ICAM-1	R&D Systems	mouse	5 µg/ml	10 µg/ml
VCAM-1	R&D Systems	mouse	10 µg/ml	30 µg/ml
E-selectin	R&D Systems	mouse	10 ug/ml	10 µg/ml
CD 44	Sigma-Aldrich	rabbit	10 µg/ml	NA
α4 Integrin	R&D Systems	mouse	10 µg/ml	5 µg/ml
αvβ6 Integrin, Clone 53a2	Dr John Marshall (Barts Cancer Institue)	rat	10 µg/ml	10 µg/ml
α5 Integrin, Clone P1D6	Millipore	mouse	10 µg/ml	10 µg/ml
α9β1	Millipore	mouse	5 µg/ml	5 µg/ml
CLEVER-1	Dr Sirpa Jalkenen (Institute of Molecular Medicine, Finland)	mouse	10 µg/ml	20 µg/ml

3.14 Tissue Microarray (TMA)

For IHC validation, in-house tissue microarrays (TMA) were constructed of 0.6 mm representative cores of the 18 primary PDAC Croatian cases spotted in triplicate with a manual arrayer (Beecher Scientific). Normal donor pancreas was used for orientation. The 40 cases of primary PDAC from BTL had been included previously on a TMA of 80 cases of primary PDAC (kind gift from Mr Hemant Kocher). The matched metastatic LNs were analysed as whole sections due to the limited amount of malignant infiltrate in some of the cases.

3.15 Immunohistochemistry (IHC)

Three candidate proteins were selected for IHC validation on 4 µm sections using the Discovery XT system according to the manufacturer's protocols (Ventana Medical Systems Inc., Illkirch, France) using commercially available antibodies at the following dilutions: S100P (R&D systems, Abingdon, UK) 1:100; 14-3-3 sigma (Abcam, Cambridge, UK) 1:50 and moesin (Abcam, Cambridge, UK) 1:200. All sections were scored by two independent observers, with any discrepancies being resolved by consultation. Sections were evaluated for both intensity (0 = no stain; 1 = background; 2 = mild; 3 = moderate; 4 = severe) and percentage of epithelial cells that stained positive (0 = 0-5 %; 1 = 6-25 %; 2 = 26-50 %; 3 = 51-75 %; 4 = > 75 %). Total scores were derived from a sum of the intensity and percentage of immunoreactive cells (187). A total score of > 2 was considered positive.

4 µm sections of FFPE mouse tissue (orthotopic pancreatic tumours and peri-pancreatic LN) were stained with anti-mouse LYVE-1 (Abcam, Cambridge, UK) at a 1:100 dilution in order to visualise lymphatics, and anti-human cytokeratin-8 (Epitomics, California, USA) in order to visualise pancreatic cancer cells.

3.16 Functional Assays

3.16.1 Proliferation Assays

2.5×10^4 cells/well were plated into 24-well plates (Becton-Dickinson, Oxford, UK), and left to adhere overnight in a humidified atmosphere (5% CO_2 at 37^oC). Cells

remained in this humidified atmosphere for the duration of the experiment, and were removed only for quantitation. At this time, cells were overlayed with 500 µl of 1% trypsin EDTA. Following a 3 minute incubation in a humidified atmosphere (5% CO_2 at 37^oC), the plate was tapped sharply to dislodge any adherent cells. 500 µl of DMEM supplemented with 10% FCS then was added to each well in order to inactivate the trypsin. The cell suspensions from each well then were transferred to 1.5 ml Eppendorf tubes. Cells were counted using a haemocytometer every 24 hours for a period of five days.

3.16.2 siRNA Transfection

2×10^5 S5L cells were plated into six-well plates (Becton-Dickinson, Oxford, UK) and incubated overnight in a humidified atmosphere (5% CO_2 at 37^oC). A standard Interferin (Polyplus) protocol was then followed according to the manufacturer's instructions. Briefly, S100P or non-targeting siRNA (both from Dharmacon, Chicago, USA) were diluted to a final concentration of 50 nM in serum-free media (Sigma, Poole, UK) with Interferin (Polypus, Strasbourg, France) and incubated with the cells for 24 hours in a humidified atmosphere (5% CO_2 at 37^oC). The cells were incubated in DMEM media supplemented with 10% FCS thereafter for a further 48 hours in a humidified atmosphere (5% CO_2 at 37^oC), at which time cells were harvested for Western Blot analysis.

3.16.3 Invasion Assays

Invasion assays were done using Biocoat Matrigel Invasion Chambers with 8 µm pores (Becton-Dickinson, Oxford, UK). 2.5 x 10^4 cells in 500 µl serum-free DMEM were added to the upper chamber, and 700 µl DMEM supplemented with 10% FCS was added to the lower chamber; cultures were incubated for 48 h in a humidified atmosphere (5% CO_2 at 37^{o}C). Cells that had moved through the pores were fixed in 100% methanol and stained with 1% Giemsa blue (Sigma, Poole, UK). The number of invaded cells was counted by averaging five random fields (x20 objective, Zeiss Axiophot microscope, Hertfordshire, UK).

3.16.4 Cancer cell – HDLEC Adhesion Assays

Adhesion assays were performed using 96-well plates (Becton-Dickinson, Oxford, UK). Initially, 50 µl of FN (Becton-Dickinson, Oxford, UK) at a 0.5 µg/ml concentration was added to each well and left to set for one hour at 37^{o}C. 1.5 x 10^4 HDLEC were then seeded into each well and left to settle overnight in a humidified atmosphere (5% CO_2 at 37^{o}C). The following day, HDLEC were either stimulated with IFNγ (100 ng/ml, Peprotech, London, UK) or TNFα (10 ng/ml, R&D Systems, Abingdo, UK), or left in media alone, for 24 hours. The next day, V3L or S5L cells were labelled with the red fluorescent dye $DiIC_{12}$ (Becton-Dickinson, Oxford, UK) at a final concentration of 10 µg/ml for one hour at 37^{o}C. Medium containing the relevant cytokines was removed from HDLEC; HDLEC were washed with PBS and 1 x 10^4 fluorescent cancer cells in a 50 µl volume of Optimem I Reduced Serum Media (Invitrogen, Paisely, UK) then were added to each well. Co-cultures were incubated

for 45 minutes in a humidified atmosphere (5% CO_2 at 37^oC), after which, each well was washed thrice with PBS to remove any non-adherent cancer cells. Fluorescence was quantified using the Fluostar Optima (BMG Labtech, Ortenberg, Germany) in relation to a standard curve to determine the absolute number of adherent cancer cells.

For function blocking experiments, HDLEC were incubated with 50 µl of the appropriate blocking antibodies (**Table 4**) for 1 hour in a humidified atmosphere (5% CO_2 at 37^oC), with any unbound antibody thereafter being washed off with PBS, prior to the addition of fluorescently-labelled cancer cells.

3.16.5 Hyaluronic Acid (HA) Binding Assays

These assays were performed in 96-well plates (Becton-Dickinson, Oxford, UK). 50 µl of fluorescein hyaluronic acid (Sigma, Poole, UK) at a 1 mg/ml concentration was added to each well, and left to set for one hour at 37^oC. 1 x 10^4 V3L or S5L cells suspended in 50 µl of Optimem I Reduced Serum Media (Invitrogen, Paisley, UK) were then added per well, and left to incubate at 37^oC for one hour. Wells were washed three times with PBS to remove any non-adherent HA. The amount of remaining HA in each well was quantified using the Fluostar Optima (BMG LabTech, Ortenberg, Germany) in relation to a standard curve.

3.16.6 Fibronectin (FN) Binding Assays

These assays were performed in 96-well plates (Becton-Dickinson, Oxford, UK). 50 µl of FN (BD Biosciences, Oxford, UK) at a 20 µg/ml concentration was added to each well, and left to set overnight at 4^{o}C. The next day, V3L or S5L cells (1 x 10^4 per 50 µl of Optimem I Reduced Serum Media (Invitrogen, Paisley, UK)), which had been labelled with the red fluorescent dye $DiIC_{12}$ (BD Biosciences, Oxford, UK) earlier that day, then were added to each well, and left to incubate in a humidified atmosphere (5% CO_2 at 37^{o}C) for 45 minutes. Wells were washed three times with PBS to remove any non-adherent cells. The number of adherent cells was then quantified on the Fluostar Optima (BMG LabTech, Ortenberg, Germany) in relation to a standard curve.

3.16.7 Permeability and Translymphatic Endothelial Migration (TLEM) Assays

These assays were performed in 24-well Migration Chambers with 8 µm pores (Becton-Dickinson, Oxford, UK). Initially, 100 µl of FN at a 0.5 µg/ml concentration (Becton-Dickinson, Oxford, UK) was added to the upper chamber of each well and left to set at 4^{o}C overnight. At D0, 2.5 x 10^5 HDLEC were seeded onto the FN, and left overnight in a humidified atmosphere (5% CO_2 at 37^{o}C) to form a confluent monolayer. At D1, 5 x 10^5 V3L or S5L cells were seeded onto this monolayer in 500 µl of Optimem I Reduced Serum Media (Invitrogen, Paisley, UK) containing 2 million MW FITC-Dextran (Sigma, Poole, UK) at a 1 mg/ml concentration (**Figure 6**). 700 µl of Optimem I Reduced Serum Media (without FITC-Dextran) was then added to the lower chamber, in order to establish a diffusion gradient. Permeability through the

HDLEC monolayer was quantified by measuring the amount of FITC-Dextran that permeated into the lower chamber at 1, 4, 8, 12 and 24 hours post-seeding in relation to a standard curve on the Fluostar Optima (BMG Labtech, Ortenberg, Germany) (**Figure 7**). For example, at one hour post-seeding, the inserts were moved into new wells containg 700 µl of Optimem I Reduced Serum Media (without FITC-Dextran), which were used for the next time-point. Then 50 µl of media from each of the inital wells was transferred to a 96-well plate containing a standard curve of FITC-Dextran (serial 1:2 dilutions of 1 mg/ml stock concentration) from which the FITC-Dextran concentration of each test sample was extrapolated. Standards and test samples were measured in triplicate.

At D2, the inserts containing the co-cultures (**Figure 8**) were moved into a new 24-well plate (Becton-Dickinson, Oxford, UK). Upper chambers were replenished with 500 µl Optimem I Reduced Serum Media, whilst 700 µl of DMEM containing 10% FCS was added to the bottom chamber as an attractant. The number of cells which had migrated into the lower chamber was quantified 72 hours later using the Coulter Counter (Beckman Coulter, Inc., High Wycombe, UK).

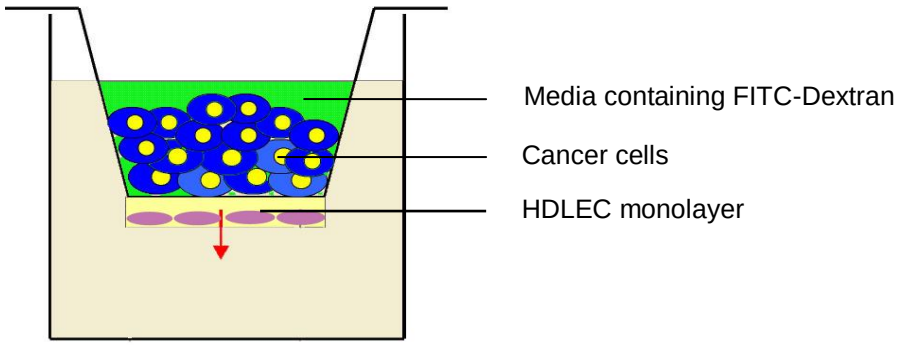

Figure 6 Permeability assay schema. 5 x 10^5 cancer cells (blue) were seeded onto a HDLEC monolayer (mauve) in 500 µl of Optimem I Reduced Serum Media containing 1 mg/ml of FITC-Dextran (2 million MW; green). This insert, which contained both cell types, was then inserted into a 24-well plate; each well contained 700 µl Optimem I Reduced Serum Media without FITC-Dextran (fawn). The red arrow represents the diffusion gradient. The amount of FITC-Dextran that permeated through the HDLEC monolayer over time was used as a measure of permeability.

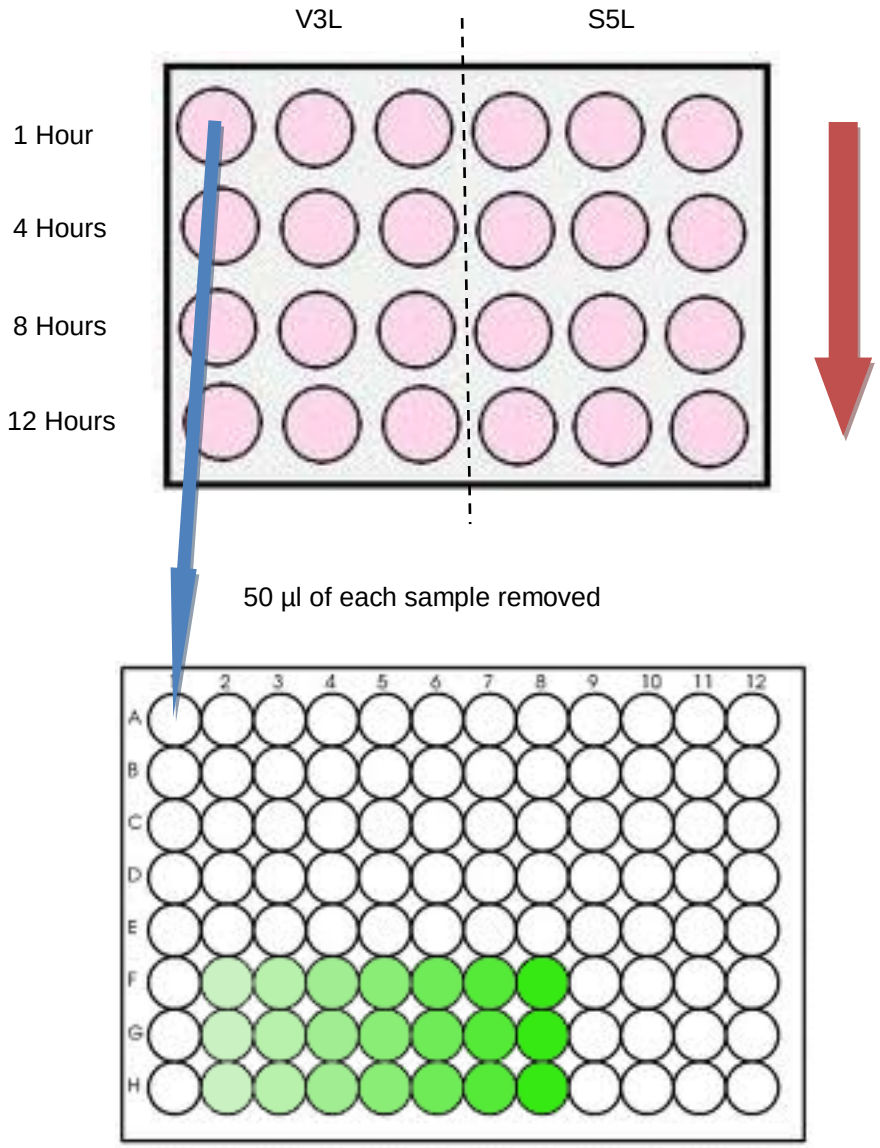

Figure 7 Measuring permeability. At each time-point, inserts were moved to new wells containing 700 µl Optimem I Reduced Serum Media (red arrow). Then 50 µl of media from each used well was transferred (in triplicate) to a 96-well plate (blue arrow). The amount of FITC-Dextran that had permeated through the HDLEC monolayer into the bottom well at each time-point was quantified in relation to a standard curve (green) using a fluorescent plate-reader.

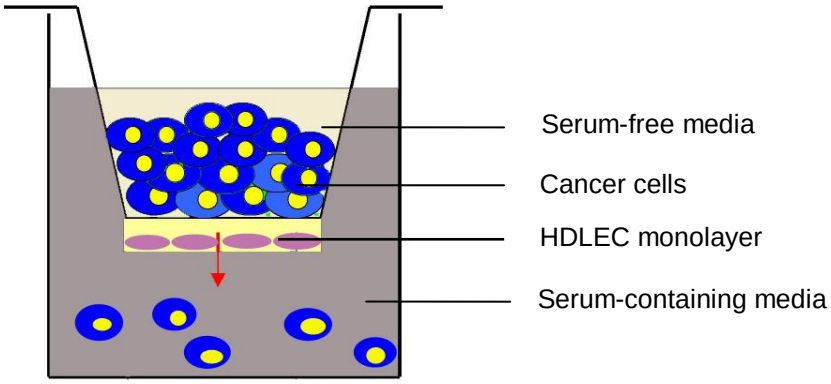

Figure 8 Translymphatic endothelial migration assay schema. Inserts containing cancer cells (blue) and HDLEC (mauve), which had been used to measure permeability over 24 hours, were moved into new 24-well plates. The top wells were replenished with 500 µl Optimem I Reduced Serum Media (Serum-free media; fawn), whilst 700 µl of DMEM (grey) which had been supplemented with 10% FCS was added to the lower wells. The latter served as a chemoattractant. The migration of cancer cells through the HDLEC monolayer then was quantified over 48 hours.

3.16.8 Luciferase Assay

Quantification of luciferase expression of V3L and S5L cells *in vitro* was done using the Luciferase Assay System (Promega, Southampton, UK). Briefly, 5 x 10^5 cells were lysed in 1 x lysis buffer. The sample was centrifuged at 12,000 x g for 15 seconds at room temperature, after which the supernatant was transferred to a new 1.5 ml Eppendorf tube. Serial 1:10 dilutions were performed on these stock samples. These samples then were quantified using a VICTOR 1420 Multilabel Counter (Perkin Elmer, Massachusetts, USA).

3.16.9 Soft Agar Assays

A total of 200 cells in a single-cell suspension were mixed, on ice, in 5 ml of DMEM medium with 0.3% agarose (Sigma, Poole UK). After 20 minutes, 1 ml of DMEM containing 10% FCS was added. Cultures were incubated in a humidified atmosphere (5% CO_2 at 37^{o}C) for 18 days, at which point the wells were photographed on a Stemi SV11 microscope (Zeiss, Hertfordshire, UK). The total number of colonies was counted, and the total area of the colonies was determined using ImageJ software. Briefly, the microscopy images initially were converted into grey-scale format using Adobe Photoshop CS4 software; these grey-scale images were then opened in ImageJ. Colonies were highlighted using the 'wand' tool, and the total area then was quantified using the 'measure' tool.

3.17 Mouse Models

Mice were anaesthetised using inhalation anaesthesia (Isoflurane with Oxygen and Nitrous Oxide) for both induction and maintenance.

For the orthotopic pancreatic mouse model (n = 10 per group), a 2 cm incision was made in the abdominal wall, parallel to the ribcage. After exteriorisation of the pancreas and spleen, 40 μl of cell suspension (containing 6.5 x 10^5 V3L or S5L cells suspended in PBS) was injected into the tail of the pancreas using an insulin syringe, and a 29 gauge x ½ inch needle (Southern Syringe Services, Leicester, UK). The injection site was dabbed gently with a cotton swab (Southern Syringe Services, Leicester, UK) immediately following injection to ensure that no leakage occurred. Skin and muscle were sutured using Vicryl 4.0 (Southern Syringe Services, Leicester, UK). Immediately after surgery, mice were transferred to a 'recovery cage', which contained food and water, and which was heated externally using a heater. As only inhalation anaesthesia was used for induction and maintenance, recovery usually occurred within 30 minutes post-operatively. Mice were monitored daily thereafter, initially to ensure that the sutures had healed adequately, and thereafter to ensure that they were not showing signs of ill health. Mice were imaged weekly from week 1 post-operation using the IVIS imaging system to monitor both the growth of the primary tumour and the potential development of metastases (see below). The experiment was terminated at 10 weeks post-injection.

In order to assess site-specific growth, mice (n = 7 per group) were subjected to the above-mentioned procedure, with the following modifications:

5×10^5 V3L or S5L cells were injected in a 40 µl volume into the spleen in order to seed to the liver; and 1×10^5 V3L or S5L cells were injected in a 10 µl volume using a 30 gauge x 5 mm custom syringe (Hamilton Syringes) into the right axillary lymph node, following a 1 cm incision into the overlying skin. The former experiment was terminated at 6 weeks, the latter at 10 weeks, post-injection.

Lastly, 5×10^5 V3L or S5L cells in a 200 µl volume were injected directly into the tail vein in order to assess experimental metastasis. No anaesthesia was given for this procedure. Mice were pre-warmed using warm air in order to dilate the blood vessels. This experiment was terminated at 4 weeks post-injection.

3.18 Bioluminescence Imaging *in vivo*

Mice received an intraperitoneal injection of 150 µl of D-luciferin (Caliper Life Sciences, Cheshire, UK) diluted with distilled water to a final concentration of 15 mg/ml. Thereafter, they were anaesthetised using inhalation anaesthesia (Isoflurane with Oxygen and Nitrous Oxide) for the duration of the imaging procedure. Images were taken using the IVIS-100 (Xenogen, Caliper Life Sciences, Cheshire, UK) at 10 minutes post-injection. Regions of interest (ROI) were calculated for each mouse. ROI calculates the signal intensity for a standardised area for each mouse, and is a quantitative measure of bioluminescence, and thus tumour growth. The ROI for each mouse were plotted weekly until each experiment was terminated. In addition, average ROIs for each experimental group (i.e. V3L and S5L) were calculated for the duration of each experiment.

3.19 Processing of Mouse Tissues

Harvested tissues (tumours, normal pancreas, duodenum, liver, lungs, any tissue suspicious for metastasis, and lymph nodes) were either formalin-fixed and paraffin-embedded, or snap-frozen in liquid nitrogen. Frozen tissue was stored in 2 ml cryovials at -80^{o}C. All tumours were weighed prior to processing.

3.20 Ingenuity Pathway Analysis (IPA)

Proteomics data were analysed using IPA (version 4.0), a web-based application (http://www.ingenuity.com/) that identifies biologically relevant pathways from gene and/or protein expression data. This software is based on the IKPB (Knowledge Base database), one of the largest curated bioinformatics databases containing millions of computable relationships between genes, proteins, drugs and diseases. IPA builds biological networks and explores signalling pathways based on entered experimental data and known published associations. Furthermore, scores are generated for each network, quantifying the likelihood of associations not being due to chance alone (e.g., a score of 2 gives a 99% confidence, with higher scores signifying greater confidence). Based on these scores, IPA prioritises networks, identifies associated proteins, and assigns the most significant biological functions to each network. The global functional analysis feature calculates this significance using a right-tailed Fisher's exact test, with a p-value ≤ 0.05 being considered significant.

3.21 Statistics and Target Selection

3.21.1 Normalisation of MudPIT data

Proteins initially were filtered to exclude those that appeared only in MudPIT experiment 1 or experiment 2. The remaining proteins, common to both experiments, then were filtered according to spectral count. Data were normalised to correct for the differences in spectral counts between samples as follows:

Spectral count of individual protein x ((Total LN spectral count ÷ Total PDAC spectral count) + 0.01)

A corrective factor of 0.01 was used to eliminate any zeroes for g-test calculations. As two experiments were performed, a mean spectral count was calculated for PDAC and LN samples, respectively. All proteins with a mean spectral count between 0 and 5 in both samples were excluded from downstream analysis due to the limited sensitivity of the mass spectrometer, particularly when dealing with a low number of replicate samples.

3.21.2 G-test Analysis of MudPIT data

For the remaining proteins a g-test was performed. The g-test (likelihood ratio; goodness-of-fit) has been shown to be superior for samples with less than three measurements (90). It calculates the x^2-distribution with one degree of freedom. A g-value of ≥ 3.8 is considered significant.

The original equation used for the calculation of the g-value is as follows:

$$g = 2f_{obs}1 \ln(f_{obs}1/f_{exp}1) + 2f_{obs}2 \ln (f_{obs}2/f_{exp}2)$$

Where $f_{obs}1$ = observed value in sample 1

$f_{obs}2$ = observed value in sample 2

$f_{exp}1$ = expected frequencies in sample 1

$f_{exp}2$= expected frequencies in sample 2

The null hypothesis is that there is no differential expression between the 2 samples.

Therefore

$$f_{obs}1 = f_{obs}2 = (f_{obs}1 + f_{obs}2)/2$$

This also is equal to the mean of the observed counts between all samples ($mean_T$).

Therefore the equation becomes

$$g = 2\ f_{obs}1 \ln(f_{obs}1/mean_T) + 2\ f_{obs}2 \ln (f_{obs}2/mean_T)$$

Which becomes

$$g = 2\ [(f_{obs}1 \ln(f_{obs}1/mean_T) + f_{obs}2 \ln(f_{obs}2/mean_T)]$$

3.21.3 IHC Validation

For IHC validation, the average score for each matched case was calculated, and a Mann-Whitney test was performed to determine differential expression between primary PDAC and metastatic LN samples. A p-value ≤ 0.05 was considered significant.

3.21.4 Experiments conducted *in vitro*

All the *in vitro* experiments were repeated three times in triplicate. A paired Student's t-test was then performed, with a p-value of ≤ 0.05 being considered significant. Error bars show standard error of the mean (SEM).

3.21.5 Experiments conducted *in vivo*

A Mann-Whitney test was performed on all data, with a p-value of ≤ 0.05 being considered significant. Error bars show standard error of the mean (SEM).

4. RESULTS (Part I): PROTEOMICS

4.1. LCM and MudPIT Analysis

In order to differentiate the malignant epithelia from the surrounding connective tissue, sections were stained with haematoxylin before LCM. Seven matched cases (10,000 - 15,000 cells/case) were dissected in total, with four and three cases subsequently being pooled. This resulted in four pooled samples – two PDACs and two matched LN metastases – each comprising 10 µg of protein (40,000 - 45,000 cells) that were used for downstream Multidimensional Protein Identification Technology (MudPIT) analysis. Representative sections of a malignant pancreatic duct before and after LCM are shown in **Figure 9**, together with the subsequent workflow for analysis.

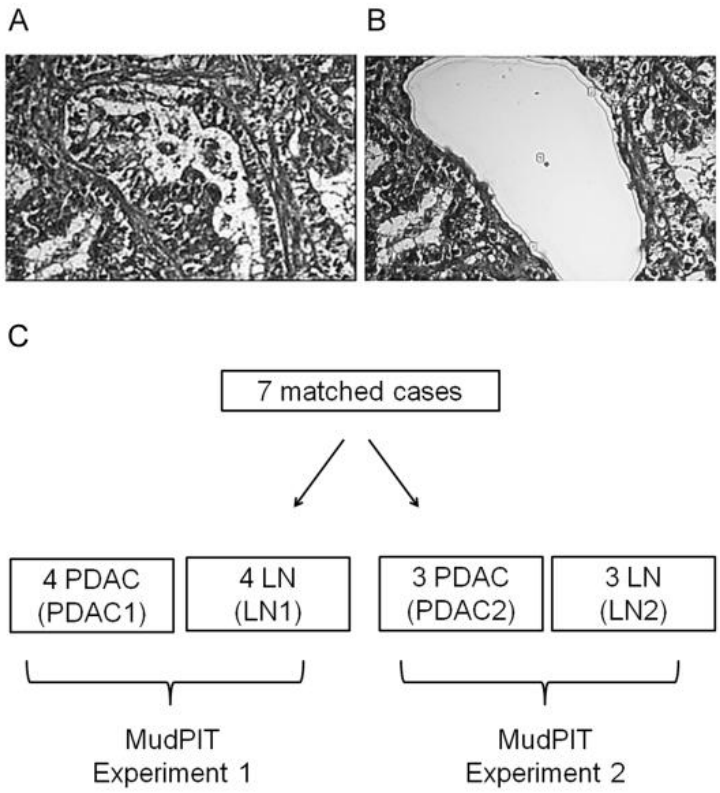

Figure 9 Laser Capture Microdissection (LCM). Representative images (100x magnification) show a malignant pancreatic duct before (**A)** and after (**B)** LCM. The workflow for LCM is shown in (**C)**.

In total, 1504 proteins were identified across both experiments. **Table 5** displays the total number of proteins identified, as well as the total spectral counts, for each sample. Spectral counts reflect the number of peptides identified *in silico* and the number of times those matched peptides were observed. Spectral count has been shown to be a semi-quantitative measure of abundance across samples, with a linear correlation to relative abundance over a two order of magnitude linear dynamic range (89). This correlation is seen in our samples – the higher the number of total

spectral counts, the higher the number of identified proteins. On average, a lower number of proteins were seen in primary PDACs as opposed to LN metastases. However, this did not affect the statistical analysis, as samples were normalised before being tested for differential expression. Normalisation corrects for the differences in total spectral count seen between samples, and ensures a 'level playing field' before differential expression is calculated. The False Discovery Rate (FDR), which represents the number of false positives or the number of peptides that were incorrectly identified, was < 1.5% for all samples.

Table 5 MudPIT results. The total number of proteins, as well as the total spectral counts, identified in PDAC samples and matched LN metastases. The false discovery rate (FDR) for all samples was <1.5%.

	PDAC 1	**PDAC 2**	**LN 1**	**LN 2**
Total no. of proteins	598	858	858	1119
Total spectral counts	4794	7723	8066	11049
Total unique peptides	2577	4213	4068	5696
Mean spectral count	8.017	9.001	9.401	9.874
Mean unique peptides	4.309	4.910	4.741	5.090
No. of reverse hits	4	8	6	8
% FDR	1.329	0.924	1.389	0.710

The relationship between the proteins found across both experiments is illustrated in the Venn diagram in **Figure 10**. Of the 1504 proteins found, 650 were found in only one of the two MudPIT experiments and were thus excluded from further analysis. The remaining 854 proteins were commonly expressed in both experiments (**Appendix I**); these represent the proteome of primary PDAC and LN metastases. Following filtering on the basis of spectral count, a statistical g-test was performed – this resulted in a list of 115 significantly differentially expressed proteins (g-value ≥ 3.8) (**Table 6**).

Table 6 List of 115 significantly differentially expressed proteins. The 854 proteins common to all four samples were subjected to a g-test to determine which proteins were significantly differentially expressed ($g \geq 3.8$). Of these, S100P (high g-value), 14-3-3 sigma (intermediate g-value) and moesin (low g-value; all three proteins are highlighted in red), were selected for validation using immunohistochemistry (IHC). The IHC served to validate the statistical approach used, as well as to validate the up-regulation of the candidate proteins.

Identified Proteins	Accession No.	MW	G-Value
TUBA4A Tubulin alpha-4A chain	IPI00007750	50 kDa	49.76
TPM4 Isoform 2 of Tropomyosin alpha-4 chain	IPI00216975	33 kDa	34.52
HNRNPH1 Heterogeneous nuclear ribonucleoprotein H	IPI00013881	49 kDa	33.13
YWHAH 14-3-3 protein eta	IPI00216319	28 kDa	31.75
KRT7 Keratin, type II cytoskeletal 7	IPI00306959	51 kDa	27.77
CSE1L Isoform 1 of Exportin-2	IPI00022744	110 kDa	27.59
IQGAP2 Isoform 1 of Ras GTPase-activating-like protein IQGAP2	IPI00299048	181 kDa	25.12
COL12A1 Isoform 4 of Collagen alpha-1(XII) chain	IPI00302944	325 kDa	24.28
H2AFY2 Core histone macro-H2A.2	IPI00220994	40 kDa	22.05
S100P Protein S100-P	IPI00017526	10 kDa	20.66
ENO2 Gamma-enolase	IPI00216171	47 kDa	20.66
LCP1 Plastin-2	IPI00010471	70 kDa	18.80
TUBB2A Tubulin beta-2A chain	IPI00013475	50 kDa	18.72
KRT20 Keratin, type I cytoskeletal 20	IPI00021298	48 kDa	17.58
TPM1 tropomyosin 1 alpha chain isoform 7	IPI00216134	29 kDa	16.56
RPL8 60S ribosomal protein L8	IPI00012772	28 kDa	16.51
S100A10 Protein S100-A10	IPI00183695	11 kDa	16.51
CCT5 T-complex protein 1 subunit epsilon	IPI00010720	60 kDa	16.51
HNRNPA1 Isoform A1-B of Heterogeneous nuclear ribonucleoprotein A1	IPI00215965	39 kDa	16.27
TNC Isoform 1 of Tenascin	IPI00031008	241 kDa	16.20
YWHAZ 14-3-3 protein zeta/delta	IPI00021263	28 kDa	15.79
DSP Isoform DPI of Desmoplakin	IPI00013933	332 kDa	14.25
FLNB Isoform 1 of Filamin-B	IPI00289334	278 kDa	14.25
SPTBN1 Isoform Long of Spectrin beta chain, brain 1	IPI00005614	275 kDa	14.22
CTSG Cathepsin G	IPI00028064	29 kDa	14.21

TRIM28 Isoform 1 of Transcription intermediary factor 1-beta	IPI00438229	89 kDa	13.49
MARCKS Myristoylated alanine-rich C-kinase substrate	IPI00219301	32 kDa	13.49
PKM2 Isoform M1 of Pyruvate kinase isozymes M1/M2	IPI00220644	58 kDa	12.52
YWHAQ 14-3-3 protein theta	IPI00018146	28 kDa	12.21
HBA1;HBA2 Hemoglobin subunit alpha	IPI00410714	15 kDa	12.03
LGALS4 Galectin-4	IPI00009750	36 kDa	11.16
SFN Isoform 1 of 14-3-3 protein sigma	IPI00013890	28 kDa	11.12
FGB Fibrinogen beta chain	IPI00298497	56 kDa	10.84
IQGAP1 Ras GTPase-activating-like protein IQGAP1	IPI00009342	189 kDa	10.58
YWHAG 14-3-3 protein gamma	IPI00220642	28 kDa	10.48
DMBT1 Isoform 1 of Deleted in malignant brain tumors 1 protein	IPI00099110	261 kDa	10.37
ERH Enhancer of rudimentary homolog	IPI00029631	12 kDa	10.18
CRYZ Quinone oxidoreductase	IPI00000792	35 kDa	9.76
UQCRC2 Cytochrome b-c1 complex subunit 2, mitochondrial	IPI00305383	48 kDa	9.76
HSD17B4 Peroxisomal multifunctional enzyme type 2	IPI00019912	80 kDa	9.76
S100A8 Protein S100-A8	IPI00007047	11 kDa	9.72
WDR1 Isoform 2 of WD repeat-containing protein 1	IPI00216256	58 kDa	9.69
PGM1 Isoform 1 of Phosphoglucomutase-1	IPI00219526	61 kDa	9.07
KRT14 Keratin, type I cytoskeletal 14	IPI00384444	52 kDa	8.78
RPS4X 40S ribosomal protein S4, X isoform	IPI00217030	30 kDa	8.76
PRKDC Isoform 1 of DNA-dependent protein kinase catalytic subunit	IPI00296337	469 kDa	8.70
SFPQ Isoform Long of Splicing factor, proline- and glutamine-rich	IPI00010740	76 kDa	8.34
CTNNB1 Isoform 1 of Catenin beta-1	IPI00017292	85 kDa	8.29
HADHA Trifunctional enzyme subunit alpha, mitochondrial	IPI00031522	83 kDa	8.10
RPL15 60S ribosomal protein L15	IPI00470528	24 kDa	7.92
KRT18 Keratin, type I cytoskeletal 18	IPI00554788	48 kDa	7.90
HNRNPF Heterogeneous nuclear ribonucleoprotein F	IPI00003881	46 kDa	7.84
TAGLN2 Transgelin-2	IPI00550363	22 kDa	7.82
UGDH UDP-glucose 6-dehydrogenase	IPI00031420	55 kDa	7.62
LRPPRC Leucine-rich PPR motif-containing protein, mitochondrial	IPI00783271	158 kDa	7.54
HBB Hemoglobin subunit beta	IPI00654755	16 kDa	7.29
MPO Isoform H17 of Myeloperoxidase	IPI00007244	84 kDa	7.02
DEFA1;LOC728358 Neutrophil defensin 1	IPI00005721	10 kDa	6.93
MVP Major vault protein	IPI00000105	99 kDa	6.83
ITPR3 Inositol 1,4,5-trisphosphate receptor type 3	IPI00291607	304 kDa	6.82

PDCD6 Programmed cell death protein 6	IPI00025277	22 kDa	6.82
AKR1B10 Aldo-keto reductase family 1 member B10	IPI00105407	36 kDa	6.82
HNRNPM Isoform 1 of Heterogeneous nuclear ribonucleoprotein M	IPI00171903	78 kDa	6.61
YWHAB Isoform Long of 14-3-3 protein beta/alpha	IPI00216318	28 kDa	6.61
TLN1 Talin-1	IPI00298994	270 kDa	6.59
C22orf28 UPF0027 protein C22orf28	IPI00550689	55 kDa	6.54
EVPL Envoplakin	IPI00023711	232 kDa	6.54
PDXDC1 Isoform 1 of Pyridoxal-dependent decarboxylase domain-containing protein 1	IPI00384689	87 kDa	6.54
RPL4 60S ribosomal protein L4	IPI00003918	48 kDa	6.54
ARPC1B Actin-related protein 2/3 complex subunit 1B	IPI00005160	41 kDa	6.50
PSMA1 Isoform Short of Proteasome subunit alpha type-1	IPI00016832	30 kDa	6.50
HSPA1B;HSPA1A Heat shock 70 kDa protein 1	IPI00304925	70 kDa	6.28
PFKL Isoform 1 of 6-phosphofructokinase, liver type	IPI00332371	85 kDa	6.24
CPT1A Isoform 1 of Carnitine O-palmitoyltransferase 1, liver isoform	IPI00032038	88 kDa	5.96
LIMA1 Isoform Beta of LIM domain and actin-binding protein 1	IPI00008918	85 kDa	5.96
TUFM Tu translation elongation factor, mitochondrial precursor	IPI00027107	50 kDa	5.84
THBS1 Thrombospondin-1	IPI00296099	129 kDa	5.80
KTN1 Isoform 1 of Kinectin	IPI00328753	156 kDa	5.75
RAB14 Ras-related protein Rab-14	IPI00291928	24 kDa	5.73
OGDH 2-oxoglutarate dehydrogenase E1 component, mitochondrial	IPI00098902	116 kDa	5.72
EIF4A3 Eukaryotic initiation factor 4A-III	IPI00009328	47 kDa	5.65
APEX1 DNA-(apurinic or apyrimidinic site) lyase	IPI00215911	36 kDa	5.52
PARP1 Poly [ADP-ribose] polymerase 1	IPI00449049	113 kDa	5.52
PLS1 Plastin-1	IPI00032304	70 kDa	5.52
RPS15A 40S ribosomal protein S15a	IPI00221091	15 kDa	5.52
CYCS Cytochrome c	IPI00465315	12 kDa	5.51
TMSB4X Thymosin beta-4	IPI00220828	5 kDa	5.51
CTNNA1 Isoform 1 of Catenin alpha-1	IPI00215948	100 kDa	5.08
RPL5 60S ribosomal protein L5	IPI00000494	34 kDa	5.05
DYNC1H1 Cytoplasmic dynein 1 heavy chain 1	IPI00456969	532 kDa	4.89
HNRNPL Heterogeneous nuclear ribonucleoprotein L	IPI00027834	64 kDa	4.77
GOT1 Aspartate aminotransferase, cytoplasmic	IPI00219029	46 kDa	4.77
LMNB1 Lamin-B1	IPI00217975	66 kDa	4.76
LMNA Isoform A of Lamin-A/C	IPI00021405	74 kDa	4.71

FBN1 Fibrillin-1	IPI00328113	312 kDa	4.65
NONO Non-POU domain-containing octamer-binding protein	IPI00304596	54 kDa	4.61
CCT4 T-complex protein 1 subunit delta	IPI00302927	58 kDa	4.53
VDAC1 Voltage-dependent anion-selective channel protein 1	IPI00216308	31 kDa	4.53
EFHD2 EF-hand domain-containing protein D2	IPI00060181	27 kDa	4.53
EHD1 EH domain-containing protein 1	IPI00017184	61 kDa	4.53
AIFM1 Isoform 1 of Apoptosis-inducing factor 1, mitochondrial	IPI00000690	67 kDa	4.53
PCBP2 poly(rC) binding protein 2 isoform b	IPI00012066	38 kDa	4.35
ALDOA Fructose-bisphosphate aldolase A	IPI00465439	39 kDa	4.33
PCBP1 Poly(rC)-binding protein 1	IPI00016610	37 kDa	4.28
ANXA4 annexin IV	IPI00793199	36 kDa	4.24
HMGA1 Isoform HMG-I of High mobility group protein HMG-I/HMG-Y	IPI00179700	12 kDa	4.23
HIST1H1E Histone H1.4	IPI00217467	22 kDa	4.20
SRI Sorcin	IPI00027175	22 kDa	4.14
FUBP1 Isoform 1 of Far upstream element-binding protein 1	IPI00375441	68 kDa	4.02
VIM Vimentin	IPI00418471	54 kDa	4.01
KPNB1 Importin subunit beta-1	IPI00001639	97 kDa	3.93
SFRS1 Isoform ASF-1 of Splicing factor, arginine/serine-rich 1	IPI00215884	28 kDa	3.86
PA2G4 Proliferation-associated protein 2G4	IPI00299000	44 kDa	3.86
HSPB1 Heat shock protein beta-1	IPI00025512	23 kDa	3.82
MSN Moesin	IPI00219365	68 kDa	3.76

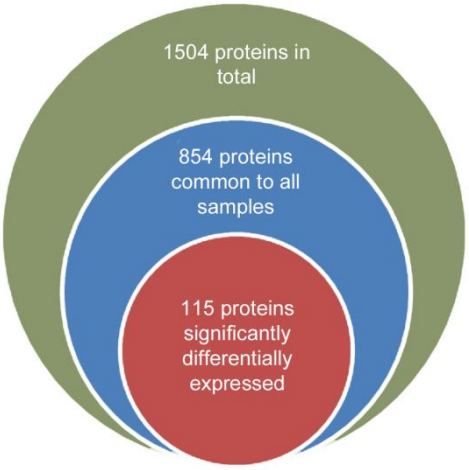

Figure 10 Relationship between the proteins found using MudPIT. Of the 1504 proteins found in total, 854 proteins were seen in all four samples analysed. Of these 854 proteins, 115 proteins were found to be significantly differentially expressed following a statistical g-test (g-value ≥ 3.8).

Quantification of the subcellular compartmental distribution (**Figure 11**) showed that most of the classified proteins were cytoplasmic (57.6%) and nuclear (18.3%). Cell membrane constituted 8.9% of the proteome. 8.5% of the proteome was found to be extracellular, whilst the remaining proteins (6.7%) could not be classified or were unknown.

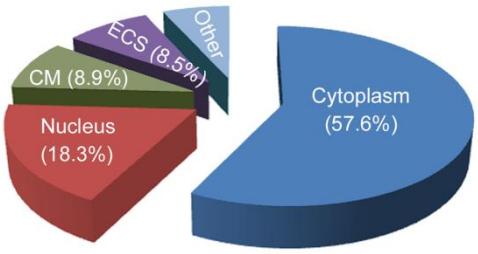

Figure 11 Subcellular compartmentalisation of 854 proteome. The majority of the 854 proteins were cytoplasmic (57.6%) and nuclear (18.3%), with cell membrane (CM) proteins being less well represented. Some proteins in the proteome (8.5%) originated from the extracellular space (ECS). The remaining 6.7% of the 854 proteome could not be classified or were unknown, and thus, are depicted as 'other'.

IPA analysis demonstrated that the top five biological functions within the 854 discovered proteins were: cellular growth and proliferation (165 proteins); cell death (132 proteins); cellular movement (90 proteins); cell-to-cell signalling (69 proteins) and protein synthesis (44 proteins) (**Figure 12**). Qualitative analysis of this proteome highlighted a number of proteins involved in these top five biological functions: integrins α2, α3, αV, β1, and β4 (growth and proliferation, cellular movement and signalling); eight of the 21 known S100 proteins, namely S100A4, S100 A6, S100A8, S100A9, S100A10, S100A11, S100A16 and S100P (growth and proliferation, cellular movement and signalling); IQGAP1 and IQGAP2 (cellular movement and signalling); cathepsins B, G and Z (cellular movement); and lastly, α –, β – and δ – catenin (signalling). In addition, six out of seven members of the 14-3-3 family of regulatory proteins (14-3-3- β/α, γ, ζ/δ, η, θ, and σ), which have the capacity to bind various

signalling molecules also appeared in the proteome; moreover, all of these were significantly differentially expressed between PDAC and LN metastasis.

Comparison of our 854 proteins with previously reported proteomic data on the pancreas (tissues, pancreatic juice, serum and urine) using the Pancreatic Expression Database (http://www.pancreasexpression.org), showed a 29% overlap; the proteins common to all studies, including ours, are listed in **Appendix II**.

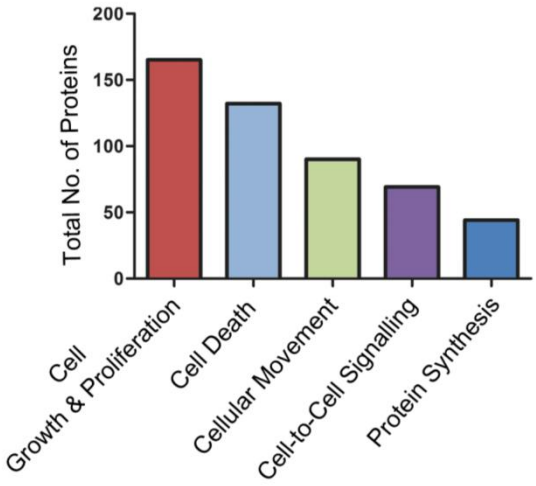

Figure 12 Top five biological functions associated with the 854 proteome. Ingenuity Pathway Analysis (IPA) ranked cell growth and proliferation as the top biological function associated with the 854 identified proteins. This was followed by cell death, cellular movement, cell-to-cell signalling and protein synthesis.

4.2 Validation of MudPIT Data using IHC

Three proteins with high, intermediate and low g-values, respectively were chosen for further validation by IHC in a larger series of 55 matched cases of primary PDAC and LN metastases The IHC served both to validate the statistical approach used to analyse the MudPIT data, as well as to confirm the up-regulation of the candidate proteins in LN metastases. Proteomic analysis showed that S100P (g-value = 20.66) and 14-3-3 sigma (g-value = 11.12) were significantly up-regulated in metastatic LN specimens (**Table 6** – highlighted in red). Although moesin had an equivocal g-value of 3.76, we chose to investigate it further as it had previously been shown to be up-regulated in association with LN metastasis.

S100P was successfully analysed in 52/55 cases; whilst 14-3-3 sigma and moesin were successfully analysed in 51/55 cases. Some cases had to be omitted from the final analysis due to technical loss of tissue cores. Both S100P ($p = 0.05$) and 14-3-3 sigma ($p < 0.001$) were confirmed to be significantly up-regulated in LN metastatic epithelia by IHC (**Figures 13** and **14**). All of the 52 cases analysed showed high levels of S100P expression in both the primary PDAC and LN metastases, with S100P localising to both the cytoplasm and nucleus (**Figure 13A-D**). In contrast, 14-3-3 sigma expression was restricted to the cytoplasm of malignant epithelia (**Figure 14A-D**). Only six primary PDACs did not express 14-3-3 sigma, and of those, four showed up-regulation in matched LN metastases, whilst two metastatic LN were negative for 14-3-3 sigma expression.

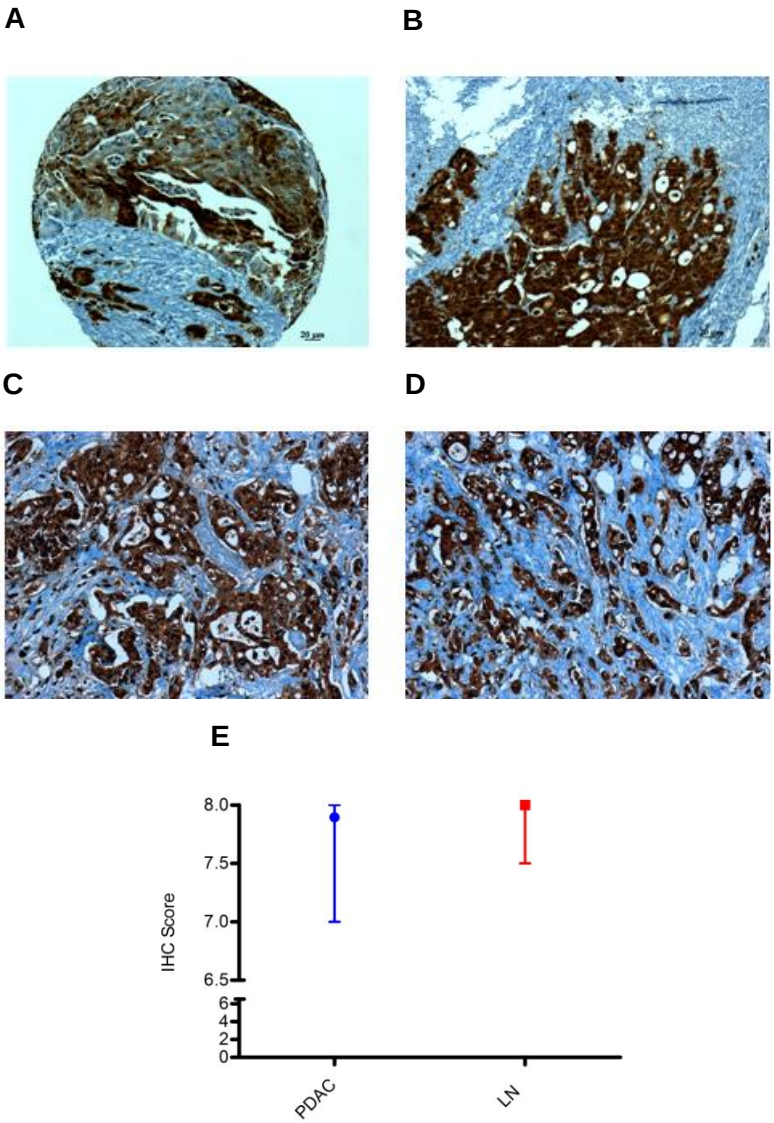

Figure 13 IHC validation of S100P differential expression (n = 52). Representative images of primary PDAC (**A** and **C**) and matched LN metastases (**B** and **D**; 100x magnification) show that S100P was strongly expressed in both primary PDACs and LN metastases, localising to the nucleus and cytoplasm. In addition, a graphical representation of the IHC scores (median with inter-quartile range) is shown in **E**; thus, S100P was confirmed to be up-regulated in LN metastases (p = 0.05).

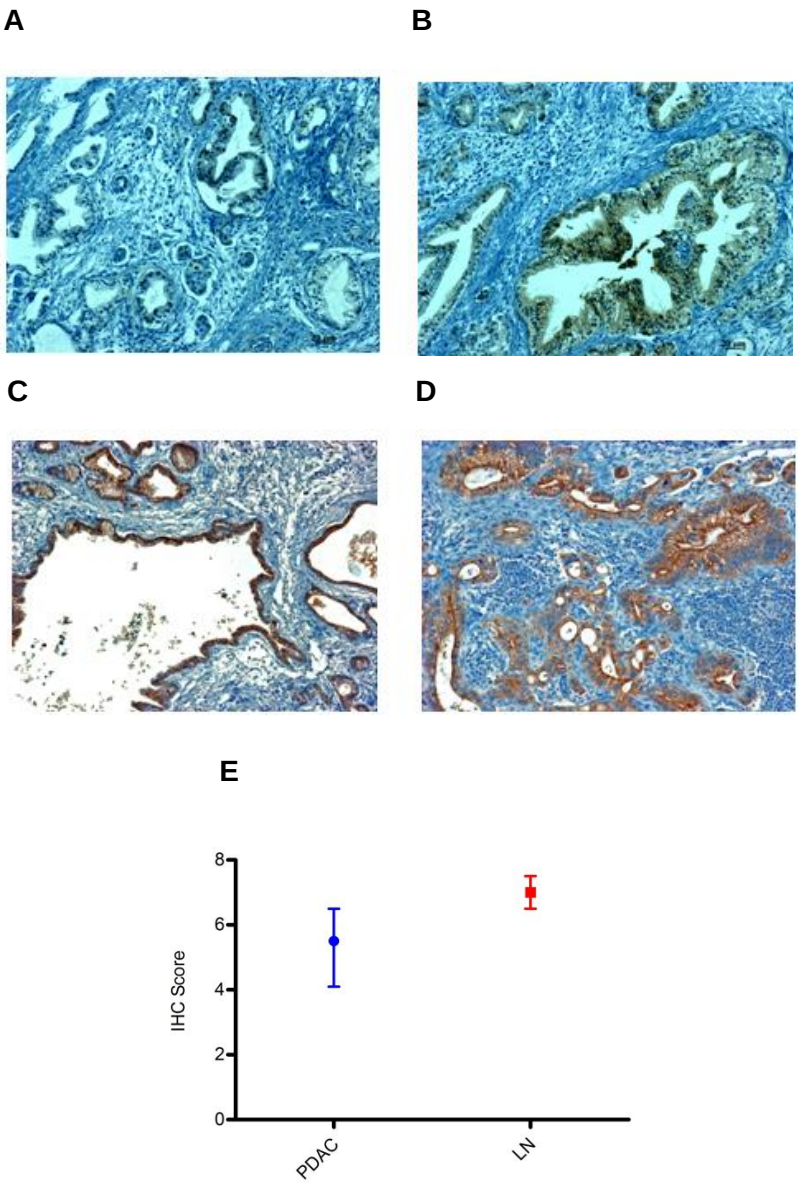

Figure 14 IHC validation of 14-3-3 sigma differential expression (n = 51). Representative images of primary PDAC (**A** and **C**) and matched LN metastases (**B** and **D**; 100x magnification) show that 14-3-3 sigma was expressed exclusively in the cytoplasm of malignant epithelia. LN metastases showed an increase in 14-3-3 sigma expression relative to primary PDAC ($p < 0.001$), in keeping with MudPIT data. Quantification of differential expression is shown in **E** (IHC scores: median with inter-quartile range).

Moesin (**Figure 15**) was variably expressed by the epithelial components of both primary PDAC and metastatic LN. Only 15/51 matched cases expressed moesin; with four cases showing higher expression in matched LN metastases. Thus, moesin was not found to be significant differentially expressed ($p = 0.88$). In addition, moesin was expressed by various stromal elements in both primary PDAC and LN metastases. Of note, the LN parenchyma stained strongly positive for moesin.

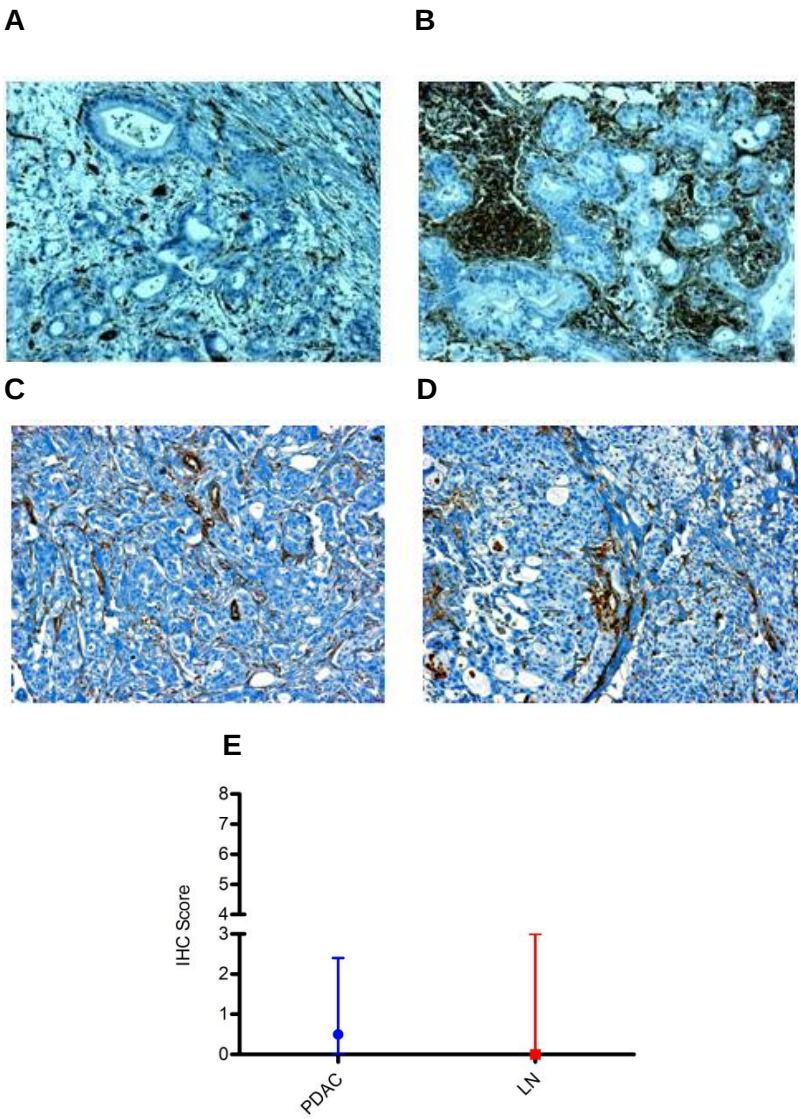

Figure 15 IHC validation of moesin expression (n = 51). Representative images of primary PDAC (**A** and **C**) and matched LN metastases (**B** and **D**; 100x magnification) show that moesin was not expressed in the malignant epithelia of most of the cases analysed; moreover it was expressed by stromal elements in both primary PDACs and LN metastases. As can be seen in **B**, the LN parenchyma was highly immunoreactive. A graphical representation of the IHC scores (median with inter-quartile range) is shown in **E**; moesin was not found to be significantly differentially expressed.

5. DISCUSSION (Part I): PROTEOMICS

Using the Liquid Tissue MS Protein Prep Kit, we were able to analyse the proteomes of primary PDAC and matched LN metastases from FFPE tissues. As these samples were obtained from patients who qualified for surgical resection, we consider these proteins to be particularly relevant for therapeutic target discovery. Pre-fractionation of our samples during MudPIT greatly increased the number of proteins identified, yielding 1504 proteins from only 10 µg of tissue per sample; thus, the obtained proteome is, to our knowledge, the first and certainly the largest of its kind within the field. The full proteome will be made publically accessible through the Pancreatic Expression Database (188).

It has been shown that increasing the number of sample replicates in MudPIT analysis increases the number of commonly identified proteins by 30% per replicate (i.e. two replicates result in a 60% overlap, whilst three replicates result in a 90% overlap) (89,189). This is in keeping with our results, where 854 proteins (57%) were common to both experiments. Interestingly however, whilst these previously reported experiments were conducted on replicates of homogenous tissue (e.g. normal mouse liver), our samples were from seven different donors, with individual heterogenous tumours. Despite this heterogeneity, only 115 of the 854 proteins (13.5%) were significantly differentially expressed, suggesting that LN metastases largely resemble their tumours of origin, which is in keeping with published transcriptomic data (69).

A caveat to this interpretation however, is that whilst MudPIT increases protein yield, it remains an evolving technology which only 'scratches the surface' of the complex mammalian proteome. Thus, considering that the technique itself is approximately 75% reproducible (89); in light of the fact that duplicates were analysed which select for a 60% overlap (89); and bearing in mind that the G-test quantitates larger fold-changes better than smaller changes in differential protein expression (90), one has to wonder if these data reflect the limitations of current day proteomics, rather than biological diversity of the samples analysed. Had we not been limited by the scarcity of tissue samples, time and/or by cost, it would have been interesting to test if adding a third sample replicate, or adding more patient samples to the LCM pool would have altered the results. Furthermore, considering that homeostasis often is maintained by incremental or qualitative changes (e.g. phosporylation) to protein expression, it is also plausible that by sampling the most abundant proteins with the greatest fold-changes in expression between the two anatomical sites, one actually misses those proteins that are potentially responsible for the dynamic, pathophysiological changes occurring during carcinogenesis and metastasis. However, in order to overcome this, one would need either to increase the amount of starting material used in the analysis, which was not possible in this study, or select for these qualitative changes during peptide separation, which would have decreased substantially the number of proteins observed overall. Thus, whilst questions remain as to how much variability is needed for lymphatic metastasis to occur, the 854 protein proteome of PDAC and matched LN metastases is a valuable, initial step towards understanding the proteomic changes underlying metastatic PDAC.

The IHC served both to validate the statistical approach used to analyse the MudPIT data, as well as to confirm the up-regulation of the candidate proteins in LN metastases. Even though moesin had an equivocal g-value, we wished to investigate its expression using IHC as it previously had been identified as a marker of lymphatic metastasis in PDAC (72). As only 29% of matched primary PDAC and LN metastatic epithelia in our study showed moesin expression, our data do not support the previous findings. Thus, the IHC findings were in agreement with the MudPIT data for this protein. Interestingly, Cui et al. did find that 15 of the 42 (35.7%) moesin positive primary PDACs analysed in their study expressed moesin in various stromal cells as well as in the ductal epithelia (72). We found moesin expression to be predominantly stromal, both in primary PDAC and LN metastases. This is perhaps of more practical significance, as it precludes its choice as an epithelial-specific therapeutic target.

We chose to validate one member of the 14-3-3 protein family, as six of these seven evolutionarily-related proteins were found to be significantly differentially expressed between primary PDAC and LN metastases. These proteins can bind more than 100 different proteins, and can potentially affect many processes within the cell, including signal transduction, apoptosis, cell cycle regulation and cytoskeletal organisation (190). The precise mechanisms of action of the 14-3-3 protein family are still poorly understood. Broadly speaking however, they can regulate enzyme activity; act as localisation anchors, localising various proteins to specific compartments within the cell; and are scaffolds or adaptor molecules, facilitating protein-protein interactions (190).

14-3-3 sigma, or stratifin, has been shown previously to be absent in the normal pancreas, but up-regulated in PanINs and primary PDAC (93,191–193). We have now confirmed that 14-3-3 sigma expression is up-regulated in LN metastases relative to primary PDAC. Interestingly, 14-3-3 sigma is expressed solely by epithelial cells and almost exclusively forms homodimers (other members of the family can form heterodimers) (194), and is therefore more amenable to specific targeting. Furthermore, in normal cells, 14-3-3 sigma is up-regulated by TP53 and BRCA1, halting the cell cycle in response to DNA damage (194). This raises interesting questions as to why 14-3-3 sigma expression is increased in primary PDAC, in which TP53 mutations are commonly found. In addition, the observed up-regulation of 14-3-3 sigma in LN metastatic lesions is also seemingly counterintuitive. There are two possible explanations for this. 14-3-3 sigma has been observed in the cerebrospinal fluid (CSF) of patients who have undergone traumatic brain injury or transient cerebral ischaemia (195). Although it was not found to have any functional effects in the CSF of these patients, it was noted as a marker of tissue damage. Thus, it could serve the same role in PDAC. A more intriguiging explanation, however, comes from studies of co-cultures human keratinocytes and fibroblasts (196–198). Not only is 14-3-3 sigma a marker of differentiation in skin epithelia, but differentiated keratinocytes also can secrete 14-3-3 sigma, which then is taken up by surrounding fibroblasts (196). This secreted form of the protein has been shown to increase matrix metalloproteinase-1 (MMP-1) and MMP-3 expression in the stromal compartment (196,197). The role of the MMPs in cancer metastasis is well-established, and it would be interesting to explore this potential cross-talk mechanism in the context of PDAC. This could be done in various ways. One could screen a number of pancreatic cancer cell lines, with varying metastatic capabilities,

for 14-3-3 sigma secretion. Having established that these cells do indeed secrete this protein, one could then modify the above-mentioned co-cultures to include pancreatic cancer cells in combination with pancreatic stellate cells, in order to determine if 14-3-3 sigma secretion by the cancer cells stimulates MMP secretion by the stellate cells *in vitro*. In addition, primary PDAC samples could be stained, using IHC, for 14-3-3 sigma and MMP-1 and MMP-3, in order to determine the relevance of this hypothesis in human tissues.

As described in 1.2.3 (pg 43-44), S100P, a 10.4 kDa calcium-binding protein, already has been associated with PDAC (91–97). We have shown previously that S100P is absent in normal pancreatic ductal epithelia, progressively increased in PanIN lesions, expressed in > 90% of primary PDACs, and that it increases invasion by mediating changes in the actin cytoskeleton and up-regulating cathepsin D *in vitro* (91,92,94). S100P also has been shown to be expressed at higher levels in PDAC as compared to chronic pancreatitis (93). Furthemore, S100P has been shown to bind to the receptor for advanced glycation end-products (RAGE), increasing pancreatic cancer growth, survival and invasion both *in vitro* and *in vivo*; a mechanism of action which is potentially targetable using cromolyn, or analogues thereof (95–97). Through this study, we have shown that S100P is up-regulated in LN metastases with a high g-value using MudPIT analysis, and a marginally significant p-value ($p = 0.05$) using IHC. This discrepancy could be due to two technical factors. Firstly, both primary PDAC and LN metastases stained strongly positive for S100P, resulting in a minimal quantitative difference. Secondly, despite the high g-value, the observed spectral counts obtained for S100P with MudPIT were low; this most likely reflects the limited sensitivity of mass spectrometry at present. It

could also indicate that S100P is masked by a more abundant protein during MudPIT, or that some inherent physicochemical property of the protein causes it to be lost during fractionation, resulting in it being underrepresented. However, the spatio-temporal expression pattern of S100P, as well as its well-established role in PDAC growth and invasion, makes it a viable therapeutic target.

Interestingly, S100P recently has been shown to directly interact with IQGAP1 (199), one of the significantly differentially expressed proteins found in this study (**Table 6**). IQGAP1, a member of the IQGAP family, is a multidomain protein that can interact with a number of partners, affecting intracellular signal transduction and cellular movement by modulating the actin cytoskeleton and microtubule dynamics (199,200). Heil et al (199) showed that calcium-bound S100P, through its interaction with IQGAP1, down-regulates MEK signalling downstream of the EGF receptor. Importantly, this interaction does not affect IQGAP1's ability to bind Cdc42 and Rac1. Thus, S100P potentially can affect cell movement and cellular proliferation in different ways. Furthermore, it has been shown that S100P can activate ezrin (201), increasing transendothelial migration of non-small cell lung cancer cells *in vitro* (202). Both these mechanisms could also, therefore, potentially affect lymphatic invasion in PDAC.

Thus, we have shown in this study that comparative proteomic analysis of FFPE tissue is a valid approach for the investigation of pancreatic malignancy. In addition to establishing the first proteome of primary PDAC and matched LN metastases, we have identified S100P and 14-3-3 sigma as two proteins that may represent viable epithelial-specific targets for the treatment of both primary and metastatic disease.

6. RESULTS (Part II): THE ROLE OF S100P IN LYMPHATIC METASTASIS IN PDAC

6.1 Analysis of S100P in Lymphatic Metastasis in PDAC *in vitro*

As described in 1.2.3 (pg 43-44), S100P has been a long-standing focus of interest in our laboratory. We have shown that S100P is absent in normal pancreatic ductal epithelia, progressively increased in PanIN lesions, expressed in > 90 % of primary PDACs, and that it increases invasion by mediating changes in the actin cytoskeleton and up-regulating cathepsin D *in vitro* (91,92,94). Recently, we have shown S100P to be a potential candidate gene involved in the haematological dissemination of PDAC, increasing transendothelial migration both *in vitro* and *in vivo* (Sayka Barry, PhD Thesis, 2009). Furthermore, the secretion of S100P by pancreatic cancer cells has been reported to stimulate primary tumour growth, survival and metastasis by interacting with RAGE (95). Evidence is thus accumulating that S100P contributes to metastasis in PDAC, but the role of this protein in lymphatic metastasis in PDAC is still unknown. Having validated the relative increase in S100P expression in LN metastases, we chose to further investigate its potential role in lymphatic invasion *in vitro* and *in vivo*.

6.1.1 Creation and Characterisation of V3L and S5L Cell Lines

We aimed to create an orthotopic pancreatic mouse model to evaluate the effects of S100P on primary tumour growth, as well as its potential role in metastasis. As

S100P is not expressed endogenously in mice (203), the transgenic $KRAS^{G12D}$ and/or the $KRAS^{G12D}$/TP53 mouse models, would not be relevant to the investigation of S100P without further engineering. In order to allow for the imaging of tumours and/or metastases in real-time *in vivo*, the V3 and S5 cell lines (94) were further engineered to express luciferase using a lentivirus (204). This was performed with the help of Dr David Gould, Bone and Joint Research Unit, William Harvey Institute. Following transduction, characterisation of the V3 $Luciferase^{+}$ (V3L) and S5 $Luciferase^{+}$ (S5L) cell lines was performed in order to ensure that the luciferase transfection had not resulted in functional alteration, i.e. proliferation, invasion and anchorage-independent growth.

6.1.1.1 Confirmation of S100P over-expression

S100P expression was evaluated in V3L and S5L cells at both the transcript (**Figure 16**) and protein levels (**Figure 17**). S5L cells were found to express significantly higher levels of both S100P mRNA ($p = 0.04$) and protein ($p = 0.03$). However, I was only able to show protein expression using a V5 antibody, and not using an antibody to S100P. In order to confirm that the observed protein was, in fact, S100P, a transient silencing experiment was performed. The Western blots and siRNA knockdown experiments also were performed by Kate Lines, a fellow PhD student in the laboratory, after I had optimised the protocols, in order to ensure that the data were reproducible.

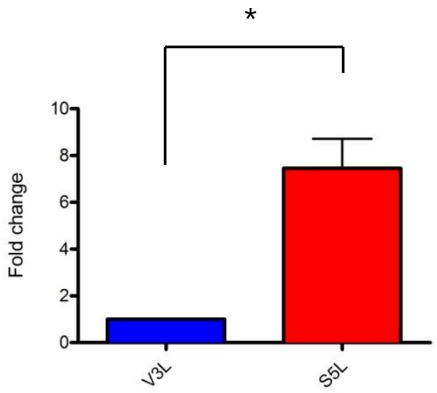

Figure 16 qPCR for S100P *in vitro.* Extracted mRNA from V3L and S5L cell lines was analysed for S100P transcript; S5L cells express significantly higher levels of S100P mRNA than V3L cells ($p = 0.04$).

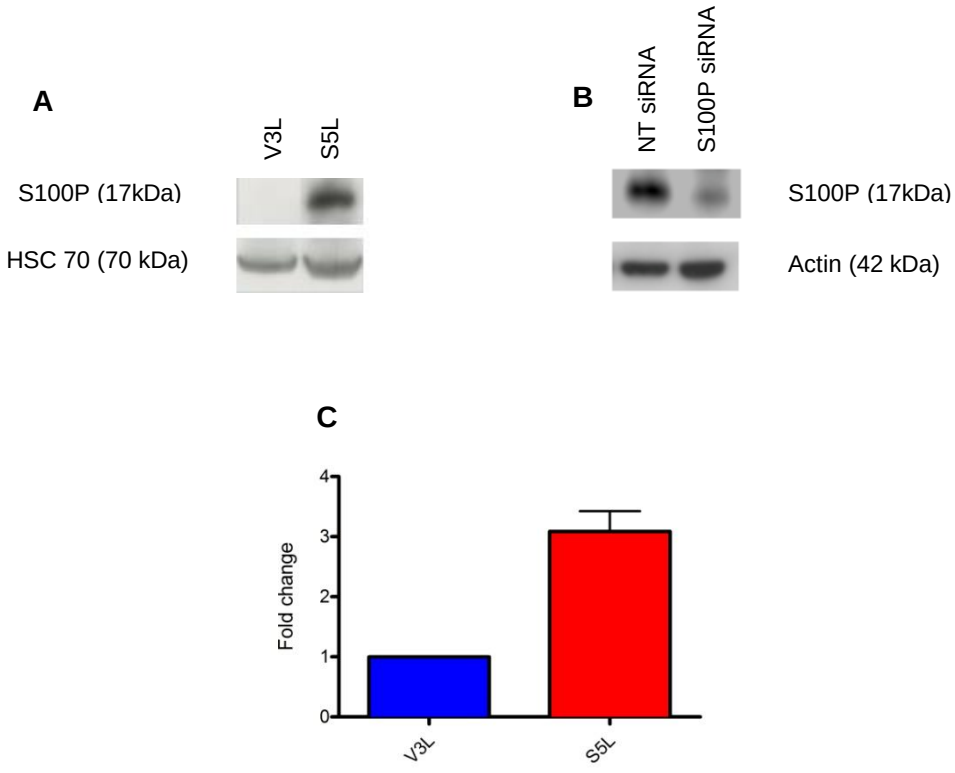

Figure 17 Confirmation of S100P protein expression. Representative Western blots (**A** performed by me; **B** performed by Kate Lines) showing the expression of V5-tagged S100P in V3L and S5L cells, as well as in the S5L cell line following knockdown with either non-targeting control siRNA (NT siRNA) or siRNA to S100P. Densitometry (**C**) confirmed that S100P protein is significantly over-expression in S5L cells ($p = 0.03$). The silencing experiments were performed in order to confirm the specificity of the V5-antibody in detecting S100P protein, as well as to show that the Western blot could be reproduced by someone else in the lab. HSC-70 and actin were used as loading controls.

6.1.1.2 Functional Characterisation

In order to confirm that the luciferase transduction was successful, and that it did not alter the behaviour of the V3L and S5L cell lines *in vitro*, a series of functional characterisation experiments were performed.

Quantification of luciferase expression *in vitro* showed that the V3L and S5L cell lines expressed equivalent amounts of luciferase (**Figure 18**), i.e 50 V3L cells expressed the same amount of luciferase as 50 S5L cells; the same result was seen when 5 x 10^5 cells were used. Thus, any differences in bioluminescence imaging seen *in vivo* would represent a true difference in growth or metastasis, and not reflect a difference in luciferase transduction between the two cell lines.

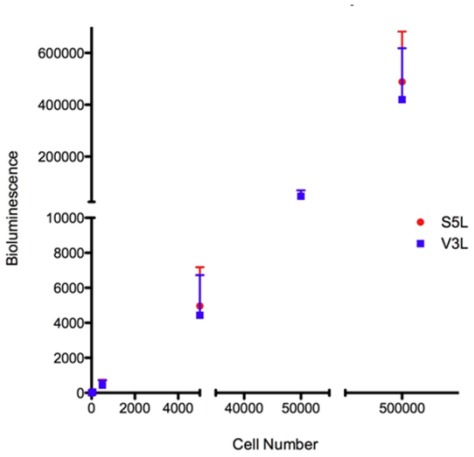

Figure 18 Quantification of luciferase expression *in vitro*. Luciferase quantification was performed on serial 1:10 dilutions of 5 x 10^5 V3L and S5L cells following lentiviral transduction. No differences were seen between the two cell lines.

In the V3 and S5 cell lines, no difference in proliferation between the two cell lines had been seen up to 96 hours *in vitro* (94). The same result was obtained using the V3L and S5L cell lines (**Figure 19**).

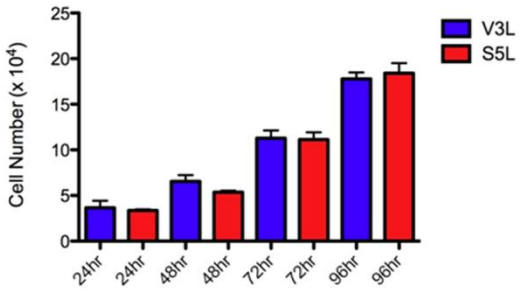

Figure 19 Proliferation assays. At Day 0, 2.5 x 10^4 V3L and S5L cells were seeded into 24-well plates. Daily counts were performed using a haemocytometer. The experiment lasted five days in total. No differences were seen between the two cell lines, in keeping with data obtained using the V3 and S5 cell lines.

It had previously been shown that the S5 cell line was significantly more invasive than the V3 cell line in Matrigel assays *in vitro* (94). Thus, these assays were repeated using the luciferase-expressing cell lines. As can be seen in **Figure 20**, the S5L cells were significantly more invasive than V3L cells ($p = 0.0002$), in keeping with previous data.

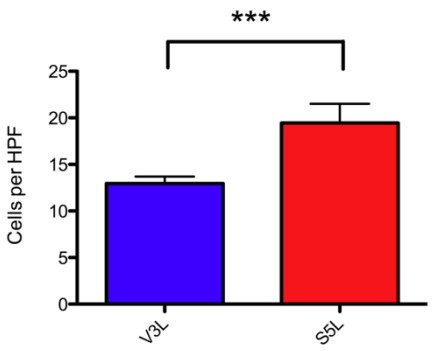

Figure 20 S100P increases invasion *in vitro*. Invasion assays were performed on V3L and S5L cells in Matrigel-coated transwell chambers. A significantly higher number of S5L cells had invaded through the Matrigel barrier after 48 hours ($p = 0.0002$). (HPF = high power field; x20 objective)

Soft agar assays were performed to assess the tumourigenicity of both these cell lines (**Figure 21**). No significant differences, neither in the total number, nor in the average area of colonies formed, were observed, indicating that S100P does not affect anchorage-independent growth.

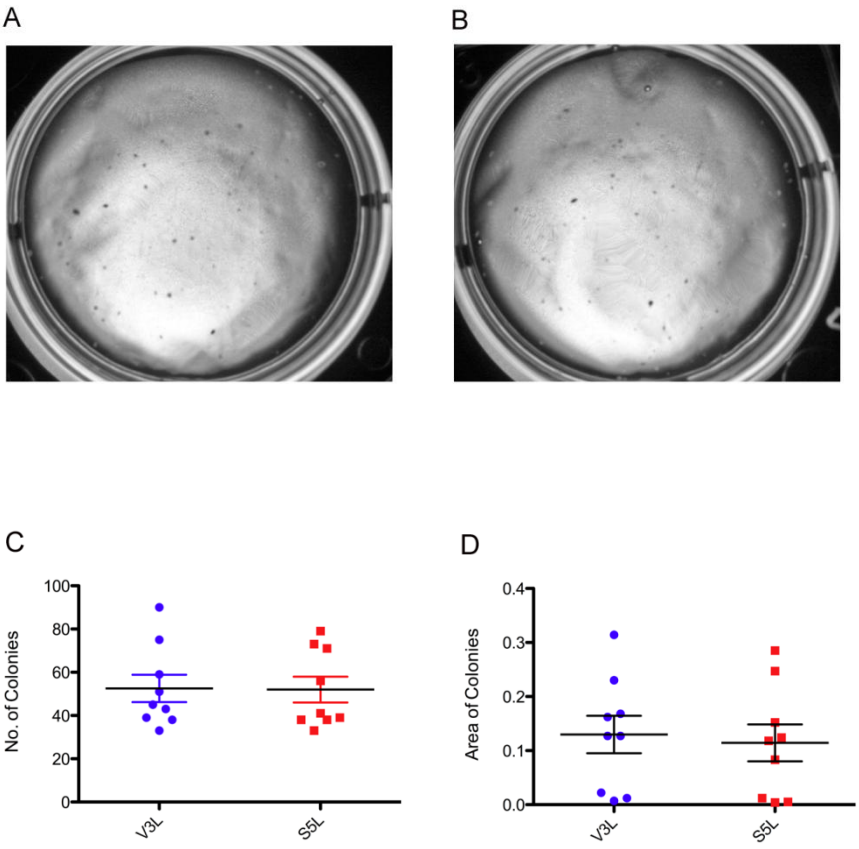

Figure 21 Soft agar assays. 200 V3L or S5L cells in a single suspension were mixed in 0.3% agarose and left to grow for 18 days (**A** = V3L; **B** = S5L; both images taken at 40x magnification). The average number of colonies (**C**), as well as the average area of the colonies formed (**D**), was then quantified using ImageJ software. No differences were seen between the two cell lines.

6.1.2 Interaction of the V3L and S5L Cell Lines with Human Dermal Lymphatic Endothelial Cells

Human Dermal Lymphatic Endothelial Cells (HDLEC), which were purchased at passage three and used until passage seven, were used as a proxy for pancreatic lymphatics *in vitro*. Co-cultures, containing V3L or S5L cells in combination with HDLEC, were established to investigate cancer cell adhesion to HDLEC; permeability through a HDLEC monolayer; and translymphatic endothelial cell migration.

6.1.2.1 Confirmation of the Lymphatic Lineage of HDLEC

HDLEC were fluorescently stained for the lymphatic-specific markers LYVE-1 and podoplanin (**Figure 22**) to verify that these cells were truly lymphatic, and not blood vascular, endothelial cells. All experiments were conducted between passage three and seven, as cells became senescent thereafter.

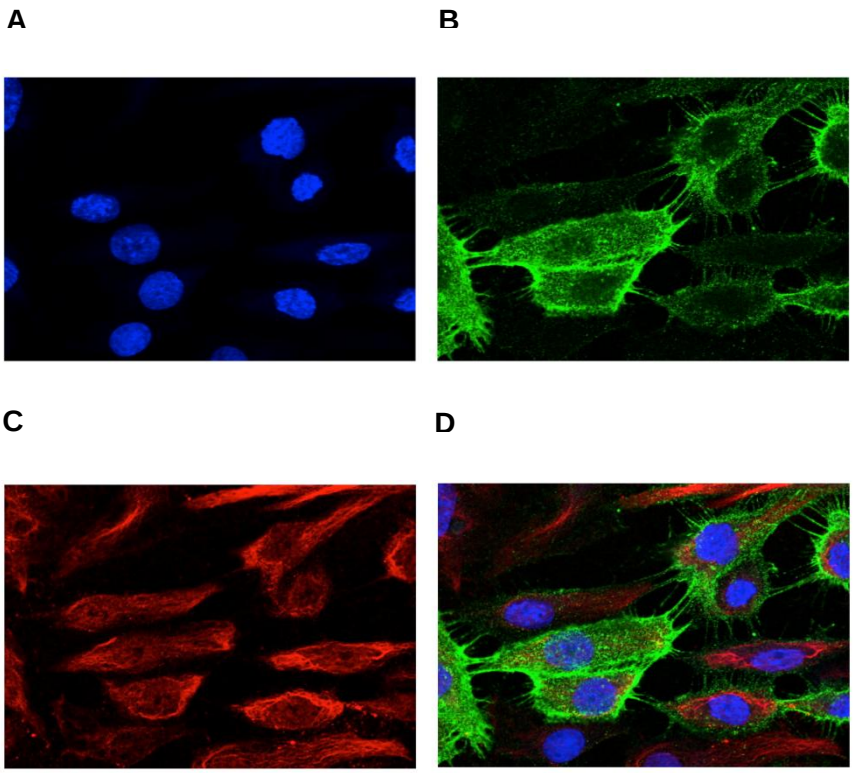

Figure 22 Verification of the lymphatic lineage of human dermal lymphatic endothelial cells (HDLEC). In order to ensure that a pure population of lymphatic cells was used in all experiments, cells were immunofluorescently stained for the lymphatic markers LYVE-1 (**B**) and podoplanin (**C**). A merged image is shown in (**D**). (All images at 63x magnification under oil immersion)

6.1.2.2 Activating HDLEC

For the functional assays, HDLEC were stimulated with either IFNγ (100 ng/ml) or TNFα (10 ng/ml) for 24 hours prior to the addition of V3L or S5L cells. These concentrations were chosen based on previously published data (151). ICAM-1, VCAM-1 and E-selectin were used as markers of activation status following

determination of basal levels of expression on resting HDLEC by flow cytometry (**Figure 23**), as these three markers previously had been shown to increase following TNFα stimulation of HDLEC (151). At rest, HDLEC did not express VCAM-1 or E-selectin, but did express ICAM-1. Following stimulation with IFNγ, ICAM-1 expression was maintained at levels equivalent to that at rest ($p = 0.36$), and cells did not express VCAM-1 or E-selectin. TNFα stimulation significantly increased ICAM-1 ($p = 0.04$) and E-selectin ($p = 0.04$) expression. Whilst VCAM-1 expression did increase following treatment with TNFα, the increase was not statistically significant ($p = 0.07$). Representative histograms (for ICAM-1) of the flow cytometry experiments, including statistical quantification of the number of positive cells, are shown in **Figure 24**. The geometric mean was used as a measure of mean fluorescent intensity (MFI) and indicates expression levels, and has been shown on all subsequent graphs.

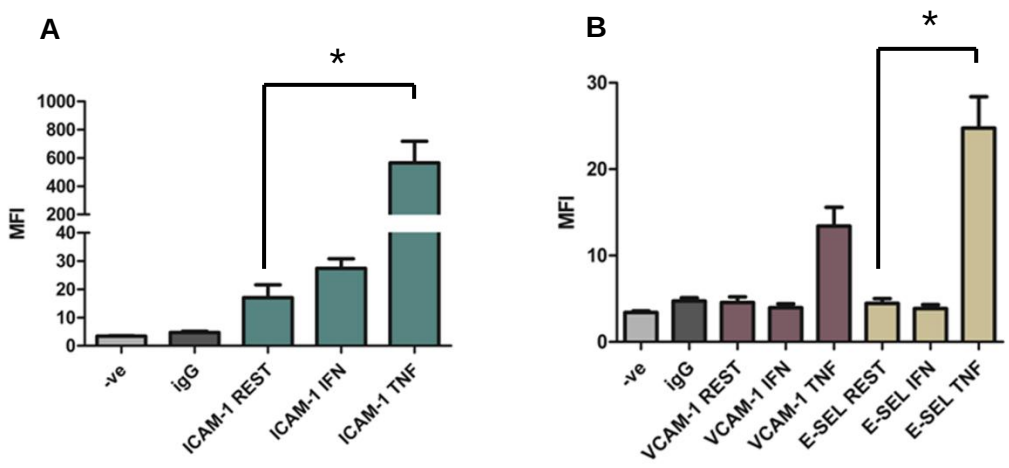

Figure 23 Cell surface expression of ICAM-1, VCAM-1 and E-selectin on HDLEC. As can be seen in **A**, resting HDLEC express ICAM-1. IFNγ stimulation (100 ng/ml) maintained ICAM-1 expression at equivalent levels to those seen at rest ($p = 0.36$) whilst TNFα stimulation (10 ng/ml) significantly up-regulated ICAM-1 expression ($p = 0.04$). In contrast, VCAM-1 and E-selectin are not expressed on resting HDLEC (**B**), nor are they expressed following IFNγ stimulation. Although VCAM-1 expression did increase upon TNFα stimulation, this increase was not statistically significant ($p = 0.07$). TNFα stimulation did significantly increase the cell surface expression of E-selectin ($p = 0.04$).

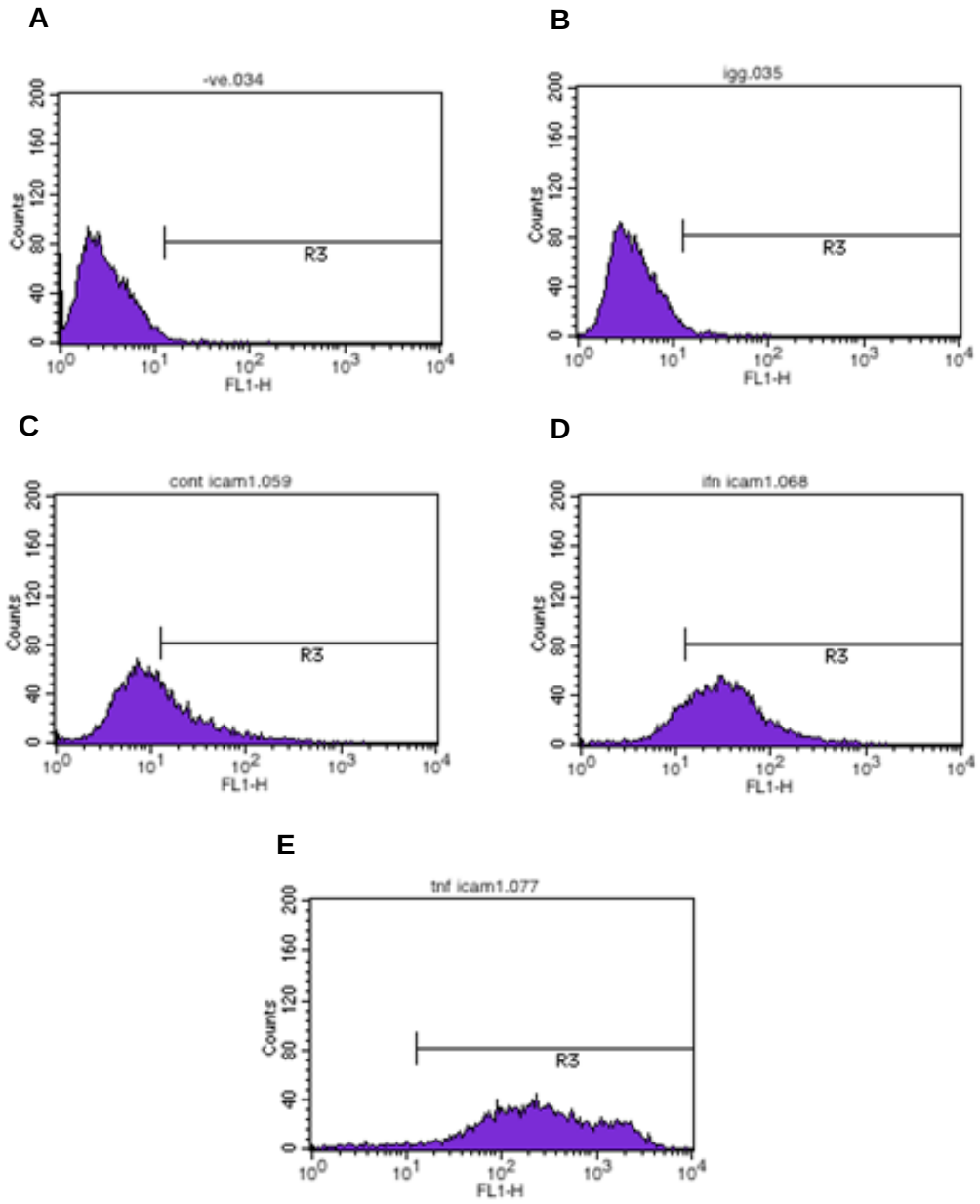

Figure 24 Representative histograms of the flow cytometry experiments. Histograms are shown for a negative control (**A**), IgG control (**B**) and ICAM-1 cell surface expression at rest (**C**) and following IFNγ (100 ng/ml; **D**) and TNFα (10 ng/ml; **E**) stimulation. The geometric mean was used as a measure of mean fluorescent intensity (MFI) which is shown on all subsequent graphs.

Flow cytometry was performed to assess the cell surface expression of LYVE-1 (**Figure 25**), both to confirm the lymphatic lineage by a method other than ICC, and as it previously had been shown that TNFα stimulation ablates LYVE-1 expression on HDLEC (104,151). We were able to reproduce these findings. LYVE-1 was found to be significantly expressed on resting HDLEC ($p = 0.01$), relative to the negative and IgG controls. Cytokine stimulation with both IFNγ ($p = 0.02$), and TNFα ($p = 0.007$), significantly decreased LYVE-1 surface expression relative to levels observed on resting HDLEC.

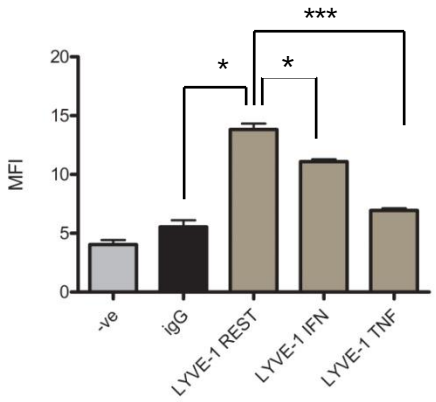

Figure 25 Cell surface expression of LYVE-1 on HDLEC. Resting HDLEC express significant levels of LYVE-1 ($p = 0.01$). This confirms that these endothelial cells are lymphatic in lineage. LYVE-1 expression significantly decreased following IFNγ stimulation (100 ng/ml; $p = 0.02$) and TNFα stimulation (10 ng/ml; $p = 0.007$). (MFI = mean fluorescent intensity)

Having reproduced the data reported by Johnson et al. (104,151), flow cytometry was performed on resting and cytokine-stimulated HDLEC to assess the cell surface expression of CLEVER-1 and the fibronectin-binding integrins α4β1, α5β1 and α9β1, both at rest and following cytokine stimulation (**Figures 26 - 28**).

CLEVER-1 (**Figure 26**) was expressed on resting HDLEC (geometric mean = 8.9), and this expression was significantly higher than the IgG control (p = 0.0009). Of note, CLEVER-1 expression was constant i.e. the levels seen on resting HDLEC were similar to levels seen on activated HDLEC (geometric mean following IFNγ stimulation = 8.5 (p = 0.75), and TNFα stimulation = 10.3 (p = 0.07)).

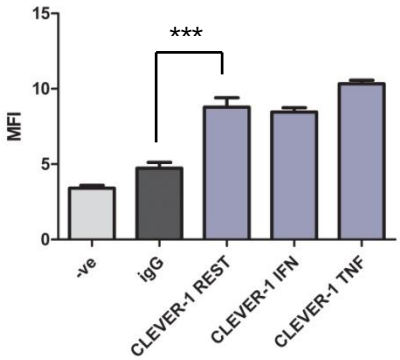

Figure 26 Cell surface expression of CLEVER-1 on HDLEC. Resting HDLEC express CLEVER-1 at the cell surface at significantly higher levels than the IgG control (p = 0.0009). Following cytokine stimulation with both IFNγ (100 ng/ml) and TNFα (10 ng/ml), CLEVER-1 expression is maintained at levels similar to that seen on resting HDLEC. (MFI = mean fluorescent intensity)

HDLEC expressed high levels of α5β1 integrin at rest, relative to the IgG control (p = 0.0003) (**Figure 27**). Interestingly, expression of this integrin decreased significantly following IFNγ treatment (p = 0.04), but increased significantly following TNFα (p = 0.02) stimulation, compared to levels seen at rest. In contrast, HDLEC were found to express low levels of α4β1 and α9β1 at rest (geometric means: α4β1 = 6.7 and α9β1 = 9.3) (**Figure 28**). As was the case for α5β1 integrin, IFNγ stimulation decreased the cell surface expression of these integrins (geometric means: α4β1 = 4.8 and α9β1 = 5.3) whilst TNFα stimulation increased their expression (geometric means: α4β1 = 10.5 and α9β1 = 15.0). None of these changes reached statistical significance however.

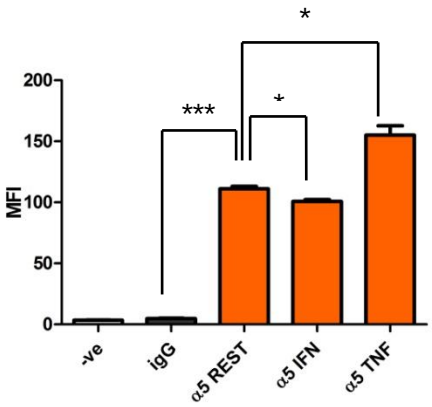

Figure 27 Cell surface expression of α5β1 integrin on HDLEC. Resting HDLEC express α5β1 at the cell surface, relative to IgG control (p = 0.0003). Following IFNγ (100 ng/ml) stimulation, expression significantly decreased (p = 0.04) as compared to levels seen at rest. However, following TNFα (10 ng/ml), α5β1 expression significantly increased (p = 0.02). (MFI = mean fluorescent intensity)

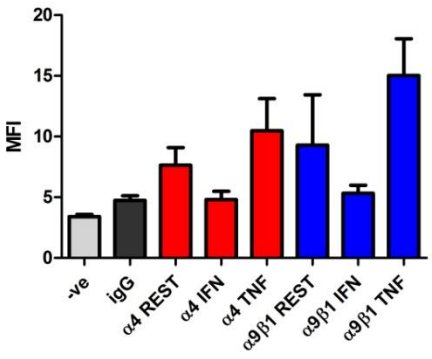

Figure 28 Cell surface expression of α4β1 and α9β1 integrins on HDLEC. Resting HDLEC express low levels of α4β1 and α9β1. Following cytokine stimulation with IFNγ (100 ng/ml), cell surface expression of both these integrins decreases to levels seen on negative and IgG controls. Although both α4β1 and α9β1 increased following TNFα stimulation (10 ng/ml) expression, these increases did not reach statistical significance. (MFI = mean fluorescent intensity)

6.1.2.3 S100P Increases Adhesion to Activated HDLEC

The adhesion of V3L and S5L cells to resting and activated HDLEC was tested to determine if S100P affects adhesion (**Figure 29**). At rest, no differences were seen between the adhesive behaviour of the two cell lines. Following IFNγ stimulation, S5L cells were significantly better able to adhere to HDLEC than V3L cells ($p = 0.01$). Interestingly, stimulation with TNFα significantly decreased the adhesion of V3L cells as compared with basal V3L adhesion to resting HDLEC ($p = 0.03$), but did not alter the number of adherent S5L cells in comparison to that seen at rest. Thus, this decrease in V3L adhesion resulted in a significant difference between V3L and S5L cell adhesion following TNFα stimulation ($p = 0.02$). These results indicate that

cancer cell adhesion to HDLEC is not activation dependent, but also show that V3L cells are less able to bind to activated HDLEC than S5L cells.

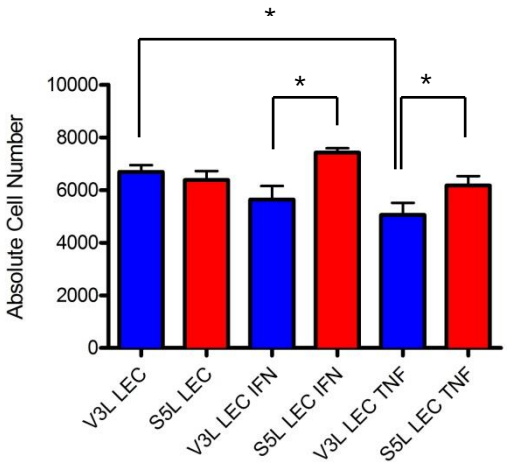

Figure 29 Adhesion of V3L and S5L cells to HDLEC. The ability of V3L and S5L cells to adhere to HDLEC was tested at rest and following HDLEC activation. No differences were seen between the two cell lines in adhesion to resting lymphatics. However, S5L cells were significantly better able to bind to IFN-γ (100 ng/ml) activated HDLEC than V3L cells ($p = 0.01$). Although S5L adhesion to TNF-α (10 ng/ml) stimulated HDLEC was equivalent to that seen at rest, V3L adhesion following TNF-α stimulation was significantly decreased ($p = 0.03$). Thus, S5L cells appear to adhere better to TNF-α activated HDLEC than V3L cells ($p = 0.02$).

In order to assess whether or not these differences in adhesion were due to the effects of S100P, the experiments were repeated using recombinant S100P (100 nM), which was added to the media surrounding both HDLEC and V3L cells (**Figure**

30). Surprisingly, the presence of recombinant S100P in the assay significantly decreased the adhesion of V3L cells to resting HDLEC (p = 0.03). No change in adhesion was seen when HDLEC were stimulated with IFNγ. However, V3L adhesion to HDLEC which had been stimulated with TNFα for 24 hours significantly increased in the presence of recombinant S100P (p = 0.008).

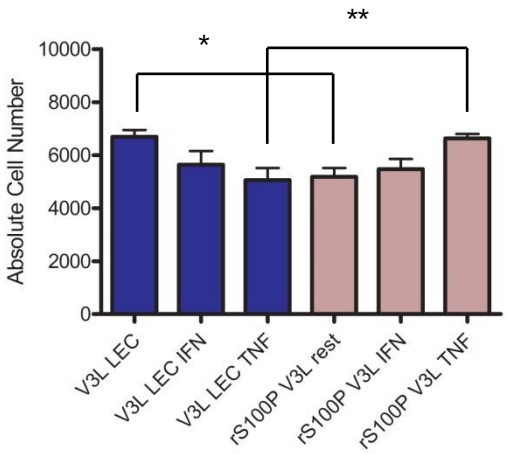

Figure 30 The effects of recombinant S100P on V3L adhesion to HDLEC. In order to assess if the observed differences in adhesion to activated HDLEC between the V3L and S5L cell lines were mediated by S100P, recombinant S100P (100 nM) was added to the media surrounding both HDLEC and V3L cells, and adhesion was quantified after 45 minutes. The presence of recombinant S100P significantly decreased adhesion to resting HDLEC (p = 0.03). No change in adhesion was seen when HDLEC were stimulated with IFNγ (100 ng/ml) for 24 hours. However, the presence of recombinant S100P significantly increased the adhesion of V3L cells to HDLEC which had been stimulated with TNFα (10 ng/ml) for 24 hours (p = 0.008).

6.1.2.4 V3L and S5L Cells Adhere to HDLEC via Different Receptors

6.1.2.4.1 Function Blocking Assays

In order to determine which receptors might be involved in and/or mediate the observed differences in adhesion of V3L and S5L cells to HDLEC, function blocking experiments were performed using antibodies to ICAM-1, VCAM-1, E-selectin, LYVE-1, β1 integrin, α4 integrin, α9β1 integrin, α5β1 and CLEVER-1 (**Figures 32 – 37;** summarised in **Table 7** below). A function blocking antibody to the epithelial-specific β6 integrin was used as a negative control, since HDLEC, V3L and S5L cells do not express this integrin (**Figure 31**). β6 blockade did not alter the binding of cancer cells to resting HDLEC, or of S5L cells to IFNγ-stimulated and TNFα-stimulated HDLEC. Whilst β6 blockade did appear to have an effect on the binding of V3L cells to activated HDLEC, this did not reach statistical significance ($p = 0.07$ following IFNγ-stimulation and $p = 0.08$ following TNFα-stimulation).

V3L adhesion to resting HDLEC is mediated by multiple receptors, including LYVE-1 ($p = 0.02$), CLEVER-1 (0.04), α4 integrin ($p = 0.03$), α9β1 ($p = 0.02$), and β1 integrin ($p = 0.03$) (**Figures 32 and 33**). However, only CLEVER-1 and α5 integrin appear to be involved in V3L adhesion to activated HDLEC. Surprisingly, CLEVER-1 and α5 integrin blockade significantly increased V3L adhesion to IFNγ-stimulated HDLEC (CLEVER-1: $p = 0.003$; α5 integrin: $p = 0.008$) and TNFα-stimulated HDLEC

(CLEVER-1: p = 0.03; α5 integrin: p = 0.003). α5 integrin does not appear to be involved in V3L adhesion to resting HDLEC.

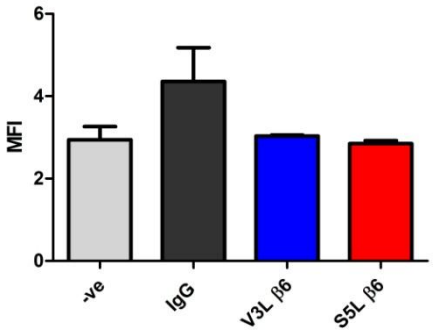

Figure 31 V3L and S5L cells do not express β6 integrin at the cell surface. Flow cytometry for β6 integrin was negative on both the V3L and S5L cell lines. Thus, β6 function blocking antibody was used as a control in the integrin function blocking experiments.

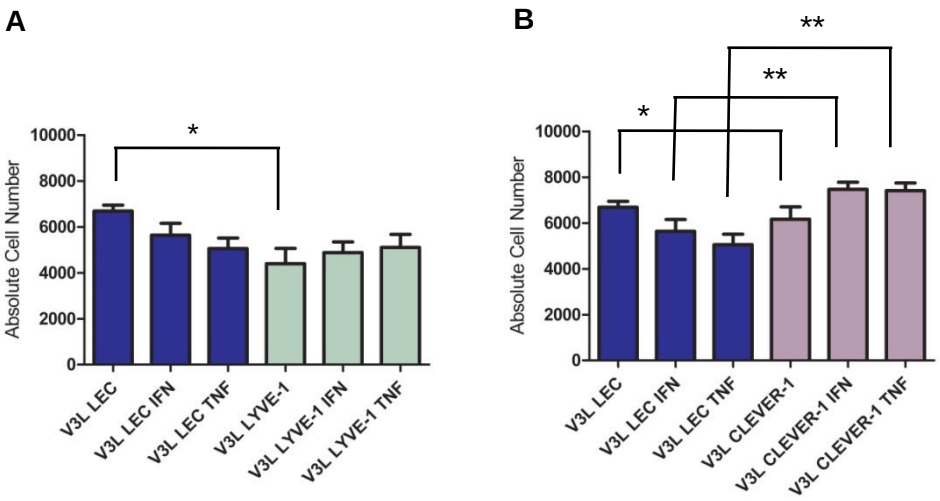

Figure 32 LYVE-1 and CLEVER-1 mediate V3L adhesion to HDLEC. Functional blocking antibodies to LYVE-1 and CLEVER-1 were used to evaluate if these molecules are involved in V3L adhesion to resting and activated HDLEC. As can be seen in **A**, LYVE-1 blockade significantly decreased adhesion to resting HDLEC ($p = 0.02$), but not to activated HDLEC. Conversely, CLEVER-1 blockade (**B**) significantly decreased V3L adhesion to resting HDLEC ($p = 0.04$), but significantly increased V3L adhesion to IFNγ–stimulated ($p = 0.003$) and TNFα–stimulated ($p = 0.03$) HDLEC.

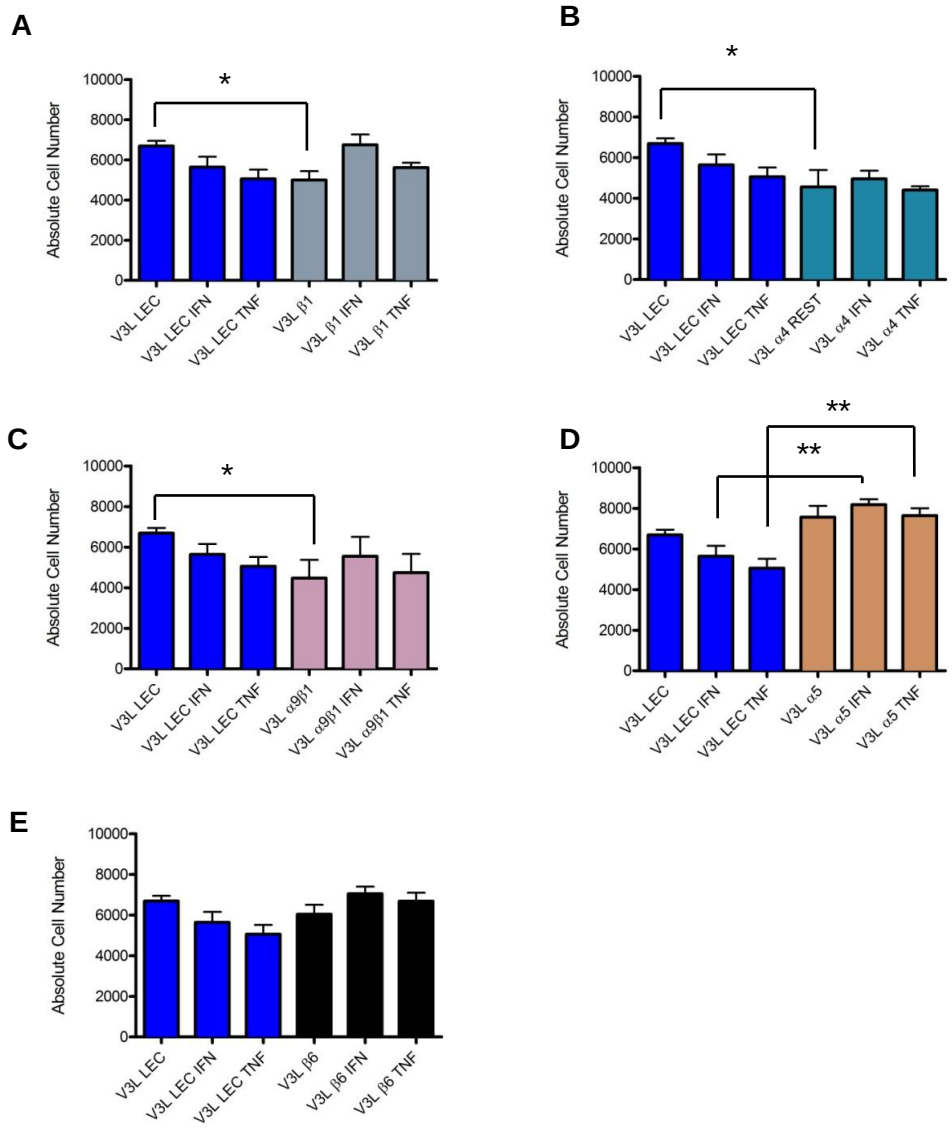

Figure 33 The β1 integrins (α4β1, α5β1 and α9β1) appear to mediate V3L adhesion to resting HDLEC. Function blocking antibodies to the integrin subunits β1 (**A**, p = 0.03), α4 (**B**, p = 0.03), and to the integrin α9β1 (**C**, p = 0.02), significantly decreased adhesion to resting HDLEC. None of these integrins appear to mediate V3L adhesion to activated HDLEC. In contrast, functional blockade of α5 (**D**) significantly increased V3L adhesion to IFNγ–stimulated (p = 0.008) and TNFα–stimulated (p = 0.003) HDLEC, but did not appear to be involved in V3L adhesion to resting HDLEC. Functional blockade of the integrin β6 (**E**, negative control) did not affect adhesion to resting HDLEC but did appear to have some effect on V3L binding to activated HDLEC. This did not reach statistical significance however.

Blocking LYVE-1 significantly decreased S5L adhesion to resting HDLEC ($p = 0.004$), as well as to HDLEC stimulated with IFNγ ($p = 0.03$) (**Figure 34**). In contrast to V3L cells, CLEVER-1 did not appear to play a role in S5L adhesion to both resting and activated HDLEC. None of the β1 integrins were found to mediate S5L adhesion to resting HDLEC (**Figure 35**). Rather, these integrins appear to be recruited following HDLEC activation. Whilst β1 blockade significantly decreased adhesion after IFNγ ($p = 0.001$) and TNFα ($p = 0.02$) stimulation, α4 ($p = 0.01$) and α9β1 ($p = 0.01$) were found to mediate adhesion to IFNγ-stimulated HDLEC. However, neither of these integrins appear to mediate adhesion to TNFα-stimulated HDLEC. Functional blockade of the integrin α5 did not affect S5L adhesion to resting and/or activated HDLEC.

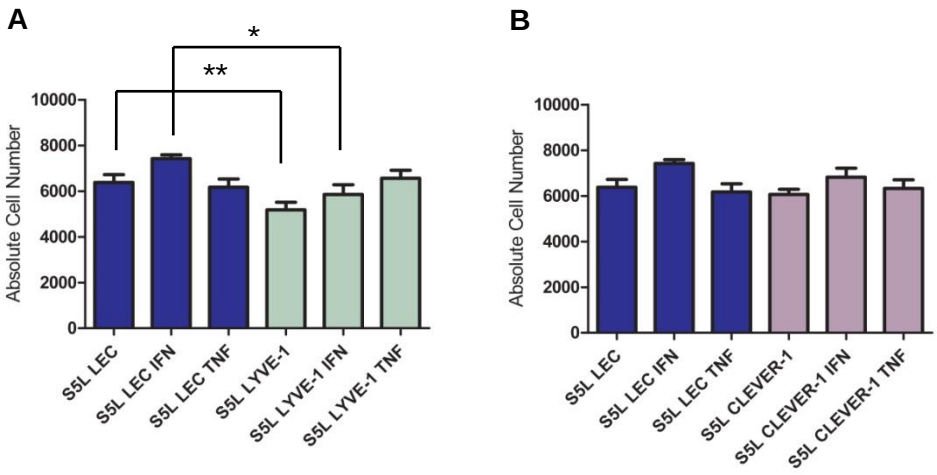

Figure 34 LYVE-1, but not CLEVER-1, appears to mediate S5L adhesion to HDLEC. Function blocking antibodies to LYVE-1 (**A**) and CLEVER-1 (**B**) were used to determine if these molecules mediate S5L adhesion to resting and activated HDLEC. As can be seen in **A**, S5L adhesion to resting ($p = 0.004$) and IFNγ–stimulated HDLEC ($p = 0.03$) significantly decreased following LYVE-1 functional blockade; S5L adhesion to TNFα-stimulated HDLEC was unaffected. Functional blockade of CLEVER-1 did not affect S5L adhesion to resting or activated HDLEC (**B**).

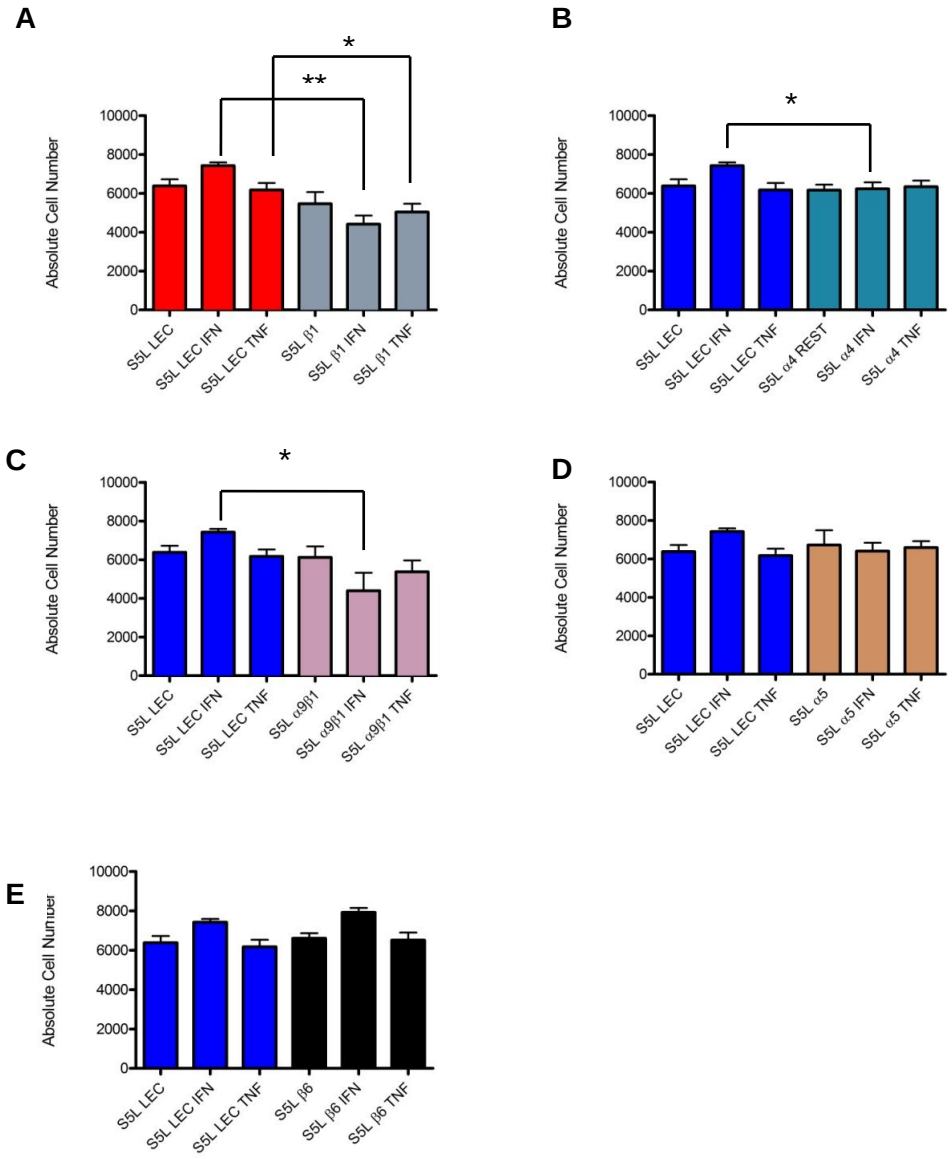

Figure 35 The β1 integrins (α4β1 and α9β1) appear to mediate S5L adhesion to activated, but not resting, HDLEC. A function blocking antibody to the integrin subunit β1 significantly decreased S5L adhesion to IFNγ–stimulated (**A**, p = 0.001) and TNFα–stimulated (**A**, p = 0.02) HDLEC. Functional blockade of the integrin subunit α4 significantly decreased S5L adhesion to IFNγ–stimulated HDLEC (**B**, p = 0.01), as did a function blocking antibody to the integrin α9β1 (**C**, p = 0.01). However, neither of these integrins appear to affect S5L adhesion to TNFα–stimulated HDLEC. Functional blockade of the integrins α5 (**D**), and β6 (**E**, negative control) did not affect S5L adhesion to resting and/or activated HDLEC.

ICAM-1, VCAM-1 and E-selectin were not found to mediate cancer cell adhesion to HDLEC, neither at rest, nor following activation (**Figures 36** and **37**).

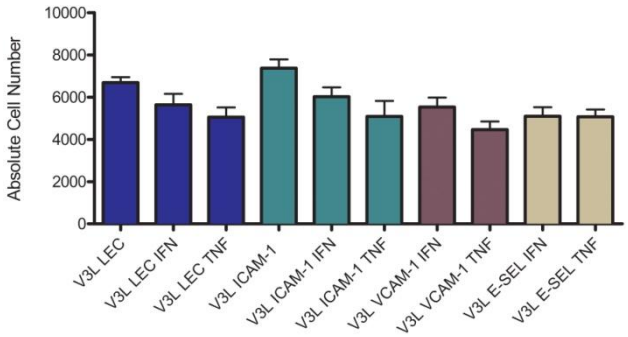

Figure 36 ICAM-1, VCAM-1 and E-Selectin do not appear to mediate V3L adhesion to HDLEC. Function blocking antibodies to ICAM-1, VCAM-1 and E-Selectin were used to evaluate if these molecules mediated V3L adhesion to resting and activated HDLEC. As VCAM-1 and E-selectin are not expressed on the surface of resting HDLEC (shown in Figure 22), these molecules were only functionally blocked on activated HDLEC. None of these molecules appear to mediate adhesion to resting and/or activated HDLEC.

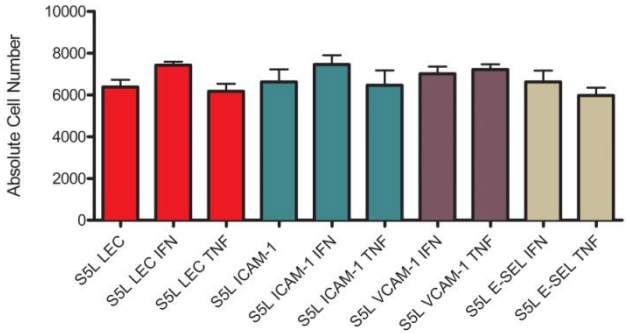

Figure 37 ICAM-1, VCAM-1 and E-Selectin do not appear to mediate S5L adhesion to HDLEC. Function blocking antibodies to ICAM-1, VCAM-1 and E-Selectin were used to evaluate if these molecules mediated S5L adhesion to resting and activated HDLEC. As VCAM-1 and E-selectin are not expressed on the surface of resting HDLEC (shown in Figure 22), these molecules were only functionally blocked on activated HDLEC. None of these molecules appear to mediate adhesion to resting and/or activated HDLEC.

Table 7 Summary of the adhesion molecules involved in V3L and S5L adhesion to resting and activated HDLEC. Experiments utilising function blocking antibodies to the tabulated adhesion molecules showed that V3L adhesion to resting HDLEC is mediated by LYVE-1, CLEVER-1, and the β1 integrins (α4β1, α5β1 and α9β1). Only CLEVER-1 and α5β1 integrin were found to mediate V3L adhesion to activated HDLEC, and functional blockade of both these molecules was found to increase V3L adhesion to activated HDLEC. In contrast, only LYVE-1 was found to mediate S5L adhesion to resting HDLEC. In addition, LYVE-1, together with the integrins α4β1 and α9β1, were found to mediate S5L adhesion to IFNγ-stimulated HDLEC. A function blocking antibody to the integrin subunit β1 did significantly decrease S5L adhesion to TNF-stimulated HDLEC; however no other integrin subunit was found to mediate this adhesion.

	V3L + HDLEC	V3L + IFNγ + HDLEC	V3L + TNFα + HDLEC	S5L + HDLEC	S5L + IFNγ + HDLEC	S5L + TNFα + HDLEC
ICAM-1	-	-	-	-	-	-
VCAM-1	NA	-	-	NA	-	-
E-Selectin	NA	-	-	NA	-	-
LYVE-1	↓	-	-	↓↓	↓	-
CLEVER-1	↓	↑↑	↑↑	-	-	-
β1	↓	-	-	-	↓↓	↓
α4	↓	-	-	-	↓	-
α9β1	↓	-	-	-	↓	-
α5	-	↑↑	↑↑	-	-	-

6.1.2.4.2 V3L and S5L Adhesion Receptor Profiles

Having identified which HDLEC adhesion receptors mediate the adhesion of cancer cells to lymphatic endothelium, V3L and S5L cells were examined for any adhesion receptors that could bind directly to these receptors, namely VCAM-1 (which binds the integrins α4β1 and α9β1) and CD44 (which can bind LYVE-1), using flow cytometry. In addition, as both LYVE-1 and the β1 integrins can bind ECM as previously described (101,104,127,131,140–144), cancer cells were analysed for the cell surface expression receptors that are known to bind to HA (CD44 and ICAM-1). A previous screen of the Panc-1 parental cell line, from which the V3L and S5L cells were derived, had shown that these cells express the FN-binding integrins, αvβ3, αvβ5, αvβ8 and α5. We had hoped to analyse the V3L and S5L cells for these integrins, but no antibodies for the three αv integrins were available at the time at which these experiments were performed. The flow cytometry results are shown in **Figure 38**. Both V3L and S5L cells expressed equivalent levels of the hyaluronon-binding receptors ICAM-1 and CD44. Neither cell line expressed VCAM-1. Thus, the V3L and S5L cells appear to express adhesion molecules that bind preferentially to ECM components, rather than receptors that can directly interact with cognate receptors on HDLEC.

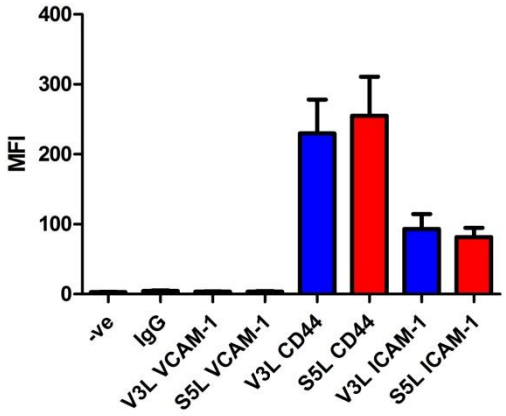

Figure 38 Cancer cell flow cytometry. V3L and S5L cells were analysed for the cell surface expression of adhesion molecules that could directly bind to the adhesion molecules expressed by HDLEC, namely VCAM-1 and CD44. Cells were also tested for adhesion receptors that could bind the ECM protein, hyaluronic acid (HA) i.e CD44 and ICAM-1. Both V3L and S5L cells expressed CD44 (which can bind LYVE-1 directly) and ICAM-1 which can bind HA at equivalent levels. Neither of the cell lines expressed VCAM-1 (which can directly bind to the integrins α4β1 and α9β1).

6.1.2.4.3 Hyaluronic Acid and Fibronectin Binding Assays

As no obvious changes in the adhesion receptor profiles tested were seen between V3L and S5L cells, we wondered if the differences in adhesion might be due to differences in the ability of these cells to bind to the ECM components, HA and FN. Thus, binding assays were performed. No differences were seen between the two

cell lines in their ability to bind HA (**Figure 39**). However, a significantly higher number of S5L cells were able to bind FN (**Figure 40**; p = 0.03).

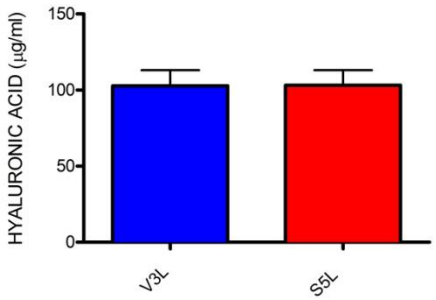

Figure 39 V3L and S5L cells show equivalent binding to hyaluronic acid. $1x10^4$ V3L or S5L cells were plated onto FITC-labelled hyaluronic acid (HA; 1 mg/ml). One hour later, the HA was washed off and the amount of bound HA was quantified in relation to a standard curve using a fluorescent plate reader. No differences were seen between the two cell lines in their capacity to bind HA.

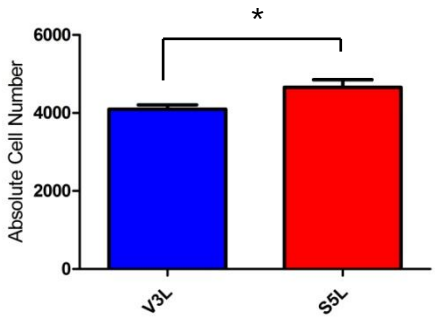

Figure 40 S5L cells bind FN better than V3L cells. 1 x 10^4 V3L or S5L cells were plated onto fibronectin (20 µg/ml; FN). After 45 minutes, any non-adherent cells were washed off and the number of bound cells was quantified in relation to a standard curve using a fluorescent plate reader. A significantly higher number of S5L cells were able to bind FN than V3L cells ($p = 0.03$).

6.1.2.5 S100P Increases Permeability and Migration through a HDLEC Monolayer

In order to assess the effect of S100P on translymphatic endothelial migration (TLEM), we first had to establish a confluent HDLEC monolayer *in vitro*. A series of optimisation experiments were performed to determine the number of HDLEC that had to be plated to allow for a confluent monolayer to form overnight. Structurally, the monolayer was visualised by H&E staining following fixation. Functionally, monolayer integrity was assessed through the quantification of permeability to FITC-Dextran (2 million MW). Initially, 1 x 10^5 and 2 x 10^5 cells were seeded onto membranes coated with fibronectin (0.5 µg/ml). The following day, the permeability of these cell layers was tested. Although the permeability decreased as the number

of HDLEC increased (**Figure 41**), histological assessment showed that membranes were not completely covered by HDLEC. Thus, the number of cells initially seeded was increased to 2.5 x 10^5. As can be seen in **Figure 42**, this resulted in an adequate HDLEC monolayer, both structurally and functionally.

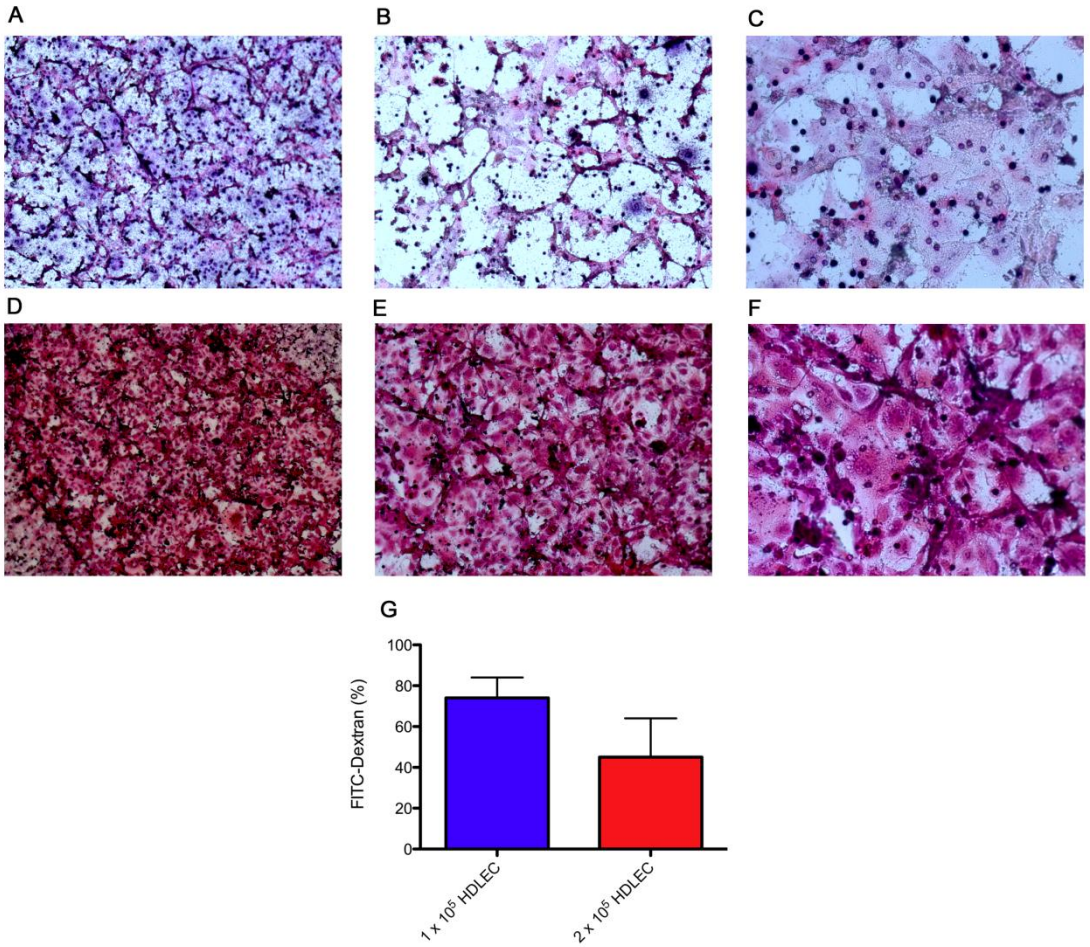

Figure 41 Pilot FITC-Dextran evaluation of HDLEC monolayer. Either 1 x 10^5 (**A - C**) or 2 x 10^5 HDLEC (**D - F**) were seeded onto fibronectin (0.5 µg/ml) and left to settle overnight. The integrity of the monolayer was then assessed by measuring permeability to FITC-Dextran (2 million MW) at 20 minutes (**G**). Membranes onto which the HDLEC has been seeded were fixed in methanol, and stained with H&E; representative images of these membranes are shown (**A** and **D** at 50x magnification; **B** and **E** at 100x magnification; **C** and **F** at 200x magnification). Neither concentration of cells resulted in a complete monolayer, though permeability to FITC-Dextran decreased as the number of seeded HDLEC increased. (n = 1 in duplicate).

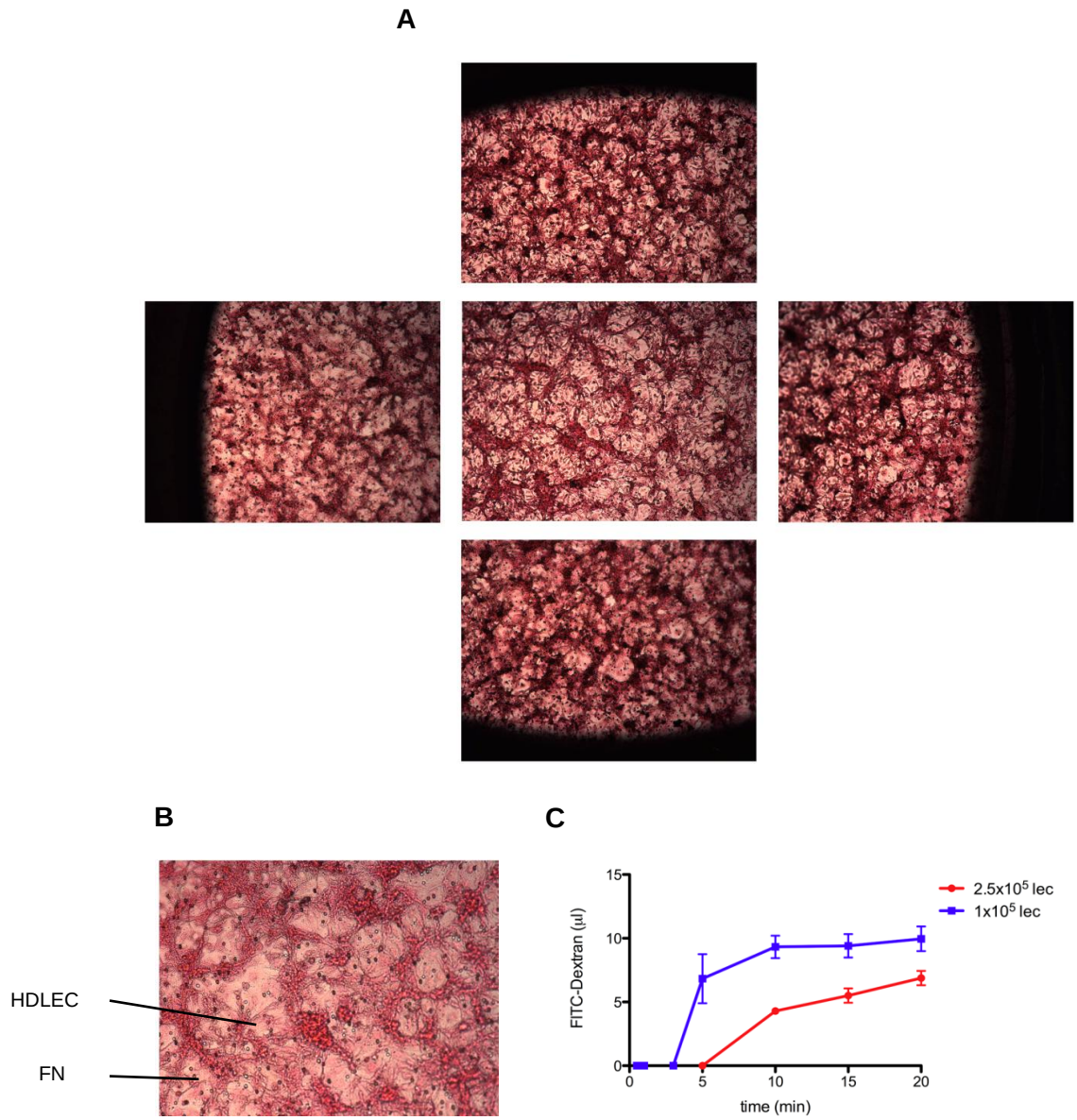

Figure 42 Optimal HDLEC monolayer. 2.5 x 10^5 HDLEC were seeded onto fibronectin (0.5 µg/ml) and left to settle overnight. **A** (50x magnification) shows a representative membrane, with images taken at five different points in order to construct a composite image. As can be seen, the entire transwell membrane is covered with HDLEC; fibronectin (FN) is also visible between HDLEC. The centre of the membrane is shown at 100x magnification in **B**. Functionally (**C**), this monolayer was significantly less permeable to FITC-Dextran (2 million MW) than monolayers comprising 1 x 10^5 HDLEC were ($p = 0.04$). ($n = 1$ in triplicate).

Having established a confluent monolayer, permeability and TLEM assays were performed. Co-cultures containing S5L cells caused monolayers to become significantly more permeable to FITC-Dextran at one (p = 0.02), four (p = 0.002) and eight (p = 0.007) hours (**Figure 43**), as compared to co-cultures containing an equal number of V3L cells. As a fixed concentration of FITC-Dextran was used, this trend continued up to 24 hours, but was not significant after eight hours. No cells had migrated through the monolayer at 24 hours.

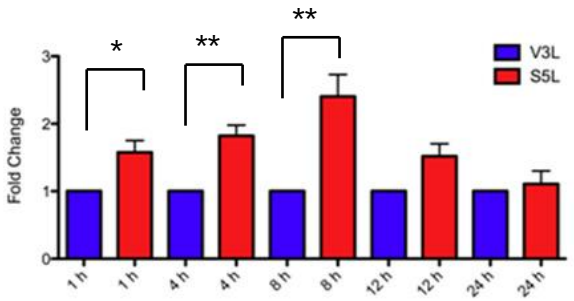

Figure 43 S100P increases permeability through a HDLEC monolayer. 5 x 10^5 V3L or S5L cells were plated onto HDLEC monolayers in 500 µl of Opti-MEM Reduced Serum Medium I containing 1 mg/ml of FITC-dextran (2 million MW). The permeability of the monolayer was assessed by quantifying the amount of FITC-Dextran in the bottom well over 24 hours. The permeability of S5L wells was significantly higher at one (p = 0.02), four (p = 0.002) and eight hours (p = 0.007), than wells containing an equal number of V3L cells. No cells had migrated through the monolayers at 24 hours (the wells were analysed at this time for cells using a Coulter counter).

The migration of cancer cells through the monolayer over the next 48 hours was quantified (i.e. an end-point measurement was taken at 72 hours after seeding of cancer cells onto the monolayer). A significantly higher number of S5L cells had migrated through the HDLEC monolayer at 72 hours (**Figure 44**; p = 0.006).

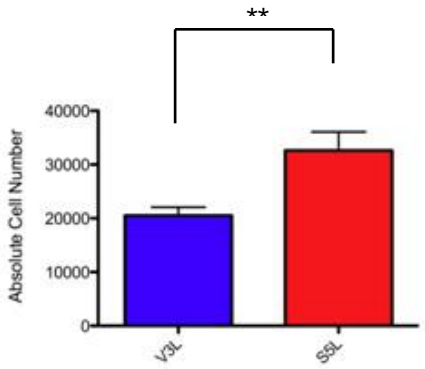

Figure 44 S100P increases translymphatic endothelial migration (TLEM). The increase in permeability seen in the first 24 hours after seeding was followed by an increase in cancer cell migration over the next 48 hours. Thus, at 72 hours, the number of migrated S5L cells was significantly higher than the number of migrated V3L cells (p = 0.006).

6.2 Analysis of the Roles of S100P *in vivo*

As mentioned previously, because mice do not express endogenous S100P (203), the transgenic $KRAS^{G12D}$ and/or the $KRAS^{G12D}$/TP53 mouse models would not be relevant for preclinical therapeutic evaluation of S100P targeting therapies without further engineering. Thus, together with Dr Wasfi Alrawashdeh, a clinical research fellow in our laboratory, a CD1 nude mouse orthotopic model of pancreatic cancer was created using the V3L and S5L cells. Using bioluminescence, we aimed to investigate the potential roles of S100P in primary pancreatic tumour growth and the potential occurrence of spontaneous metastasis (lymphatic and haematological). We hoped that this model would be useful for the future evaluation of novel therapies.

6.2.1 Pilot Study

A pilot study was performed in order to determine if the parental V3 and S5 cells would grow orthotopically in the pancreas; if any metastases would spontaneously develop; and if the pancreas and/or metastases could be adequately imaged and quantified using bioluminescence.

Three groups (n = 5 animals per group) of mice were used. The first two groups had either 2 x 10^6 V3 or S5 cells injected orthotopically into the pancreas. Mice were

killed at various time-points, with organs being harvested for histological examination (**Figure 45**). The experiment was terminated at four months post-injection. All 10 animals grew pancreatic tumours (tumour sizes ranged from 1 x 1 mm^2 to 15 x 23 mm^2), but no metastases (lymphatic or haematological) were seen in either group.

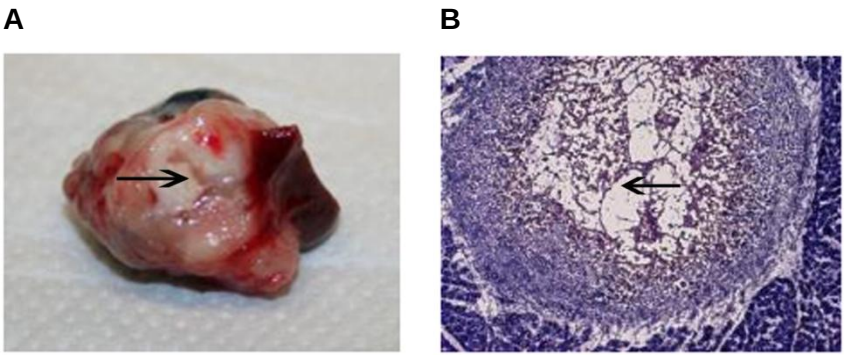

Figure 45 A representative orthotopic S5 tumour. 2 x 10^6 V5 or S5 cells were orthotopically injected into the pancreas of CD1 nude mice. A macroscopic tumour (**A**) excised at four months post-injection, together with the corresponding H&E section (**B**; 100x magnification), is shown above. Arrows highlight areas of central necrosis. Orthotopic implantation of both V3 and S5 cells resulted in primary tumour growth.

The third, or imaging, group had S5 cells injected subcutaneously and orthotopically into the pancreas. The rationale behind this double injection was that we hoped to use the size of the subcutaneous tumours as an indirect guide as to when to image the orthotopic pancreatic tumours. A smaller number of cells, 6.5 x 10^5 cells, were injected in this group due to a technical error (i.e. cells were incorrectly counted prior to suspension in PBS for injection). Despite this error, however, four of the five animals grew tumours (sizes ranged from 4 x 5 mm^2 to 7 x 8 mm^2 for subcutaneous tumours, and from 10 x 14 mm^2 to 12 x 25 mm^2 for orthotopic pancreatic tumours). In addition, lymphatic metastases were seen in the peri-pancreatic LNs (**Figure 46**). In fact, lymphatic invasion of the pancreatic lymphatic vasculature was seen as early as six weeks post-injection. No haematological metastases were seen in any of the mice, as evidenced by histological examination of livers and lungs which were resected from these animals post-mortem.

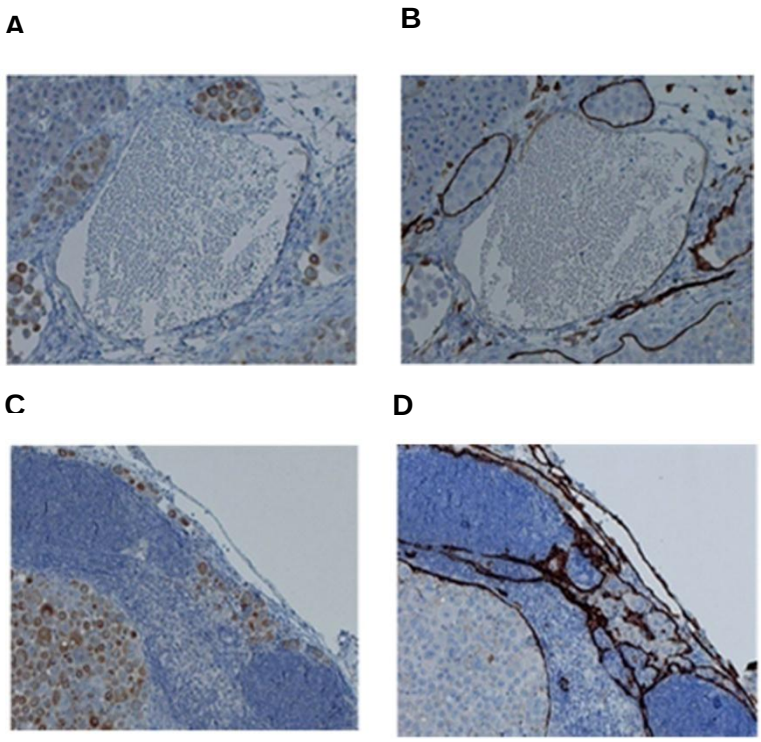

Figure 46 S5 cells metastasise to peri-pancreatic lymph nodes (LN). An imaging group (n = 5), in which 6.5 x 10^5 S5 cells had been injected, developed LN metastases. Representative images of a peri-tumoural lymphatic vessel (100x magnification) stained for the anti-human epithelial marker, cytokeratin-8 (**A**), and the murine lymphatic marker LYVE-1 (**B**) showed that S5 cells had invaded these vessels. Furthemore, cytokeratin-8 positive S5 cells were seen in peri-pancreatic LN (**C**; 100x magnification. **D** shows a peri-pancreatic LN stained for LYVE-1 (100x magnification).

Lastly, in order to confirm that the orthotopic pancreatic tumours could be imaged using bioluminescence, tumours were imaged using a luciferase-expressing Vaccinia

virus (kind gift from Dr Yaohe Wang). The virus was injected intravenously by Dr Crispin Hiley (clinical research fellow working with Dr Wang), followed by an intra-peritoneal injection of D-luciferin (15 mg/ml). Thereafter, animals were imaged using the IVIS system. We were able to image orthotopic tumours reproducibly, while they were as small as 2 mm^3 (**Figure 47**).

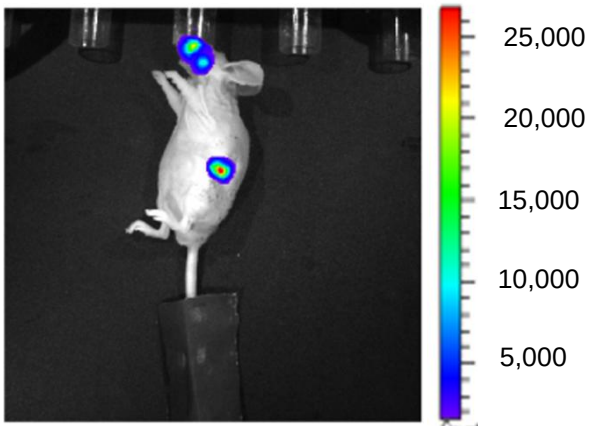

Figure 47 Bioluminescence imaging of S5 orthotopic pancreatic tumours. A luciferase-expressing Vaccinia virus was injected into the tail veins of S5 imaging mice, followed by the intra-peritoneal administration of D-luciferin (15 mg/ml). This mouse was killed after imaging; at this point, the tumour was excised and measured. The tumour shown above measured 2 mm^3.

6.2.2 Orthotopic Pancreatic Mouse Model using Luciferase-Transduced Cells

After the pilot study, the V3L and S5L cell lines were created and characterised as described in 6.1.1 (pages 119-126). The orthotopic pancreatic injections were repeated using 6.5 x 10^5 V3L and S5L cells (n = 10 per group) in order to evaluate the effects of S100P over-expression on primary pancreatic tumour growth, as well as to determine if the lymphatic invasion seen in the pilot study was reproducible. Mice were imaged from one week post-injection on a weekly basis for real-time assessment of primary tumour growth and the occurrence of spontaneous metastasis.

6.2.2.1 S100P Accelerates Primary Pancreatic Tumour Growth

From as early as week one post-injection, larger pancreatic tumours were seen in S5L animals as compared with V3L animals using bioluminescence (**Figure 48**). One S5L mouse had to be killed at operation due to peri-operative trauma, resulting in only nine S5L animals being used in the experiment. The experiment was terminated at nine weeks post-injection for two reasons: firstly, the earliest evidence of lymphatic invasion was seen at six weeks post-injection in the pilot study; and secondly, a significant difference in bioluminescence imaging between V3L and S5L tumour growth was seen by eight weeks (**Figure 49**; p = 0.002). Upon killing, tumours were harvested and weighed (**Figure 50**). S5L tumours weighed significantly more than V3L tumours (p = 0.01). One S5L mouse became ill, and had

to be killed at an earlier time-point, and thus was excluded from the analysis. A tumour was present in this mouse, but it measured 1 mm^3 and could not be weighed.

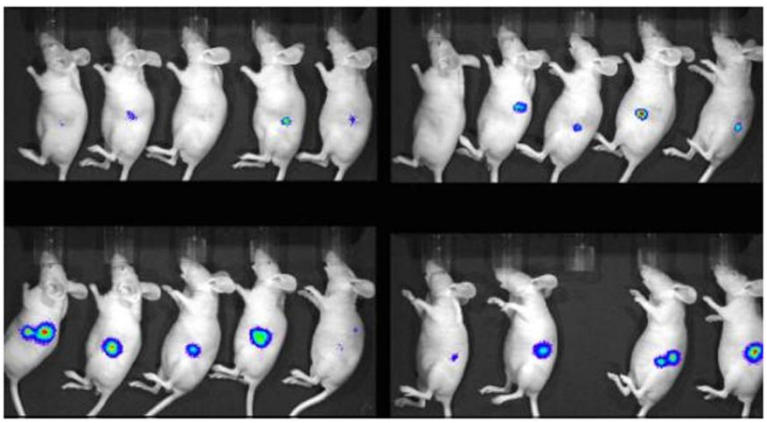

Figure 48 Bioluminescence imaging of orthotopic pancreatic tumours at week 1 post-injection. The orthotopic pancreas mouse model was repeated using 6.5 x 10^5 V3L and S5L cells following *in vitro* characterisation, in order to confirm the results of the pilot study. V3L animals (n = 10) are shown in the upper panel, with S5L animals (n = 9; one mouse had to be killed at operation due to peri-operative trauma) shown in the lower panel. Orthotopic tumours are already present in both groups, with larger tumours being seen in the S5L group (quantification shown in Figure 48).

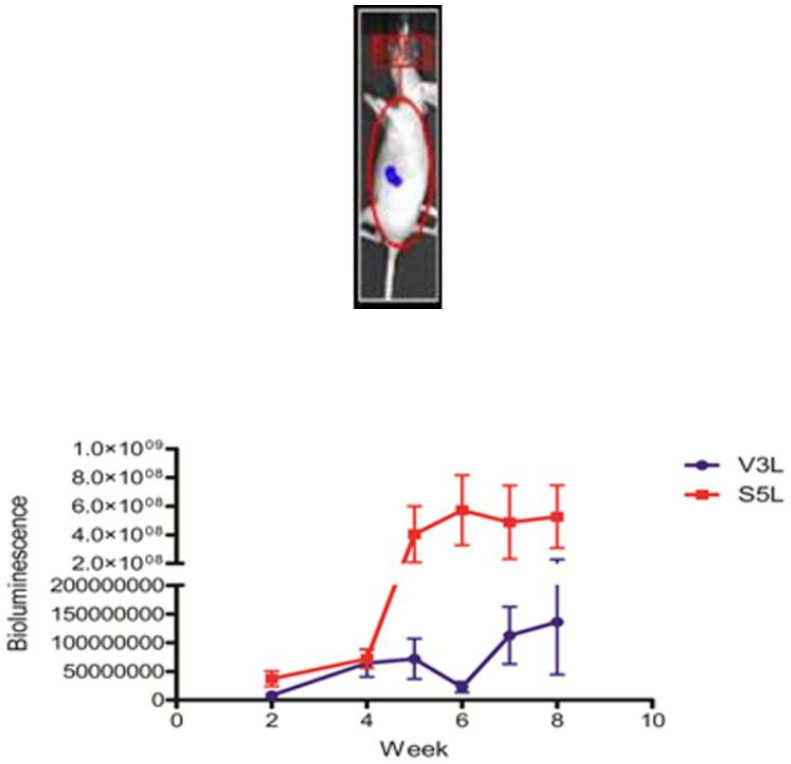

Figure 49 S5L orthotopic pancreatic tumours grow at a faster rate than V3L orthotopic pancreatic tumours. Regions of interest (ROI) were quantified weekly for each animal, and the average bioluminescence was plotted for each group. ROI calculates the signal intensity for a standardised area for each mouse, and is a quantitative measure of bioluminescence, and thus tumour growth. The S5L group (n = 9) showed a significantly higher rate of tumour growth than the V3L group (n=10; p = 0.002), as calculated by a linear regression of the weekly plots of average bioluminescence for each group.

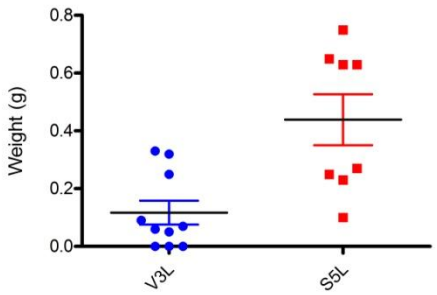

Figure 50 S5L orthotopic pancreatic tumours are larger than time-matched V3L orthotopic pancreatic tumours. V3L and S5L orthotopic pancreatic tumours were allowed to grow for nine weeks, after which tumours were harvested and weighed. S5L tumours (n = 8) were significantly larger than V3L tumours (n = 10; p = 0.01). One S5L animal had to be excluded from the analysis as it became ill, and had to be killed at an earlier time-point. A 1 mm^3 tumour could be seen at necropsy which could not be weighed.

Harvested tumours were analysed for S100P mRNA expression (**Figure 51**). S5L tumours expressed approximately three times more S100P transcript than V3L tumours (p = 0.01).

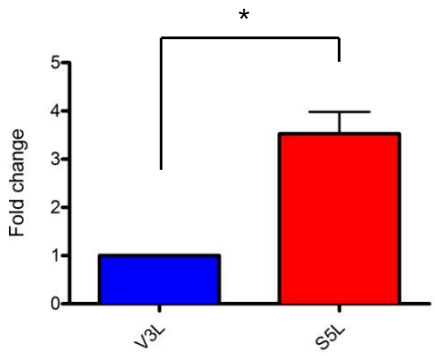

Figure 51 S5L orthotopic pancreatic tumours express higher levels of S100P transcript. qPCR was performed on RNA extracted from fresh frozen V3L and S5L orthotopic pancreatic tumours for S100P expression. On average, S5L tumours expressed 3x more S100P transcript than V3L tumours ($p = 0.01$).

However, in this experiment, lymphatic invasion was seen in both V3L and S5L primary tumours (**Figure 52**), both peri- and intra- tumourally. A 24-point Chalkley graticule was used to evaluate tumours for lymphatic vessel density (LVD) and the percentage of cancer-filled lymphatics. No significant differences were seen between the V3L and S5L tumours. Furthermore, no invaded LNs were found in either experimental group.

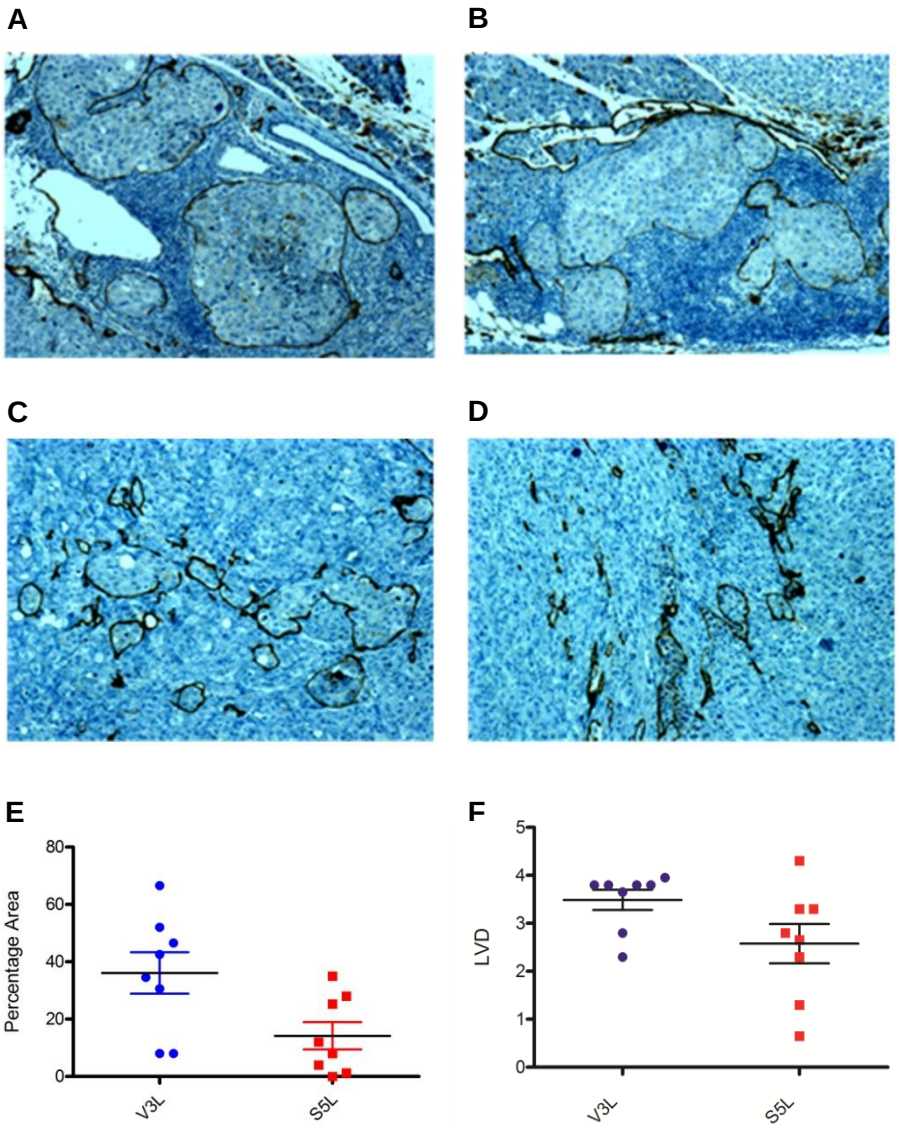

Figure 52 Quantification of peri-tumoural and intra-tumoural lymphatic invasion. Cancer cells were noted inside peri-tumoural (**A** and **B**) and intra-tumoural (**C** and **D**) lymphatic vessels in both V3L (**A** and **C**) and S5L (**B** and **D**) animals. Representative sections (100x magnification) from time-matched orthotopic pancreatic tumours were stained for LYVE-1; tumours were then assessed for the percentage area of cancer-filled lymphatics (**E**) and for lymphatic vessel density (LVD) (**F**) using a 24-piece Chalkley graticule. No differences were found between the two groups, both in terms of percentage area of cancer-filled lymphatics ($p = 0.07$) and LVD ($p = 0.08$).

We attempted to confirm these findings by repeating the orthotopic pancreatic injections (n = 7 per group). We also had planned on lengthening the duration of the experiment, in order to determine if a larger primary tumour size would select for spontaneous metastasis. Unfortunately, due to an outbreak of infection in both V3L and S5L cages, the experiment was compromised and had to be terminated at ten weeks post-injection. Data from this experiment were thus inconclusive.

6.2.3 The Effects of S100P on Site-Specific Growth *in vivo*

A previous experiment conducted in our laboratory had shown that S5 cells (18/18 mice) grew better subcutaneously than V3 cells (3/18 mice) in nu/nu mice. This, in conjunction with the data from the CD1 nude orthotopic pancreatic mouse model described above, led us to explore if S100P could affect site-specific tumour growth. Thus, we created three experimental metastasis mouse models to determine if the expression of S100P by cancer cells accelerated tumour growth in the liver (n = 7 per group), lungs (n = 7 per group) or right axillary LN (n = 7 per group).

6.2.3.1 Tail Vein Injections

5×10^5 V3L or S5L cells were injected directly into the tail vein of CD1 nude mice (n = 7 per group). Mice were imaged weekly using bioluminescence. The experiment was terminated at four weeks post-injection, at which time the lungs, pancreas, spleen, liver, duodenum and pancreatic LN were harvested from each mouse for

histological examination. No evidence of tumour growth was seen in either group (**Figure 53**).

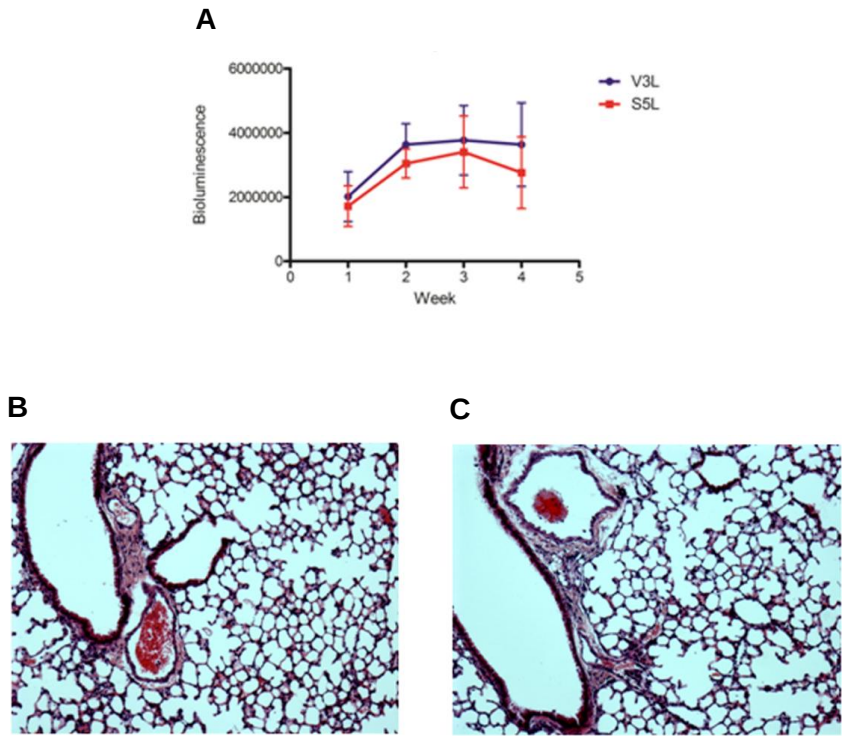

Figure 53 Tail vein injections of V3L and S5L cells. 5 x 10^5 V3L or S5L cells were injected into the tail veins of CD1 nude mice (n = 7 per group). Mice were imaged weekly using bioluminescence (**A**), and the experiment was terminated at four weeks post-injection. Representative H&E sections through the lungs of a V3L (**B**) and S5L (**C**) animal at 100x magnification are shown. No tumours grew in either group.

6.2.3.2 Intrasplenic Injections

5 x 10^5 V3L or S5L cells were injected into the spleen, in order to seed cells to the liver. Mice were imaged weekly using bioluminescence. The experiment was terminated at six weeks post-injection, at which time the lungs, pancreas, spleen, liver, duodenum, small bowel and large bowel and pancreatic LN were harvested from each mouse for histological examination. No evidence of tumour growth was seen in either group (**Figure 54** and **55**).

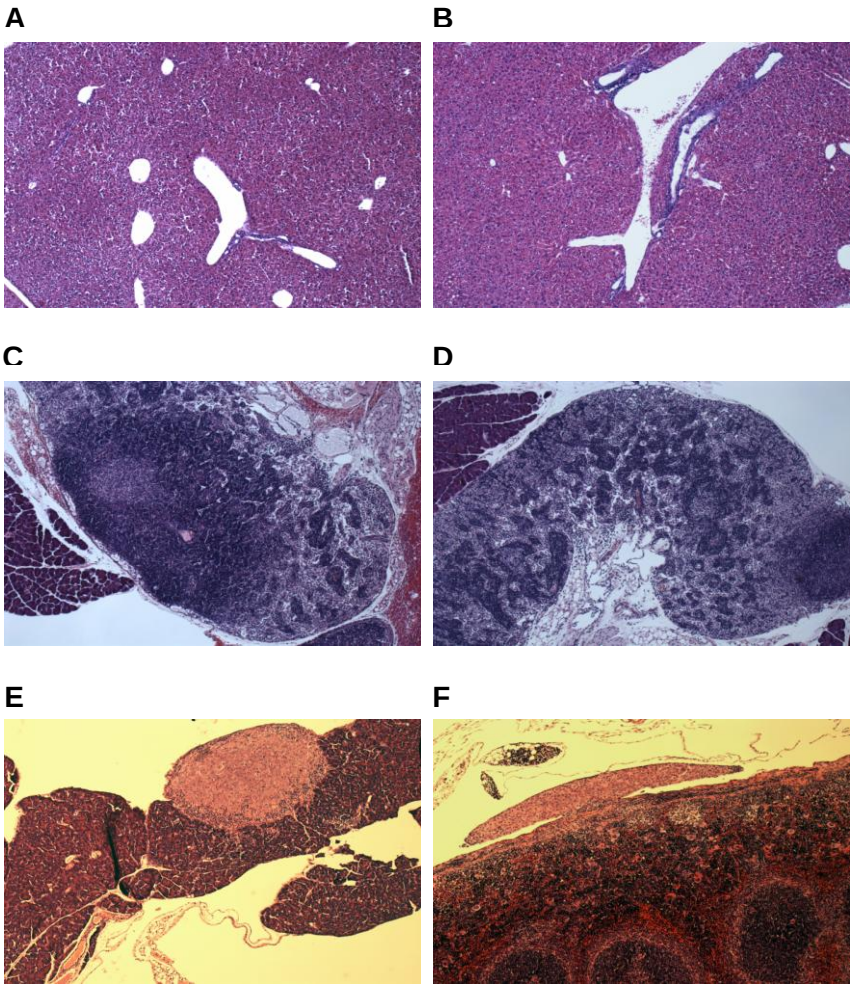

Figure 54 Intrasplenic injections of V3L and S5L cells. 5 x 10^5 V3L or S5L cells were injected orthotopically into the spleens of CD1 nude mice (n = 7 per group) in order to induce liver metastasis experimentally. Animals were imaged weekly using bioluminescence until 6 weeks post-injection, at which time the experiment was terminated. Neither group grew tumours in the liver (representative H&E images of the liver of a V3L animal (**A**) and S5L animal (**B**) are shown at 50x magnification. Furthermore, no positive peri-pancreatic lymph nodes (LN) were seen in any of the 14 animals (representative H&E images of peri-pancreatic LN from a V3L (**C**) and S5L (**D**) animal are shown at 50x magnification). Only one S5L animal grew an orthotopic pancreatic tumour (**E**) as well as a splenic tumour (**F**); representative H&E images shown at 50x magnification.

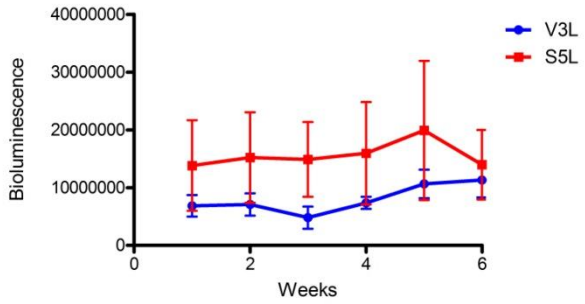

Figure 55 Bioluminescence imaging of mice after orthotopic intrasplenic injections. Although differences in bioluminescence were seen between the two groups, these were not statistically significant.

6.2.3.3 Intranodal Injections

1 x 10^5 V3L or S5L cells were injected directly into the right axillary lymph node of CD1 nude mice (n = 7 per group). Mice were imaged weekly using bioluminescence. The experiment was terminated at ten weeks post-injected, at which time axillary, inguinal and pancreatic lymph nodes were harvested, together with pancreas, spleen, liver and duodenum for histological examination. No evidence of tumour growth was seen in either group (**Figure 56**).

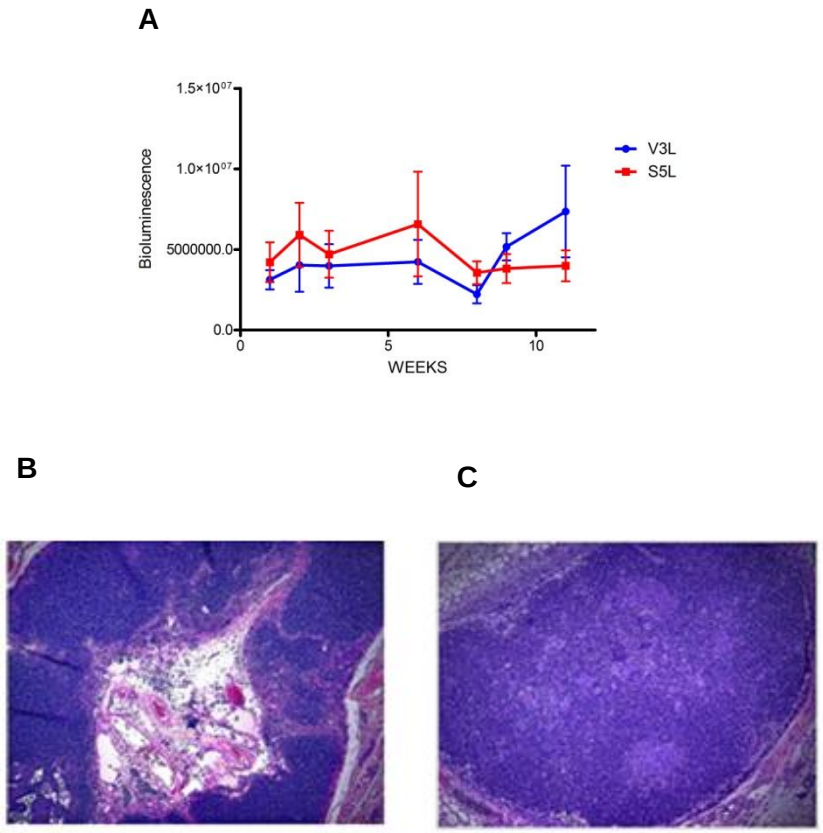

Figure 56 Intranodal injections of V3L and S5L cells. 1 x 10^5 V3L or S5L cells were injected into the right axillary lymph nodes of CD1 nude mice (n = 7 per group). Mice were imaged weekly using bioluminescence (**A**), and the experiment was terminated at nine weeks post-injection. **B** and **C** show representative H&E sections through the right axillary LN of a V3L (**B**) and S5L (**C**) animal at 50x magnification. No tumours grew in either group.

7. DISCUSSION (Part II): THE ROLE OF S100P IN LYMPHATIC METASTASIS IN PDAC

As discussed earlier, S100P, a 10.4 kDa calcium-binding protein, previously has been found to contribute to the progression of PDAC, in a number of studies (91–97), many of which were performed in our laboratory (91,92,94). Thus, we decided to investigate the potential roles of S100P in lymphatic invasion further, both *in vitro* and *in vivo*.

We were able to show that the luciferase transduction did not alter the expression of S100P in the V3L and S5L cell lines, neither at a mRNA nor at a protein level. Furthermore, the functional behaviour of these two cell lines *in vitro* did not change i.e. V3L and S5L cell lines mirrored the parental V3 and S5 cell lines in terms of proliferation and invasion (94). We also were able to show that both cell lines expressed equivalent levels of luciferase, and were able to grow in soft agar, a surrogate for tumourigenic capacity. Thus, we concluded that these cell lines probably could be used to develop a CD1 nude orthotopic mouse model of PDAC.

The co-culture experiments performed using cancer cells in conjunction with HDLEC yielded some intriguing results. These experiments aimed to evaluate if cancer cell adhesion to HDLEC governs migration into lymphatic vessels, or if TLEM can proceed even in the face of weak binding between cancer cells and HDLEC. In 1981, GL Nicolson published a paper entitled ‘Metastatic tumour cell attachment and invasion assay utilizing vascular endothelial cell monolayers’, which describes his analysis of the ‘intravasation’ step of the metastatic cascade (179). These

experiments were performed using co-cultures of endothelial cells and melanoma cell lines with varying metastatic capacities. Nicolson found that intravasation was initiated by tumour cell attachment to a blood vascular endothelial cell monolayer. Indeed, tumour cell lines that were more metastatic attached better to these monolayers than less metastatic cell lines. Furthermore, tumour cells preferentially attached at or near endothelial intercellular junctions, and this attachment facilitated endothelial cell retraction (**Figure 57**). Retraction was defined as the 'breaking of intercellular junctions between endothelial cells, a retraction of the endothelial cell edges, and subsequent cell rounding with exposure of the basal lamina'. Once cells had retracted, a haptotactic gradient was established; as cancer cells bound slowly and weakly to endothelial cells, but bound quickly and strongly to basal lamina, cells preferentially moved towards the basal lamina underlying the endothelial cell monolayer. Invasive cells were then able to degrade and migrate through the basal lamina beneath the endothelial cell monolayer.

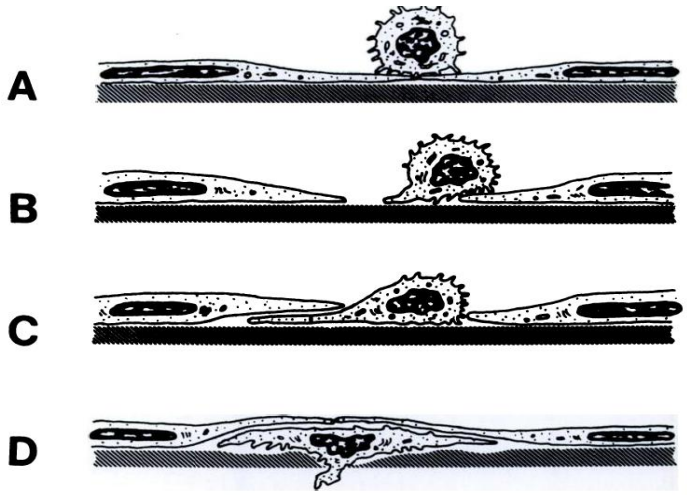

Figure 57 Endothelial retraction allows for the transmigration of tumour cells. A tumour cell attaches to the abluminal surface of blood endothelium, near the intercellular junctions (**A**). This causes the endothelial cells to retract (**B**). The tumour cell then migrates through the retracted endothelium, due to a haptotactic gradient between the endothelial cells (to which tumour cells can bind weakly) and the basal lamina (to which tumour cells can bind strongly) (**C**). Once the tumour cell has migrated through the monolayer, the endothelial intercellular junction reforms (**D**). The tumour cell can then migrate through the basal lamina. (179)).

A variety of endothelial cells were used in Nicolson's study: bovine aortic endothelial cells; HUVECs and murine lung and brain capillary endothelial cells. Thus, the experiments comprehensively represented all branches of the blood vascular tree (i.e. in terms of vessel size) (179). Interestingly, none of the melanoma cells were able to adhere to aortic endothelia, whilst most cells (melanoma, sarcoma, and platelets) were able to bind to murine capillary endothelia and HUVECs. This

suggests that adhesion to endothelium probably is more important in smaller vessels. Notably, fibroblasts were unable to bind to capillary endothelia (179). This is interesting in light of the more recent emergence of the concept of fibroblast-led cancer cell invasion (205). Fibroblast-led invasion has been shown to occur during collective cell invasion; fibroblasts at the leading edge of tumours create 'tracks' in ECM along which epithelial cancer cells invade. It would be interesting to adapt the 3D co-cultures used in these experiments to include endothelial cells, to determine if or how this fibroblast-led invasion changes during intravasation. Nicolson's experiments also were conducted in the absence of flow, or under static conditions. Whilst this is not truly representative of the blood vasculature, it is relevant to lymphatics where propulsion of lymph occurs at a relatively slow rate.

The concept of 'retraction', as applied to blood vascular endothelium, has been developed substantially over the last three decades (206–208). Endothelial permeability has been shown to be controlled by a variety of chemical and mechanical stimuli, originating both in the blood (e.g. thrombin from activated platelets and pulsatile blood flow) and in the tissues surrounding blood vessels (e.g. histamine released from mast cells and TNFα secreted by activated leukocytes) (208). Furthermore, confluent blood vascular endothelial cells (BVEC) behave differently from sparse BVEC (206). When confluent, BVEC exhibit an epitheliod phenotype with apical-basal polarity. Cell-to-cell contact inhibits growth and motility, and protects the cells from apoptosis. Under sparse conditions, like angiogenesis, however, BVEC become fibroblastic and motile, and begin to proliferate. Blood vessel integrity is maintained by the stability of intercellular junctions, and by changes in the actomyosin cytoskeleton within endothelial cells. Many adhesion

molecules have been shown to play a role in mediating junctional stability, and their involvement is usually governed largely by the nature of the stimulus. However, VE-cadherin as emerged as being central to maintaining blood vessel integrity (206). Indeed, VE-cadherin knockout mice are embryonically lethal due to vascular insufficiency (209). Furthermore, this member of the calcium-dependent cadherin family of proteins has been found to serve as an interface between the ECM and the intracellular compartment. In quiescent BVEC, VE-cadherin couples with VEGFR-2, preventing endocytosis of VEGFR-2, securing the endothelial cell barrier (210). In the presence of VEGF however, VE-cadherin is internalised, destabalising intercellular junctions (211–213). In addition, VE-cadherin has been shown to stimulate the Rho GTPases Rac and Cdc42, which aids in the assembly and maturation of endothelial cell junctions (214,215). In the context of metastasis, it has been shown that adhesion of breast MDA MB231 cancer cells to the HUVECs alters VE-cadherin intercellular localisation and permeability (216). Furthermore, it has been shown that the pancreatic cancer cell lines MiaPACA2 and Panc1 increase permeability through a HUVEC monolayer via two mechanisms: first, by redistributing VE-cadherin and PECAM, destabalising intercellular junctions; and second by mediating changes in the actin cytoskeleton (217). Whilst these phenomena are well-established for BVEC, their relevance to the lymphatic vasculature has yet to be explored.

Indeed, only one study to date has evaluated ‘retraction’ in the context of the lymphatic vasculature. This study, in essence, recreated Nicolson’s original experiment: M21 melanoma cells were seeded onto bovine lymphatic endothelial cells (obtained from the thoracic duct) under static conditions; cultures were fixed,

stained and analysed using scanning electron microscopy. The M21 melanoma cells were found to induce a retraction of the LEC monolayer, resulting in TLEM (218). A flaw of this study is that only LEC obtained from collecting lymphatics, and not capillary lymphatics, were used. It is these lymphatic capillaries which serve as a point of entry during metastasis. Furthermore, only one melanoma cell line was used; the authors could have included cell lines with different metastatic potentials, as Nicolson did (179). However, it must be remembered that this study, however flawed, for the first time, established the relevance of endothelial cell retraction to the lymphatic vasculature and that this phenomenon occurs in the presence of added cancer cells.

We sought to evaluate the effects of S100P over-expression in pancreatic cancer on the interaction of tumour cells with the lymphatic endothelium. To that end, the V3L and S5L cells were tested for their ability to migrate through a HDLEC monolayer. Our data suggest that, at least in the context of S100P over-expression, cancer cell adhesion to resting lymphatic endothelium is not essential for TLEM. This conclusion can be drawn from two results: firstly, V3L cells adhered just as well to resting HDLEC as S5L cells; and secondly, a significantly higher number of S5L cells migrated through a resting HDLEC monolayer at 72 hours. This suggests that the observed difference in TLEM is not mediated by cell-to-cell contact. Rather, it suggests that a greater haptotactic gradient for migration exists when S100P is over-expressed. The FN binding assays showed a statistically significant difference between V3L and S5L binding. Thus, theorectically, as V3L and S5L cells bind equally as well to HDLEC, but S5L cells bind better to FN, a greater haptotactic gradient exists for S5L TLEM than V3L TLEM. However, as the observed difference

in FN binding between the two cell lines was small (12.5%), the biological relevance of this remains doubtful. There is a possibility that the concentration of FN used in these assays was suboptimal for adhesion. Thus, had I had more time, I would have liked to have repeated the assay using a range of FN concentrations. An alternative to this co-culture model is one in which V3L and S5L adhesion to mouse tissue explants containing the throrac duct, and/or smaller lymphatic capillaries (if possible), is tested. Finally, the invasion assays showed S5L invasion through Matrigel to be significantly higher than V3L invasion *in vitro*. This supports the argument that S100P over-expression increases degradation of, and thus invasion through, the basal lamina underlying the intima following TLEM.

We aimed to assess 'retraction' functionally using the permeability assays. Our data show that permeability through a resting HDLEC monolayer from one to eight hours in culture was significantly higher for S5L cells than V3L cells. As the assays were conducted on resting HDLEC, we assume that there was no difference in the adhesion of V3L and S5L cells to the lymphatic monolayer. Thus, this increase in permeability was not mediated by cell-to-cell contact. As this change began at one hour post-seeding, it suggests that retraction of the lymphatic endothelium, rather than apoptosis (which usually occurs within six to eight hours), is responsible for this increased permeability; however this requires further investigation. This could have been confirmed by treating HDLEC with recombinant S100P, V3L conditioned media (CM), S5L CM, and a negative control, after which cells could have been fixed and stained for phalloidin to allow for the quantification of intercellular 'gaps'. Alternatively, the potential retraction of HDLEC could have been imaged in real-time using time-lapse microscopy. In order to confirm that these effects were due to

S100P, the experiment would also have to include conditioned media harvested from cells in which S100P had been silenced using siRNA.

Finally, both the permeability and the TLEM assays would need to be repeated using additional pancreatic cancer cell lines which express high levels of endogenous S100P, such as the BXPC3 cell line. This would serve to validate the increase in permeability and TLEM seen with the S5L cell line, in which S100P had been induced. Furthermore, transient knockdown of S100P, both in the S5L and BXPC3 cell lines using siRNA, would need to be performed in order to confirm that the observed increase in permeability and TLEM was indeed due to S100P. Unfortunately, by the time I had arrived at this point in my investigations, there simply was no time available to conduct these experiments.

As the data from these functional studies had not highlighted cell-to-cell contact as being central to the interaction between V3L or S5L cells and HDLEC, we wanted to investigate the paracrine effects of cancer cell supernatant on HDLEC. It has been reported previously that S100P is secreted by pancreatic cancer cells, and interacts with RAGE on these cells, creating an autocrine loop that promotes growth, survival and invasion both *in vitro* and *in vivo* (95,96). Thus, we questioned if a similar paracrine mechanism exists between the S5L cells and HDLEC.

Unfortunately, our attempts to quantify S100P protein expression in the supernatants of V3L and S5L cells by Western blotting were inconclusive. The detection of the product from the S100P construct in cell lysates required much optimisation since most commercially available S100P antibodies (from various companies, both mono-

and poly- clonal, and directed at both the N- and C-terminals) were unable to detect S100P in the S5L cell line. We were only able to detect intracellular S100P using a V5-antibody, which recognised the tagged C-terminus of our construct. This antibody failed to detect S100P in conditioned media from the S5L cell line. Thus, although this suggests that S100P might not be secreted by S5L cells, we cannot confidently exclude the possibility that this represents a technical shortcoming. Furthermore, there are no commercial ELISA kits which adequately detect S100P in cell supernatants available at present. Had I had more time, I would liked to have tried to develop an ELISA assay in-house, using the V5-antibody and a few different S100P antibodies, in order to analyse V3L and S5L supernatants for the presence of this protein. In addition, HDLEC were negative for RAGE using flow cytometry. Again, this experiment needs to be repeated using a different RAGE antibody to exclude technical error. However, it seems unlikely that secreted S100P, at least in the S5L cell line, stimulates HDLEC via RAGE.

In order to assess the potential functional effects of secreted S100P on cancer cell adhesion to HDLEC, recombinant S100P was added to the media surrounding both cancer cells and HDLEC for the duration of the assay. Interestingly, recombinant S100P significantly decreased V3L adhesion to resting HDLEC. A possible explanation for this could be that S100P binds calcium, which is essential for integrin activation. This hypothesis could be confirmed by repeating the assay using calcium-depleted media, or by adding a calcium-binding molecule like EDTA. Alternatively, it suggests that secreted S100P does not activate HDLEC in the same manner as IFNγ and TNFα. Had I had more time, I could have confirmed this by repeating the

flow cytometry experiments following pre-treatment of HDLEC with recombinant S100P.

Conversely, the addition of recombinant S100P significantly increased V3L adhesion to TNFα activated HDLEC, resulting in levels comparable to those seen with S5L cells. This effect was not seen following IFNγ stimulation of HDLEC. These data could support the premise that recombinant S100P decreases integrin activation, as the flow cytometry results showed that TNFα upregulated integrin expression, perhaps to a level that adequately compensates for the calcium-binding effects of recombinant S100P. Alternatively, it is known that S100P over-expression in our cell line results in the translocation of S100P to the nucleus (94). Furthermore, as mentioned previously, S100P can bind to RAGE receptors on pancreatic cancer cells, activating NF-KB signalling (190,199), which, in turn, can increase TNFα production (219). Thus, S100P over-expression could result in an increase in TNFα production by pancreatic cancer cells, which then would activate the lymphatic endothelium. This hypothesis would need to be confirmed by quantifying TNFα levels in V3L and S5L supernatant. Should this prove true, then the observed increase in S5L adhesion to activated HDLEC becomes important, as it may confer a metastatic advantage in the context of cancer inflammation.

Not only can differences in adhesion facilitate different rates of cancer cell invasion, but the molecules facilitating adhesion have long been recognised as a defining factor in the type of cancer cell movement underlying invasion (147). Thus, we sought to define what mediated V3L and S5L attachment to HDLEC. Our results highlight the complexity of these interactions.

Whilst we were able to show that V3L cells adhere to resting lymphatic endothelium via LYVE-1, CLEVER-1 and the integrin subunits α4, α9 and β1, we have yet to define what mediates V3L attachment to activated lymphatic endothelium. Interestingly, function blocking antibodies to CLEVER-1 and the integrin subunit α5 significantly increased V3L adhesion to activated HDLEC. Whilst this may seem counter-intuitive, the same trend has been observed with CLEVER-1 blockade in relation to dendritic cell cell adhesion to lymphatic endothelium (154). Perhaps of even greater significance however, is that whilst CLEVER-1 blockade increased dendritic cell adhesion to lymphatics, it decreased dendritic cell TLEM (154). A similar mechanism might, therefore, exist for V3L TLEM and should be investigated further. The observed increase in adhesion to activated HDLEC seen with α5β1 blockade also warrants further investigation. This could be done by repeating the TLEM assay, using the same function blocking antibodies which were used in the adhesion assays.

S5L cells adhered to HDLEC in a different fashion. S5L adhesion to resting endothelium was mediated by LYVE-1. This receptor also mediated attachment to IFNγ-stimulated HDLEC. CLEVER-1 and α5β1 blockade had no effect on S5L adhesion to HDLEC, resting or activated. In contrast to V3L cells, β1 integrin-dependent adhesion occurred only when HDLEC were activated. Specifically, α4β1 and α9β1 integrin mediated S5L adhesion to IFNγ-stimulated HDLEC. This raises an interesting question regarding the type of cell movement adopted by S5L cells in the context of inflammation. Collective cell migration is known to be β1-dependent (147), and our results indicate that S5L preferentially use β1-integrins to adhere to IFNγ-stimulated HDLEC. Furthermore, a previous gene expression profiling experiment of

the parental V3 and S5 cell lines showed a significant increase in E-cadherin in the S5 cells (Sayka Barry, PhD Thesis, 2009); again suggesting an increase in epithelial cohesion. However, further investigation is required to resolve this.

None of the molecules analysed appear to mediate S5L adhesion to TNFα–stimulated HDLEC. This suggests that other molecules which have not been decribed in the literature may be present on HDLEC, and mediate functional interactions between lymphatic endothelium and cancer cells. Furthermore, the fact that blocking one adhesion molecule at a time resulted only in a small, yet significant, decrease in cancer cell adhesion to HDLEC suggests that adhesion potentially is mediated by a number of receptors acting in concert together. It would be interesting to repeat the function blocking experiments using combinations of different antibodies, to see if cancer cell adhesion to HDLEC can be totally ablated. Unfortunately, I was unable to perform these experiments due to a shortage of time.

The lack of cognate adhesion receptors on V3L and S5L cells seen using flow cytometry suggests that it is possible that the ECM plays an important role in cancer cell adhesion to HDLEC (**Figure 58**). Whilst we were able to show that V3L and S5L cells express equivalent levels of the HA binding molecules CD44 and ICAM-1, we have yet to determine which FN-binding integrin(s) are expressed by these cells. Regardless, it is possible that FN and HA potentially act as a bridge between cancer cells and lymphatic endothelial cells. The importance of HA in facilitating cancer cell adhesion to blood endothelium, as well as its importance in haematological metastasis, has been described previously (220–222). In 1995, Zhang et al. showed, using a melanoma cell line expressing high levels of HA (HA-H) and a melanoma cell

line expressing low levels of HA (HA-L), that the HA-H cells formed a greater number of metastatic nodules in the lungs of C57BL/6 mice than HA-L cells, following tail vein injection (220). Furthermore, the survival of mice into which HA-H cells had been injected was significantly decreased. Interestingly, this paper also assessed the ability of these two cell lines to bind to CD44 positive, SV40-transformed lymphoid endothelial cells (SVEC4-10). HA-H cells were better able to adhere to SVEC4-10 cells, and this adhesion was significantly decreased in the presence of hyaluronidase and/or function blocking antibodies to CD44 (220). HA has been shown subsequently to facilitate adhesion and transendothelial migration in both prostate and colon carcinoma *in vitro* (221,222). Had I had more time, I would have liked to have repeated the HA binding assays incorporating hyaluronidase, to assess the importance of HA in mediating V3L and S5L adhesion to HDLEC.

As lymphatics are responsible for clearing debris and ECM, it may be beneficial for cancer cells to tether themselves to these matrix components in order to gain entry into lymphatics. Furthermore, due to the presence of button-hole junctions, lymphatics theoretically are easier to enter than blood vessels. It is possible that instead of having to ‘unzip’ the VE-cadherin in lymphatics, cancer cells can use the ECM to increase traction on the lymphatic vasculature, causing a ‘bulging’ of these button-holes, and allowing cancer cells to gain entry. This is however speculative, and requires further elucidation. I would have like to have tried to image this *in vitro*, had time permitted. This could have been done by establishing co-cultures of HDLEC with V3L or S5L cells; each cell type could have been fluorescently labelled with cell trackers, and the cells could have been placed in fluorescently-labelled

ECM (either HA or FN). Using confocal microscopy, I then would have tried to image these potential ‘bridges’.

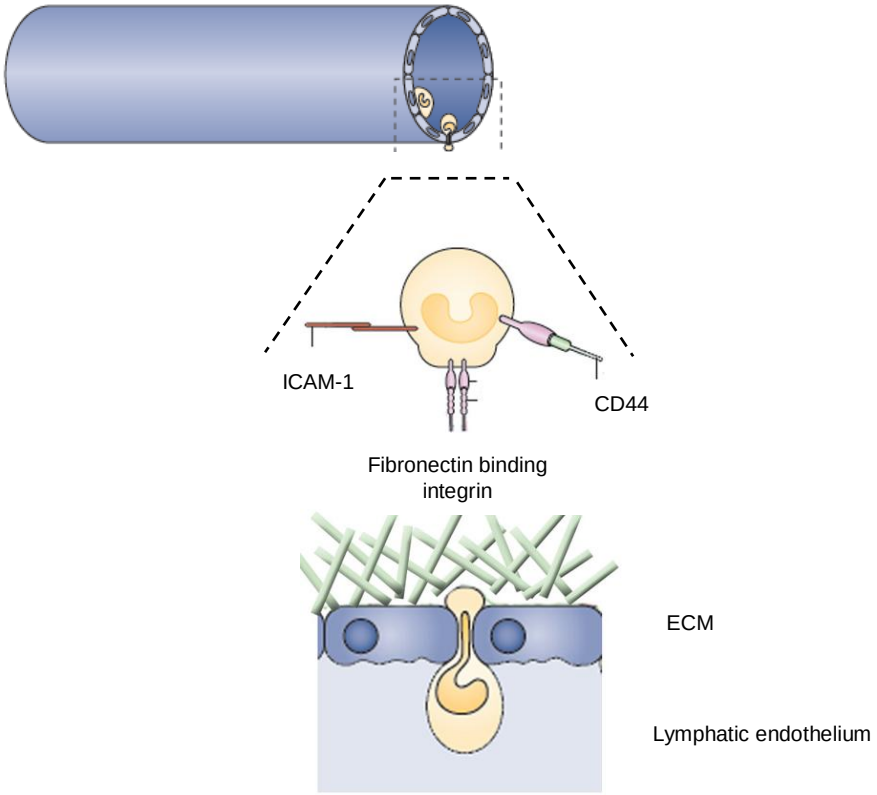

Figure 58 Schematic diagram depicting the potential mechanism through which the extracellular matrix (ECM) facilitates binding between cancer cells and lymphatic endothelium, allowing for translymphatic endothelial migration (TLEM). V3L and S5L cells express the hyaluronic acid binding molecules CD44 and ICAM-1, as well as fibronectin binding integrins. These allow cancer cells to bind to the ECM. The ECM, in turn, acts as a ‘bridge’, allowing cancer cells to bind to the lymphatic endothelium. In addition, the traction forces generated by this binding open up gaps in between lymphatic endothelial cells, allowing for paracellular transmigration. (Adapted from Nourshargh et al. (223))

Thus, whilst these *in vitro* experiments provide valuable clues as to the roles of S100P in lymphatic invasion, further investigation is required to determine the precise mechanisms through which it operates.

It has been shown previously, in an orthotopic mouse model, that cromolyn decreases the growth and invasion of S100P-expressing tumours (96). Thus, we wanted to develop a CD1 nude orthotopic mouse model in our laboratory in which these drugs (i.e. cromolyn and its analogues), as well as any other novel therapies to S100P, could be investigated preclinically. Furthermore, we hoped to use this model to confirm the effects of S100P over-expression on primary pancreatic tumour growth, and/or the occurrence of spontaneous metastases.

We were able to confirm, in the pilot study, that establishing a S100P over-expressing orthotopic mouse model was feasible: there was no peri- or post-operative morbidity or mortality associated with the surgical procedure; and the animals showed no signs of illness up to four months post-injection, at which point tumour growth was substantial. We were able to confirm that both V3 and S5 cells grow orthotopically in the pancreas of CD1 nude mice. Furthermore, data from the imaging group suggested that using a smaller number of injected cells could be beneficial as it resulted in lymphatic invasion. Thus, 6.5×10^5 cells were used in subsequent experiments. In addition, as caliper tumour measurements were found to be user-dependent and thus variable, we decided that tumour weight would be a more objective measure of tumour growth upon killing. Lastly, we concluded that

bioluminescence imaging adequately measured primary pancreatic tumour growth in real time.

The findings of the pilot, and subsequent two repeats, of the orthotopic injections highlight the difficulties associated with animal models. Firstly, whilst we observed LN metastases in the pilot study, we were unable to reproduce these data in the subsequent experiment. One possible explanation for this is that the parental V3 and S5 cell lines were used in the pilot study, whilst the V3L and S5L cell lines were used in the second experiment. Thus, although the *in vitro* data did not show any functional alterations in the V3L and S5L cell lines, it is possible that the luciferase transduction did alter the behaviour of these cell lines *in vivo*. This could have been confirmed by repeating the orthotopic injections using the parental V3 and S5 cell lines, however, this would preclude bioluminescent imaging, and thus, was not performed. Secondly, it is possible that a larger number of cells was injected during the pilot study than was thought, as an error with cell counting occurred prior to orthotopic injection. Thus, it is possible that larger tumours occurred earlier in the pilot study than in the repeat experiment, and that these larger tumours were more prone to direct invasion of the surrounding LN, as well as true lymphovascular invasion (observed on H&E sections). We were unable to confirm this, as tumours were not weighed in the pilot study. In addition, caliper measurements were taken only in two dimensions, and thus were sub-optimal for calculated conversions. Thirdly, in the pilot experiment, cells were injected at two sites i.e. subcutaneously and into the pancreas. There is emerging evidence that soluble factors released from primary subcutaneous tumours may result in the formation of a premetastatic niche, which increases haematological dissemination (224). Hiratsuka et al. showed, in

C57BL/6 mice bearing subcutaneous Lewis Lung Carcinoma (LLC) and B16 melanoma tumours, that S100A8 and S100A9 are up-regulated in the lung premetastatic niche. These soluble factors increased the extravasation of cancer cells following tail vein injection, and thus increased the number of lung metastases. In addition, the observed increase in lung metastases significantly decreased in the presence of neutralising antibodies to S100A8 and S100A9. Furthermore, pretreatment of normal controls with serum from tumour-bearing mice resulted in the upregulation of S100A8 and S100A9 in the lungs, and an increase in lung metastases following tail vein injection (224). Thus, it is possible that the presence of subcutaneous tumours in the pilot experiment contributed to development of metastasis. And finally, the third experiment, which was meant to resolve these discrepancies, had to be terminated early due to an infection contracted post-operatively. This highlights the complexities of animal experiments, and emphasises the importance of ensuring that neoplasms are kept free of mouse pathogens in order to obtain interpretable data (225).

Despite this, we were able to show reproducibly that S100P accelerates primary tumour growth, in keeping with data obtained in the previous study by Arumugam et al. (95). Furthermore, we were able to adequately monitor this growth from as early as one week post-injection using bioluminescence. Thus, this model can be used in the future to evaluate the effects of novel therapies against S100P on primary tumour growth.

We were also able to demonstrate the presence of both V3L and S5L cells in peri- and intra-tumoural lymphatic vessels in our model. This confirms that both the V3L

and S5L cell lines are able to intravasate into lymphatics. The *in vitro* TLEM data suggest that the S5L cells would invade at a faster rate. Thus, as no positive peri-pancreatic LN were found at ten weeks, the data from the repeat experiment suggest that lymphovascular invasion occurs within ten weeks post-injection. It would be interesting to define when the first evidence of lymphovascular invasion arises, as well as to test if this occurs at an earlier time-point when S100P is over-expressed as compared to the control cells that show no endoegenous S100P. This could be done by repeating the orthotopic experiment using the V3L and S5L cell lines, and killing at least five mice weekly, looking for histological evidence of lymphovascular invasion.

As no evidence of spontaneous metastases was seen in this model, we decided to experimentally induce metastasis in CD1 nude mice in order to assess if the V3L and S5L are able to survive in vessels, extravasate and colonise distant tissues. Our data suggest that neither of these cell lines can survive in blood vessels (tail vein injections); extravasate from blood vessels (tail vein injections and splenic injections); or establish growth at specific sites i.e. liver, lungs and lymph nodes. However, it is possible that the strain of mouse used affected the results obtained. Thus, as all of these experiments were conducted in the CD1 nude mouse, they could be repeated in a different immunodeficient mouse strain in order to evaluate if this affected the occurrence of metastasis or not.

Thus, although the data from the *in vivo* studies clearly show a role for S100P in accelerating primary pancreatic tumour growth, and although there is evidence that S100P is involved in the process of communication between carcinoma cells and the

lymphatic endothelium, these data do not support a causative role for S100P in inducing lymphatic and/or haematological metastasis.

8. CONCLUDING REMARKS

Although lymphatic invasion is known to be an early and important step in the dissemination of PDAC, few studies have analysed the molecular mechanisms underlying this process (66,67,69–72). Only one previous study had examined this process at a protein level, by analysing primary pancreatic tumours using MALDI-TOF and correlating the data obtained to clinicopathological parameters (72). For that reason, we sought to analyse the molecular mechanisms underlying lymphatic invasion in PDAC using a shotgun proteomics approach. This is the first study to analyse the metastatic LN from patients with resectable PDAC; to compare protein expression from primary PDAC epithelia to protein expression in LN metastatic epithelia; and to use LCM FFPE tissue samples for the proteomic investigation of metastatic PDAC.

From our analysis, we were able to validate that two candidate molecules, S100P and 14-3-3 sigma, were up-regulated significantly in LN metastases relative to primary PDAC. As the study was performed on tissue which had been fixed at a specific point in disease progression however, it is important to note that these findings could be co-incidental, and do not imply a causative role for either of these proteins in PDAC pathogenesis. Further investigation would be required in order to prove a causal association. Regardless, both of these molecules represent viable therapeutic targets. These data have been published (226), and will be made available to the general public through the Pancreatic Expression Database (188).

Due to its well-established role in PanIN progression and PDAC in human tissue samples (91,93), and based on previously published data supporting a causative role for S100P in PDAC invasion both *in vitro* and *in vivo* (92,94–97), we went on to investigate the roles of S100P in lymphatic invasion in PDAC.

This is the first study to attempt to co-culture pancreatic cancer cell lines with HDLEC, and to use these co-cultures to investigate the interactions of pancreatic cancer cells with lymphatic endothelial cells. Furthermore, it is the first study to look specifically at the effects of S100P over-expression on the adhesion of pancreatic cancer cells to HDLEC; on permeability through a HDLEC monolayer; and on TLEM. We feel that the data arising from these studies are promising in some regards, though disappointing in others. Using the V3L and S5L cell lines, we were able to show that S100P over-expression alters the molecules involved in adhesion to resting and activated HDLEC, and increases permeability and TLEM through a HDLEC monolayer. Further work, however, is required both to confirm that these data are of a general significance (e.g. by repeating the experiments using addition pancreatic cancer cell lines which express high levels of endogenous S100P), and to prove that these functional changes are mediated by S100P specifically (e.g. using siRNA knockdown). So far, however, the data seem to suggest a causative role for S100P in lymphovascular invasion.

This conclusion was challenged by our *in vivo* data. Whilst we were able to show that S100P over-expression accelerates primary pancreatic tumour growth, we were not able to demonstrate that S100P over-expression causes spontaneous lymphatic and/or haematological metastasis. Furthermore, although lymphovascular invasion

was noted in primary tumours, this was seen in both V3L and S5L orthotopic tumours to the same extent. In addition, the experimental metastasis and site-specific growth experiments did not result in growth in the lungs, liver and/or LN. Thus, we conclude that S100P alone does not cause lymphatic invasion in the CD1 nude mouse. It is possible that the strain of mouse used affected the outcome, and thus, these experiments would need to be confirmed in a different immunodeficient mouse strain, before concluding that they are a true representation of the impact of S100P expression on *in vivo* behaviour.

Finally, we were able to develop a CD1 nude orthotopic mouse model that can be used for the preclinical evaluation of novel therapies targeting S100P in our laboratory. Specifically, this model can be used to assess the effects of such therapies on primary tumour growth and this, in itself, might well be a useful system to exploit in seeking novel anti-PDAC therapeutic approaches.

9. REFERENCES

1. Jemal A, Siegel R, Ward E, Murray T, Xu J, Thun MJ. Cancer statistics, 2007. CA Cancer J Clin. 2007;57:43–66.

2. Parkin DM, Bray F, Ferlay J, Pisani P. Global cancer statistics, 2002. CA Cancer J Clin. 2005;55:74–108.

3. Hruban RH, Goggins M, Parsons J, Kern SE. Progression model for pancreatic cancer. Clin Cancer Res. 2000;6:2969–72.

4. Hruban RH, Adsay NV, Albores-Saavedra J, Compton C, Garrett ES, Goodman SN, et al. Pancreatic intraepithelial neoplasia: a new nomenclature and classification system for pancreatic duct lesions. Am J Surg Pathol. 2001;25:579–86.

5. Kumar V. Robbins and Cotran's pathologic basis of disease. 7th ed. /. Philadelphia Pa. ;;London: Elsevier Saunders; 2004.

6. van Heek NT, Meeker AK, Kern SE, Yeo CJ, Lillemoe KD, Cameron JL, et al. Telomere shortening is nearly universal in pancreatic intraepithelial neoplasia. Am. J. Pathol. 2002 Nov;161(5):1541–7.

7. Harley C. Telomeres and telomerase in aging and cancer. Current Opinion in Genetics & Development. 1995 Apr;5:249–55.

8. Weinberg R. The biology of cancer. New York: Garland Science; 2007.

9. Hackett JA, Greider CW. Balancing instability: dual roles for telomerase and telomere dysfunction in tumorigenesis. Oncogene. 2002 Jan 21;21(4):619–26.

10. Gisselsson D. Telomere dysfunction triggers extensive DNA fragmentation and evolution of complex chromosome abnormalities in human malignant tumors. Proceedings of the National Academy of Sciences. 2001 Oct 2;98:12683–8.

11. McClintock B. The Stability of Broken Ends of Chromosomes in Zea Mays. Genetics. 1941;26(2):234–82.

12. O'Hagan RC, Chang S, Maser RS, Mohan R, Artandi SE, Chin L, et al. Telomere dysfunction provokes regional amplification and deletion in cancer genomes. Cancer Cell. 2002 Aug;2(2):149–55.

13. Artandi SE, Chang S, Lee SL, Alson S, Gottlieb GJ, Chin L, et al. Telomere dysfunction promotes non-reciprocal translocations and epithelial cancers in mice. Nature. 2000 Aug 10;406(6796):641–5.

14. Rudolph KL, Millard M, Bosenberg MW, DePinho RA. Telomere dysfunction and evolution of intestinal carcinoma in mice and humans. Nat. Genet. 2001 Jun;28(2):155–9.

15. Grochola L-F, Greither T, Taubert HW, Möller P, Knippschild U, Udelnow A, et al. Prognostic relevance of hTERT mRNA expression in ductal adenocarcinoma of the pancreas. Neoplasia. 2008 Sep;10(9):973–6.

16. Hashimoto Y, Murakami Y, Uemura K, Hayashidani Y, Sudo T, Ohge H, et al. Detection of human telomerase reverse transcriptase (hTERT) expression in tissue and pancreatic juice from pancreatic cancer. Surgery. 2008 Jan;143:113–25.

17. Nakashima A, Murakami Y, Uemura K, Hayashidani Y, Sudo T, Hashimoto Y, et al. Usefulness of human telomerase reverse transcriptase in pancreatic juice as a biomarker of pancreatic malignancy. Pancreas. 2009 Jul;38(5):527–33.

18. Argilla D, Chin K, Singh M, Hodgson JG, Bosenberg M, de Solórzano CO, et al. Absence of telomerase and shortened telomeres have minimal effects on skin and pancreatic carcinogenesis elicited by viral oncogenes. Cancer Cell. 2004 Oct;6(4):373–85.

19. Chin L, Artandi SE, Shen Q, Tam A, Lee SL, Gottlieb GJ, et al. p53 deficiency rescues the adverse effects of telomere loss and cooperates with telomere dysfunction to accelerate carcinogenesis. Cell. 1999 May 14;97(4):527–38.

20. Day JD, Digiuseppe JA, Yeo C, Lai-Goldman M, Anderson SM, Goodman SN, et al. Immunohistochemical evaluation of HER-2/neu expression in pancreatic adenocarcinoma and pancreatic intraepithelial neoplasms. Hum Pathol. 1996;27:119–24.

21. Apple SK, Hecht JR, Lewin DN, Jahromi SA, Grody WW, Nieberg RK. Immunohistochemical evaluation of K-ras, p53, and HER-2/neu expression in hyperplastic, dysplastic, and carcinomatous lesions of the pancreas: evidence for multistep carcinogenesis. Hum. Pathol. 1999 Feb;30(2):123–9.

22. Satoh K, Sasano H, Shimosegawa T, Koizumi M, Yamazaki T, Mochizuki F, et al. An immunohistochemical study of the c-erbB-2 oncogene product in intraductal mucin-hypersecreting neoplasms and in ductal cell carcinomas of the pancreas. Cancer. 1993;72:51–6.

23. Saxby AJ, Nielsen A, Scarlett CJ, Clarkson A, Morey A, Gill A, et al. Assessment of HER-2 status in pancreatic adenocarcinoma: correlation of immunohistochemistry, quantitative real-time RT-PCR, and FISH with aneuploidy and survival. Am. J. Surg. Pathol. 2005 Sep;29(9):1125–34.

24. Vernimmen D, Gueders M, Pisvin S, Delvenne P, Winkler R. Different mechanisms are implicated in ERBB2 gene overexpression in breast and in other cancers. Br. J. Cancer. 2003 Sep 1;89(5):899–906.

25. Tsiambas E, Karameris A, Dervenis C, Lazaris AC, Giannakou N, Gerontopoulos K, et al. HER2/neu expression and gene alterations in pancreatic ductal adenocarcinoma: a comparative immunohistochemistry and chromogenic in situ hybridization study based on tissue microarrays and computerized image analysis. JOP. 2006;7(3):283–94.

26. Komoto M, Nakata B, Amano R, Yamada N, Yashiro M, Ohira M, et al. HER2 overexpression correlates with survival after curative resection of pancreatic cancer. Cancer Science. 2009 Jul;100(7):1243–7.

27. Bergmann F, Moldenhauer G, Herpel E, Gaida MM, Strobel O, Werner J, et al. Expression of L1CAM, COX-2, EGFR, c-KIT and Her2/neu in anaplastic pancreatic cancer: putative therapeutic targets? Histopathology. 2010 Mar;56(4):440–8.

28. Bekaii-Saab TS, Roda JM, Guenterberg KD, Ramaswamy B, Young DC, Ferketich AK, et al. A phase I trial of paclitaxel and trastuzumab in combination with interleukin-12 in patients with HER2/neu-expressing malignancies. Mol. Cancer Ther. 2009 Nov;8(11):2983–91.

29. Smit VT, Boot AJ, Smits AM, Fleuren GJ, Cornelisse CJ, Bos JL. KRAS codon 12 mutations occur very frequently in pancreatic adenocarcinomas. Nucleic Acids Res. 1988 Aug 25;16(16):7773–82.

30. Hingorani SR, Petricoin EF, Maitra A, Rajapakse V, King C, Jacobetz MA, et al. Preinvasive and invasive ductal pancreatic cancer and its early detection in the mouse. Cancer Cell. 2003 Dec;4(6):437–50.

31. Park SW, Davison JM, Rhee J, Hruban RH, Maitra A, Leach SD. Oncogenic KRAS Induces Progenitor Cell Expansion and Malignant Transformation in Zebrafish Exocrine Pancreas. Gastroenterology. 2008 Jun;134(7):2080–90.

32. Shi C, Hong S-M, Lim P, Kamiyama H, Khan M, Anders RA, et al. KRAS2 Mutations in Human Pancreatic Acinar-Ductal Metaplastic Lesions Are Limited to Those with PanIN: Implications for the Human Pancreatic Cancer Cell of Origin. Molecular Cancer Research. 2009 Feb;7(2):230–6.

33. Feldmann G, Beaty R, Hruban RH, Maitra A. Molecular genetics of pancreatic intraepithelial neoplasia. Journal of Hepato-Biliary-Pancreatic Surgery. 2007 May 29;14:224–32.

34. Caldas C, Hahn SA, da Costa LT, Redston MS, Schutte M, Seymour AB, et al. Frequent somatic mutations and homozygous deletions of the p16 (MTS1) gene in pancreatic adenocarcinoma. Nat. Genet. 1994 Sep;8(1):27–32.

35. Schutte M, Hruban RH, Geradts J, Maynard R, Hilgers W, Rabindran SK, et al. Abrogation of the Rb/p16 tumor-suppressive pathway in virtually all pancreatic carcinomas. Cancer Res. 1997 Aug 1;57(15):3126–30.

36. Ueki T, Toyota M, Sohn T, Yeo CJ, Issa JP, Hruban RH, et al. Hypermethylation of multiple genes in pancreatic adenocarcinoma. Cancer Res. 2000 Apr 1;60(7):1835–9.

37. Wilentz RE, Geradts J, Maynard R, Offerhaus GJ, Kang M, Goggins M, et al. Inactivation of the p16 (INK4A) tumor-suppressor gene in pancreatic duct lesions: loss of intranuclear expression. Cancer Res. 1998 Oct 15;58(20):4740–4.

38. Redston MS, Caldas C, Seymour AB, Hruban RH, da Costa L, Yeo CJ, et al. p53 mutations in pancreatic carcinoma and evidence of common involvement of homocopolymer tracts in DNA microdeletions. Cancer Res. 1994 Jun 1;54(11):3025–33.

39. Vogelstein B, Kinzler KW. Cancer genes and the pathways they control. Nat. Med. 2004 Aug;10(8):789–99.

40. Hingorani SR, Wang L, Multani AS, Combs C, Deramaudt TB, Hruban RH, et al. Trp53R172H and KrasG12D cooperate to promote chromosomal instability and widely metastatic pancreatic ductal adenocarcinoma in mice. Cancer Cell. 2005 May;7(5):469–83.

41. Maitra A, Adsay NV, Argani P, Iacobuzio-Donahue C, De Marzo A, Cameron JL, et al. Multicomponent analysis of the pancreatic adenocarcinoma progression model using a pancreatic intraepithelial neoplasia tissue microarray. Mod. Pathol. 2003 Sep;16(9):902–12.

42. Hahn SA, Schutte M, Hoque AT, Moskaluk CA, da Costa LT, Rozenblum E, et al. DPC4, a candidate tumor suppressor gene at human chromosome 18q21.1. Science. 1996 Jan 19;271(5247):350–3.

43. Wilentz RE, Iacobuzio-Donahue CA, Argani P, McCarthy DM, Parsons JL, Yeo CJ, et al. Loss of expression of Dpc4 in pancreatic intraepithelial neoplasia: evidence that DPC4 inactivation occurs late in neoplastic progression. Cancer Res. 2000 Apr 1;60(7):2002–6.

44. Aguirre AJ, Bardeesy N, Sinha M, Lopez L, Tuveson DA, Horner J, et al. Activated Kras and Ink4a/Arf deficiency cooperate to produce metastatic pancreatic ductal adenocarcinoma. Genes Dev. 2003 Dec 15;17(24):3112–26.

45. Izeradjene K, Combs C, Best M, Gopinathan A, Wagner A, Grady WM, et al. Kras(G12D) and Smad4/Dpc4 haploinsufficiency cooperate to induce mucinous cystic neoplasms and invasive adenocarcinoma of the pancreas. Cancer Cell. 2007 Mar;11(3):229–43.

46. Fidler IJ. Timeline: The pathogenesis of cancer metastasis: the ‘seed and soil’ hypothesis revisited. Nat Rev Cancer. 2003 Jun;3(6):453–8.

47. Fidler IJ, Kripke ML. Metastasis results from preexisting variant cells within a malignant tumor. Science. 1977;197:893–5.

48. Fidler IJ, Hart IR. Biological diversity in metastatic neoplasms: origins and implications. Science. 1982;217:998–1003.

49. Jones S, Chen WD, Parmigiani G, Diehl F, Beerenwinkel N, Antal T, et al. Comparative lesion sequencing provides insights into tumor evolution. Proc Natl Acad Sci U S A. 2008;105:4283–8.

50. Ramaswamy S, Ross KN, Lander ES, Golub TR. A molecular signature of metastasis in primary solid tumors. Nat Genet. 2003;33:49–54.

51. Hanahan D, Weinberg RA. The hallmarks of cancer. Cell. 2000 Jan 7;100(1):57–70.

52. Fidler IJ, Kripke ML. Genomic analysis of primary tumors does not address the prevalence of metastatic cells in the population. Nat Genet. 2003;34:23; author reply 25.

53. Bernards R, Weinberg RA. A progression puzzle. Nature. 2002;418:823.

54. Klein CA. Parallel progression of primary tumours and metastases. Nat Rev Cancer. 2009;9:302–12.

55. Klein CA, Blankenstein TJF, Schmidt-Kittler O, Petronio M, Polzer B, Stoecklein NH, et al. Genetic heterogeneity of single disseminated tumour cells in minimal residual cancer. Lancet. 2002 Aug 31;360(9334):683–9.

56. Klein CA, Seidl S, Petat-Dutter K, Offner S, Geigl JB, Schmidt-Kittler O, et al. Combined transcriptome and genome analysis of single micrometastatic cells. Nat. Biotechnol. 2002 Apr;20(4):387–92.

57. Klein CA, Schmidt-Kittler O, Schardt JA, Pantel K, Speicher MR, Riethmüller G. Comparative genomic hybridization, loss of heterozygosity, and DNA sequence analysis of single cells. Proc. Natl. Acad. Sci. U.S.A. 1999 Apr 13;96(8):4494–9.

58. Schlimok G, Funke I, Holzmann B, Göttlinger G, Schmidt G, Häuser H, et al. Micrometastatic cancer cells in bone marrow: in vitro detection with anti-cytokeratin and in vivo labeling with anti-17-1A monoclonal antibodies. Proc. Natl. Acad. Sci. U.S.A. 1987 Dec;84(23):8672–6.

59. Schmidt-Kittler O, Ragg T, Daskalakis A, Granzow M, Ahr A, Blankenstein TJF, et al. From latent disseminated cells to overt metastasis: genetic analysis of systemic breast cancer progression. Proc. Natl. Acad. Sci. U.S.A. 2003 Jun 24;100(13):7737–42.

60. Stoecklein NH, Hosch SB, Bezler M, Stern F, Hartmann CH, Vay C, et al. Direct genetic analysis of single disseminated cancer cells for prediction of outcome and therapy selection in esophageal cancer. Cancer Cell. 2008 May;13(5):441–53.

61. Weckermann D, Polzer B, Ragg T, Blana A, Schlimok G, Arnholdt H, et al. Perioperative activation of disseminated tumor cells in bone marrow of patients with prostate cancer. J. Clin. Oncol. 2009 Apr 1;27(10):1549–56.

62. Husemann Y, Geigl JB, Schubert F, Musiani P, Meyer M, Burghart E, et al. Systemic spread is an early step in breast cancer. Cancer Cell. 2008;13:58–68.

63. Podsypanina K, Du YC, Jechlinger M, Beverly LJ, Hambardzumyan D, Varmus H. Seeding and propagation of untransformed mouse mammary cells in the lung. Science. 2008;321:1841–4.

64. Paget S. The distribution of secondary growths in cancer of the breast. 1889. Cancer Metastasis Rev. 1989;8:98–101.

65. Embuscado EE, Laheru D, Ricci F, Yun KJ, de Boom Witzel S, Seigel A, et al. Immortalizing the complexity of cancer metastasis: genetic features of lethal metastatic pancreatic cancer obtained from rapid autopsy. Cancer Biol Ther. 2005;4:548–54.

66. Nakamura T, Furukawa Y, Nakagawa H, Tsunoda T, Ohigashi H, Murata K, et al. Genome-wide cDNA microarray analysis of gene expression profiles in pancreatic cancers using populations of tumor cells and normal ductal epithelial cells selected for purity by laser microdissection. Oncogene. 2004;23:2385–400.

67. Kim HN, Choi DW, Lee KT, Lee JK, Heo JS, Choi SH, et al. Gene expression profiling in lymph node-positive and lymph node-negative pancreatic cancer. Pancreas. 2007;34:325–34.

68. Jones S, Zhang X, Parsons DW, Lin JC, Leary RJ, Angenendt P, et al. Core signaling pathways in human pancreatic cancers revealed by global genomic analyses. Science. 2008;321:1801–6.

69. Campagna D, Cope L, Lakkur SS, Henderson C, Laheru D, Iacobuzio-Donahue CA. Gene expression profiles associated with advanced pancreatic cancer. Int J Clin Exp Pathol. 2008;1:32–43.

70. Yachida S, Jones S, Bozic I, Antal T, Leary R, Fu B, et al. Distant metastasis occurs late during the genetic evolution of pancreatic cancer. Nature. 2010;467:1114–7.

71. Campbell PJ, Yachida S, Mudie LJ, Stephens PJ, Pleasance ED, Stebbings LA, et al. The patterns and dynamics of genomic instability in metastatic pancreatic cancer. Nature. 2010;467:1109–13.

72. Cui Y, Wu J, Zong M, Song G, Jia Q, Jiang J, et al. Proteomic profiling in pancreatic cancer with and without lymph node metastasis. Int J Cancer. 2009;124:1614–21.

73. Hood BL, Darfler MM, Guiel TG, Furusato B, Lucas DA, Ringeisen BR, et al. Proteomic analysis of formalin-fixed prostate cancer tissue. Mol. Cell Proteomics. 2005 Nov;4(11):1741–53.

74. Guo T, Wang W, Rudnick PA, Song T, Li J, Zhuang Z, et al. Proteome analysis of microdissected formalin-fixed and paraffin-embedded tissue specimens. J Histochem Cytochem. 2007;55:763–72.

75. Nirmalan NJ, Harnden P, Selby PJ, Banks RE. Mining the archival formalin-fixed paraffin-embedded tissue proteome: opportunities and challenges. Mol Biosyst. 2008;4:712–20.

76. Scicchitano MS, Dalmas DA, Boyce RW, Thomas HC, Frazier KS. Protein extraction of formalin-fixed, paraffin-embedded tissue enables robust proteomic profiles by mass spectrometry. J Histochem Cytochem. 2009;57:849–60.

77. Sprung RW, Brock JW, Tanksley JP, Li M, Washington MK, Slebos RJ, et al. Equivalence of protein inventories obtained from formalin-fixed paraffin-

embedded and frozen tissue in multidimensional liquid chromatography-tandem mass spectrometry shotgun proteomic analysis. Mol Cell Proteomics. 2009;8:1988–98.

78. Reimel BA, Pan S, May DH, Shaffer SA, Goodlett DR, McIntosh MW, et al. Proteomics on Fixed Tissue Specimens - A Review. Curr Proteomics. 2009;6:63–9.

79. Prieto DA, Hood BL, Darfler MM, Guiel TG, Lucas DA, Conrads TP, et al. Liquid Tissue: proteomic profiling of formalin-fixed tissues. Biotechniques. 2005;Suppl:32–5.

80. Patel V, Hood BL, Molinolo AA, Lee NH, Conrads TP, Braisted JC, et al. Proteomic analysis of laser-captured paraffin-embedded tissues: a molecular portrait of head and neck cancer progression. Clin Cancer Res. 2008;14:1002–14.

81. Yates JR, Ruse CI, Nakorchevsky A. Proteomics by Mass Spectrometry: Approaches, Advances, and Applications. Annual Review of Biomedical Engineering. 2009;11:49–79.

82. Cagney G, Park S, Chung C, Tong B, O'Dushlaine C, Shields DC, et al. Human tissue profiling with multidimensional protein identification technology. J Proteome Res. 2005;4:1757–67.

83. Delahunty CM, Yates JR. MudPIT: multidimensional protein identification technology. Biotechniques. 2007;43:563, 565, 567 passim.

84. Wolters DA, Washburn MP, Yates JR. An automated multidimensional protein identification technology for shotgun proteomics. Anal Chem. 2001;73:5683–90.

85. Lim MS, Elenitoba-Johnson KSJ. Proteomics in pathology research. Lab. Invest. 2004 Oct;84(10):1227–44.

86. Whitelegge JP. Plant proteomics: BLASTing out of a MudPIT. Proc. Natl. Acad. Sci. U.S.A. 2002 Sep 3;99(18):11564–6.

87. Alves P, Arnold RJ, Novotny MV, Radivojac P, Reilly JP, Tang H. Advancement in protein inference from shotgun proteomics using peptide detectability. Pac Symp Biocomput. 2007;409–20.

88. Tang H, Arnold RJ, Alves P, Xun Z, Clemmer DE, Novotny MV, et al. A computational approach toward label-free protein quantification using predicted peptide detectability. Bioinformatics. 2006 Jul 15;22(14):e481–488.

89. Liu H, Sadygov RG, Yates JR. A model for random sampling and estimation of relative protein abundance in shotgun proteomics. Anal Chem. 2004;76:4193–201.

90. Zhang B, VerBerkmoes NC, Langston MA, Uberbacher E, Hettich RL, Samatova NF. Detecting differential and correlated protein expression in label-free shotgun proteomics. J Proteome Res. 2006;5:2909–18.

91. Crnogorac-Jurcevic T, Missiaglia E, Blaveri E, Gangeswaran R, Jones M, Terris B, et al. Molecular alterations in pancreatic carcinoma: expression profiling shows that dysregulated expression of S100 genes is highly prevalent. J. Pathol. 2003 Sep;201(1):63–74.

92. Dowen SE, Crnogorac-Jurcevic T, Gangeswaran R, Hansen M, Eloranta JJ, Bhakta V, et al. Expression of S100P and its novel binding partner S100PBPR in early pancreatic cancer. Am J Pathol. 2005;166:81–92.

93. Logsdon CD, Simeone DM, Binkley C, Arumugam T, Greenson JK, Giordano TJ, et al. Molecular profiling of pancreatic adenocarcinoma and chronic pancreatitis identifies multiple genes differentially regulated in pancreatic cancer. Cancer Res. 2003 May 15;63(10):2649–57.

94. Whiteman HJ, Weeks ME, Dowen SE, Barry S, Timms JF, Lemoine NR, et al. The role of S100P in the invasion of pancreatic cancer cells is mediated through cytoskeletal changes and regulation of cathepsin D. Cancer Res. 2007;67:8633–42.

95. Arumugam T, Simeone DM, Van Golen K, Logsdon CD. S100P promotes pancreatic cancer growth, survival, and invasion. Clin. Cancer Res. 2005 Aug 1;11(15):5356–64.

96. Arumugam T, Ramachandran V, Logsdon CD. Effect of cromolyn on S100P interactions with RAGE and pancreatic cancer growth and invasion in mouse models. J. Natl. Cancer Inst. 2006 Dec 20;98(24):1806–18.

97. Arumugam T, Simeone DM, Schmidt AM, Logsdon CD. S100P stimulates cell proliferation and survival via receptor for activated glycation end products (RAGE). J. Biol. Chem. 2004 Feb 13;279(7):5059–65.

98. Butler MG, Isogai S, Weinstein BM. Lymphatic development. Birth Defects Res C Embryo Today. 2009;87:222–31.

99. Tammela T, Alitalo K. Lymphangiogenesis: Molecular mechanisms and future promise. Cell. 2010;140:460–76.

100. Hosking B, Makinen T. Lymphatic vasculature: a molecular perspective. Bioessays. 2007;29:1192–202.

101. Banerji S, Ni J, Wang SX, Clasper S, Su J, Tammi R, et al. LYVE-1, a new homologue of the CD44 glycoprotein, is a lymph-specific receptor for hyaluronan. J. Cell Biol. 1999 Feb 22;144(4):789–801.

102. Nightingale TD, Frayne MEF, Clasper S, Banerji S, Jackson DG. A Mechanism of Sialylation Functionally Silences the Hyaluronan Receptor LYVE-1 in Lymphatic Endothelium. Journal of Biological Chemistry. 2008 Dec;284(6):3935–45.

103. Gale NW, Prevo R, Espinosa J, Ferguson DJ, Dominguez MG, Yancopoulos GD, et al. Normal Lymphatic Development and Function in Mice Deficient for

the Lymphatic Hyaluronan Receptor LYVE-1. Molecular and Cellular Biology. 2006 Nov;27(2):595–604.

104. Johnson LA, Prevo R, Clasper S, Jackson DG. Inflammation-induced Uptake and Degradation of the Lymphatic Endothelial Hyaluronan Receptor LYVE-1. Journal of Biological Chemistry. 2007 Sep;282(46):33671–80.

105. Wicki A, Christofori G. The potential role of podoplanin in tumour invasion. Br J Cancer. 2006 Dec;96(1):1–5.

106. Schacht V, Ramirez MI, Hong Y-K, Hirakawa S, Feng D, Harvey N, et al. T1alpha/podoplanin deficiency disrupts normal lymphatic vasculature formation and causes lymphedema. EMBO J. 2003 Jul 15;22(14):3546–56.

107. Bertozzi CC, Schmaier AA, Mericko P, Hess PR, Zou Z, Chen M, et al. Platelets regulate lymphatic vascular development through CLEC-2-SLP-76 signaling. Blood. 2010 Apr;116(4):661–70.

108. Uhrin P, Zaujec J, Breuss JM, Olcaydu D, Chrenek P, Stockinger H, et al. Novel function for blood platelets and podoplanin in developmental separation of blood and lymphatic circulation. Blood. 2010 Jan;115(19):3997–4005.

109. Kato Y, Kaneko M, Sata M, Fujita N, Tsuruo T, Osawa M. Enhanced expression of Aggrus (T1alpha/podoplanin), a platelet-aggregation-inducing factor in lung squamous cell carcinoma. Tumour Biol. 2005 Aug;26(4):195–200.

110. Kimura N, Kimura I. Podoplanin as a marker for mesothelioma. Pathol. Int. 2005 Feb;55(2):83–6.

111. Martín-Villar E, Scholl FG, Gamallo C, Yurrita MM, Muñoz-Guerra M, Cruces J, et al. Characterization of human PA2.26 antigen (T1alpha-2, podoplanin), a small membrane mucin induced in oral squamous cell carcinomas. Int. J. Cancer. 2005 Mar 1;113(6):899–910.

112. Schacht V, Dadras SS, Johnson LA, Jackson DG, Hong Y-K, Detmar M. Up-regulation of the lymphatic marker podoplanin, a mucin-type transmembrane glycoprotein, in human squamous cell carcinomas and germ cell tumors. Am. J. Pathol. 2005 Mar;166(3):913–21.

113. Shibahara J, Kashima T, Kikuchi Y, Kunita A, Fukayama M. Podoplanin is expressed in subsets of tumors of the central nervous system. Virchows Arch. 2006 Apr;448(4):493–9.

114. Wicki A, Lehembre F, Wick N, Hantusch B, Kerjaschki D, Christofori G. Tumor invasion in the absence of epithelial-mesenchymal transition: podoplanin-mediated remodeling of the actin cytoskeleton. Cancer Cell. 2006 Apr;9(4):261–72.

115. Martín-Villar E, Megías D, Castel S, Yurrita MM, Vilaró S, Quintanilla M. Podoplanin binds ERM proteins to activate RhoA and promote epithelial-mesenchymal transition. J. Cell. Sci. 2006 Nov 1;119(Pt 21):4541–53.

116. Mishima K, Watabe T, Saito A, Yoshimatsu Y, Imaizumi N, Masui S, et al. Prox1 induces lymphatic endothelial differentiation via integrin alpha9 and other signaling cascades. Mol. Biol. Cell. 2007 Apr;18(4):1421–9.

117. Witte MH, Jones K, Wilting J, Dictor M, Selg M, McHale N, et al. Structure function relationships in the lymphatic system and implications for cancer biology. Cancer Metastasis Rev. 2006 Jun;25(2):159–84.

118. Baluk P, Fuxe J, Hashizume H, Romano T, Lashnits E, Butz S, et al. Functionally specialized junctions between endothelial cells of lymphatic vessels. J Exp Med. 2007;204:2349–62.

119. McCloskey KD, Hollywood MA, Thornbury KD, Ward SM, McHale NG. Kit-like immunopositive cells in sheep mesenteric lymphatic vessels. Cell Tissue Res. 2002 Oct;310(1):77–84.

120. McCloskey KD, Toland HM, Hollywood MA, Thornbury KD, McHale NG. Hyperpolarisation-activated inward current in isolated sheep mesenteric lymphatic smooth muscle. J. Physiol. (Lond.). 1999 Nov 15;521 Pt 1:201–11.

121. McHale NG, Meharg MK. Co-ordination of pumping in isolated bovine lymphatic vessels. J. Physiol. (Lond.). 1992 May;450:503–12.

122. Moore K. Clinically oriented anatomy. 5th ed. Philadelphia: Lippincott Williams & Wilkins; 2006.

123. van der Putte SC. The development of the lymphatic system in man. Adv Anat Embryol Cell Biol. 1975;51(1):3–60.

124. Sabin FR. On the origin of the lymphatic system from the veins and the development of the lymph hearts and thoracic duct in the pig. American Journal of Anatomy. 1902 May 26;1:367–89.

125. Karkkainen MJ, Mäkinen T, Alitalo K. Lymphatic endothelium: a new frontier of metastasis research. Nat. Cell Biol. 2002 Jan;4(1):E2–5.

126. Joukov V, Kumar V, Sorsa T, Arighi E, Weich H, Saksela O, et al. A recombinant mutant vascular endothelial growth factor-C that has lost vascular endothelial growth factor receptor-2 binding, activation, and vascular permeability activities. J. Biol. Chem. 1998 Mar 20;273(12):6599–602.

127. Bazigou E, Xie S, Chen C, Weston A, Miura N, Sorokin L, et al. Integrin-alpha9 is required for fibronectin matrix assembly during lymphatic valve morphogenesis. Dev Cell. 2009;17:175–86.

128. Huntington G. The genetic interpretation of the development of the mammalian lymphatic system. Anat Rec. 1908;2:19–46.

129. Wilting J, Papoutsi M, Schneider M, Christ B. The lymphatic endothelium of the avian wing is of somitic origin. Dev. Dyn. 2000 Mar;217(3):271–8.

130. Wilting J, Aref Y, Huang R, Tomarev SI, Schweigerer L, Christ B, et al. Dual origin of avian lymphatics. Dev. Biol. 2006 Apr 1;292(1):165–73.

131. Paupert J, Sounni NE, Noël A. Lymphangiogenesis in post-natal tissue remodeling: Lymphatic endothelial cell connection with its environment. Molecular Aspects of Medicine. 2011 Apr;32(2):146–58.

132. Podgrabinska S, Braun P, Velasco P, Kloos B, Pepper MS, Skobe M. Molecular characterization of lymphatic endothelial cells. Proc. Natl. Acad. Sci. U.S.A. 2002 Dec 10;99(25):16069–74.

133. Helm C-LE, Zisch A, Swartz MA. Engineered blood and lymphatic capillaries in 3-D VEGF-fibrin-collagen matrices with interstitial flow. Biotechnol. Bioeng. 2007 Jan 1;96(1):167–76.

134. Brideau G, Mäkinen MJ, Elamaa H, Tu H, Nilsson G, Alitalo K, et al. Endostatin overexpression inhibits lymphangiogenesis and lymph node metastasis in mice. Cancer Res. 2007 Dec 15;67(24):11528–35.

135. Kojima T, Azar DT, Chang J-H. Neostatin-7 regulates bFGF-induced corneal lymphangiogenesis. FEBS Lett. 2008 Jul 23;582(17):2515–20.

136. Sironen RK, Tammi M, Tammi R, Auvinen PK, Anttila M, Kosma V-M. Hyaluronan in human malignancies. Experimental Cell Research. 2011 Feb;317(4):383–91.

137. Ou J-J, Wu F, Liang H-J. Colorectal tumor derived fibronectin alternatively spliced EDA domain exserts lymphangiogenic effect on human lymphatic endothelial cells. Cancer Biol. Ther. 2010 Feb;9(3):186–91.

140. Hynes RO. Cell-matrix adhesion in vascular development. J. Thromb. Haemost. 2007 Jul;5 Suppl 1:32–40.

141. Hynes RO, Bader BL, Hodivala-Dilke K. Integrins in vascular development. Braz. J. Med. Biol. Res. 1999 May;32(5):501–10.

142. Hynes RO. Integrins: bidirectional, allosteric signaling machines. Cell. 2002 Sep 20;110(6):673–87.

143. Hynes RO. The emergence of integrins: a personal and historical perspective. Matrix Biol. 2004 Oct;23(6):333–40.

144. Garmy-Susini B, Avraamides CJ, Schmid MC, Foubert P, Ellies LG, Barnes L, et al. Integrin alpha4beta1 signaling is required for lymphangiogenesis and tumor metastasis. Cancer Res. 2010;70:3042–51.

145. Kocher HM, Sohail M, Benjamin IS, Patel AG. Technical limitations of lymph node mapping in pancreatic cancer. European Journal of Surgical Oncology (EJSO). 2007 Sep;33(7):887–91.

146. Pai RK, Beck AH, Mitchem J, Linehan DC, Chang DT, Norton JA, et al. Pattern of lymph node involvement and prognosis in pancreatic

adenocarcinoma: direct lymph node invasion has similar survival to node-negative disease. Am. J. Surg. Pathol. 2011 Feb;35(2):228–34.

147. Friedl P, Wolf K. Tumour-cell invasion and migration: diversity and escape mechanisms. Nat Rev Cancer. 2003;3:362–74.

148. Willms-Kretschmer K, Flax MH, Cotran RS. The fine structure of the vascular response in hapten-specific delayed hypersensitivity and contact dermatitis. Lab Invest. 1967;17:334–49.

149. Pober JS. Warner-Lambert/Parke-Davis award lecture. Cytokine-mediated activation of vascular endothelium. Physiology and pathology. Am J Pathol. 1988;133:426–33.

150. Hunt BJ, Jurd KM. Endothelial cell activation. A central pathophysiological process. BMJ. 1998;316:1328–9.

151. Johnson LA, Clasper S, Holt AP, Lalor PF, Baban D, Jackson DG. An inflammation-induced mechanism for leukocyte transmigration across lymphatic vessel endothelium. J Exp Med. 2006;203:2763–77.

152. Kawai Y, Kaidoh M, Ohhashi T. MDA-MB-231 produces ATP-mediated ICAM-1-dependent facilitation of the attachment of carcinoma cells to human lymphatic endothelial cells. AJP: Cell Physiology. 2008 Sep;295(5):C1123–C1132.

153. Irjala H, Alanen K, Grénman R, Heikkilä P, Joensuu H, Jalkanen S. Mannose receptor (MR) and common lymphatic endothelial and vascular endothelial receptor (CLEVER)-1 direct the binding of cancer cells to the lymph vessel endothelium. Cancer Res. 2003 Aug 1;63(15):4671–6.

154. Salmi M. CLEVER-1 mediates lymphocyte transmigration through vascular and lymphatic endothelium. Blood. 2004 Dec;104(13):3849–57.

155. Shields JD, Emmett MS, Dunn DBA, Joory KD, Sage LM, Rigby H, et al. Chemokine-mediated migration of melanoma cells towards lymphatics--a mechanism contributing to metastasis. Oncogene. 2007 May 10;26(21):2997–3005.

156. Skobe M, Hamberg LM, Hawighorst T, Schirner M, Wolf GL, Alitalo K, et al. Concurrent induction of lymphangiogenesis, angiogenesis, and macrophage recruitment by vascular endothelial growth factor-C in melanoma. Am. J. Pathol. 2001 Sep;159(3):893–903.

157. Skobe M, Hawighorst T, Jackson DG, Prevo R, Janes L, Velasco P, et al. Induction of tumor lymphangiogenesis by VEGF-C promotes breast cancer metastasis. Nat. Med. 2001 Feb;7(2):192–8.

158. He Y, Rajantie I, Pajusola K, Jeltsch M, Holopainen T, Yla-Herttuala S, et al. Vascular endothelial cell growth factor receptor 3-mediated activation of lymphatic endothelium is crucial for tumor cell entry and spread via lymphatic vessels. Cancer Res. 2005 Jun 1;65(11):4739–46.

159. Issa A, Le TX, Shoushtari AN, Shields JD, Swartz MA. Vascular Endothelial Growth Factor-C and C-C Chemokine Receptor 7 in Tumor Cell-Lymphatic Cross-talk Promote Invasive Phenotype. Cancer Research. 2009 Jan;69(1):349–57.

160. Mandriota SJ, Jussila L, Jeltsch M, Compagni A, Baetens D, Prevo R, et al. Vascular endothelial growth factor-C-mediated lymphangiogenesis promotes tumour metastasis. EMBO J. 2001 Feb 15;20(4):672–82.

161. Kopfstein L, Veikkola T, Djonov VG, Baeriswyl V, Schomber T, Strittmatter K, et al. Distinct roles of vascular endothelial growth factor-D in lymphangiogenesis and metastasis. Am. J. Pathol. 2007 Apr;170(4):1348–61.

162. Tang RF, Itakura J, Aikawa T, Matsuda K, Fujii H, Korc M, et al. Overexpression of lymphangiogenic growth factor VEGF-C in human pancreatic cancer. Pancreas. 2001 Apr;22(3):285–92.

163. Kurahara H, Takao S, Maemura K, Shinchi H, Natsugoe S, Aikou T. Impact of vascular endothelial growth factor-C and -D expression in human pancreatic cancer: its relationship to lymph node metastasis. Clin. Cancer Res. 2004 Dec 15;10(24):8413–20.

164. Schneider M, Büchler P, Giese N, Giese T, Wilting J, Büchler MW, et al. Role of lymphangiogenesis and lymphangiogenic factors during pancreatic cancer progression and lymphatic spread. Int. J. Oncol. 2006 Apr;28(4):883–90.

165. Sipos B, Kojima M, Tiemann K, Klapper W, Kruse ML, Kalthoff H, et al. Lymphatic spread of ductal pancreatic adenocarcinoma is independent of lymphangiogenesis. J Pathol. 2005;207:301–12.

166. Beasley NJP, Prevo R, Banerji S, Leek RD, Moore J, van Trappen P, et al. Intratumoral lymphangiogenesis and lymph node metastasis in head and neck cancer. Cancer Res. 2002 Mar 1;62(5):1315–20.

167. Hall FT, Freeman JL, Asa SL, Jackson DG, Beasley NJ. Intratumoral lymphatics and lymph node metastases in papillary thyroid carcinoma. Arch. Otolaryngol. Head Neck Surg. 2003 Jul;129(7):716–9.

168. Kyzas PA, Geleff S, Batistatou A, Agnantis NJ, Stefanou D. Evidence for lymphangiogenesis and its prognostic implications in head and neck squamous cell carcinoma. J. Pathol. 2005 Jun;206(2):170–7.

169. Bailey JM, Mohr AM, Hollingsworth MA. Sonic hedgehog paracrine signaling regulates metastasis and lymphangiogenesis in pancreatic cancer. Oncogene. 2009;28:3513–25.

170. Schulz P, Scholz A, Rexin A, Hauff P, Schirner M, Wiedenmann B, et al. Inducible re-expression of p16 in an orthotopic mouse model of pancreatic cancer inhibits lymphangiogenesis and lymphatic metastasis. Br J Cancer. 2008;99:110–7.

171. Marincola FM, Drucker BJ, Siao DY, Hough KL, Holder WD Jr. The nude mouse as a model for the study of human pancreatic cancer. J. Surg. Res. 1989 Dec;47(6):520–9.

172. Loukopoulos P, Kanetaka K, Takamura M, Shibata T, Sakamoto M, Hirohashi S. Orthotopic transplantation models of pancreatic adenocarcinoma derived from cell lines and primary tumors and displaying varying metastatic activity. Pancreas. 2004;29:193–203.

173. Partecke LI, Sendler M, Kaeding A, Weiss FU, Mayerle J, Dummer A, et al. A syngeneic orthotopic murine model of pancreatic adenocarcinoma in the C57/BL6 mouse using the Panc02 and 6606PDA cell lines. Eur Surg Res. 2011;47(2):98–107.

174. Vonlaufen A, Joshi S, Qu C, Phillips PA, Xu Z, Parker NR, et al. Pancreatic stellate cells: partners in crime with pancreatic cancer cells. Cancer Res. 2008 Apr 1;68(7):2085–93.

175. Xu Z, Vonlaufen A, Phillips PA, Fiala-Beer E, Zhang X, Yang L, et al. Role of pancreatic stellate cells in pancreatic cancer metastasis. Am. J. Pathol. 2010 Nov;177(5):2585–96.

176. Fu X, Guadagni F, Hoffman RM. A metastatic nude-mouse model of human pancreatic cancer constructed orthotopically with histologically intact patient specimens. Proc. Natl. Acad. Sci. U.S.A. 1992 Jun 15;89(12):5645–9.

177. Fidler IJ, Hart IR. Biological diversity in metastatic neoplasms: origins and implications. Science. 1982 Sep 10;217(4564):998–1003.

178. Nicolson GL, Brunson KW, Fidler IJ. Specificity of arrest, survival, and growth of selected metastatic variant cell lines. Cancer Res. 1978 Nov;38(11 Pt 2):4105–11.

179. Nicolson GL. Metastatic tumor cell attachment and invasion assay utilizing vascular endothelial cell monolayers. J. Histochem. Cytochem. 1982 Mar;30(3):214–20.

180. Giavazzi R, Campbell DE, Jessup JM, Cleary K, Fidler IJ. Metastatic behavior of tumor cells isolated from primary and metastatic human colorectal carcinomas implanted into different sites in nude mice. Cancer Res. 1986;46:1928–33.

181. Jimenez RE, Hartwig W, Antoniu BA, Compton CC, Warshaw AL, Fernández-Del Castillo C. Effect of matrix metalloproteinase inhibition on pancreatic cancer invasion and metastasis: an additive strategy for cancer control. Ann. Surg. 2000 May;231(5):644–54.

182. Foster PJ, Dunn EA, Karl KE, Snir JA, Nycz CM, Harvey AJ, et al. Cellular magnetic resonance imaging: in vivo imaging of melanoma cells in lymph nodes of mice. Neoplasia. 2008 Mar;10(3):207–16.

183. Ntziachristos V, Ripoll J, Wang LV, Weissleder R. Looking and listening to light: the evolution of whole-body photonic imaging. Nature Biotechnology. 2005 Mar;23:313–20.

184. Bouvet M, Yang M, Nardin S, Wang X, Jiang P, Baranov E, et al. Chronologically-specific metastatic targeting of human pancreatic tumors in orthotopic models. Clin. Exp. Metastasis. 2000;18(3):213–8.

185. Bouvet M, Wang J, Nardin SR, Nassirpour R, Yang M, Baranov E, et al. Real-time optical imaging of primary tumor growth and multiple metastatic events in a pancreatic cancer orthotopic model. Cancer Res. 2002 Mar 1;62(5):1534–40.

186. Kwon S, Davies-Venn C, Sevick-Muraca EM. In vivo dynamic imaging of intestinal motions using diet-related autofluorescence. Neurogastroenterology & Motility. 2012 May;24(5):494–7.

187. Allred DC, Harvey JM, Berardo M, Clark GM. Prognostic and predictive factors in breast cancer by immunohistochemical analysis. Mod Pathol. 1998;11:155–68.

188. Chelala C, Hahn SA, Whiteman HJ, Barry S, Hariharan D, Radon TP, et al. Pancreatic Expression database: a generic model for the organization, integration and mining of complex cancer datasets. BMC Genomics. 2007;8:439.

189. Ghaemmaghami S, Huh WK, Bower K, Howson RW, Belle A, Dephoure N, et al. Global analysis of protein expression in yeast. Nature. 2003;425:737–41.

190. van Hemert MJ, Steensma HY, van Heusden GP. 14-3-3 proteins: key regulators of cell division, signalling and apoptosis. Bioessays. 2001 Oct;23(10):936–46.

191. Okada T, Masuda N, Fukai Y, Shimura T, Nishida Y, Hosouchi Y, et al. Immunohistochemical expression of 14-3-3 sigma protein in intraductal papillary-mucinous tumor and invasive ductal carcinoma of the pancreas. Anticancer Res. 2006 Aug;26(4B):3105–10.

192. Zervos EE, Tanner SM, Osborne DA, Bloomston M, Rosemurgy AS, Ellison EC, et al. Differential gene expression in patients genetically predisposed to pancreatic cancer. J. Surg. Res. 2006 Oct;135(2):317–22.

193. Sitek B, Sipos B, Alkatout I, Poschmann G, Stephan C, Schulenborg T, et al. Analysis of the Pancreatic Tumor Progression by a Quantitative Proteomic Approach and Immunhistochemical Validation. Journal of Proteome Research. 2009 Apr 3;8:1647–56.

194. Morrison DK. The 14-3-3 proteins: integrators of diverse signaling cues that impact cell fate and cancer development. Trends Cell Biol. 2009;19:16–23.

195. Siman R, McIntosh TK, Soltesz KM, Chen Z, Neumar RW, Roberts VL. Proteins released from degenerating neurons are surrogate markers for acute brain damage. Neurobiol. Dis. 2004 Jul;16(2):311–20.

196. Ghahary A, Marcoux Y, Karimi-Busheri F, Li Y, Tredget EE, Kilani RT, et al. Differentiated keratinocyte-releasable stratifin (14-3-3 sigma) stimulates MMP-1 expression in dermal fibroblasts. J. Invest. Dermatol. 2005 Jan;124(1):170–7.

197. Ghaffari A, Li Y, Karami A, Ghaffari M, Tredget EE, Ghahary A. Fibroblast extracellular matrix gene expression in response to keratinocyte-releasable stratifin. J. Cell. Biochem. 2006 May 15;98(2):383–93.

198. Medina A, Ghaffari A, Kilani RT, Ghahary A. The role of stratifin in fibroblast-keratinocyte interaction. Mol. Cell. Biochem. 2007 Nov;305(1-2):255–64.

199. Heil A, Nazmi AR, Koltzscher M, Poeter M, Austermann J, Assard N, et al. S100P is a novel interaction partner and regulator of IQGAP1. J Biol Chem. 286:7227–38.

200. White CD, Brown MD, Sacks DB. IQGAPs in cancer: a family of scaffold proteins underlying tumorigenesis. FEBS Lett. 2009;583:1817–24.

201. Koltzscher M, Neumann C, König S, Gerke V. Ca2+-dependent binding and activation of dormant ezrin by dimeric S100P. Mol. Biol. Cell. 2003 Jun;14(6):2372–84.

202. Austermann J, Nazmi AR, Muller-Tidow C, Gerke V. Characterization of the Ca2+-regulated Ezrin-S100P Interaction and Its Role in Tumor Cell Migration. Journal of Biological Chemistry. 2008 Aug 20;283:29331–40.

203. Shang X, Cheng H, Zhou R. Chromosomal mapping, differential origin and evolution of the S100 gene family. Genet. Sel. Evol. 2008 Aug;40(4):449–64.

204. Kulbe H, Thompson R, Wilson JL, Robinson S, Hagemann T, Fatah R, et al. The Inflammatory Cytokine Tumor Necrosis Factor- Generates an Autocrine Tumor-Promoting Network in Epithelial Ovarian Cancer Cells. Cancer Research. 2007 Jan 15;67:585–92.

205. Gaggioli C, Hooper S, Hidalgo-Carcedo C, Grosse R, Marshall JF, Harrington K, et al. Fibroblast-led collective invasion of carcinoma cells with differing roles for RhoGTPases in leading and following cells. Nat. Cell Biol. 2007 Dec;9(12):1392–400.

206. Dejana E. Endothelial cell–cell junctions: happy together. Nature Reviews Molecular Cell Biology. 2004 Apr;5(4):261–70.

207. Guelte A, Dwyer J, Gavard J. Jumping the barrier: VE-cadherin, VEGF and other angiogenic modifiers in cancer. Biology of the Cell. 2011 Dec;103(12):593–605.

208. Wojciak-Stothard B, Ridley AJ. Rho GTPases and the regulation of endothelial permeability. Vascular Pharmacology. 2002 Nov;39(4-5):187–99.

209. Carmeliet P, Lampugnani MG, Moons L, Breviario F, Compernolle V, Bono F, et al. Targeted deficiency or cytosolic truncation of the VE-cadherin gene in

mice impairs VEGF-mediated endothelial survival and angiogenesis. Cell. 1999 Jul 23;98(2):147–57.

210. Lampugnani MG, Orsenigo F, Gagliani MC, Tacchetti C, Dejana E. Vascular endothelial cadherin controls VEGFR-2 internalization and signaling from intracellular compartments. J. Cell Biol. 2006 Aug 14;174(4):593–604.

211. Eliceiri BP, Paul R, Schwartzberg PL, Hood JD, Leng J, Cheresh DA. Selective requirement for Src kinases during VEGF-induced angiogenesis and vascular permeability. Mol. Cell. 1999 Dec;4(6):915–24.

212. Gavard J, Gutkind JS. VEGF controls endothelial-cell permeability by promoting the beta-arrestin-dependent endocytosis of VE-cadherin. Nat. Cell Biol. 2006 Nov;8(11):1223–34.

213. Wallez Y, Cand F, Cruzalegui F, Wernstedt C, Souchelnytskyi S, Vilgrain I, et al. Src kinase phosphorylates vascular endothelial-cadherin in response to vascular endothelial growth factor: identification of tyrosine 685 as the unique target site. Oncogene. 2007 Feb 15;26(7):1067–77.

214. Lampugnani MG, Zanetti A, Breviario F, Balconi G, Orsenigo F, Corada M, et al. VE-cadherin regulates endothelial actin activating Rac and increasing membrane association of Tiam. Mol. Biol. Cell. 2002 Apr;13(4):1175–89.

215. Kouklis P, Konstantoulaki M, Malik AB. VE-cadherin-induced Cdc42 signaling regulates formation of membrane protrusions in endothelial cells. J. Biol. Chem. 2003 May 2;278(18):16230–6.

216. Cai J, Jiang WG, Mansel RE. Phosphorylation and disorganization of vascular-endothelial cadherin in interaction between breast cancer and vascular endothelial cells. Int. J. Mol. Med. 1999 Aug;4(2):191–5.

217. Nakai K, Tanaka T, Murai T, Ohguro N, Tano Y, Miyasaka M. Invasive human pancreatic carcinoma cells adhere to endothelial tri-cellular corners and increase endothelial permeability. Cancer Sci. 2005 Nov;96(11):766–73.

218. Ding Z, Liu Z, Bi Y, Tian H, Li G, Song T. Morphological study of the interaction between M21 melanoma and lymphatic endothelium. Lymphology. 2005 Jun;38(2):87–91.

219. Karin M, Cao Y, Greten FR, Li Z-W. NF-κB IN CANCER: FROM INNOCENT BYSTANDER TO MAJOR CULPRIT. Nature Reviews Cancer. 2002 Apr 1;2:301–10.

220. Zhang L, Underhill CB, Chen L. Hyaluronan on the surface of tumor cells is correlated with metastatic behavior. Cancer Res. 1995 Jan 15;55(2):428–33.

221. Fujisaki T, Tanaka Y, Fujii K, Mine S, Saito K, Yamada S, et al. CD44 stimulation induces integrin-mediated adhesion of colon cancer cell lines to endothelial cells by up-regulation of integrins and c-Met and activation of integrins. Cancer Res. 1999 Sep 1;59(17):4427–34.

222. Simpson MA. Manipulation of Hyaluronan Synthase Expression in Prostate Adenocarcinoma Cells Alters Pericellular Matrix Retention and Adhesion to Bone Marrow Endothelial Cells. Journal of Biological Chemistry. 2002 Jan 14;277(12):10050–7.

223. Nourshargh S, Hordijk PL, Sixt M. Breaching multiple barriers: leukocyte motility through venular walls and the interstitium. Nature Reviews Molecular Cell Biology. 2010 May;11:366–78.

224. Hiratsuka S, Watanabe A, Aburatani H, Maru Y. Tumour-mediated upregulation of chemoattractants and recruitment of myeloid cells predetermines lung metastasis. Nat. Cell Biol. 2006 Dec;8(12):1369–75.

225. Talmadge JE, Singh RK, Fidler IJ, Raz A. Murine models to evaluate novel and conventional therapeutic strategies for cancer. Am. J. Pathol. 2007 Mar;170(3):793–804.

226. Naidoo K, Jones R, Dmitrovic B, Wijesuriya N, Kocher H, Hart IR, et al. Proteome of formalin-fixed paraffin-embedded pancreatic ductal adenocarcinoma and lymph node metastases. The Journal of Pathology. 2011;n/a-n/a.

Appendix I

Appendix I tabulates the 854 proteome of PDAC and matched LN metastases in alphabetical order (MW = molecular weight).

Identified Proteins	Accession No.	MW
- 22 kDa protein	IPI00219910	22 kDa
A1BG Alpha-1B-glycoprotein	IPI00022895	54 kDa
A2M Alpha-2-macroglobulin	IPI00478003	163 kDa
AARS Alanyl-tRNA synthetase, cytoplasmic	IPI00027442	107 kDa
ABCF1 Isoform 1 of ATP-binding cassette sub-family F member 1	IPI00873899	96 kDa
ABHD11 Isoform 4 of Abhydrolase domain-containing protein 11	IPI00171152	34 kDa
ABHD14B Isoform 1 of Abhydrolase domain-containing protein 14B	IPI00063827	22 kDa
ABLIM1 Isoform 1 of Actin-binding LIM protein 1	IPI00329495	88 kDa
ACAA2 3-ketoacyl-CoA thiolase, mitochondrial	IPI00001539	42 kDa
ACADVL cDNA FLJ56425, highly similar to Very-long-chain specific acyl-CoAdehydrogenase, mitochondrial	IPI00028031	75 kDa
ACAT1 Acetyl-CoA acetyltransferase, mitochondrial	IPI00030363	45 kDa
ACBD3 Golgi resident protein GCP60	IPI00009315	61 kDa
ACO2 Aconitate hydratase, mitochondrial	IPI00017855	85 kDa
ACOT2 Isoform 1 of Acyl-coenzyme A thioesterase 2, mitochondrial	IPI00220906	53 kDa
ACP1 Isoform 2 of Low molecular weight phosphotyrosine protein phosphatase	IPI00218847	18 kDa
ACTB Actin, cytoplasmic 1	IPI00021439	42 kDa
ACTN1 Alpha-actinin-1	IPI00013508	103 kDa
ACTN4 Alpha-actinin-4	IPI00013808	105 kDa
ACTR2 Actin-related protein 2	IPI00005159	45 kDa
ACTR3 Actin-related protein 3	IPI00028091	47 kDa
ADAM10 ADAM 10	IPI00013897	84 kDa
ADD1 Isoform 1 of Alpha-adducin	IPI00019901	81 kDa
AEBP1 Isoform 1 of Adipocyte enhancer-binding protein 1	IPI00745313	131 kDa
AFG3L2 AFG3-like protein 2	IPI00001091	89 kDa
AGR2 AGR2	IPI00007427	22 kDa
AGRN Agrin	IPI00374563	215 kDa
AHCY Adenosylhomocysteinase	IPI00012007	48 kDa
AHNAK Neuroblast differentiation-associated protein AHNAK	IPI00021812	629 kDa
AHNAK2 Isoform 1 of Protein AHNAK2	IPI00856045	617 kDa
AIFM1 Isoform 1 of Apoptosis-inducing factor 1, mitochondrial	IPI00000690	67 kDa
AK2 Isoform 3 of Adenylate kinase isoenzyme 2, mitochondrial	IPI00172460	22 kDa
AK3 GTP:AMP phosphotransferase mitochondrial	IPI00465256	26 kDa

AKR1A1 Alcohol dehydrogenase [NADP+]	IPI00220271	37 kDa
AKR1B1 Aldose reductase	IPI00413641	36 kDa
AKR1B10 Aldo-keto reductase family 1 member B10	IPI00105407	36 kDa
AKR1C1 Aldo-keto reductase family 1 member C1	IPI00029733	37 kDa
AKR7A2 Aflatoxin B1 aldehyde reductase member 2	IPI00305978	40 kDa
AKR7A3 Aflatoxin B1 aldehyde reductase member 3	IPI00293721	37 kDa
ALB Isoform 1 of Serum albumin	IPI00745872	69 kDa
ALDH18A1 Isoform Long of Delta-1-pyrroline-5-carboxylate synthetase	IPI00008982	87 kDa
ALDH1A1 Retinal dehydrogenase 1	IPI00218914	55 kDa
ALDH2 Aldehyde dehydrogenase, mitochondrial	IPI00006663	56 kDa
ALDH7A1 aldehyde dehydrogenase 7 family, member A1	IPI00221234	58 kDa
ALDH9A1 aldehyde dehydrogenase 9A1	IPI00479877	56 kDa
ALDOA Fructose-bisphosphate aldolase A	IPI00465439	39 kDa
ALDOC Fructose-bisphosphate aldolase C	IPI00418262	39 kDa
ANP32B Isoform 1 of Acidic leucine-rich nuclear phosphoprotein 32 family member B	IPI00007423	29 kDa
ANXA1 Annexin A1	IPI00218918	39 kDa
ANXA10 Annexin A10	IPI00296528	37 kDa
ANXA2 Annexin A2	IPI00455315	39 kDa
ANXA3 Annexin A3	IPI00024095	36 kDa
ANXA4 annexin IV	IPI00793199	36 kDa
ANXA5 Annexin A5	IPI00329801	36 kDa
ANXA6 annexin VI isoform 2	IPI00002459	75 kDa
AP1M2 Isoform 1 of AP-1 complex subunit mu-2	IPI00002552	48 kDa
AP2A1 Isoform B of AP-2 complex subunit alpha-1	IPI00256684	105 kDa
AP2B1 Isoform 1 of AP-2 complex subunit beta-1	IPI00784156	105 kDa
APEH Acylamino-acid-releasing enzyme	IPI00337741	81 kDa
APEX1 DNA-(apurinic or apyrimidinic site) lyase	IPI00215911	36 kDa
APOA1 Apolipoprotein A-I	IPI00021841	31 kDa
APRT Adenine phosphoribosyltransferase	IPI00218693	20 kDa
ARCN1 Putative uncharacterized protein DKFZp686M09245	IPI00298520	62 kDa
ARF1 ADP-ribosylation factor 1	IPI00215914	21 kDa
ARF4 ADP-ribosylation factor 4	IPI00215918	21 kDa
ARHGAP1 cDNA FLJ60782, highly similar to Rho-GTPase-activating protein 1	IPI00020567	53 kDa
ARPC1B Actin-related protein 2/3 complex subunit 1B	IPI00005160	41 kDa
ARPC2 Actin-related protein 2/3 complex subunit 2	IPI00005161	34 kDa
ARPC3 Actin-related protein 2/3 complex subunit 3	IPI00005162	21 kDa
ARPC5 Isoform 1 of Actin-related protein 2/3 complex subunit 5	IPI00550234	16 kDa
ASL Argininosuccinate lyase	IPI00220267	52 kDa
ASS1 Argininosuccinate synthase	IPI00020632	51 kDa
ATIC Bifunctional purine biosynthesis protein PURH	IPI00289499	65 kDa
ATL3 Isoform 1 of Atlastin-3	IPI00550523	61 kDa
ATP1A1 Isoform Long of Sodium/potassium-transporting ATPase subunit alpha-1	IPI00006482	113 kDa
ATP1B1 Isoform 1 of Sodium/potassium-transporting ATPase subunit beta-1	IPI00747849	35 kDa

ATP2A2 Isoform SERCA2A of Sarcoplasmic/endoplasmic reticulum calcium ATPase 2	IPI00177817	110 kDa
ATP5A1 ATP synthase subunit alpha, mitochondrial	IPI00440493	60 kDa
ATP5B ATP synthase subunit beta, mitochondrial	IPI00303476	57 kDa
ATP5F1 ATP synthase subunit b, mitochondrial	IPI00029133	29 kDa
ATP5H Isoform 1 of ATP synthase subunit d, mitochondrial	IPI00220487	18 kDa
ATP5O ATP synthase subunit O, mitochondrial	IPI00007611	23 kDa
ATP6V1A V-type proton ATPase catalytic subunit A	IPI00007682	68 kDa
ATP6V1B2 V-type proton ATPase subunit B, brain isoform	IPI00007812	57 kDa
B2M Beta-2-microglobulin	IPI00004656	14 kDa
BAIAP2L1 Brain-specific angiogenesis inhibitor 1-associated protein 2-like protein 1	IPI00179326	57 kDa
BCAP31 B-cell receptor-associated protein 31	IPI00218200	28 kDa
BCAS1 Isoform 1 of Breast carcinoma-amplified sequence 1	IPI00025311	62 kDa
BGN Biglycan	IPI00010790	42 kDa
BLVRA Biliverdin reductase A	IPI00294158	33 kDa
BPNT1 Isoform 1 of 3'(2'),5'-bisphosphate nucleotidase 1	IPI00410214	33 kDa
BUB3 Mitotic checkpoint protein BUB3	IPI00013468	37 kDa
C17orf28 Isoform 3 of UPF0663 transmembrane protein C17orf28	IPI00247634	63 kDa
C19orf21 Uncharacterized protein C19orf21	IPI00217121	75 kDa
C21orf33 Isoform Long of ES1 protein homolog, mitochondrial	IPI00024913	28 kDa
C22orf28 UPF0027 protein C22orf28	IPI00550689	55 kDa
C3 Complement C3 (Fragment)	IPI00783987	187 kDa
C4A Complement C4-A	IPI00032258	193 kDa
CA2 Carbonic anhydrase 2	IPI00218414	29 kDa
CALD1 Isoform 4 of Caldesmon	IPI00218696	63 kDa
CALM3;CALM1;CALM2 Calmodulin	IPI00075248	17 kDa
CALR Calreticulin	IPI00020599	48 kDa
CAND1 Isoform 1 of Cullin-associated NEDD8-dissociated protein 1	IPI00100160	136 kDa
CANX cDNA FLJ55574, highly similar to Calnexin	IPI00020984	72 kDa
CAP1 Isoform 1 of Adenylyl cyclase-associated protein 1	IPI00008274	52 kDa
CAPG Macrophage-capping protein	IPI00027341	39 kDa
CAPN1 Calpain-1 catalytic subunit	IPI00011285	82 kDa
CAPN2 Calpain-2 catalytic subunit	IPI00289758	80 kDa
CAPNS1 Calpain small subunit 1	IPI00025084	28 kDa
CAPZA1 F-actin-capping protein subunit alpha-1	IPI00005969	33 kDa
CAT Catalase	IPI00465436	60 kDa
CBR1 Carbonyl reductase [NADPH] 1	IPI00295386	30 kDa
CCDC109A Isoform 1 of Coiled-coil domain-containing protein 109A	IPI00171573	40 kDa
CCDC6 Coiled-coil domain-containing protein 6	IPI00000634	66 kDa
CCT2 T-complex protein 1 subunit beta	IPI00297779	57 kDa
CCT3 chaperonin containing TCP1, subunit 3 isoform b	IPI00290770	60 kDa
CCT4 T-complex protein 1 subunit delta	IPI00302927	58 kDa
CCT5 T-complex protein 1 subunit epsilon	IPI00010720	60 kDa
CCT6A T-complex protein 1 subunit zeta	IPI00027626	58 kDa

CCT7 T-complex protein 1 subunit eta	IPI00018465	59 kDa
CCT8 59 kDa protein	IPI00302925	59 kDa
CD44 Isoform 12 of CD44 antigen	IPI00297160	39 kDa
CD63 CD63 antigen	IPI00215998	26 kDa
CDH1 Cadherin 1, type 1, E-cadherin (Epithelial), isoform CRA_c	IPI00000513	91 kDa
CEACAM5 Carcinoembryonic antigen-related cell adhesion molecule 5	IPI00027486	77 kDa
CFL1 Cofilin-1	IPI00012011	19 kDa
CGN cingulin	IPI00844508	137 kDa
CHD4 Isoform 1 of Chromodomain-helicase-DNA-binding protein 4	IPI00000846	218 kDa
CHMP4B Charged multivesicular body protein 4b	IPI00025974	25 kDa
CKAP4 Isoform 1 of Cytoskeleton-associated protein 4	IPI00141318	66 kDa
CLIC1 Chloride intracellular channel protein 1	IPI00010896	27 kDa
CLIC3 Chloride intracellular channel protein 3	IPI00000692	27 kDa
CLPTM1 Isoform 2 of Cleft lip and palate transmembrane protein 1	IPI00107357	78 kDa
CLTC Isoform 1 of Clathrin heavy chain 1	IPI00024067	192 kDa
CMPK1 cytidine monophosphate (UMP-CMP) kinase 1, cytosolic isoform a	IPI00219953	26 kDa
CNDP2 Cytosolic non-specific dipeptidase	IPI00177728	53 kDa
CNN1 Calponin-1	IPI00021264	33 kDa
CNN3 Calponin-3	IPI00216682	36 kDa
CNP Isoform CNPI of 2',3'-cyclic-nucleotide 3'-phosphodiesterase	IPI00220993	45 kDa
COL12A1 Isoform 4 of Collagen alpha-1(XII) chain	IPI00302944	325 kDa
COL14A1 Isoform 1 of Collagen alpha-1(XIV) chain	IPI00176193	194 kDa
COL18A1 Isoform 2 of Collagen alpha-1(XVIII) chain	IPI00022822	154 kDa
COL1A1 Collagen alpha-1(I) chain	IPI00297646	139 kDa
COL1A2 Collagen alpha-2(I) chain	IPI00304962	129 kDa
COL3A1 Isoform 1 of Collagen alpha-1(III) chain	IPI00021033	139 kDa
COL4A1 Putative uncharacterized protein COL4A1	IPI00743696	161 kDa
COL4A2 Collagen alpha-2(IV) chain	IPI00306322	168 kDa
COL6A1 Collagen alpha-1(VI) chain	IPI00291136	109 kDa
COL6A2 Isoform 2C2 of Collagen alpha-2(VI) chain	IPI00304840	109 kDa
COL6A3 Isoform 1 of Collagen alpha-3(VI) chain	IPI00022200	344 kDa
COPA Isoform 1 of Coatomer subunit alpha	IPI00295857	138 kDa
COPB1 Coatomer subunit beta	IPI00295851	107 kDa
COPB2 Coatomer subunit beta'	IPI00220219	102 kDa
COPE epsilon subunit of coatomer protein complex isoform c	IPI00399319	29 kDa
COPG Coatomer subunit gamma	IPI00783982	98 kDa
CORO7 Coronin-7	IPI00027996	101 kDa
COTL1 Coactosin-like protein	IPI00017704	16 kDa
COX4I1 Cytochrome c oxidase subunit 4 isoform 1, mitochondrial	IPI00006579	20 kDa
COX5A Cytochrome c oxidase subunit 5A, mitochondrial	IPI00025086	17 kDa
CP Ceruloplasmin	IPI00017601	122 kDa
CPNE3 Copine-3	IPI00024403	60 kDa
CPT1A Isoform 1 of Carnitine O-palmitoyltransferase 1, liver isoform	IPI00032038	88 kDa
CPT2 Carnitine O-palmitoyltransferase 2, mitochondrial	IPI00012912	74 kDa

CRYZ Quinone oxidoreductase	IPI00000792	35 kDa
CS Citrate synthase, mitochondrial	IPI00025366	52 kDa
CSDE1 Isoform Long of Cold shock domain-containing protein E1	IPI00470891	89 kDa
CSE1L Isoform 1 of Exportin-2	IPI00022744	110 kDa
CSRP1 Cysteine and glycine-rich protein 1	IPI00442073	21 kDa
CSTB Cystatin-B	IPI00021828	11 kDa
CTNNA1 Isoform 1 of Catenin alpha-1	IPI00215948	100 kDa
CTNNB1 Isoform 1 of Catenin beta-1	IPI00017292	85 kDa
CTNND1 Isoform 1AB of Catenin delta-1	IPI00182469	107 kDa
CTSD Cathepsin D	IPI00011229	45 kDa
CTSG Cathepsin G	IPI00028064	29 kDa
CTSZ Cathepsin Z	IPI00002745	34 kDa
CTTN Src substrate cortactin	IPI00029601	62 kDa
CYB5A Isoform 2 of Cytochrome b5	IPI00182933	11 kDa
CYB5R1 NADH-cytochrome b5 reductase 1	IPI00470674	34 kDa
CYB5R3 Isoform 1 of NADH-cytochrome b5 reductase 3	IPI00328415	34 kDa
CYCS Cytochrome c	IPI00465315	12 kDa
CYFIP1 Isoform 1 of Cytoplasmic FMR1-interacting protein 1	IPI00644231	145 kDa
CYP2S1 Isoform 2 of Cytochrome P450 2S1	IPI00164018	62 kDa
DAK Dihydroxyacetone kinase	IPI00551024	59 kDa
DARS Aspartyl-tRNA synthetase, cytoplasmic	IPI00216951	57 kDa
DBN1 Isoform 1 of Drebrin	IPI00003406	71 kDa
DBNL Isoform 3 of Drebrin-like protein	IPI00101968	49 kDa
DCD Dermcidin	IPI00027547	11 kDa
DCN Isoform A of Decorin	IPI00012119	40 kDa
DCXR L-xylulose reductase	IPI00448095	26 kDa
DDAH1 N(G),N(G)-dimethylarginine dimethylaminohydrolase 1	IPI00220342	31 kDa
DDAH2 N(G),N(G)-dimethylarginine dimethylaminohydrolase 2	IPI00000760	30 kDa
DDOST dolichyl-diphosphooligosaccharide-protein glycosyltransferase precursor	IPI00297084	51 kDa
DDRGK1 Isoform 1 of Uncharacterized protein C20orf116	IPI00028387	36 kDa
DDX17 DEAD box polypeptide 17 isoform 1	IPI00023785	80 kDa
DDX21 Isoform 1 of Nucleolar RNA helicase 2	IPI00015953	87 kDa
DDX23 Probable ATP-dependent RNA helicase DDX23	IPI00006725	96 kDa
DDX6 Probable ATP-dependent RNA helicase DDX6	IPI00030320	54 kDa
DEFA1;LOC728358 Neutrophil defensin 1	IPI00005721	10 kDa
DHRS4 peroxisomal short-chain alcohol dehydrogenase	IPI00106913	30 kDa
DHX15 Putative pre-mRNA-splicing factor ATP-dependent RNA helicase DHX15	IPI00396435	91 kDa
DHX9 ATP-dependent RNA helicase A	IPI00844578	141 kDa
DLD Dihydrolipoyl dehydrogenase, mitochondrial	IPI00015911	54 kDa
DLST Dihydrolipoyllysine-residue succinyltransferase component of 2-oxoglutarate dehydrogenase complex, mitochondrial	IPI00420108	49 kDa
DMBT1 Isoform 1 of Deleted in malignant brain tumors 1 protein	IPI00099110	261 kDa
DMD Isoform 4 of Dystrophin	IPI00006091	427 kDa

DNAJA1 DnaJ homolog subfamily A member 1	IPI00012535	45 kDa
DNAJB1 DnaJ homolog subfamily B member 1	IPI00015947	38 kDa
DNPEP aspartyl aminopeptidase	IPI00015856	53 kDa
DPP3 Isoform 1 of Dipeptidyl-peptidase 3	IPI00020672	83 kDa
DPYSL2 Dihydropyrimidinase-related protein 2	IPI00257508	62 kDa
DPYSL3 DPYSL3 protein	IPI00029111	74 kDa
DSG2 Desmoglein-2	IPI00028931	122 kDa
DSP Isoform DPI of Desmoplakin	IPI00013933	332 kDa
DYNC1H1 Cytoplasmic dynein 1 heavy chain 1	IPI00456969	532 kDa
DYNC1I2 Isoform 2C of Cytoplasmic dynein 1 intermediate chain 2	IPI00216348	68 kDa
ECH1 Delta(3,5)-Delta(2,4)-dienoyl-CoA isomerase, mitochondrial	IPI00011416	36 kDa
ECHS1 Enoyl-CoA hydratase, mitochondrial	IPI00024993	31 kDa
EEA1 Early endosome antigen 1	IPI00329536	162 kDa
EEF1A1 Elongation factor 1-alpha 1	IPI00396485	50 kDa
EEF1D Elongation factor 1-delta	IPI00023048	31 kDa
EEF1G cDNA FLJ56389, highly similar to Elongation factor 1-gamma	IPI00000875	56 kDa
EEF2 Elongation factor 2	IPI00186290	95 kDa
EFHD2 EF-hand domain-containing protein D2	IPI00060181	27 kDa
EFTUD2 116 kDa U5 small nuclear ribonucleoprotein component	IPI00003519	109 kDa
EHD1 EH domain-containing protein 1	IPI00017184	61 kDa
EHD2 EH domain-containing protein 2	IPI00100980	61 kDa
EIF2S1 Eukaryotic translation initiation factor 2 subunit 1	IPI00219678	36 kDa
EIF2S3 Eukaryotic translation initiation factor 2 subunit 3	IPI00297982	51 kDa
EIF3A Eukaryotic translation initiation factor 3 subunit A	IPI00029012	167 kDa
EIF3B Isoform 1 of Eukaryotic translation initiation factor 3 subunit B	IPI00396370	92 kDa
EIF3C;EIF3CL Eukaryotic translation initiation factor 3 subunit C	IPI00016910	105 kDa
EIF3D Eukaryotic translation initiation factor 3 subunit D	IPI00006181	64 kDa
EIF3EIP Eukaryotic translation initiation factor 3, subunit E interacting protein	IPI00465233	71 kDa
EIF3I Eukaryotic translation initiation factor 3 subunit I	IPI00012795	37 kDa
EIF4A3 Eukaryotic initiation factor 4A-III	IPI00009328	47 kDa
EIF4B cDNA FLJ54492, highly similar to Eukaryotic translation initiation factor 4B	IPI00012079	70 kDa
EIF4G1 eukaryotic translation initiation factor 4 gamma, 1 isoform 2	IPI00384463	167 kDa
ELAVL1 cDNA FLJ60076, highly similar to ELAV-like protein 1	IPI00301936	39 kDa
EMILIN1 EMILIN-1	IPI00013079	107 kDa
EML4 Echinoderm microtubule-associated protein-like 4	IPI00001466	109 kDa
ENO1 Isoform alpha-enolase of Alpha-enolase	IPI00465248	47 kDa
ENO2 Gamma-enolase	IPI00216171	47 kDa
EPB41L2 Band 4.1-like protein 2	IPI00015973	113 kDa
EPHX1 Epoxide hydrolase 1	IPI00009896	53 kDa
EPPK1 epiplakin 1	IPI00010951	556 kDa
EPRS Bifunctional aminoacyl-tRNA synthetase	IPI00013452	171 kDa
EPS8 Epidermal growth factor receptor kinase substrate 8	IPI00290337	92 kDa
EPS8L1 Isoform 1 of Epidermal growth factor receptor kinase substrate 8-like	IPI00301250	80 kDa

protein 1		
EPS8L3 Isoform 1 of Epidermal growth factor receptor kinase substrate 8-like protein 3	IPI00181833	67 kDa
ERH Enhancer of rudimentary homolog	IPI00029631	12 kDa
ERO1L ERO1-like protein alpha	IPI00386755	54 kDa
ESD S-formylglutathione hydrolase	IPI00411706	31 kDa
ETFA Electron transfer flavoprotein subunit alpha, mitochondrial	IPI00010810	35 kDa
ETFB Isoform 1 of Electron transfer flavoprotein subunit beta	IPI00004902	28 kDa
ETHE1 Protein ETHE1, mitochondrial	IPI00003766	28 kDa
EVPL Envoplakin	IPI00023711	232 kDa
EWSR1 Ewing sarcoma breakpoint region 1, isoform CRA_h	IPI00009841	69 kDa
EZR Ezrin	IPI00746388	69 kDa
FAM129B Niban-like protein 1	IPI00456750	83 kDa
FARSA Phenylalanyl-tRNA synthetase alpha chain	IPI00031820	58 kDa
FARSB Phenylalanyl-tRNA synthetase beta chain	IPI00300074	66 kDa
FASN Fatty acid synthase	IPI00026781	273 kDa
FBLN1 Isoform B of Fibulin-1	IPI00218803	77 kDa
FBN1 Fibrillin-1	IPI00328113	312 kDa
FBP1 Fructose-1,6-bisphosphatase 1	IPI00073772	37 kDa
FERMT2 Isoform 1 of Fermitin family homolog 2	IPI00000856	78 kDa
FGA Isoform 1 of Fibrinogen alpha chain	IPI00021885	95 kDa
FGB Fibrinogen beta chain	IPI00298497	56 kDa
FGG Isoform Gamma-B of Fibrinogen gamma chain	IPI00021891	52 kDa
FH Isoform Mitochondrial of Fumarate hydratase, mitochondrial	IPI00296053	55 kDa
FKBP3 FK506-binding protein 3	IPI00024157	25 kDa
FKBP4 FK506-binding protein 4	IPI00219005	52 kDa
FLJ12529 Isoform 1 of Cleavage and polyadenylation specificity factor subunit 7	IPI00550821	52 kDa
FLNA Isoform 2 of Filamin-A	IPI00302592	280 kDa
FLNB Isoform 1 of Filamin-B	IPI00289334	278 kDa
FLOT1 Flotillin-1	IPI00027438	47 kDa
FN1 Isoform 1 of Fibronectin	IPI00022418	263 kDa
FSCN1 Fascin	IPI00163187	55 kDa
FTH1 Ferritin heavy chain	IPI00554521	21 kDa
FTL Ferritin	IPI00375676	21 kDa
FUBP1 Isoform 1 of Far upstream element-binding protein 1	IPI00375441	68 kDa
FUBP3 Isoform 1 of Far upstream element-binding protein 3	IPI00377261	62 kDa
FUS Isoform Short of RNA-binding protein FUS	IPI00221354	53 kDa
G3BP2 Isoform A of Ras GTPase-activating protein-binding protein 2	IPI00009057	54 kDa
G6PD Isoform Long of Glucose-6-phosphate 1-dehydrogenase	IPI00216008	64 kDa
GALE UDP-glucose 4-epimerase	IPI00553131	38 kDa
GANAB cDNA FLJ61290, highly similar to Neutral alpha-glucosidase AB	IPI00383581	113 kDa
GAPDH Glyceraldehyde-3-phosphate dehydrogenase	IPI00219018	36 kDa
GARS Glycyl-tRNA synthetase	IPI00783097	83 kDa
GATM Isoform Mitochondrial of Glycine amidinotransferase, mitochondrial	IPI00032103	48 kDa

GBF1 Golgi-specific brefeldin A-resistance guanine nucleotide exchange factor 1	IPI00021954	206 kDa
GCA Grancalcin	IPI00004524	24 kDa
GDI1 Rab GDP dissociation inhibitor alpha	IPI00010154	51 kDa
GDI2 cDNA FLJ60299, highly similar to Rab GDP dissociation inhibitor beta	IPI00031461	51 kDa
GFPT1 Isoform 1 of Glucosamine--fructose-6-phosphate aminotransferase [isomerizing] 1	IPI00217952	79 kDa
GIGYF2 Isoform 2 of PERQ amino acid-rich with GYF domain-containing protein 2	IPI00647635	153 kDa
GLO1 Lactoylglutathione lyase	IPI00220766	21 kDa
GLT25D1 Glycosyltransferase 25 family member 1	IPI00168262	72 kDa
GLUD1 Glutamate dehydrogenase 1, mitochondrial	IPI00016801	61 kDa
GMDS GDP-mannose 4,6 dehydratase	IPI00030207	42 kDa
GMPS GMP synthase [glutamine-hydrolyzing]	IPI00029079	77 kDa
GNAS Isoform XLas-1 of Guanine nucleotide-binding protein G(s) subunit alpha isoforms XLas	IPI00095891	111 kDa
GNB2 Guanine nucleotide-binding protein G(I)/G(S)/G(T) subunit beta-2	IPI00003348	37 kDa
GNB2L1 Guanine nucleotide-binding protein subunit beta 2-like 1	IPI00641950	38 kDa
GOLGA3 Isoform 1 of Golgin subfamily A member 3	IPI00305267	167 kDa
GOLGB1 Golgin subfamily B member 1	IPI00004671	376 kDa
GOLM1 Golgi membrane protein 1	IPI00171411	46 kDa
GOT1 Aspartate aminotransferase, cytoplasmic	IPI00219029	46 kDa
GOT2 Aspartate aminotransferase, mitochondrial	IPI00018206	47 kDa
GPD2 Isoform 1 of Glycerol-3-phosphate dehydrogenase, mitochondrial	IPI00017895	81 kDa
GPI Glucose-6-phosphate isomerase	IPI00027497	63 kDa
GPX1 glutathione peroxidase 1 isoform 1	IPI00293975	22 kDa
GPX2 Glutathione peroxidase 2	IPI00298176	22 kDa
GRB2 Isoform 1 of Growth factor receptor-bound protein 2	IPI00021327	25 kDa
GRHPR Glyoxylate reductase/hydroxypyruvate reductase	IPI00037448	36 kDa
GSN Isoform 1 of Gelsolin	IPI00646773	81 kDa
GSS Glutathione synthetase	IPI00010706	52 kDa
GSTK1 Glutathione S-transferase kappa 1	IPI00219673	25 kDa
GSTO1 Glutathione S-transferase omega-1	IPI00019755	28 kDa
GSTP1 Glutathione S-transferase P	IPI00219757	23 kDa
GSTT1 Glutathione S-transferase theta-1	IPI00741097	27 kDa
GTF2I Isoform 1 of General transcription factor II-I	IPI00054042	112 kDa
H1F0 Histone H1.0	IPI00550239	21 kDa
H2AFY H2A histone family, member Y isoform 2	IPI00059366	39 kDa
H2AFY2 Core histone macro-H2A.2	IPI00220994	40 kDa
HADHA Trifunctional enzyme subunit alpha, mitochondrial	IPI00031522	83 kDa
HADHB Trifunctional enzyme subunit beta, mitochondrial	IPI00022793	51 kDa
HARS Histidyl-tRNA synthetase, cytoplasmic	IPI00021808	57 kDa
HBA1;HBA2 Hemoglobin subunit alpha	IPI00410714	15 kDa
HBB Hemoglobin subunit beta	IPI00654755	16 kDa
HDAC1 Histone deacetylase 1	IPI00013774	55 kDa

HDGF Hepatoma-derived growth factor	IPI00020956	27 kDa
HDLBP Vigilin	IPI00022228	141 kDa
HEBP1 Heme-binding protein 1	IPI00148063	21 kDa
HIBCH Isoform 1 of 3-hydroxyisobutyryl-CoA hydrolase, mitochondrial	IPI00419802	43 kDa
HIST1H1B Histone H1.5	IPI00217468	23 kDa
HIST1H1E Histone H1.4	IPI00217467	22 kDa
HK1 Isoform 1 of Hexokinase-1	IPI00018246	102 kDa
HLA-A HLA class I histocompatibility antigen, A-69 alpha chain	IPI00760554	41 kDa
HLA-DQA1 MHC class II antigen	IPI00719648	29 kDa
HMGA1 Isoform HMG-I of High mobility group protein HMG-I/HMG-Y	IPI00179700	12 kDa
HMGB1 High mobility group protein B1	IPI00419258	25 kDa
HNRNPA1 Isoform A1-B of Heterogeneous nuclear ribonucleoprotein A1	IPI00215965	39 kDa
HNRNPA2B1 43 kDa protein	IPI00874030	43 kDa
HNRNPA3 Isoform 1 of Heterogeneous nuclear ribonucleoprotein A3	IPI00419373	40 kDa
HNRNPAB Isoform 2 of Heterogeneous nuclear ribonucleoprotein A/B	IPI00334587	36 kDa
HNRNPC Isoform C1 of Heterogeneous nuclear ribonucleoproteins C1/C2	IPI00216592	32 kDa
HNRNPD Isoform 1 of Heterogeneous nuclear ribonucleoprotein D0	IPI00028888	38 kDa
HNRNPF Heterogeneous nuclear ribonucleoprotein F	IPI00003881	46 kDa
HNRNPH1 Heterogeneous nuclear ribonucleoprotein H	IPI00013881	49 kDa
HNRNPH3 Isoform 1 of Heterogeneous nuclear ribonucleoprotein H3	IPI00013877	37 kDa
HNRNPK Isoform 1 of Heterogeneous nuclear ribonucleoprotein K	IPI00216049	51 kDa
HNRNPL Heterogeneous nuclear ribonucleoprotein L	IPI00027834	64 kDa
HNRNPM Isoform 1 of Heterogeneous nuclear ribonucleoprotein M	IPI00171903	78 kDa
HNRNPR Heterogeneous nuclear ribonucleoprotein R	IPI00012074	71 kDa
HNRNPU Isoform Short of Heterogeneous nuclear ribonucleoprotein U	IPI00479217	89 kDa
HNRNPUL1 Isoform 1 of Heterogeneous nuclear ribonucleoprotein U-like protein 1	IPI00013070	96 kDa
HNRNPUL2 Heterogeneous nuclear ribonucleoprotein U-like protein 2	IPI00456887	85 kDa
HP1BP3 Isoform 1 of Heterochromatin protein 1-binding protein 3	IPI00642238	61 kDa
HSD17B10 Isoform 1 of 3-hydroxyacyl-CoA dehydrogenase type-2	IPI00017726	27 kDa
HSD17B4 Peroxisomal multifunctional enzyme type 2	IPI00019912	80 kDa
HSP90AA1 heat shock protein 90kDa alpha (cytosolic), class A member 1 isoform 1	IPI00382470	98 kDa
HSP90AB1 Heat shock protein HSP 90-beta	IPI00414676	83 kDa
HSP90B1 Endoplasmin	IPI00027230	92 kDa
HSPA1B;HSPA1A Heat shock 70 kDa protein 1	IPI00304925	70 kDa
HSPA4 Heat shock 70 kDa protein 4	IPI00002966	94 kDa
HSPA5 HSPA5 protein	IPI00003362	72 kDa
HSPA8 Isoform 1 of Heat shock cognate 71 kDa protein	IPI00003865	71 kDa
HSPA9 Stress-70 protein, mitochondrial	IPI00007765	74 kDa
HSPB1 Heat shock protein beta-1	IPI00025512	23 kDa
HSPD1 60 kDa heat shock protein, mitochondrial	IPI00784154	61 kDa
HSPE1 10 kDa heat shock protein, mitochondrial	IPI00220362	11 kDa
HSPG2 Basement membrane-specific heparan sulfate proteoglycan core protein	IPI00024284	469 kDa

HUWE1 482 kDa protein	IPI00179298	482 kDa
HYOU1 Hypoxia up-regulated protein 1	IPI00000877	111 kDa
IARS2 Isoleucyl-tRNA synthetase, mitochondrial	IPI00017283	114 kDa
IDH1 Isocitrate dehydrogenase [NADP] cytoplasmic	IPI00027223	47 kDa
IDH2 Isocitrate dehydrogenase [NADP], mitochondrial	IPI00011107	51 kDa
IDH3A Isoform 1 of Isocitrate dehydrogenase [NAD] subunit alpha, mitochondrial	IPI00030702	40 kDa
IGF2BP3 Isoform 1 of Insulin-like growth factor 2 mRNA-binding protein 3	IPI00658000	64 kDa
IGJ immunoglobulin J chain	IPI00178926	18 kDa
ILF2 Interleukin enhancer-binding factor 2	IPI00005198	43 kDa
ILF3 Isoform 5 of Interleukin enhancer-binding factor 3	IPI00219330	75 kDa
IMMT Isoform 1 of Mitochondrial inner membrane protein	IPI00009960	84 kDa
INF2 Isoform 2 of Inverted formin-2	IPI00876962	135 kDa
IQGAP1 Ras GTPase-activating-like protein IQGAP1	IPI00009342	189 kDa
IQGAP2 Isoform 1 of Ras GTPase-activating-like protein IQGAP2	IPI00299048	181 kDa
ISG15 Interferon-induced 17 kDa protein	IPI00375631	18 kDa
ITGA2 Integrin alpha-2	IPI00013744	129 kDa
ITGA3 Isoform Alpha-3A of Integrin alpha-3	IPI00215995	117 kDa
ITGAV Isoform 1 of Integrin alpha-V	IPI00027505	116 kDa
ITGB1 Isoform Beta-1C of Integrin beta-1	IPI00217561	92 kDa
ITGB4 Isoform Beta-4C of Integrin beta-4	IPI00027422	202 kDa
ITIH2 Inter-alpha-trypsin inhibitor heavy chain H2	IPI00305461	106 kDa
ITPR3 Inositol 1,4,5-trisphosphate receptor type 3	IPI00291607	304 kDa
IVD Isovaleryl-CoA dehydrogenase, mitochondrial	IPI00645805	46 kDa
JUP cDNA FLJ60424, highly similar to Junction plakoglobin	IPI00789324	63 kDa
JUP Junction plakoglobin	IPI00554711	82 kDa
KARS Lysyl-tRNA synthetase	IPI00014238	68 kDa
KCTD12 BTB/POZ domain-containing protein KCTD12	IPI00060715	36 kDa
KHSRP KH-type splicing regulatory protein	IPI00479786	73 kDa
KIAA0564 Isoform 3 of Uncharacterized protein KIAA0564	IPI00158296	161 kDa
KIAA1967 Isoform 1 of Protein KIAA1967	IPI00182757	103 kDa
KIF13B Kinesin-like protein KIF13B	IPI00021753	203 kDa
KIF5B Kinesin-1 heavy chain	IPI00012837	110 kDa
KLC4 Isoform 1 of Kinesin light chain 4	IPI00398812	69 kDa
KPNB1 Importin subunit beta-1	IPI00001639	97 kDa
KRT1 Keratin, type II cytoskeletal 1	IPI00220327	66 kDa
KRT10 Keratin, type I cytoskeletal 10	IPI00009865	60 kDa
KRT14 Keratin, type I cytoskeletal 14	IPI00384444	52 kDa
KRT16 Keratin, type I cytoskeletal 16	IPI00217963	51 kDa
KRT17 Keratin, type I cytoskeletal 17	IPI00450768	48 kDa
KRT18 Keratin, type I cytoskeletal 18	IPI00554788	48 kDa
KRT19 Keratin, type I cytoskeletal 19	IPI00479145	44 kDa
KRT2 Keratin, type II cytoskeletal 2 epidermal	IPI00021304	66 kDa
KRT20 Keratin, type I cytoskeletal 20	IPI00021298	48 kDa
KRT7 keratin 7	IPI00847342	51 kDa

KRT7 Keratin, type II cytoskeletal 7	IPI00306959	51 kDa
KRT8 Keratin, type II cytoskeletal 8	IPI00554648	54 kDa
KRT9 Keratin, type I cytoskeletal 9	IPI00019359	62 kDa
KTN1 Isoform 1 of Kinectin	IPI00328753	156 kDa
LAD1 Ladinin-1	IPI00514234	57 kDa
LAMA5 Laminin subunit alpha-5	IPI00783665	400 kDa
LAMB1 Laminin subunit beta-1	IPI00013976	198 kDa
LAMB2 Laminin subunit beta-2	IPI00296922	196 kDa
LAMB3 Laminin subunit beta-3	IPI00299404	130 kDa
LAMC1 Laminin subunit gamma-1	IPI00298281	178 kDa
LAMC2 Isoform Long of Laminin subunit gamma-2	IPI00015117	131 kDa
LAP3 Isoform 1 of Cytosol aminopeptidase	IPI00419237	56 kDa
LASP1 Isoform 1 of LIM and SH3 domain protein 1	IPI00000861	30 kDa
LCP1 Plastin-2	IPI00010471	70 kDa
LDHA Isoform 1 of L-lactate dehydrogenase A chain	IPI00217966	37 kDa
LDHB L-lactate dehydrogenase B chain	IPI00219217	37 kDa
LETM1 LETM1 and EF-hand domain-containing protein 1, mitochondrial	IPI00017592	83 kDa
LGALS1 Galectin-1	IPI00219219	15 kDa
LGALS3 Galectin-3	IPI00465431	26 kDa
LGALS3BP Galectin-3-binding protein	IPI00023673	65 kDa
LGALS4 Galectin-4	IPI00009750	36 kDa
LGALS9 Isoform Long of Galectin-9	IPI00010477	40 kDa
LIMA1 Isoform Beta of LIM domain and actin-binding protein 1	IPI00008918	85 kDa
LMCD1 LIM and cysteine-rich domains protein 1	IPI00303258	41 kDa
LMNA Isoform A of Lamin-A/C	IPI00021405	74 kDa
LMNB1 Lamin-B1	IPI00217975	66 kDa
LMNB2 Lamin-B2	IPI00009771	70 kDa
LMO7 Isoform 3 of LIM domain only protein 7	IPI00291802	154 kDa
LPP Lipoma-preferred partner	IPI00023704	66 kDa
LRBA Lipopolysaccharide-responsive and beige-like anchor protein	IPI00002255	319 kDa
LRPPRC Leucine-rich PPR motif-containing protein, mitochondrial	IPI00783271	158 kDa
LTBP2 Latent-transforming growth factor beta-binding protein 2	IPI00292150	195 kDa
LUC7L2 Isoform 1 of Putative RNA-binding protein Luc7-like 2	IPI00006932	47 kDa
LUM Lumican	IPI00020986	38 kDa
LYPLA1 cDNA FLJ60607, highly similar to Acyl-protein thioesterase 1	IPI00007321	28 kDa
LYZ Lysozyme C	IPI00019038	17 kDa
MACF1 Microtubule-actin cross-linking factor 1, isoform 4	IPI00432363	670 kDa
MAGT1 magnesium transporter 1	IPI00301202	42 kDa
MAP2K1 Dual specificity mitogen-activated protein kinase kinase 1	IPI00219604	43 kDa
MAPK1 Mitogen-activated protein kinase 1	IPI00003479	41 kDa
MAPK3 Mitogen-activated protein kinase 3	IPI00018195	43 kDa
MARCKS Myristoylated alanine-rich C-kinase substrate	IPI00219301	32 kDa
MAT2A S-adenosylmethionine synthetase isoform type-2	IPI00010157	44 kDa
MAT2B Isoform 1 of Methionine adenosyltransferase 2 subunit beta	IPI00002324	38 kDa

MATR3 Matrin-3	IPI00017297	95 kDa
MDH1 Malate dehydrogenase, cytoplasmic	IPI00291005	36 kDa
MDH2 Malate dehydrogenase, mitochondrial	IPI00291006	36 kDa
MIF;LOC284889 Macrophage migration inhibitory factor	IPI00293276	12 kDa
MLEC Malectin	IPI00029046	32 kDa
MLPH Isoform 1 of Melanophilin	IPI00012201	66 kDa
MMAA MMAA protein	IPI00217023	47 kDa
MPO Isoform H17 of Myeloperoxidase	IPI00007244	84 kDa
MPST 3-mercaptopyruvate sulfurtransferase	IPI00165360	33 kDa
MSN Moesin	IPI00219365	68 kDa
MTCH2 Mitochondrial carrier homolog 2	IPI00003833	33 kDa
MT-CO2 Cytochrome c oxidase subunit 2	IPI00017510	26 kDa
MTDH Protein LYRIC	IPI00328715	64 kDa
MTHFD1 C-1-tetrahydrofolate synthase, cytoplasmic	IPI00218342	102 kDa
MUC5AC Mucin-5AC (Fragment)	IPI00103397	527 kDa
MUC5B mucin 5, subtype B, tracheobronchial	IPI00855918	597 kDa
MVP Major vault protein	IPI00000105	99 kDa
MYH10 Isoform 1 of Myosin-10	IPI00397526	229 kDa
MYH11 Myosin-11	IPI00020501	227 kDa
MYH14 MYH14 variant protein	IPI00607818	232 kDa
MYH9 Isoform 1 of Myosin-9	IPI00019502	227 kDa
MYL6B;MYL6 Isoform Non-muscle of Myosin light polypeptide 6	IPI00335168	17 kDa
MYO18A Isoform 2 of Myosin-XVIIIa	IPI00334410	196 kDa
MYO1C Myosin-Ic	IPI00010418	118 kDa
MYO1D Isoform 1 of Myosin-Id	IPI00329719	116 kDa
MYO6 Isoform 2 of Myosin-VI	IPI00008455	146 kDa
MYOF Isoform 1 of Myoferlin	IPI00021048	235 kDa
NAMPT Isoform 1 of Nicotinamide phosphoribosyltransferase	IPI00018873	56 kDa
NAP1L4 cDNA FLJ59403, highly similar to Nucleosome assembly protein 1-like 4	IPI00017763	44 kDa
NAPRT1 Isoform 3 of Nicotinate phosphoribosyltransferase	IPI00880164	56 kDa
NARS Asparaginyl-tRNA synthetase, cytoplasmic	IPI00306960	63 kDa
NDRG1 Protein NDRG1	IPI00022078	43 kDa
NDUFS1 cDNA FLJ55978, highly similar to NADH-ubiquinone oxidoreductase 75 kDa subunit, mitochondrial	IPI00604664	81 kDa
NDUFS2 NADH dehydrogenase [ubiquinone] iron-sulfur protein 2, mitochondrial	IPI00025239	53 kDa
NDUFV1 Isoform 1 of NADH dehydrogenase [ubiquinone] flavoprotein 1, mitochondrial	IPI00028520	51 kDa
NFKB2 nuclear factor of kappa light polypeptide gene enhancer in B-cells 2 isoform b	IPI00807463	97 kDa
NID2 Nidogen-2	IPI00028908	151 kDa
NME2 Nucleoside diphosphate kinase	IPI00604590	33 kDa
NME3 Nucleoside diphosphate kinase 3	IPI00012315	19 kDa
NNT NAD(P) transhydrogenase, mitochondrial	IPI00337541	114 kDa
NONO Non-POU domain-containing octamer-binding protein	IPI00304596	54 kDa

NOP5/NOP58 Nucleolar protein 5	IPI00006379	60 kDa
NP cDNA FLJ25678 fis, clone TST04067, highly similar to PURINE NUCLEOSIDE PHOSPHORYLASE	IPI00017672	33 kDa
NPEPPS Puromycin-sensitive aminopeptidase	IPI00026216	103 kDa
NPM1 Isoform 2 of Nucleophosmin	IPI00220740	29 kDa
NQO1 NAD(P)H dehydrogenase [quinone] 1	IPI00012069	31 kDa
NSF Vesicle-fusing ATPase	IPI00006451	83 kDa
NSFL1C Isoform 2 of NSFL1 cofactor p47	IPI00022830	37 kDa
NUCB1 Nucleobindin-1	IPI00295542	54 kDa
NUDT21 Cleavage and polyadenylation specificity factor subunit 5	IPI00646917	26 kDa
NUMA1 Isoform 2 of Nuclear mitotic apparatus protein 1	IPI00006196	237 kDa
NUP93 Nuclear pore complex protein Nup93	IPI00397904	93 kDa
OAS3 2'-5'-oligoadenylate synthetase 3	IPI00002405	121 kDa
OGDH 2-oxoglutarate dehydrogenase E1 component, mitochondrial	IPI00098902	116 kDa
OGN cDNA FLJ59205, highly similar to Mimecan	IPI00025465	41 kDa
OLA1 Isoform 1 of Obg-like ATPase 1	IPI00290416	45 kDa
OLFM4 Olfactomedin-4	IPI00022255	57 kDa
OSBP Isoform 1 of Oxysterol-binding protein 1	IPI00024971	89 kDa
OSTF1 Osteoclast-stimulating factor 1	IPI00414836	24 kDa
OTUB1 cDNA FLJ56307, highly similar to Ubiquitin thioesterase protein OTUB1	IPI00000581	35 kDa
P4HB Protein disulfide-isomerase	IPI00010796	57 kDa
PA2G4 Proliferation-associated protein 2G4	IPI00299000	44 kDa
PABPC1 Isoform 1 of Polyadenylate-binding protein 1	IPI00008524	71 kDa
PACSIN2 Isoform 1 of Protein kinase C and casein kinase substrate in neurons protein 2	IPI00027009	56 kDa
PAFAH1B2 Platelet-activating factor acetylhydrolase IB subunit beta	IPI00026546	26 kDa
PAFAH1B3 Platelet-activating factor acetylhydrolase IB subunit gamma	IPI00014808	26 kDa
PARK7 Protein DJ-1	IPI00298547	20 kDa
PARP1 Poly [ADP-ribose] polymerase 1	IPI00449049	113 kDa
PARP4 Poly [ADP-ribose] polymerase 4	IPI00296909	193 kDa
PCBP1 Poly(rC)-binding protein 1	IPI00016610	37 kDa
PCBP2 poly(rC) binding protein 2 isoform b	IPI00012066	38 kDa
PCK2 Phosphoenolpyruvate carboxykinase [GTP], mitochondrial	IPI00294380	71 kDa
PCMT1 Isoform 1 of Protein-L-isoaspartate(D-aspartate) O-methyltransferase	IPI00411680	25 kDa
PCNP Isoform 2 of PEST proteolytic signal-containing nuclear protein	IPI00060650	14 kDa
PCYOX1 Prenylcysteine oxidase 1	IPI00384280	57 kDa
PDCD6 Programmed cell death protein 6	IPI00025277	22 kDa
PDCD6IP PDCD6IP protein	IPI00246058	97 kDa
PDHA1 Mitochondrial PDHA1	IPI00306301	48 kDa
PDHB Isoform 1 of Pyruvate dehydrogenase E1 component subunit beta, mitochondrial	IPI00003925	39 kDa
PDIA3 Protein disulfide-isomerase A3	IPI00025252	57 kDa
PDIA4 Protein disulfide-isomerase A4	IPI00009904	73 kDa
PDIA6 Isoform 2 of Protein disulfide-isomerase A6	IPI00299571	54 kDa

PDLIM5 PDZ and LIM domain protein 5	IPI00007935	64 kDa
PDXDC1 Isoform 1 of Pyridoxal-dependent decarboxylase domain-containing protein 1	IPI00384689	87 kDa
PEA15 Astrocytic phosphoprotein PEA-15	IPI00014850	15 kDa
PEBP1 Phosphatidylethanolamine-binding protein 1	IPI00219446	21 kDa
PFDN2 Prefoldin subunit 2	IPI00006052	17 kDa
PFKFB2 Isoform 2 of 6-phosphofructo-2-kinase/fructose-2,6-biphosphatase 2	IPI00220808	54 kDa
PFKL Isoform 1 of 6-phosphofructokinase, liver type	IPI00332371	85 kDa
PFKM cDNA FLJ44241 fis, clone THYMU3008436, highly similar to 6-phosphofructokinase, muscle type	IPI00465179	93 kDa
PFKP 6-phosphofructokinase type C	IPI00009790	86 kDa
PFN1 Profilin-1	IPI00216691	15 kDa
PGD 6-phosphogluconate dehydrogenase, decarboxylating	IPI00219525	53 kDa
PGK1 Phosphoglycerate kinase 1	IPI00169383	45 kDa
PGM1 Isoform 1 of Phosphoglucomutase-1	IPI00219526	61 kDa
PGM2 Phosphoglucomutase-2	IPI00550364	68 kDa
PHB Prohibitin	IPI00017334	30 kDa
PHB2 Prohibitin-2	IPI00027252	33 kDa
PKM2 Isoform M1 of Pyruvate kinase isozymes M1/M2	IPI00220644	58 kDa
PKP2 plakophilin 2 isoform 2a	IPI00847318	93 kDa
PKP3 Plakophilin-3	IPI00026952	87 kDa
PLEC1 Isoform 4 of Plectin-1	IPI00398779	516 kDa
PLS1 Plastin-1	IPI00032304	70 kDa
PLS3 plastin 3	IPI00216694	71 kDa
PML Isoform PML-1 of Probable transcription factor PML	IPI00022348	98 kDa
PNN Isoform 1 of Pinin	IPI00789041	82 kDa
POF1B Isoform 1 of Protein POF1B	IPI00103242	69 kDa
POLR2B DNA-directed RNA polymerase II subunit RPB2	IPI00027808	134 kDa
PON2 39 kDa protein	IPI00844348	39 kDa
POR NADPH--cytochrome P450 reductase	IPI00470467	77 kDa
POSTN Isoform 1 of Periostin	IPI00007960	93 kDa
PPA1 Inorganic pyrophosphatase	IPI00015018	33 kDa
PPIA Peptidyl-prolyl cis-trans isomerase A	IPI00419585	18 kDa
PPIB Peptidyl-prolyl cis-trans isomerase B	IPI00646304	24 kDa
PPL Periplakin	IPI00298057	205 kDa
PPP1CB Serine/threonine-protein phosphatase PP1-beta catalytic subunit	IPI00218236	37 kDa
PPP1R12A Isoform 1 of Protein phosphatase 1 regulatory subunit 12A	IPI00183002	115 kDa
PPP1R7 Isoform 1 of Protein phosphatase 1 regulatory subunit 7	IPI00033600	42 kDa
PPP2CA Serine/threonine-protein phosphatase 2A catalytic subunit alpha isoform	IPI00008380	36 kDa
PPP2R1A Serine/threonine-protein phosphatase 2A 65 kDa regulatory subunit A alpha isoform	IPI00554737	65 kDa
PRDX1 Peroxiredoxin-1	IPI00000874	22 kDa
PRDX2 Peroxiredoxin-2	IPI00027350	22 kDa
PRDX3 Thioredoxin-dependent peroxide reductase, mitochondrial	IPI00024919	28 kDa

PRDX4 Peroxiredoxin-4	IPI00011937	31 kDa
PRDX5 Isoform Mitochondrial of Peroxiredoxin-5, mitochondrial	IPI00024915	22 kDa
PRDX6 Peroxiredoxin-6	IPI00220301	25 kDa
PRELP Prolargin	IPI00020987	44 kDa
PRKAR1A cAMP-dependent protein kinase type I-alpha regulatory subunit	IPI00021831	43 kDa
PRKAR2A Protein kinase, cAMP-dependent, regulatory, type II, alpha, isoform CRA_b	IPI00063234	43 kDa
PRKCSH cDNA FLJ59211, highly similar to Glucosidase 2 subunit beta	IPI00026154	60 kDa
PRKDC Isoform 1 of DNA-dependent protein kinase catalytic subunit	IPI00296337	469 kDa
PRPF8 Pre-mRNA-processing-splicing factor 8	IPI00007928	274 kDa
PRSS1 Trypsin-1	IPI00011694	27 kDa
PSAP Isoform Sap-mu-0 of Proactivator polypeptide	IPI00012503	58 kDa
PSMA1 Isoform Short of Proteasome subunit alpha type-1	IPI00016832	30 kDa
PSMA3 Isoform 2 of Proteasome subunit alpha type-3	IPI00171199	28 kDa
PSMA5 Proteasome subunit alpha type-5	IPI00291922	26 kDa
PSMA7 Isoform 1 of Proteasome subunit alpha type-7	IPI00024175	28 kDa
PSMB1 Proteasome subunit beta type-1	IPI00025019	26 kDa
PSMB6 Proteasome subunit beta type-6	IPI00000811	25 kDa
PSMB8 Isoform 2 of Proteasome subunit beta type-8	IPI00215824	30 kDa
PSMB9 Isoform LMP2.L of Proteasome subunit beta type-9	IPI00000787	23 kDa
PSMC1 26S protease regulatory subunit 4	IPI00011126	49 kDa
PSMC2 26S protease regulatory subunit 7	IPI00021435	49 kDa
PSMC3 26S protease regulatory subunit 6A	IPI00018398	49 kDa
PSMC5 26S protease regulatory subunit 8	IPI00023919	46 kDa
PSMD11 Proteasome 26S non-ATPase subunit 11 variant (Fragment)	IPI00105598	48 kDa
PSMD2 26S proteasome non-ATPase regulatory subunit 2	IPI00012268	100 kDa
PSMD3 26S proteasome non-ATPase regulatory subunit 3	IPI00011603	61 kDa
PSMD6 26S proteasome non-ATPase regulatory subunit 6	IPI00014151	46 kDa
PSME1 Proteasome activator complex subunit 1	IPI00479722	29 kDa
PSME2 Putative uncharacterized protein PSME2	IPI00384051	29 kDa
PSPC1 Isoform 1 of Paraspeckle component 1	IPI00103525	59 kDa
PTBP1 Isoform 1 of Polypyrimidine tract-binding protein 1	IPI00179964	57 kDa
PTPLAD1 Protein tyrosine phosphatase-like protein PTPLAD1	IPI00008998	43 kDa
PTPN6 Isoform 1 of Tyrosine-protein phosphatase non-receptor type 6	IPI00218604	68 kDa
PTRF Isoform 1 of Polymerase I and transcript release factor	IPI00176903	43 kDa
PYGB Glycogen phosphorylase, brain form	IPI00004358	97 kDa
QARS Glutaminyl-tRNA synthetase	IPI00026665	90 kDa
QSOX1 Isoform 1 of Sulfhydryl oxidase 1	IPI00003590	83 kDa
RAB10 Ras-related protein Rab-10	IPI00016513	23 kDa
RAB11B Ras-related protein Rab-11B	IPI00020436	24 kDa
RAB14 Ras-related protein Rab-14	IPI00291928	24 kDa
RAB1B Ras-related protein Rab-1B	IPI00008964	22 kDa
RAB2A Ras-related protein Rab-2A	IPI00031169	24 kDa
RAB5C Ras-related protein Rab-5C	IPI00016339	23 kDa
RAB7A Ras-related protein Rab-7a	IPI00016342	23 kDa

RAC1 Isoform A of Ras-related C3 botulinum toxin substrate 1	IPI00010271	21 kDa
RALY RNA binding protein, autoantigenic (HnRNP-associated with lethal yellow homolog (Mouse)), isoform CRA_a (Fragment)	IPI00011268	33 kDa
RAN GTP-binding nuclear protein Ran	IPI00643041	24 kDa
RAP1B Ras-related protein Rap-1b	IPI00015148	21 kDa
RBBP4 Histone-binding protein RBBP4	IPI00328319	48 kDa
RBM14 Isoform 1 of RNA-binding protein 14	IPI00013174	69 kDa
RBM25 RNA binding motif protein 25	IPI00004273	100 kDa
RBMX Heterogeneous nuclear ribonucleoprotein G	IPI00304692	42 kDa
RBP1 retinol binding protein 1, cellular isoform a	IPI00219718	22 kDa
RCC1 regulator of chromosome condensation 1 isoform a	IPI00001661	48 kDa
RCN1 Reticulocalbin-1	IPI00015842	39 kDa
RELA RELA protein	IPI00883897	43 kDa
RNPEP Aminopeptidase B	IPI00642211	73 kDa
RPA1 Replication protein A 70 kDa DNA-binding subunit	IPI00020127	68 kDa
RPL10 60S ribosomal protein L10	IPI00554723	25 kDa
RPL10A 60S ribosomal protein L10a	IPI00412579	25 kDa
RPL11 Isoform 1 of 60S ribosomal protein L11	IPI00376798	20 kDa
RPL13 60S ribosomal protein L13	IPI00465361	24 kDa
RPL15 60S ribosomal protein L15	IPI00470528	24 kDa
RPL18 60S ribosomal protein L18	IPI00215719	22 kDa
RPL23A;hCG_16001 60S ribosomal protein L23a	IPI00021266	18 kDa
RPL27 60S ribosomal protein L27	IPI00219155	16 kDa
RPL28 60S ribosomal protein L28	IPI00182533	16 kDa
RPL3 60S ribosomal protein L3	IPI00550021	46 kDa
RPL35A 60S ribosomal protein L35a	IPI00029731	13 kDa
RPL4 60S ribosomal protein L4	IPI00003918	48 kDa
RPL5 60S ribosomal protein L5	IPI00000494	34 kDa
RPL6 60S ribosomal protein L6	IPI00329389	33 kDa
RPL8 60S ribosomal protein L8	IPI00012772	28 kDa
RPLP0 60S acidic ribosomal protein P0	IPI00008530	34 kDa
RPLP2 60S acidic ribosomal protein P2	IPI00008529	12 kDa
RPN1 Dolichyl-diphosphooligosaccharide--protein glycosyltransferase 67 kDa subunit precursor	IPI00025874	73 kDa
RPN2 Ribophorin II	IPI00028635	71 kDa
RPS12 40S ribosomal protein S12	IPI00013917	15 kDa
RPS13 40S ribosomal protein S13	IPI00221089	17 kDa
RPS14 40S ribosomal protein S14	IPI00026271	16 kDa
RPS15A 40S ribosomal protein S15a	IPI00221091	15 kDa
RPS16 40S ribosomal protein S16	IPI00221092	16 kDa
RPS18;LOC100130553 40S ribosomal protein S18	IPI00013296	18 kDa
RPS19 40S ribosomal protein S19	IPI00215780	16 kDa
RPS2 40S ribosomal protein S2	IPI00013485	31 kDa
RPS20 40S ribosomal protein S20	IPI00012493	13 kDa
RPS21 40S ribosomal protein S21	IPI00017448	9 kDa

RPS25 40S ribosomal protein S25	IPI00012750	14 kDa
RPS26 Ribosomal protein 26 (RPS26) pseudogene	IPI00186712	13 kDa
RPS28 40S ribosomal protein S28	IPI00719622	8 kDa
RPS3 40S ribosomal protein S3	IPI00011253	27 kDa
RPS3A 40S ribosomal protein S3a	IPI00419880	30 kDa
RPS4X 40S ribosomal protein S4, X isoform	IPI00217030	30 kDa
RPS6 40S ribosomal protein S6	IPI00021840	29 kDa
RPS8 40S ribosomal protein S8	IPI00216587	24 kDa
RPS9 40S ribosomal protein S9	IPI00221088	23 kDa
RPSA 33 kDa protein	IPI00413108	33 kDa
RTN4 Isoform 1 of Reticulon-4	IPI00021766	130 kDa
RUVBL2 RuvB-like 2	IPI00009104	51 kDa
S100A10 Protein S100-A10	IPI00183695	11 kDa
S100A11 Protein S100-A11	IPI00013895	12 kDa
S100A16 Protein S100-A16	IPI00062120	12 kDa
S100A4 Protein S100-A4	IPI00032313	12 kDa
S100A6 Protein S100-A6	IPI00027463	10 kDa
S100A8 Protein S100-A8	IPI00007047	11 kDa
S100A9 Protein S100-A9	IPI00027462	13 kDa
S100P Protein S100-P	IPI00017526	10 kDa
SAMHD1 SAM domain and HD domain-containing protein 1	IPI00294739	72 kDa
SCCPDH Probable saccharopine dehydrogenase	IPI00329600	47 kDa
SCP2 Isoform SCPx of Non-specific lipid-transfer protein	IPI00026105	59 kDa
SDCBP2 Isoform 1 of Syntenin-2	IPI00302318	32 kDa
SEC16A Isoform 5 of Protein transport protein Sec16A	IPI00031242	236 kDa
SEC22B Vesicle-trafficking protein SEC22b	IPI00006865	25 kDa
SEC23A Protein transport protein Sec23A	IPI00017375	86 kDa
SEC31A Isoform 3 of Protein transport protein Sec31A	IPI00305152	122 kDa
SELENBP1 cDNA FLJ55757, highly similar to Selenium-binding protein 1	IPI00012303	57 kDa
SEPT2 Septin-2	IPI00014177	41 kDa
SEPT7 Isoform 1 of Septin-7	IPI00033025	51 kDa
SEPT9 septin 9 isoform a	IPI00784614	65 kDa
SERBP1 Isoform 1 of Plasminogen activator inhibitor 1 RNA-binding protein	IPI00410693	45 kDa
SERPINA1 Isoform 1 of Alpha-1-antitrypsin	IPI00553177	47 kDa
SERPINA3 cDNA FLJ35730 fis, clone TESTI2003131, highly similar to ALPHA-1-ANTICHYMOTRYPSIN	IPI00550991	51 kDa
SERPINB1 Leukocyte elastase inhibitor	IPI00027444	43 kDa
SERPINB5 Serpin B5	IPI00783625	42 kDa
SERPINB6 Putative uncharacterized protein DKFZp686I04222	IPI00413451	46 kDa
SERPINH1 Serpin H1	IPI00032140	46 kDa
SET Isoform 1 of Protein SET	IPI00072377	33 kDa
SF3A1 Splicing factor 3 subunit 1	IPI00017451	89 kDa
SF3B1 Splicing factor 3B subunit 1	IPI00026089	146 kDa
SF3B2 splicing factor 3B subunit 2	IPI00221106	100 kDa
SF3B3 Isoform 1 of Splicing factor 3B subunit 3	IPI00300371	136 kDa

SFN Isoform 1 of 14-3-3 protein sigma	IPI00013890	28 kDa
SFPQ Isoform Long of Splicing factor, proline- and glutamine-rich	IPI00010740	76 kDa
SFRS1 Isoform ASF-1 of Splicing factor, arginine/serine-rich 1	IPI00215884	28 kDa
SFRS2 Splicing factor, arginine/serine-rich 2	IPI00005978	25 kDa
SFRS6 Isoform SRP55-3 of Splicing factor, arginine/serine-rich 6	IPI00215879	38 kDa
SFXN3 sideroflexin 3	IPI00793874	36 kDa
SH3BGRL SH3 domain-binding glutamic acid-rich-like protein	IPI00025318	13 kDa
SHMT2 Serine hydroxymethyltransferase, mitochondrial	IPI00002520	56 kDa
SLC12A2 Isoform 1 of Solute carrier family 12 member 2	IPI00022649	131 kDa
SLC25A24 Isoform 1 of Calcium-binding mitochondrial carrier protein SCaMC-1	IPI00337494	53 kDa
SLC25A3 Isoform A of Phosphate carrier protein, mitochondrial	IPI00022202	40 kDa
SLC25A5 ADP/ATP translocase 2	IPI00007188	33 kDa
SLC2A1 Solute carrier family 2, facilitated glucose transporter member 1	IPI00220194	54 kDa
SLC9A3R1 Ezrin-radixin-moesin-binding phosphoprotein 50	IPI00003527	39 kDa
SMC1A Structural maintenance of chromosomes protein 1A	IPI00291939	143 kDa
SNCG Gamma-synuclein	IPI00297714	13 kDa
SND1 Staphylococcal nuclease domain-containing protein 1	IPI00140420	102 kDa
SNRNP200 Isoform 1 of U5 small nuclear ribonucleoprotein 200 kDa helicase	IPI00420014	245 kDa
SNRNP70 Isoform 2 of U1 small nuclear ribonucleoprotein 70 kDa	IPI00219483	51 kDa
SNRPB Isoform SM-B' of Small nuclear ribonucleoprotein-associated proteins B and B'	IPI00027285	25 kDa
SNRPD1 Small nuclear ribonucleoprotein Sm D1	IPI00302850	13 kDa
SNRPD3 Small nuclear ribonucleoprotein Sm D3	IPI00017964	14 kDa
SNX27 Isoform 2 of Sorting nexin-27	IPI00640980	60 kDa
SORBS1 Isoform 9 of Sorbin and SH3 domain-containing protein 1	IPI00002491	87 kDa
SORD Sorbitol dehydrogenase	IPI00216057	38 kDa
SPR Sepiapterin reductase	IPI00017469	28 kDa
SPTAN1 Isoform 1 of Spectrin alpha chain, brain	IPI00844215	285 kDa
SPTBN1 Isoform Long of Spectrin beta chain, brain 1	IPI00005614	275 kDa
SQRDL Sulfide:quinone oxidoreductase, mitochondrial	IPI00009634	50 kDa
SRC Isoform 2 of Proto-oncogene tyrosine-protein kinase Src	IPI00328867	61 kDa
SRI Sorcin	IPI00027175	22 kDa
SRRM2 Isoform 1 of Serine/arginine repetitive matrix protein 2	IPI00782992	300 kDa
SSB Lupus La protein	IPI00009032	47 kDa
SSR4 Translocon-associated protein subunit delta precursor	IPI00019385	20 kDa
STAT1 Isoform Alpha of Signal transducer and activator of transcription 1-alpha/beta	IPI00030781	87 kDa
STAT6 Isoform 1 of Signal transducer and activator of transcription 6	IPI00030782	94 kDa
STIM1 Stromal interaction molecule 1	IPI00299063	77 kDa
STIP1 Stress-induced-phosphoprotein 1	IPI00013894	63 kDa
STOM Erythrocyte band 7 integral membrane protein	IPI00219682	32 kDa
STOML2 Stomatin-like protein 2	IPI00334190	39 kDa
STT3A Dolichyl-diphosphooligosaccharide--protein glycosyltransferase subunit STT3A	IPI00297492	81 kDa

SUB1 Activated RNA polymerase II transcriptional coactivator p15	IPI00221222	14 kDa
SUPT16H FACT complex subunit SPT16	IPI00026970	120 kDa
SYNCRIP Isoform 1 of Heterogeneous nuclear ribonucleoprotein Q	IPI00018140	70 kDa
TAGLN Transgelin	IPI00216138	23 kDa
TAGLN2 Transgelin-2	IPI00550363	22 kDa
TALDO1 Transaldolase	IPI00744692	38 kDa
TAP2 Antigen peptide transporter 2	IPI00328112	76 kDa
TCP1 T-complex protein 1 subunit alpha	IPI00290566	60 kDa
TF Serotransferrin	IPI00022463	77 kDa
TGFBI Transforming growth factor-beta-induced protein ig-h3	IPI00018219	75 kDa
TGM2 Isoform 1 of Protein-glutamine gamma-glutamyltransferase 2	IPI00294578	77 kDa
THBS1 Thrombospondin-1	IPI00296099	129 kDa
THRAP3 Thyroid hormone receptor-associated protein 3	IPI00104050	109 kDa
TJP1 Isoform Long of Tight junction protein ZO-1	IPI00216219	195 kDa
TJP2 Isoform A1 of Tight junction protein ZO-2	IPI00003843	134 kDa
TJP3 TJP3 protein	IPI00744036	105 kDa
TKT cDNA FLJ54957, highly similar to Transketolase	IPI00643920	69 kDa
TLN1 Talin-1	IPI00298994	270 kDa
TMED10 Transmembrane emp24 domain-containing protein 10	IPI00028055	25 kDa
TMED2 Transmembrane emp24 domain-containing protein 2	IPI00016608	23 kDa
TMED4 Isoform 1 of Transmembrane emp24 domain-containing protein 4	IPI00296259	26 kDa
TMEM43 Transmembrane protein 43	IPI00301280	45 kDa
TMEM63A Transmembrane protein 63A	IPI00006006	92 kDa
TMOD3 Tropomodulin-3	IPI00005087	40 kDa
TMPO Isoform Beta of Lamina-associated polypeptide 2, isoforms beta/gamma	IPI00030131	51 kDa
TMSB4X Thymosin beta-4	IPI00220828	5 kDa
TNC Isoform 1 of Tenascin	IPI00031008	241 kDa
TNKS1BP1 Isoform 1 of 182 kDa tankyrase 1-binding protein	IPI00304589	182 kDa
TNS1 Tensin-1	IPI00307545	186 kDa
TNXB Isoform XB of Tenascin-X	IPI00025276	464 kDa
TOR1AIP1 Similar to Torsin-1A-interacting protein 1	IPI00644766	48 kDa
TPD52L2 Isoform 2 of Tumor protein D54	IPI00221178	20 kDa
TPM1 Isoform 3 of Tropomyosin alpha-1 chain	IPI00216135	33 kDa
TPM1 tropomyosin 1 alpha chain isoform 7	IPI00216134	29 kDa
TPM2 Isoform 2 of Tropomyosin beta chain	IPI00220709	33 kDa
TPM3 Isoform 2 of Tropomyosin alpha-3 chain	IPI00218319	29 kDa
TPM4 Isoform 1 of Tropomyosin alpha-4 chain	IPI00010779	29 kDa
TPM4 Isoform 2 of Tropomyosin alpha-4 chain	IPI00216975	33 kDa
TPP2 Tripeptidyl-peptidase 2	IPI00020416	138 kDa
TPR Nucleoprotein TPR	IPI00742682	267 kDa
TRAP1 Heat shock protein 75 kDa, mitochondrial	IPI00030275	80 kDa
TRIM25 Tripartite motif-containing protein 25	IPI00029629	71 kDa
TRIM28 Isoform 1 of Transcription intermediary factor 1-beta	IPI00438229	89 kDa
TRIM29 Isoform Alpha of Tripartite motif-containing protein 29	IPI00073096	66 kDa

TSN Translin	IPI00018768	26 kDa
TST Thiosulfate sulfurtransferase	IPI00216293	33 kDa
TSTA3 GDP-L-fucose synthetase	IPI00014361	36 kDa
TTC38 Tetratricopeptide repeat protein 38	IPI00550644	53 kDa
TTLL3;ARPC4 Actin-related protein 2/3 complex subunit 4	IPI00554811	20 kDa
TTN Isoform 2 of Titin	IPI00023283	3806 kDa
TUBA4A Tubulin alpha-4A chain	IPI00007750	50 kDa
TUBB Tubulin beta chain	IPI00011654	50 kDa
TUBB2A Tubulin beta-2A chain	IPI00013475	50 kDa
TUBB2C Tubulin beta-2C chain	IPI00007752	50 kDa
TUFM Tu translation elongation factor, mitochondrial precursor	IPI00027107	50 kDa
TXNDC5 Thioredoxin domain-containing protein 5	IPI00171438	48 kDa
TXNL1 Thioredoxin-like protein 1	IPI00305692	32 kDa
TXNRD1 Isoform 5 of Thioredoxin reductase 1, cytoplasmic	IPI00554786	55 kDa
TYMP Thymidine phosphorylase	IPI00292858	50 kDa
UBA1 Ubiquitin-like modifier-activating enzyme 1	IPI00645078	118 kDa
UBC;RPS27A;UBB ubiquitin and ribosomal protein S27a precursor	IPI00179330 (+22)	18 kDa
UBR4 Isoform 4 of E3 ubiquitin-protein ligase UBR4	IPI00640981	574 kDa
UCHL3 Ubiquitin carboxyl-terminal hydrolase isozyme L3	IPI00011250	26 kDa
UGDH UDP-glucose 6-dehydrogenase	IPI00031420	55 kDa
UGP2 Isoform 1 of UTP--glucose-1-phosphate uridylyltransferase	IPI00329331	57 kDa
UQCRC1 Cytochrome b-c1 complex subunit 1, mitochondrial	IPI00013847	53 kDa
UQCRC2 Cytochrome b-c1 complex subunit 2, mitochondrial	IPI00305383	48 kDa
UQCRFS1 Cytochrome b-c1 complex subunit Rieske, mitochondrial	IPI00026964	30 kDa
USO1 Putative uncharacterized protein DKFZp451D234	IPI00031583	109 kDa
USP14 Ubiquitin carboxyl-terminal hydrolase 14	IPI00219913	56 kDa
VAPA Vesicle-associated membrane protein-associated protein A	IPI00170692	28 kDa
VARS Valyl-tRNA synthetase	IPI00000873	140 kDa
VASP Vasodilator-stimulated phosphoprotein	IPI00301058	40 kDa
VAT1 Synaptic vesicle membrane protein VAT-1 homolog	IPI00156689	42 kDa
VCAN Isoform V0 of Versican core protein	IPI00009802	373 kDa
VCL Isoform 1 of Vinculin	IPI00291175	117 kDa
VCP Transitional endoplasmic reticulum ATPase	IPI00022774	89 kDa
VDAC1 Voltage-dependent anion-selective channel protein 1	IPI00216308	31 kDa
VIL1 Villin-1	IPI00218852	93 kDa
VILL Isoform 2 of Villin-like protein	IPI00215851	94 kDa
VIM Vimentin	IPI00418471	54 kDa
VPS26A Vacuolar protein sorting-associated protein 26A	IPI00411426	38 kDa
VPS35 Vacuolar protein sorting-associated protein 35	IPI00018931	92 kDa
VTN Vitronectin	IPI00298971	54 kDa
VWA5A Isoform 1 of Loss of heterozygosity 11 chromosomal region 2 gene A protein	IPI00005609	86 kDa
WDR1 Isoform 2 of WD repeat-containing protein 1	IPI00216256	58 kDa

WIBG Isoform 1 of Protein wibg homolog	IPI00305092	23 kDa
XPO1 Exportin-1	IPI00298961	123 kDa
XPO7 Exportin-7	IPI00302458	124 kDa
XRCC5 ATP-dependent DNA helicase 2 subunit 2	IPI00220834	83 kDa
XRCC6 ATP-dependent DNA helicase 2 subunit 1	IPI00644712	70 kDa
YBX1 Nuclease-sensitive element-binding protein 1	IPI00031812	36 kDa
YWHAB Isoform Long of 14-3-3 protein beta/alpha	IPI00216318	28 kDa
YWHAE 14-3-3 protein epsilon	IPI00000816	29 kDa
YWHAG 14-3-3 protein gamma	IPI00220642	28 kDa
YWHAH 14-3-3 protein eta	IPI00216319	28 kDa
YWHAQ 14-3-3 protein theta	IPI00018146	28 kDa
YWHAZ 14-3-3 protein zeta/delta	IPI00021263	28 kDa
ZNF185 Isoform 1 of Zinc finger protein 185	IPI00005688	49 kDa

Appendix II

Appendix II tabulates the comparison of the 854 proteome with previous published proteomic studies on pancreatic juice, blood and urine, and shows those proteins common to all studies analysed. This comparison was performed using the Pancreatic Expression Database (http://www.pancreaticexpression.org) (188).

Emsembl Gene ID	Ensembl Protein ID	HNGC Symbol
ENSG00000121410	ENSP00000263100	A1BG
ENSG00000175899	ENSP00000323929	A2M
ENSG00000114779	ENSP00000378455	ABHD14B
ENSG00000072778	ENSP00000349297	ACADVL
ENSG00000075239	ENSP00000265838	ACAT1
ENSG00000100412	ENSP00000216254	ACO2
ENSG00000075624	ENSP00000349960	ACTB
ENSG00000072110	ENSP00000193403	ACTN1
ENSG00000130402	ENSP00000252699	ACTN4
ENSG00000138071	ENSP00000260641	ACTR2
ENSG00000115091	ENSP00000263238	ACTR3
ENSG00000106624	ENSP00000223357	AEBP1
ENSG00000124942	ENSP00000367263	AHNAK
ENSG00000063438	ENSP00000264933	AHRR
ENSG00000117448	ENSP00000397013	AKR1A1
ENSG00000198074	ENSP00000352584	AKR1B10
ENSG00000162482	ENSP00000355377	AKR7A3
ENSG00000163631	ENSP00000295897	ALB
ENSG00000165092	ENSP00000297785	ALDH1A1
ENSG00000149925	ENSP00000400452	ALDOA
ENSG00000135046	ENSP00000366109	ANXA1
ENSG00000182718	ENSP00000387545	ANXA2
ENSG00000138772	ENSP00000264908	ANXA3
ENSG00000196975	ENSP00000377833	ANXA4
ENSG00000164111	ENSP00000296511	ANXA5
ENSG00000118137	ENSP00000236850	APOA1
ENSG00000198931	ENSP00000367615	APRT
ENSG00000130429	ENSP00000389631	ARPC1B
ENSG00000138363	ENSP00000236959	ATIC
ENSG00000152234	ENSP00000282050	ATP5A1
ENSG00000110955	ENSP00000262030	ATP5B
ENSG00000166710	ENSP00000340858	B2M
ENSG00000182492	ENSP00000327336	BGN
ENSG00000090013	ENSP00000263368	BLVRB
ENSG00000100220	ENSP00000216038	C22orf28
ENSG00000125730	ENSP00000245907	C3

ENSG00000104267	ENSP00000285379	CA2
ENSG00000198668	ENSP00000349467	CALM1
ENSG00000143933	ENSP00000272298	CALM2
ENSG00000160014	ENSP00000291295	CALM3
ENSG00000179218	ENSP00000320866	CALR
ENSG00000127022	ENSP00000394817	CANX
ENSG00000131236	ENSP00000361883	CAP1
ENSG00000042493	ENSP00000386315	CAPG
ENSG00000116489	ENSP00000263168	CAPZA1
ENSG00000121691	ENSP00000241052	CAT
ENSG00000159228	ENSP00000290349	CBR1
ENSG00000166226	ENSP00000299300	CCT2
ENSG00000150753	ENSP00000280326	CCT5
ENSG00000146731	ENSP00000275603	CCT6A
ENSG00000135624	ENSP00000258091	CCT7
ENSG00000105388	ENSP00000402431	CEACAM5
ENSG00000172757	ENSP00000309629	CFL1
ENSG00000230685	ENSP00000409979	CLIC1
ENSG00000187955	ENSP00000297848	COL14A1
ENSG00000134871	ENSP00000353654	COL4A2
ENSG00000142156	ENSP00000355180	COL6A1
ENSG00000142173	ENSP00000300527	COL6A2
ENSG00000163359	ENSP00000295550	COL6A3
ENSG00000047457	ENSP00000264613	CP
ENSG00000116791	ENSP00000339399	CRYZ
ENSG00000117984	ENSP00000384947	CTSD
ENSG00000100448	ENSP00000216336	CTSG
ENSG00000100243	ENSP00000379603	CYB5R3
ENSG00000011465	ENSP00000376862	DCN
ENSG00000153904	ENSP00000284031	DDAH1
ENSG00000206395	ENSP00000382936	DDAH2
ENSG00000091140	ENSP00000205402	DLD
ENSG00000187908	ENSP00000342210	DMBT1
ENSG00000132002	ENSP00000254322	DNAJB1
ENSG00000092964	ENSP00000309539	DPYSL2
ENSG00000104823	ENSP00000221418	ECH1
ENSG00000127884	ENSP00000357535	ECHS1
ENSG00000104529	ENSP00000317399	EEF1D
ENSG00000167658	ENSP00000307940	EEF2
ENSG00000084623	ENSP00000362688	EIF3I
ENSG00000143924	ENSP00000320663	EML4
ENSG00000074800	ENSP00000234590	ENO1
ENSG00000136628	ENSP00000355890	EPRS
ENSG00000166147	ENSP00000325527	FBN1
ENSG00000165140	ENSP00000364475	FBP1
ENSG00000171560	ENSP00000306361	FGA
ENSG00000171564	ENSP00000306099	FGB
ENSG00000171557	ENSP00000336829	FGG
ENSG00000091483	ENSP00000355518	FH
ENSG00000136068	ENSP00000295956	FLNB
ENSG00000115414	ENSP00000352696	FN1
ENSG00000075618	ENSP00000371798	FSCN1

ENSG00000087086	ENSP00000366525	FTL
ENSG00000111640	ENSP00000384819	GAPDH
ENSG00000171766	ENSP00000388809	GATM
ENSG00000148672	ENSP00000277865	GLUD1
ENSG00000172354	ENSP00000305260	GNB2
ENSG00000090615	ENSP00000204726	GOLGA3
ENSG00000148180	ENSP00000362924	GSN
ENSG00000100983	ENSP00000216951	GSS
ENSG00000148834	ENSP00000358727	GSTO1
ENSG00000084207	ENSP00000381607	GSTP1
ENSG00000206172	ENSP00000322421	HBA1
ENSG00000188536	ENSP00000251595	HBA2
ENSG00000244734	ENSP00000333994	HBB
ENSG00000143321	ENSP00000349878	HDGF
ENSG00000115677	ENSP00000312042	HDLBP
ENSG00000189403	ENSP00000343040	HMGB1
ENSG00000169045	ENSP00000377082	HNRNPH1
ENSG00000104824	ENSP00000221419	HNRNPL
ENSG00000153187	ENSP00000393151	HNRNPU
ENSG00000072506	ENSP00000168216	HSD17B10
ENSG00000080824	ENSP00000335153	HSP90AA1
ENSG00000096384	ENSP00000360609	HSP90AB1
ENSG00000166598	ENSP00000299767	HSP90B1
ENSG00000204389	ENSP00000364802	HSPA1A
ENSG00000232804	ENSP00000393087	HSPA1B
ENSG00000170606	ENSP00000302961	HSPA4
ENSG00000044574	ENSP00000324173	HSPA5
ENSG00000109971	ENSP00000227378	HSPA8
ENSG00000113013	ENSP00000297185	HSPA9
ENSG00000106211	ENSP00000248553	HSPB1
ENSG00000144381	ENSP00000373620	HSPD1
ENSG00000149428	ENSP00000384144	HYOU1
ENSG00000138413	ENSP00000260985	IDH1
ENSG00000182054	ENSP00000331897	IDH2
ENSG00000166411	ENSP00000299518	IDH3A
ENSG00000132465	ENSP00000254801	IGJ
ENSG00000132305	ENSP00000387262	IMMT
ENSG00000140575	ENSP00000268182	IQGAP1
ENSG00000151655	ENSP00000351190	ITIH2
ENSG00000167768	ENSP00000252244	KRT1
ENSG00000186395	ENSP00000269576	KRT10
ENSG00000111057	ENSP00000373489	KRT18
ENSG00000171345	ENSP00000355124	KRT19
ENSG00000172867	ENSP00000310861	KRT2
ENSG00000135480	ENSP00000329243	KRT7
ENSG00000170421	ENSP00000293308	KRT8
ENSG00000171403	ENSP00000246662	KRT9
ENSG00000002549	ENSP00000226299	LAP3
ENSG00000136167	ENSP00000315757	LCP1
ENSG00000134333	ENSP00000395337	LDHA
ENSG00000111716	ENSP00000229319	LDHB
ENSG00000100097	ENSP00000215909	LGALS1

ENSG00000131981	ENSP00000254301	LGALS3
ENSG00000108679	ENSP00000262776	LGALS3BP
ENSG00000071282	ENSP00000157600	LMCD1
ENSG00000160789	ENSP00000357283	LMNA
ENSG00000113368	ENSP00000261366	LMNB1
ENSG00000139329	ENSP00000266718	LUM
ENSG00000120992	ENSP00000397807	LYPLA1
ENSG00000090382	ENSP00000261267	LYZ
ENSG00000102882	ENSP00000263025	MAPK3
ENSG00000168906	ENSP00000303147	MAT2A
ENSG00000014641	ENSP00000233114	MDH1
ENSG00000146701	ENSP00000327070	MDH2
ENSG00000240972	ENSP00000215754	MIF
ENSG00000005381	ENSP00000225275	MPO
ENSG00000128309	ENSP00000411719	MPST
ENSG00000013364	ENSP00000378760	MVP
ENSG00000100345	ENSP00000216181	MYH9
ENSG00000105835	ENSP00000222553	NAMPT
ENSG00000104419	ENSP00000404854	NDRG1
ENSG00000023228	ENSP00000392709	NDUFS1
ENSG00000198805	ENSP00000354532	NP
ENSG00000105953	ENSP00000222673	OGDH
ENSG00000102837	ENSP00000219022	OLFM4
ENSG00000185624	ENSP00000327801	P4HB
ENSG00000116288	ENSP00000418770	PARK7
ENSG00000169564	ENSP00000305556	PCBP1
ENSG00000100889	ENSP00000216780	PCK2
ENSG00000063438	ENSP00000264933	PDCD6
ENSG00000170248	ENSP00000307387	PDCD6IP
ENSG00000168291	ENSP00000307241	PDHB
ENSG00000167004	ENSP00000300289	PDIA3
ENSG00000089220	ENSP00000261313	PEBP1
ENSG00000108518	ENSP00000225655	PFN1
ENSG00000102144	ENSP00000362413	PGK1
ENSG00000079739	ENSP00000360125	PGM1
ENSG00000167085	ENSP00000300408	PHB
ENSG00000133110	ENSP00000369071	POSTN
ENSG00000180817	ENSP00000362329	PPA1
ENSG00000196262	ENSP00000419425	PPIA
ENSG00000166794	ENSP00000300026	PPIB
ENSG00000213639	ENSP00000378769	PPP1CB
ENSG00000105568	ENSP00000324804	PPP2R1A
ENSG00000117450	ENSP00000361152	PRDX1
ENSG00000167815	ENSP00000301522	PRDX2
ENSG00000165672	ENSP00000298510	PRDX3
ENSG00000123131	ENSP00000368646	PRDX4
ENSG00000117592	ENSP00000342026	PRDX6
ENSG00000188783	ENSP00000411768	PRELP
ENSG00000204983	ENSP00000308720	PRSS1
ENSG00000197746	ENSP00000378394	PSAP
ENSG00000129084	ENSP00000379675	PSMA1
ENSG00000161057	ENSP00000391211	PSMC2

ENSG00000161057	ENSP00000292644	PSMC2
ENSG00000165916	ENSP00000298852	PSMC3
ENSG00000092010	ENSP00000206451	PSME1
ENSG00000132341	ENSP00000376176	RAN
ENSG00000114115	ENSP00000232219	RBP1
ENSG00000198755	ENSP00000363018	RPL10A
ENSG00000198755	ENSP00000363018	RPL10AP9
ENSG00000142676	ENSP00000363676	RPL11
ENSG00000161016	ENSP00000262584	RPL8
ENSG00000112306	ENSP00000230050	RPS12
ENSG00000140988	ENSP00000341885	RPS2
ENSG00000008988	ENSP00000009589	RPS20
ENSG00000171858	ENSP00000345957	RPS21
ENSG00000143947	ENSP00000385659	RPS27A
ENSG00000140988	ENSP00000341885	RPS2P11
ENSG00000149273	ENSP00000278572	RPS3
ENSG00000198034	ENSP00000362744	RPS4X
ENSG00000137154	ENSP00000369757	RPS6
ENSG00000143546	ENSP00000357721	S100A8
ENSG00000163220	ENSP00000357727	S100A9
ENSG00000163993	ENSP00000296370	S100P
ENSG00000101347	ENSP00000262878	SAMHD1
ENSG00000109072	ENSP00000226218	SEBOX
ENSG00000168385	ENSP00000385387	SEPT2
ENSG00000197249	ENSP00000390299	SERPINA1
ENSG00000196136	ENSP00000376795	SERPINA3
ENSG00000021355	ENSP00000370115	SERPINB1
ENSG00000149257	ENSP00000350894	SERPINH1
ENSG00000072501	ENSP00000323421	SMC1A
ENSG00000197157	ENSP00000346762	SND1
ENSG00000137767	ENSP00000260324	SQRDL
ENSG00000148175	ENSP00000286713	STOM
ENSG00000165283	ENSP00000348886	STOML2
ENSG00000149591	ENSP00000278968	TAGLN
ENSG00000158710	ENSP00000357077	TAGLN2
ENSG00000177156	ENSP00000321259	TALDO1
ENSG00000091513	ENSP00000385834	TF
ENSG00000120708	ENSP00000416330	TGFBI
ENSG00000198959	ENSP00000355330	TGM2
ENSG00000137801	ENSP00000260356	THBS1
ENSG00000137076	ENSP00000316029	TLN1
ENSG00000167460	ENSP00000300933	TPM4
ENSG00000232575	ENSP00000410071	TUBB
ENSG00000235067	ENSP00000401317	TUBBP1
ENSG00000183311	ENSP00000373058	TUBBP2
ENSG00000178952	ENSP00000322439	TUFM
ENSG00000239264	ENSP00000369081	TXNDC5
ENSG00000025708	ENSP00000252029	TYMP
ENSG00000130985	ENSP00000366568	UBA1
ENSG00000169764	ENSP00000338703	UGP2
ENSG00000010256	ENSP00000203407	UQCRC1
ENSG00000140740	ENSP00000268379	UQCRC2

ENSG00000165280	ENSP00000351777	VCP
ENSG00000213585	ENSP00000378484	VDAC1
ENSG00000026025	ENSP00000224237	VIM
ENSG00000109072	ENSP00000226218	VTN
ENSG00000071127	ENSP00000371890	WDR1
ENSG00000166913	ENSP00000300161	YWHAB
ENSG00000164924	ENSP00000379287	YWHAZ